Numerical Simulation of Boundary-Layer Control using MEMS Actuation

by

Duncan Lockerby

A thesis submitted in partial fulfilment
of the requirements for the degree of

Doctor of Philosophy in Engineering

The University of Warwick, School of Engineering

March 2001

Contents

List of Figures

List of Tables

Acknowledgements

I would like to thank everyone who has helped me during this project, but especially my supervisor, Peter Carpenter, for his continual support and guidance. I would also like to thank Chris Davies from Coventry University for his help with the numerical aspects of the research. Finally, I would like to thank Bea for proof reading and for her general help.

The research reported here was undertaken as part of: The AEROMEMS project (An investigation into the Viability of MEMS Technology for Boundary-Layer Control on Aircraft) is a collaboration between British Aerospace, Dassault Aviation, CNRS and the Universities of Warwick, Manchester, Berlin, Madrid, Athens, Lausanne and Tel-Aviv. The project is managed by British Aerospace and is partially funded by the CEC under the IMT initiative (Project Ref: BRPR CT97-0573).

Declaration

This thesis, and the material in it, is my own work. It has not been submitted for a degree at any other university.

Abstract

MEMS actuators and their effect on boundary layers is investigated using numerical simulation. The thesis is specifically focussed on jet actuators and their application to the targeted control of turbulent boundary layers.

A complete numerical model of jet-type actuators, including the popular synthetic-jet actuator, is developed. The assumed input is the voltage signal to the piezoceramic driver and the calculated output is the exit jet velocity. Thorough validation of the numerical code is presented and simulations performed to highlight the key issues in MEMS-actuator design.

The three-dimensional boundary-layer disturbance created by the MEMS actuator is modelled using a velocity-vorticity formulation of the Navier-Stokes equations. The parallel code is rigorously validated against results from linear stability theory and transitional-streak measurements. The boundary-layer code is used to determine a performance criterion for MEMS jets; it is shown that the net mass flow from a jet best determines its effectiveness. The code is also used to demonstrate the macro-scale capabilities of MEMS-scale actuators; a grid-scaling method is described and employed to facilitate this calculation.

A method is presented that enables high- and low-speed streaks to be modelled economically in otherwise undisturbed mean flows. Using this model, the fundamental principles of targeted control using MEMS actuation are explored.

The MEMS-actuator and boundary-layer models are coupled, and an investigation into the interactive effects of the two systems is described. Using the coupled code, disturbances in the boundary layer are shown to induce velocities in inactive devices. One special case occurs when an oscillating pressure field creates Helmholtz resonance within the cavity of a MEMS actuator, thus causing large mass flow rates in and out of the device. It is also suggested that the MEMS device could strongly interact with the random fluctuations of a turbulent boundary layer, leading to highly unpredictable actuator responses.

Chapter 1

Introduction and Background

Microelectromechanical systems (MEMS) are devices with both electrical and mechanical components, fabricated to micron scale using integrated-circuit batch-processing techniques. This relatively new technology has already produced many 'MEMS devices' of practical significance. Such examples include the fabrication of micro grippers for medical applications, miniature sensors for airbag control, and micron-sized neuron probes. In particular, the application of MEMS in turbulence control has inspired much interest. Reviews of the state of MEMS technology in relation to flow control are given in Mehregany *et al.* (1996), Ho and Tai (1996),(1998), Gad-el-Hak (1999), and Löfdahl and Gad-el-Hak (1999).

Potentially, there are many benefits from the successful control of turbulence including: improved combustion efficiency, suppression of flow-related noise, and most popularly, the reduction of skin-friction drag on airfoils. The latter example is perhaps the strongest motivational force behind research, as even the slightest reduction in skin-friction drag could lead to huge savings in air-transport fuel costs.

Another benefit of an active control scheme is that it would provide a tool to help understand the mysteries of turbulence. However, many people believe that turbulence is already sufficiently well understood to enable its control. The popular opinion is that the coherent structures observable in turbulent flows are

directly or indirectly responsible for the chaotic, non-deterministic nature of the turbulence. If this is true then a simple method for control exists – to *target* the coherent structures. Unfortunately, the size of these structures, in most flows of interest, are too small for conventional sensing and actuation. For this reason MEMS, with characteristic lengths of one to one hundred microns, are keenly favoured for use in turbulence control.

The current research is focussed on the actuators that would be used in control, but does not address any microfabrication issues. A review by Löfdahl and Gad-el-Hak (1999) provides a detailed description of the microfabrication techniques, MEMS sensors, and control schemes relevant to turbulence control.

Detailed reviews on the subject of turbulence control (active and passive) are given in Bushnell and McGinley (1989) and Fielder and Fernholz (1990), although most of the work relevant to this thesis has been performed since their publication. What follows is an overview of the recent research in active turbulence control in boundary layers (§1.1). Focus is then placed on a specific actuator that is thought to be a good candidate for turbulence control schemes – the synthetic jet (§1.2). This provides a background to the current research project which is then finally introduced (§1.3).

1.1 Targeted Control of Turbulence

1.1.1 Coherent Structures

It is widely thought that the non-deterministic nature of a turbulent flat-plate boundary layer is governed or triggered by coherent structures in the near-wall region. These structures are the famous 'hairpin' vortices and 'low-speed' streaks, observed by, amongst others, Kline *et al.* (1967) ('streaks' are often associated with 'streamwise vortices'). The relationship between these two structures and their role in turbulence production is still open to some interpretation (Acarlar and Smith 1987, Smith *et al.* 1991, review: Robinson 1991), although it is generally conjectured that the lift-off and subsequent breakdown of low-speed streaks is fundamental to the quasi-cyclic regeneration of turbulence (Kline *et al.* 1967, Swearingen and Blackwelder 1987). If this is truly the case, interrupting or provoking this sequence (collectively termed as the bursting process) would reduce or increase the generation of turbulence. This simple idea of targeting coherent structures forms the basis of most methods in the active control of turbulence. The scheme has been advocated by many authors including Gad-el-Hak and Blackwelder (1989), Gad-el-Hak (1993), Rathnasingham and Breuer (1997b), Jacobson and Reynolds (1998), and Carlson and Lumley (1996a,b), and is here referred to as *targeted control.*

1.1.2 Drag Reduction

The pursuit of net drag reduction has been a strong motivational force in active control, since it is estimated that even marginal drag reduction could translate to enormous savings in air-transport fuel costs. Passive control methods, such as global suction, have enjoyed limited success, since they often expend more energy than they save. The advantage of a targeted control scheme is that it can apply actuation only to the areas within the turbulent flow that contribute directly or indirectly to high skin-friction – the coherent structures. What follows

is a description of the main experimental and numerical research aimed at the negation of coherent structures and at the reduction of drag.

Experimental studies

Several experiments have been performed that investigate the effect of actuation on the coherent structures. These studies are all idealised proof-of-concept investigations, and tend to be concerned with how basic actuation can affect isolated streaks and streamwise vortices.

In experiment these structures have to be generated artificially so that their position can be reasonably controlled. Suction through a pair of minute holes was employed by Gad-el-Hak and Hussain (1986) to generate streaks and hairpin vortices in a turbulent boundary layer (a pitched delta wing was also used to generate the same structures). Gad-el-Hak and Blackwelder (1989) applied this method in a laminar boundary layer and used a suction slot positioned underneath the low-speed streaks to successfully stabilise the bursting phenomenon (a few results were also obtained in a turbulent boundary layer). At the very least this work demonstrates that the structures can be controlled by localised disturbances, although it is hard to tell how much energy was exerted in the suction.

Jacobson and Reynolds (1998) used a cylinder (and also suction holes) in their laminar-flow experiments to generate streamwise vortices and streaks which they controlled using a type of synthetic-jet actuator (synthetic jets will be discussed in some detail in §1.2). The actuator was itself capable of creating low-speed streaks that were utilised to cancel artificially generated high-speed streaks. This research is an advance on the work of Gad-el-Hak and Blackwelder (1989), since it demonstrates the control of coherent structures using a self-contained actuator – a step towards MEMS-based turbulent control. As yet, however, the actual devices are too inefficient and too large to be used as the actual drag-reducing actuators.

In a similar way, Ho and Tai (1996) reduced the shear stress underneath

a stationary artificial high-speed streak using an oscillatory flap actuator. In addition to this they developed an array of micro-sensors capable of detecting the location of non-artificial streaks.

All the previously mentioned studies of actuation were performed using artificial streaks within laminar boundary layers. Rathnasingham and Breuer (1997b), on the other hand, demonstrated active control within a fully-developed turbulent boundary layer. Their method used a linear feed-forward control algorithm to detect the randomly occurring streaks. The control scheme managed to reduce the streamwise velocity fluctuations by 31%, although reductions in skin-friction drag could not be confidently estimated. A more detailed account of this work is given in Rathnasingham (1997). This work is an advance on the likes of Gad-el-Hak and Blackwelder (1989) and Jacobson and Reynolds (1998), but only three shear-stress sensors and a single synthetic-jet actuator were involved in the experiment – many more sensors and actuators are needed to fully demonstrate the viability of active control.

Numerical Studies

The success of drag reduction relies upon the ability of an array of sensors and actuators to control many streaks simultaneously; this is referred to as distributed control. Experimental investigation is not yet at the point where distributed control can be realised, but with the aid of numerical simulations the potential can be demonstrated.

The most significant contribution to research in this field has come from Choi *et al.* (1994). Their direct numerical simulation (DNS) of turbulent channel flow was used as a testing ground for a simple distributed control scheme. In an attempt to cancel the high- and low-speed streaks, wall velocities (spanwise and normal) were set equal and opposite to the fluid velocities at a predetermined height in the channel. A drag reduction between 20-30% was obtained. When the wall velocities were set equal and in phase with the off-wall velocities, an

increase in drag was achieved.

These simulations, although impressive, are very idealised. The control applied at the wall is directly based on 'off-wall' information which in practice is unobtainable. In acknowledgement of this Choi *et al.* (1994) attempted to correlate the presence of streaks with 'wall' information only. The drag reduction from such simulations was as little as 6%. This is disappointing when considering that passive control devices, such as riblets, can achieve comparable drag reductions.

In response to this work, Lee *et al.* (1997) trained a neural network to find a more accurate correlation between wall values (shear stress in this case) and the position of streaks and streamwise vortices. This research was also performed in turbulent channel flow (DNS). The trained network was used to derive a simple and efficient control scheme capable of producing 20% drag reduction. This is a significant improvement on the previous attempts of Choi *et al.* (1994).

Koumoutsakos (1997), also furthering the work of Choi *et al.* (1994), described a method of calculating the wall vorticity flux by wall pressure measurements. The level of vorticity flux at the wall can be used to directly prescribe the level of blowing and suction required from an actuator. The method was successful in recreating some two-dimensional vortex control, previously demonstrated by Choi *et al.* (1994) using 'off-wall' information only. Later, this method was tested in DNS turbulent channel flow and was shown to be capable of reducing the drag by an impressive 40% (Koumoutsakos 1999).

Turning away from the numerical investigations of distributed control, the DNS work of Carlson and Lumley (1996a) examined the effects of raising a bump-type actuator underneath individual streaks. These channel-flow computations were performed within a minimal flow unit, defined by Jimenez and Moin (1991) as the smallest computational box capable of sustaining turbulent flow. This research enabled an investigation into how actuation can affect isolated but 'natural' streaks rather than isolated streaks that have been 'artificially' generated (Gad-el-Hak and Hussain 1986). The findings of the study support the general

hypothesis that redistributing the fluid in high-speed streaks away from the wall, reduces skin-friction. However, an inherent problem was found with the bump-type actuator; namely, that the lowering of the bump, increases the skin friction by dragging high-momentum fluid near to the wall. Also, the final actuation position protruded some way above the viscous sublayer, and was as such, not hydraulically smooth. Deflected-boundary actuation is perhaps more suited to transitional control, such as that in Breuer *et al.* (1989), where the benefits of delaying transition would outweigh the immediate skin-friction penalty.

Discussion

There is still slight doubt as to the exact cause of the high skin friction associated with the turbulent boundary layer. Orlandi and Jimenez (1994) suggest that the high skin friction is a consequence of the nonlinear nature of the turbulence and is directly linked to the low-speed, and intermittent high-speed, streaks that cover the near-wall region. Alternatively, some stage of the bursting process (perhaps the 'sweep' that follows the 'ejection') could be responsible for a high-skin-friction event. Both these ideas were acknowledged by Jacobson and Reynolds (1998) who noted that, for the purposes of control, it was not essential to know the exact mechanism, since the target for control (the streaks and associated streamwise vortices) were the same in both cases.

In this section accounts of two types of control have been given: blowing (or upward motion) under high-speed streaks, and suction under low-speed streaks. Both types of actuation reduce the spanwise variation of streamwise velocity and hence delay the associated secondary instability that is possibly responsible for high-skin-friction events and the production of turbulence (Swearingen and Blackwelder 1987). The disadvantage with suction, however, is that it directly *increases* the skin friction, since it draws high-momentum fluid nearer the wall. This would suggest that blowing underneath high-speed streaks is the most efficient mode of operation for net drag reduction. It should be recognised, however,

that suction applied to stabilise the low-speed streaks may be more effective at controlling the overall level of turbulence, owing to the low-speed streaks' more prominent role in bursting.

In light of this it seems appropriate to make a distinction between drag-reduction schemes that are primarily concerned with reducing high shear stress at the wall (direct), and drag-reduction schemes that are focussed on inhibiting an instability (indirect). The two types of targeted control are analogous to a treatment of the symptom and the cause – the latter is less immediate but probably more effective.

It should finally be noted that the belief in targeted control for active drag reduction is not without objection. For example, Schoppa and Hussain (1998) have proposed a method by which the development of streaks is subdued by large-scale non-targeted forcing. However, this particular method has not been implemented experimentally.

1.1.3 Targeted Separation Control

The findings detailed in §1.1.2 can also be applied to the control of turbulent boundary-layer separation. For example, using opposite methods to those previously described, the overall level of turbulence could be increased rather than decreased, thus increasing the boundary-layer's propensity to remain attached to its surface.

It could be argued that for separation delay a non-targeted scheme, such as that demonstrated by Seifert *et al.* (1993) would be as, if not more, efficient than a targeted scheme. Gad-el-Hak and Hussain (1986) have generated streaks in a controlled manner; in addition to this a tendency has been demonstrated for a wide class of three-dimensional disturbances to generate streaks in shear flows (Breuer and Haritonidis 1990, Landahl 1990, Henningson *et al.* 1993, Bech *et al.* 1998, Berlin and Henningson 1999). If streaks can be so readily generated in the flow, then it seems unnecessary to target the same naturally occurring structures.

However, it is known that not all streaks generate bursts, and therefore the input energy might be more efficiently spent selectively enhancing existing streaks to increase the overall rate of bursting. If the latter method is adopted, blowing underneath low-speed streaks and providing suction underneath high-speed streaks would appear to be a suitable choice of actuation to delay separation. This control is indirect and aims to provoke an instability that will in turn create turbulence.

1.1.4 Actuator Specification

The turbulent control application dictates a very challenging sensor and actuator specification. Here only the demands on the actuator's dimensions and response rate are considered (for sensor requirements see Löfdahl and Gad-el-Hak 1999, pp 121–122)

Before actuator dimensions can be proposed, typical flight conditions must be defined. For an aircraft at cruise speed (at sea level) the following values can be estimated: U_∞ (free-stream velocity)=300 m s^{-1}, v^* (friction velocity)=10 m s^{-1}, ν (kinematic viscosity)=15 mm^2 s^{-1} and ν/v^* (the wall unit)=1.5 μm. For the rest of this thesis these values will be referred to as flight-scale conditions.

The average spanwise spacing of the low-speed streaks is widely quoted as being $100\nu/v^*$ (Kline *et al.* 1967), and the length of streaks up to ten times this (Blackwelder and Eckelmann 1979). In flight conditions this equates to a 150 μm streak spacing and a 1.5 mm streak length. An actuator employed to directly manipulate these structures would be a fraction of their average spanwise spacing. For a circular jet, a suitable orifice diameter would be no greater than $40\nu/v^*$ (60 μm). Devices of such scale were not even a possibility until the fabrication technologies of MEMS, and even so, no such device has yet been employed as a flow-control actuator.

Temporal demands are also placed on the actuators by the streak characteristics. Here, the bursting frequency of the streaks defines a minimum requirement

of actuator duration (the time taken to administer its actuation). However, there has been some speculation as to whether the bursting frequency scales with inner variables (v^{*2}/ν) or outer variables (U_∞/δ^*). Rao *et al.* (1971) presented convincing results to support the suggestion that bursting frequency scales with the outer variables. More recently, Blackwelder and Haritonidis (1983) opposed this idea by noting that the sensors used in the experiments of Rao *et al.* (1971) (and similar studies) had insufficient spatial resolution. Here the frequency will be assumed to scale with inner variables; the average bursting frequency is then approximately f^+=0.04 (Blackwelder and Haritonidis, 1983). At flight scale this relates to an average time between bursts of 24 μs (f=260 kHz).

If an actuator is to be successful in controlling single coherent structures its duration should be no longer than the average period between bursts. It is likely, however, that the time a fixed actuator has to control a streak would be much less than this, since the streaks travel quickly downstream and can also move in the spanwise direction. A reasonable actuator duration would be around a fifth of the average time between bursts – 5μs. A similar estimate can be obtained by a simple analysis of the streak length and speed. The length of streaks is observed as being no less than $500\nu/v^*$, and their convection speed approximately $10v^*$ (Johansson *et al.* 1987). Therefore, the time that a streak is directly overhead a fixed actuator and in controllable territory, is roughly $50\nu/v^{*2}$ (7.5μs). What is conclusive from both estimates is that the time scale on which a device must administer actuation is very short.

In an array where each actuator is separated by 150 μm in the spanwise direction (the average streak spacing) and 0.5 mm in the streamwise direction (the average streak length), the amount of actuators required to cover a 1 m^2 surface area would be well in excess of ten million. Also note, that if each actuator performed control every one hundred burst periods then in total (for the 1 m^2 array) there would be more than eight billion actuations per second. This is a colossal number, and helps to visualise the difficulty there will be in implementing a

MEMS-based turbulent control scheme. However, intelligent control of whatever kind, should reduce the density of the array and frequency of actuation needed to achieve beneficial effects on aerodynamic performance.

1.2 The Synthetic-Jet Actuator

It is known that oscillating velocity fields can generate jets via a mechanism akin to acoustic streaming (review: Lighthill 1978). Davidson and Riley (1972), for example, produced a jet through oscillation of a cylinder perpendicular to its axis; in this case the streaming was driven by viscous dissipation. Jets generated by such streaming mechanisms are referred to as *synthetic* jets, also known as massless or zero-mass jets.

The synthetic-jet phenomenon was exploited by Jacobs *et al.* (1993) and James *et al.* (1994) who forced, at resonance, a surface-mounted piezo-electric disc to synthesise a turbulent jet via a train of vortex puffs. The streaming mechanism was also, no doubt, involved in the work of Wiltse and Glezer (1993), who used resonantly driven cantilevers to manipulate a square-conduit jet. This body of research demonstrated the flow-control potential of synthetic jets and piezo-electric actuators, and inspired further effort into the design of synthetic-jet actuators.

It was Glezer and his co-workers (Coe *et al.* 1994) who designed the micro-scale synthetic-jet actuator shown in Figure 1.1; referred to here as the diaphragm-cavity design (note: in this thesis there is a clear distinction made between *MEMS*-scale devices, $1\mu\text{m} < l < 100\mu\text{m}$, and *micro*-scale devices, $100\mu\text{m} < l < 10\text{mm}$; where l is a characteristic length scale). This design of synthetic-jet actuator has received most research attention. The device consists of a diaphragm, set within a cavity, that is driven by a piezo-electric (or electro-static) force at its resonant frequency. An orifice in the lid of the device allows fluid to be drawn into, and forced out of, the cavity.

Smith and Glezer (1998) performed a detailed experimental investigation into the synthetic jet created by these devices (also reported in Smith and Glezer 1997). It is claimed, that during the outflow cycle a vortex ring is formed at the orifice. This ring then travels away from the device under its own self-induced velocity. By the time the fluid is drawn into the cavity, the vortex ring has

moved sufficiently far away so as to be relatively unaffected; consequently a train of vortices traveling away from the orifice is generated. In their experiments the vortices rapidly undergo transition and lose their coherence. The resulting synthetic jet is turbulent.

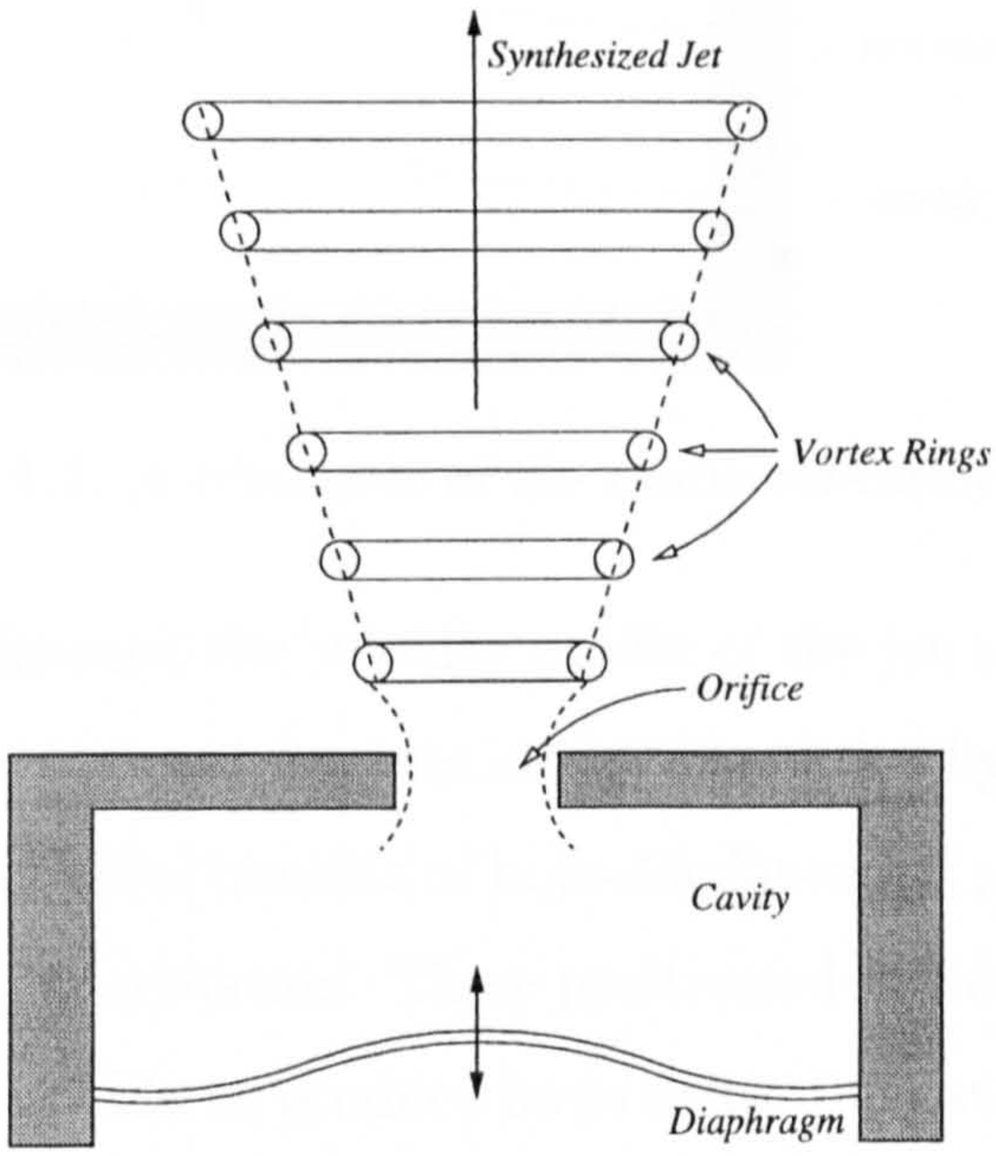

Figure 1.1: A schematic of a synthetic-jet actuator; the diaphragm-cavity design.

The experimental findings of Smith and Glezer (1997, 1998) were supported by Kral *et al.* (1997) who performed a two-dimensional numerical study of a laminar synthetic-jet. Even though the reality is three-dimensional and turbulent, the flow visualisations of Kral *et al.* (1997) provide a powerful demonstration of how the streaming is produced.

Rathnasingham and Breuer (1997a) drew attention away from the jet and instead focussed on the physics within the cavity. It was demonstrated, by the use of experimental and simple numerical models, that there was significant fluid-structure interaction between the resonant diaphragm and the fluid pressure in the cavity. Interest in the cavity was continued by Rizzetta *et al.* (1999) who solved the three-dimensional compressible Navier-Stokes equations both inside and outside of the cavity. It was shown that significant vortical disturbances could be created in the cavity during the inflow cycle of the actuator. The dimensions

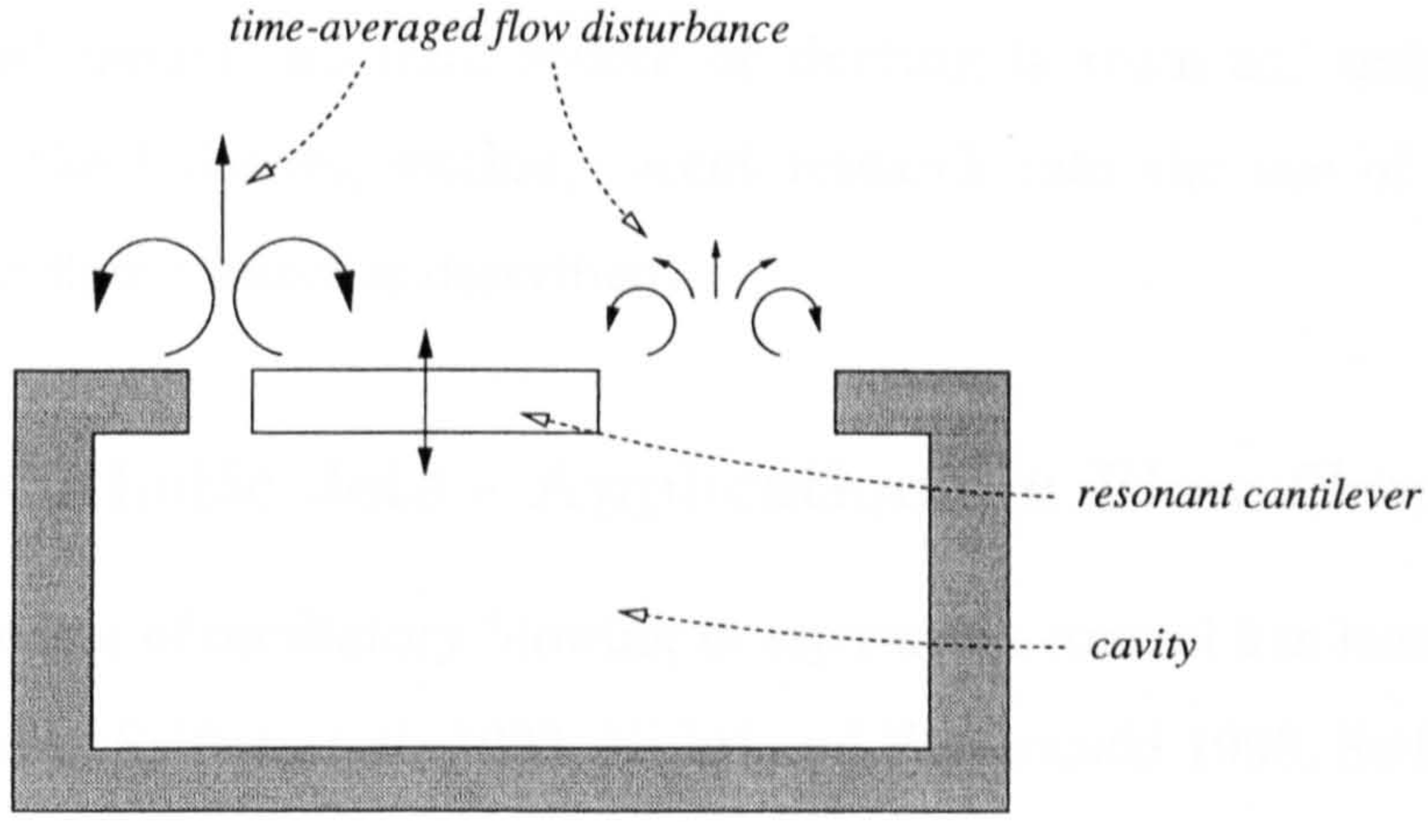

Figure 1.2: A schematic of the cantilever-cavity design.

of the cavity also influenced the velocity profile of the jet at the orifice exit.

The diaphragm-cavity actuator was slightly modified by Bryant *et al.* (1999) to demonstrate the potential benefits of high-displacement piezoelectric actuators (HGA's) in synthetic-jet actuation. These prestressed devices have the advantage of durability and being able to produce large deflections at non-resonant driving frequencies. Unfortunately, the HGA-driven synthetic-jet actuator cannot yet compete with the standard diaphragm and piezo-electric configuration.

A different synthetic-jet actuator, as shown in Figure 1.2, was designed and fabricated by Jacobson and Reynolds (1993) (as cited in Jacobson and Reynolds 1998). This design has a piezo-electric cantilever that is driven at resonance and suspended over a cavity. In between the cantilever and the cavity there are gaps of unequal width that allow unsteady flow into, and out of, the cavity. This device is referred to as the cantilever-cavity actuator (also known as the Jet and Vortex Actuator, or JaVA - Lachowicz *et al.* 1999). The types of jet generated from this device can vary dramatically with different dimensions, and thus significant effort has been spent in understanding the more complicated flow physics of the design (*experimental*: Saddoughi 1994 – as cited in Rathnasingham 1997, Lachowicz *et al.* 1998, 1999; *numerical*: Koumoutsakos 1995, Joslin *et al.* 1998 – as cited in Lachowicz *et al.* 1999).

The popularity of synthetic-jet actuators for flow-control, stems from their

self-contained design; no fluid source or ducting is required, only an applied voltage. In the following section, recent research into the use of synthetic-jet actuators for flow control is described.

1.2.1 Synthetic Jets - Applications in Flow Control.

The effectiveness of oscillatory blowing in separation control has been established experimentally (Seifert *et al.* 1993, Nishri and Wygnanski 1998, Seifert and Pack 1999, Béra *et al.* 2000) and numerically (Hassan and JanakiRam 1997, Hassan 1998, Donovan *et al.* 1998). In light of this, it would seem that synthetic-jet actuators are ideally suited to separation control, owing to their oscillatory operating mode. It should be noted that there are possibly two synthetic operating modes within a cross flow: a mixing mode where, compared to the cross flow, the oscillations are too infrequent for a jet to be synthesised and a continuous-jet mode, where the actuator is fast enough to synthesise, and be equivalent to, a continuous jet in a cross flow.

Similar fundamental uncertainties encouraged the investigation of the effect of synthetic-jet actuators on simple two-dimensional cylinder flow. Amitay *et al.* (1997, 1998) installed a pair of planar diaphragm-cavity actuators on a cylinder - these were successful in controlling the cylinder lift and drag forces. In their experiments it was found that the interaction of the synthetic jet and the cross flow resulted in a closed recirculation region and an apparent modification to the flow boundary. This substantially changed the surface pressure and could be utilised to influence separation. Mallinson *et al.* (1999) investigated similar control on a cylinder (although less thoroughly) and instead used a single diaphragm-cavity actuator with a circular orifice. Again, control over a cylinder was performed by Crook *et al.* 1999 (see also Wood *et al.* 2000), using a spanwise array of diaphragm-cavity actuators to delay separation.

Smith *et al.* (1998) fitted the cylinder model of Amitay *et al.* (1997, 1998) with an aerodynamic fairing designed to be comparable in proportion to the

NACA four-digit-series airfoils (the NACA-0015 airfoil was used in the computations/experiments of Seifert *et al.* 1993, Donovan *et al.* 1998, and Seifert and Pack 1999; and the NACA-0012 airfoil was used in the computations of Hassan and JanakiRam 1997, Hassan 1998, and Donovan *et al.* 1998). The pair of planar diaphragm-cavity actuators were capable of reattaching the flow on the simplified airfoil for angles of attack up to 18°.

Other types of flow control have been demonstrated using synthetic-jet actuators. For example, a pair of small-scale diaphragm-cavity actuators have been employed to vector a large-scale jet (Smith and Glezer 1997). Also, the control of vortex asymmetry on a hemisphere-cylinder forebody has been successfully demonstrated (Roos 1997).

The flow-control demonstrations most relevant to the focus of this thesis are those performed on streamwise vortices and streaks. Jacobson and Reynolds (1998) used a cantilever-cavity actuator to reduce the strength of high-speed streaks, and Rathnasingham and Breuer(1997b) used a diaphragm-cavity actuator to produce a similar result (more detail was given in §1.1). Although these experiments were successful, they both employed micro-scale (as opposed to MEMS scale) actuators within low-speed boundary layers. In the next section it will be discussed why synthetic jets would not be as suitable for streaks of the scale encountered in flight conditions.

1.2.2 Synthetic Jets and Targeted Control

As observed in the previous section, the flow-control potential of synthetic jets is already well established. However, this need not necessarily mean that the devices are suitable for targeted control in a turbulent boundary layer. Perhaps the most obvious concern is how the oscillatory synthetic jet will be able to affect single coherent structures in a controlled manner.

In §1.1.4 it was estimated that the actuator at flight scale should have a duration of no longer than t^+=50 (7.5μs). A reasonable demand on the synthetic-

jet actuator would be to synthesise a jet within at least a fifth of this period (t^+=10). Now considering that the synthetic jet must have several diaphragm cycles to establish itself (approx. five – Rathnasingham 1997) a fair approximation of diaphragm frequency would be around f^+=3; this allows 25 diaphragm cycles in the actuation period of t^+=50. This frequency in flight conditions is an incredibly high figure, roughly 20 MHz. Even with only five diaphragm cycles per actuation period the resulting driving frequency of 4 MHz would be very difficult to achieve. This presents a major case against the viability of using synthetic-jet actuators for targeted control.

Another practical disadvantage with the MEMS-scale synthetic-actuator concept is that there is a risk of dust clogging the device during the inflow cycle. Aircraft manufacturers see this as a serious issue, since cleaning MEMS would be a very demanding operation. Not all MEMS designs need suffer from this drawback. For example, the microvalves of Vandelli *et al.* (1998) and Yang and Kao (2000), close automatically after operation. Microvalves, however, require a fluid source and a ducting network.

Two main points have been made in this section that suggest that synthetic-jet actuators are unsuitable for targeted control. Firstly, owing to the inflow cycle of the synthetic jet, the MEMS-scale device would be likely to clog with dust. Secondly, the jet frequency would need to be around two orders of magnitude greater than the bursting frequency, so that the synthetic jet could be formed in time to control the streaks. This places tough demands on the diaphragm's driving frequency.

The successful applications demonstrated in the previous section have mainly been examples of large-scale control using smaller-scale actuators. Targeted control is different in this respect, as the coherent structures would be much more comparable to the actuator in size. An ideal actuator for targeted control would exploit the advantages of the self-contained diaphragm-cavity design but not rely on resonant or oscillatory forcing. This is considered in §1.3.

1.3 The Current Research Project

The current research project is a numerical study, and as such, allows the investigation of many issues regarding MEMS actuators and their interaction with boundary layers and streaks. This section outlines the structure of the thesis and highlights the main aspects of the current work that depart from previous research approaches.

The type of actuator that has been the focus of the project is the synthetic jet proposed by Coe *et al.* (1994) since its self-contained design is a particularly attractive feature for flow control (see Figure 1.1). Rathnasingham and Breuer (1997a) provided a starting point for the modelling of this device, but the techniques employed in this thesis are a considerable improvement on theirs and far wider in scope. The numerical model is detailed and complete; it is based on the premise that it should be capable of predicting the time-varying output given the input voltage signal to the piezoceramic driver. This modelling is described in Chapter 2.

Owing to the unsuitability of the synthetic-jet actuator for targeted control described in §1.2.2, an alternative forcing mechanism has been adopted; continuous rather than sinusoidal. The resulting jet has a puff-type response that does not have the disadvantages of the MEMS-scale synthetic jet. The model of the diaphragm-cavity actuator is tested and investigated in Chapter 3.

In this thesis, a vorticity-velocity formulation of the Navier-Stokes equations (Davies and Carpenter 1997, 1999) has been used to model the boundary-layer disturbances generated by actuation. In Chapter 4 the mathematical formulation and numerical implementation are described, followed by a code validation.

In Chapter 5, the boundary-layer code is used to investigate issues of practical concern for MEMS actuation. A large number of simulations in this thesis have been performed with undisturbed laminar boundary layers, even though the intended operating environment is turbulent. Laminar simulations are still relevant, however, since the interest lies in the near-wall region of the turbulent

boundary layer where viscous effects dominate. Also, research into MEMS actuation is still at a preliminary stage, and so information on how the devices affect boundary layers in general is still useful.

The numerical simulation of actuation within a boundary layer has been performed by Choi *et al.* (1994), Carlson and Lumley (1996a,b), Hoffman and Herbert (1997a,b), Lee *et al.* (1997), Hassan and JanakiRam (1997), Hassan (1998), and Donovan *et al.* (1998). In all of these simulations the actuation has been predetermined and imposed as a boundary condition to the flow field; the interaction between the flow disturbance and the actuator has not been modelled. One of the most novel aspects of the current research is that both the actuator and the boundary-layer disturbances are calculated simultaneously, allowing an interactive simulation to be performed. The nature of the interaction is investigated in Chapter 6.

In Chapter 7 a theoretical model is developed for the high- and low-speed streaks. This is used to undertake a study of the control of these structures using MEMS actuation with interactive and non-interactive simulations.

Finally, in Chapter 8, the main conclusions of the thesis are summarised and recommendations for further research are given.

Chapter 2

Modelling the Actuator

2.1 Introduction

Several actuator designs have been proposed for the turbulent control application, but one, first designed and micro-fabricated by Coe *et al.* (1994), has received significant research attention (Rathnasingham and Breuer 1997a,b, Smith and Glezer 1998, Rizzetta *et al.* 1999, Crook *et al.* 1999). Figure 2.1 shows a schematic of the design (there are slight design variations between references).

The diaphragm, perhaps made of silicon or brass, is mounted within a sunken cavity. The diaphragm's motion, induced by the electrostrictive force of an adhered piezo-electric device (PZT), produces pressure fluctuations inside the cavity. These pressure variations force fluid in and out of the cavity via an orifice in the device's cap. The jet actuator modelling in this thesis is aimed at this 'diaphragm-cavity' design.

The modelling approach adopted here, is based and built upon a method described by Rathnasingham and Breuer (1997a) (also adopted by Crook *et al.* 1999). Their strategy involved separating the actuator into three subsystems: the diaphragm, the cavity, and the orifice (see Figure 2.1). The relationship and behaviour of the subsystems was described using a set of differential equations,

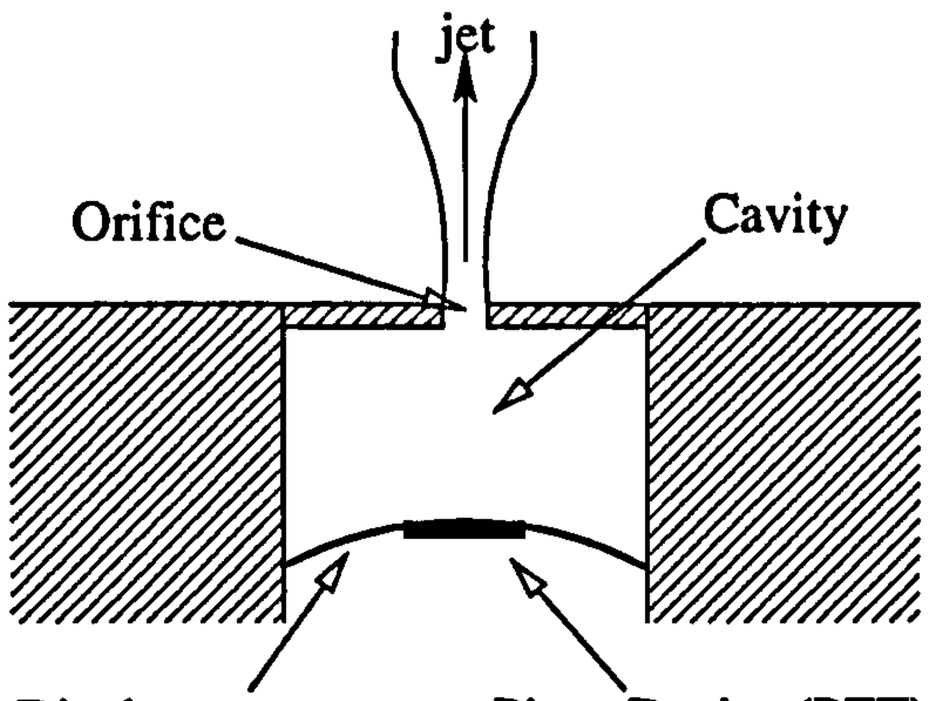

Figure 2.1: A schematic of the jet actuator

which could be solved using a Runge-Kutta, or similar numerical method. In this thesis, however, the orifice and diaphragm are modelled more accurately, and the dynamics of a circular PZT can be simulated. Although several improvements to the Rathnasingham and Breuer model have been made, the simulations of the actuator are still intended to be computationally inexpensive. The numerical economy of the model makes the coupling with a boundary-layer code feasible, and also allows many more simulations to be performed.

The current chapter details the modelling and numerical implementation of the four main components of the actuator system: The diaphragm (§2.2), the PZT (§2.3), the orifice (§2.4), and the cavity (§2.5).

A = maximum magnitude of pressure gradient Π_x (m s^{-2})

A_c = cap area of cavity (m^2)

A_d = area of diaphragm (m^2)

A_o = orifice area (m^2)

B = flexural rigidity (N m)

B_1, B_2 = flexural rigidity of material 1/2 (N m)

B_e = effective flexural rigidity (N m)

d = structural damping (kg s^{-1} m^{-2})

d_{31}, d_{32} = radial/azimuthal piezo-electric constant (m V^{-1})

E = elastic modulus (N m^{-2})

E_d, E_p = elastic modulus of diaphragm, PZT (N m^{-2})

E_1, E_2 = elastic modulus of material 1/2 (N m^{-2})

f_1, f_2 = implicit functions

F_a = applied force per unit area (N m^{-2})

i = complex variable

I = second moment of area (m^4)

I_n = modified Bessel functions

J_n = Bessel functions of the first kind

λ = mean free path (m)

k_n, k_x = dimensionless constants

K_n = the Knudsen number

l = length of orifice (m)

L = characteristic length (m)

M, M_a = applied moment per unit length (N)

M_c = mass of fluid in cavity (kg)

$\dot{M}_{out}$ = rate of mass flow through the orifice (kg s^{-1})

M_x, M_y = moment per unit length (N)

P = pressure (N m^{-2})

P_1, P_2 = pressure at station 1/2 (N m^{-2})

P_a = applied pressure (N m^{-2})

P_c = cavity pressure (N m^{-2})

q = force per unit area (N m^{-2})

r = radial coordinate (m)

r_d, r_o = radial coordinate for diaphragm/orifice (m)

r_{jn} = radial position of material join (m)

R = radius of orifice (m) in §2.4, gas constant (J kg^{-1} K^{-1}) in §2.5

R_d, R_p = radius of diaphragm/PZT (m)

t = time (s) in §2.2, §2.4, and §2.5; thickness (m) in §2.3

t_1, t_2 = thickness of material 1/2 (m)

t_d, t_p = thickness of diaphragm/PZT (m)

T = temperature (K)

u = streamwise orifice velocity (m s^{-1})

u_1, u_2 = streamwise orifice velocity at station 1/2 (m s^{-1})

$\bar{u}_d, \bar{u}_o$ = average diaphragm/orifice-flow velocity (m s^{-1})

$\bar{u}_{o,\mathrm{inc}}$ = average incompressible orifice-flow velocity (m s^{-1})

u_p, u_v = potential/viscous flow solution (m s^{-1})

u_r, u_θ = radial/azimuthal orifice velocity (m s^{-1})

u_s = steady-state velocity (m s^{-1})

U_s = steady-state velocity at centre line (m s^{-1})

V = applied voltage (V)

V_c = volume of cavity (m^3)

$w, \dot{w}, \ddot{w}$ = deflection/velocity/acceleration of diaphragm (m, m s^{-1}, m s^{-2})

x, y, z = cartesian coordinates (m)

z_n = distance to neutral surface from material join (m)

z' = coordinate with neutral surface as origin (m)

δ = small length (m)

δr = radial grid spacing (m)

$\Delta, \Delta r$ = radial grid spacing (m)

δt = time step (s)

Δt = time step (s)

Δu = velocity increment over time step (m s^{-1})

ε_p = piezo-electric strain

ε_x = longitudinal strain

ζ = dimensionless radial coordinate

θ = azimuthal coordinate

$\ddot{\theta}$ = angular acceleration (s^{-2})

κ = curvature (m^{-1})

λ = mean free path (m)

λ_n = roots of Bessel functions

μ = dynamic viscosity (kg m^{-1} s^{-1})

ν = Poisson's ratio in §2.2, §2.3; kinematic viscosity (m^2 s^{-1}) in §2.4

ν_1, ν_2 = Poisson's ratio of material 1/2

ν_e = effective Poisson's ratio

Π_x = oscillating pressure gradient $(1/\rho)\ dp/dx$ (m s^{-2})

ρ = density (kg m^{-3})

ρ_c = cavity fluid density (kg m^{-3})

ρ_1, ρ_2 = density at station 1/2 (kg m^{-3})

ρ_d = diaphragm density (kg m^{-3})

σ_e = deformation stress (N m^{-2})

σ_p = piezo-electric stress (N m^{-2})

σ_x = longitudinal stress (N m^{-2})

$\sigma_{x,1}, \sigma_{x,2}$ = longitudinal stress in material 1/2 (N m^{-2})

Φ = mode shape of diaphragm deflection

ω = frequency of pressure gradient (s^{-1})

ω_n = natural frequency (s^{-1})

$\nabla^2\nabla^2$ = the biharmonic operator (m^{-4})

2.2 The Diaphragm

The diaphragm is the forcing mechanism for the actuator. Its motion, induced by an attached PZT (see Section 2.3), affects the cavity pressure directly. If the exit jet is to be calculated accurately, then an accurate description of the cavity pressure variations, and consequently the diaphragm's motion, is needed.

Rathnasingham and Breuer (1997a) modelled the diaphragm as a piston, which described volumetric changes to the cavity similar to those resulting from an oscillating diaphragm. This method worked by assuming a sinusoidal forcing mechanism, enabling the use of a known solution for the diaphragm's response. With this analytical foreknowledge, a 2D spring and piston model was calibrated to give a fair approximation of the diaphragm's effect on the pressure in the cavity. This approach could not, however, accommodate arbitrary forcing methods, and would not guarantee an accurate description of the volumetric changes. More importantly, because the model needs to be calibrated, the method would not be of much use for designing actuators, or predicting the performance of actuator designs. In the present simulations, a time-dependent finite-difference approximation of the classical plate equation has been implemented, in order to overcome the aforementioned shortcomings.

2.2.1 Mathematical Modelling

The governing equations for a thin elastic plate are partial differential equations of the fourth order (see Jaeger 1964, Leissa 1969, Marguerre & Woernle 1969). For modelling circular diaphragms in polar co-ordinates the system can be simplified to one spatial dimension, if azimuthal symmetry is assumed; in this application there is unlikely to be significant azimuthal variation. The equation of motion for vertical, axi-symmetric, deflection of the diaphragm, $w(r,t)$, is as such:

$$\rho_d t_d \ddot{w} + d\dot{w} + B\nabla^2\nabla^2 w = P_a - P_c \tag{2.1}$$

where w is the diaphragm's deflection (the dot notation refers to time derivatives), ρ_d is the diaphragm's density, t_d is the diaphragm thickness, B is the flexural rigidity, d is the structural damping, P_a is the applied force, and P_c is the force due to the pressure in the cavity. For axi-symmetric disturbances, the biharmonic operator ($\nabla^2\nabla^2$) and the flexural rigidity (B), are defined as follows:

$$B = \frac{Et_d^3}{12\left(1-\nu^2\right)} \tag{2.2}$$

$$\left[\nabla^2\nabla^2\right] \equiv \left[\frac{\partial^4}{\partial r^4} + \frac{2}{r}\frac{\partial^3}{\partial r^3} - \frac{1}{r^2}\frac{\partial^2}{\partial r^2} + \frac{1}{r^3}\frac{\partial}{\partial r}\right] \tag{2.3}$$

where r is the radial coordinate, E is the elastic modulus, and ν is Poisson's ratio.

In this thesis, all of the diaphragm modelling is linear; this is unrealistic for large amplitude deflections where radial tension is significant. A nonlinear model, such as that used in Lucey *et al.* (1997), could be used as an improvement.

2.2.2 Numerical Solution of the Plate Equation

A second-order finite-difference form of equation (2.1) is solved using a Crank-Nicolson numerical scheme (see Ferziger, 1998 p.196). The finite-difference equation and the two basis equations are similar to those detailed in Lucey and Carpenter (1993), and are here stated:

$$w_i^{t+\delta t} = w_i^t + \frac{\delta t}{2}\left(\dot{w}_i^t + \dot{w}_i^{t+\delta t}\right) \tag{2.4}$$

$$\dot{w}_i^{t+\delta t} = \dot{w}_i^t + \frac{\delta t}{2}\left(\ddot{w}_i^t + \ddot{w}_i^{t+\delta t}\right) \tag{2.5}$$

$$\ddot{w}_i^{t+\delta t} = -\frac{1}{\rho_d t_d}\left(d\dot{w}_i^{t+\delta t} + B\nabla^2\nabla^2 w_i^{t+\delta t} - P_{a,i}^{t+\delta t} + P_c^{t+\delta t}\right) \tag{2.6}$$

The variable w_i^t is the deflection at the finite-difference grid point i, at a discrete time t. Similarly, $\dot{w}_i^t$ and $\ddot{w}_i^t$ correspond to the velocity and acceleration of the plate at the grid point i, at a discrete time t. The time step is equal to δt, and variables are evaluated at $t+\delta t$ for the new time step. The biharmonic operator, $(\nabla^2\nabla^2)$, is approximated using centred differences by:

$$\begin{aligned}\left[\nabla^2\nabla^2\right] w_i = w_i & \left(\frac{6}{(\delta r)^4}+\frac{2}{r^2(\delta r)^2}\right) - \\ & w_{i+1}\left(\frac{4}{(\delta r)^4}+\frac{2}{r(\delta r)^3}+\frac{1}{r^2(\delta r)^2}-\frac{1}{2r^3\delta r}\right) - \\ & w_{i-1}\left(\frac{4}{(\delta r)^4}-\frac{2}{r(\delta r)^3}+\frac{1}{r^2(\delta r)^2}+\frac{1}{2r^3\delta r}\right) + \\ & w_{i+2}\left(\frac{1}{(\delta r)^4}+\frac{1}{r(\delta r)^3}\right) + w_{i-2}\left(\frac{1}{(\delta r)^4}-\frac{1}{r(\delta r)^3}\right) \qquad (2.7)\end{aligned}$$

Boundary Conditions

The diaphragm is clamped at its edges, which constitutes two boundary conditions: w=0 and dw/dr=0. The first can be enforced by simply setting the deflection equal to zero at r=R:

$$w_n = 0 \qquad (2.8)$$

(r=R at the nth grid point). The second boundary condition can be satisfied by introducing a dummy variable at r=R+δr, the (n+1)th grid point. The first derivative at the clamped edge can be expressed in terms of w_{n-1} and w_{n+1} (the dummy) by a second-order finite-difference approximation:

$$\frac{dw}{dr} = \frac{w_{n+1}-w_{n-1}}{2(\delta r)^2} \qquad (2.9)$$

The boundary condition is therefore enforced by

$$w_{n+1} = w_{n-1} \qquad (2.10)$$

The third boundary condition is a symmetry condition at r=0, and is not as straightforward as the first two to implement. The first grid point at which equation (2.6) can be applied is $i = 1$ (at r=δr not at r=0). To accommodate the width of the finite-difference molecule, a dummy variable is created at $i = -1$ (r=$-\delta r$). This necessitates the definition of two more boundary conditions (or at least two different ways of expressing the same condition). The condition to be satisfied is rotational symmetry, i.e. all the odd derivatives of deflection must equal zero at r=0. This is achieved by expressing Taylor expansions at r=δr and r=$-\delta r$:

$$w(\delta r) = w(0) + \sum_{i=1}^{\infty} \frac{(\delta r)^i w^i(0)}{i!} \tag{2.11}$$

$$w(-\delta r) = w(0) + \sum_{i=1}^{\infty} \frac{(-\delta r)^i w^i(0)}{i!} \tag{2.12}$$

If all odd derivatives are equal to zero at r=0, equations (2.11) and (2.12) can be reduced to:

$$w(\delta r) = w(0) + \sum_{i=1}^{\infty} \frac{(\delta r)^{2i} w^{2i}(0)}{(2i)!} \tag{2.13}$$

$$w(-\delta r) = w(0) + \sum_{i=1}^{\infty} \frac{(\delta r)^{2i} w^{2i}(0)}{(2i)!} \tag{2.14}$$

Equation (2.14) can now be subtracted from equation (2.13) to leave

$$w(\delta r) - w(-\delta r) = 0$$

$$w_1 = w_{-1} \tag{2.15}$$

This is the first statement, and enforcement, of rotational symmetry. The second boundary condition is also an enforcement of symmetry, however, it is implemented using a non-centred finite-difference scheme. Fourth-order Taylor expan-

sions are stated for $r = \delta r$ and $r = 2\delta r$ with odd derivatives omitted:

$$w(\delta r) = w(0) + \frac{(\delta r)^2}{2} w''(0) + \mathcal{O}\left((\delta r)^4\right) \tag{2.16}$$

$$w(2\delta r) = w(0) + 2(\delta r)^2 w''(0) + \mathcal{O}\left((\delta r)^4\right) \tag{2.17}$$

The final condition is obtained by combination of equation (2.16) and (2.17):

$$3w(0) - 4w(\delta r) + w(2\delta r) = 0$$

$$3w_0 - 4w_1 + w_2 = 0 \tag{2.18}$$

Initial Conditions

The conditions of the diaphragm at t=0, are zero deflection, velocity and acceleration. If there is a suddenly applied load, a smoothing function is used so that the acceleration at t=0 is zero. This acts over as small a time as possible and is similar to the quintic function in §2.3.2 – equation (2.50).

Forming and Solving the Matrix of Equations

For an implicit solution, equation (2.6) can be rearranged to leave the deflection at the new time step ($w^{t+\delta t}$) on the left-hand side of the equation. Equations (2.4) and (2.5) can then be used to eliminate any reference to velocity ($\dot{w}$) and acceleration ($\ddot{w}$) at the updated time ($t + \delta t$). The remaining equation is evaluated at grid points from i=1 to N−1, which provides (N−1) equations with (N+3) unknowns. The four boundary conditions, equations (2.8), (2.10), (2.15) and (2.18), provide the necessary constraints for a unique solution. The set of ($N+3$) equations can be constructed in matrix form (Ax=b), and arranged such that there are no time-dependent coefficients on the left-hand side (A). Computationally this is very efficient, because during a transient solution the factorised

matrix will not need to be re-calculated at every time step. The set of linear equations is solved using LU decomposition (see Ferziger p3, 1998). The LU factorisation is performed at the beginning of a computation, using a specialised Nag library (F07ADF). Back substitutions (F07AEF) are then performed at each time step.

2.2.3 Checking the Integrity of the Diaphragm Code

The diaphragm code can be validated against known solutions from thin plate theory (for elastic plate theory refer to Jaeger 1964, Leissa 1969, and Marguerre & Woernle 1969). These simulations do not take into account any pressure feedback from the cavity, such interactive effects are investigated in Chapter 3.

The Diaphragm's Natural Frequency

The first code check is performed by comparing the numerically-calculated natural frequency with the known analytical solution from plate theory. The axisymmetric harmonic frequencies for a thin plate are given by:

$$\omega_n = k_n \sqrt{\frac{E t_d^2}{12\left(1-\nu^2\right)\rho R_d^4}} \tag{2.19}$$

where n is equal to the number of nodal circles, R_d is the radius of the diaphragm, and the first four harmonics are given by $k_1 = 10.2158$, $k_2 = 39.771$, $k_3 = 89.104$, and $k_4 = 158.183$ (values from Leissa 1969).

In order to extract the fundamental frequency from the numerical simulation, the diaphragm is given a 'kick' or 'impulse' at time zero. The diaphragm is allowed to oscillate freely and a fast Fourier transform is performed on the output. Figure 2.2 shows the comparison of the FFT results (solid line) and the analytical value (vertical dashed line) of the fundamental mode of vibration. The result demonstrates conclusively the code's accuracy in determining the natural

frequency. Note that the ability to predict higher harmonics is dependent on the number of grid points in the finite-difference model and the size of time step relative to the harmonic's period. In this calculation twenty grid points have been used and a time step that is one hundred times smaller than the natural time period.

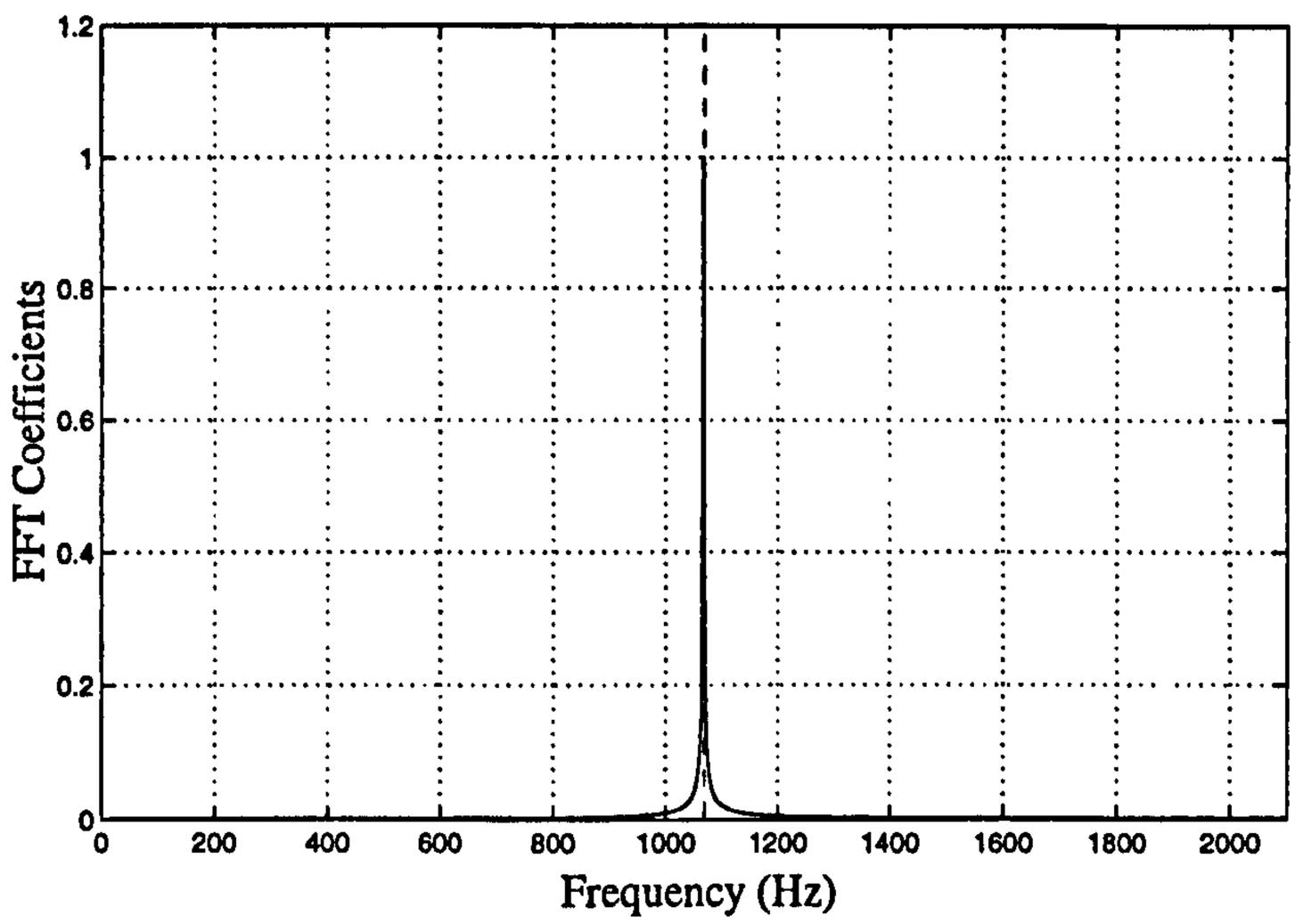

Figure 2.2: Comparison of analytically (--) and numerically (-) obtained natural frequency.

The Deflected Diaphragm

A second validation can be made against the steady-state response a plate would experience from a continuous and evenly distributed force. The analytical solution for this configuration is:

$$w = \frac{q}{64B}\left(R_d^2 - r^2\right)^2 \tag{2.20}$$

where w is the deflection at r, and q is the load per unit area. Figure (2.3) shows the comparison of equation (2.20) with an equivalent numerical simulation. The

comparison shows exact agreement.

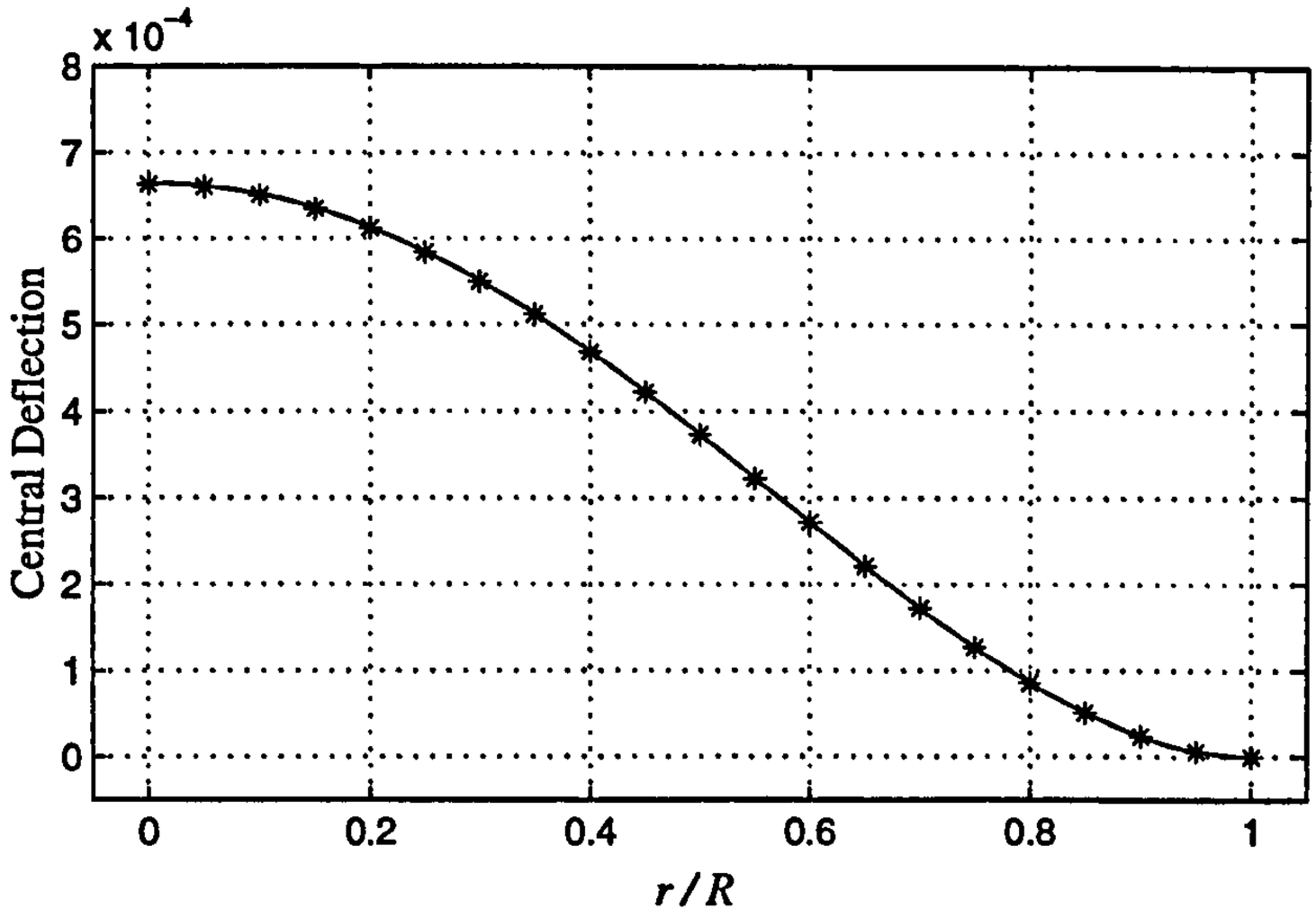

Figure 2.3: Comparison of analytical (–) and numerical (∗) steady-state solutions resulting from an evenly distributed load.

The Mode Shape of Diaphragm Vibration

The final diaphragm code check is against the mode shapes of deflection generated by different frequency forcings. Axi-symmetric mode shapes for a circular plate with a clamped edge are described by:

$$\Phi_n = J_{n-1}\left(\frac{\sqrt{k_n}r}{2R_d}\right) - \frac{J_{n-1}\left(\sqrt{k_n}\right)}{I_{n-1}\left(\sqrt{k_n}\right)} I_{n-1}\left(\frac{\sqrt{k_n}r}{2R_d}\right) \tag{2.21}$$

where J_n are Bessel functions of the first kind, I_n are modified Bessel functions, and the constants k_n are the same as for equation (2.19). Figure (2.4) shows the comparison between the first four solutions (n=1 to 4) of equation (2.21) and a ten-point finite-difference scheme. The solution accurately predicts the first two mode shapes, but begins to fail as the complexity increases on the third and fourth. Figure (2.5) shows the same comparisons, but with a finite-difference

scheme of twenty grid points. The numerical solution handles the complexity of the third harmonic comfortably, from which it can be inferred that all degrees of complexity are resolvable given a sufficiently large number of grid points. It is, however, important to decide what level is appropriate, and when additional grid points are superfluous.

The analytical cases that have been chosen to check the integrity of the diaphragm code, have compared very closely, if not exactly, with the numerical simulations; both static, and dynamic, agreement has been found. It is not unexpected that the validations have been so decisive, because the numerical and analytical solutions are based on the same linear theory. However, the purpose of this section has been to demonstrate the code's accuracy and integrity.

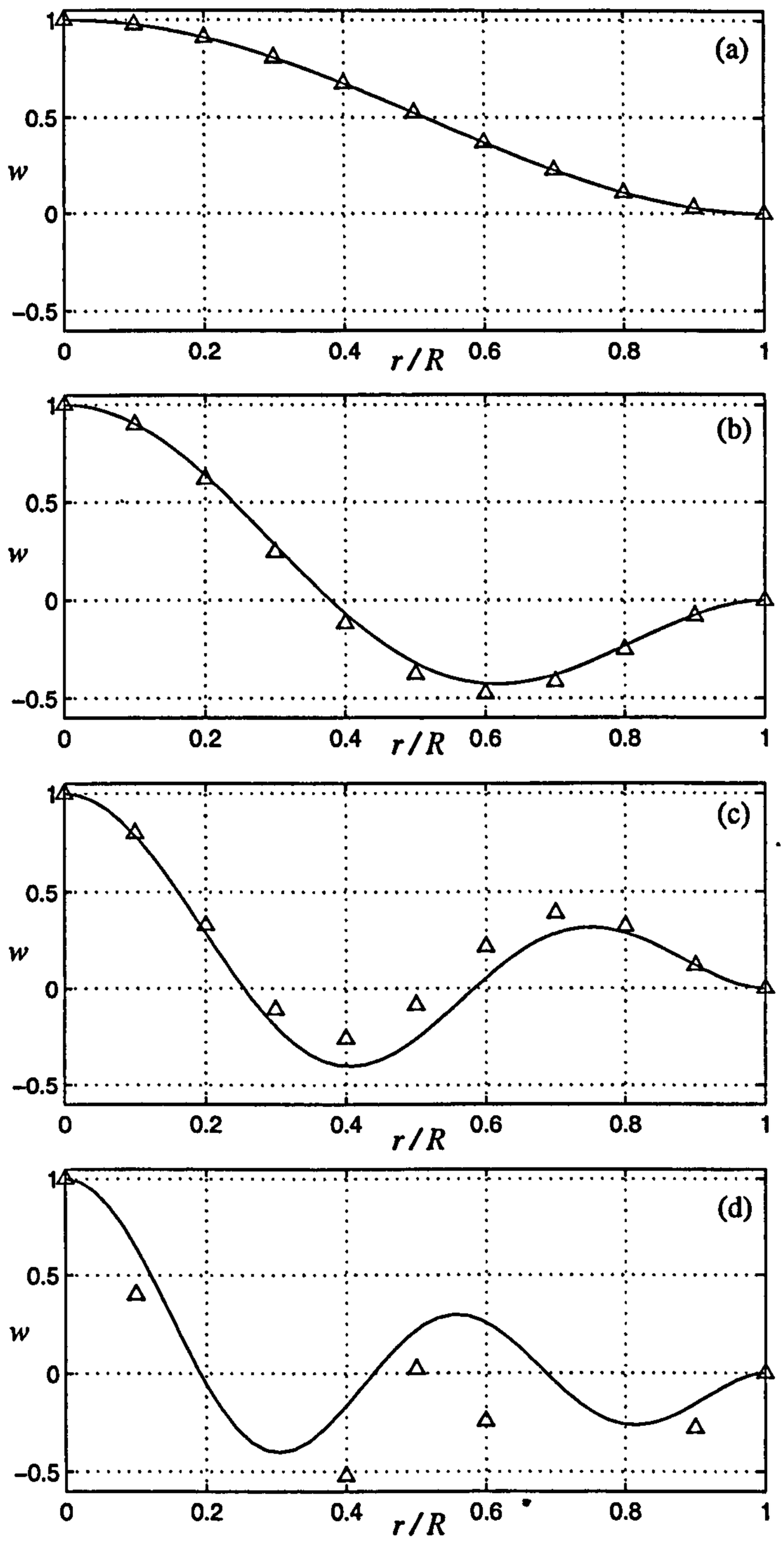

Figure 2.4: The mode shape of the ith harmonic frequency. (a) i=1, (b) i=2, (c) i=3 and (d) i=4. Comparison of the analytical solution (–) and a ten-point finite-difference scheme (Δ).

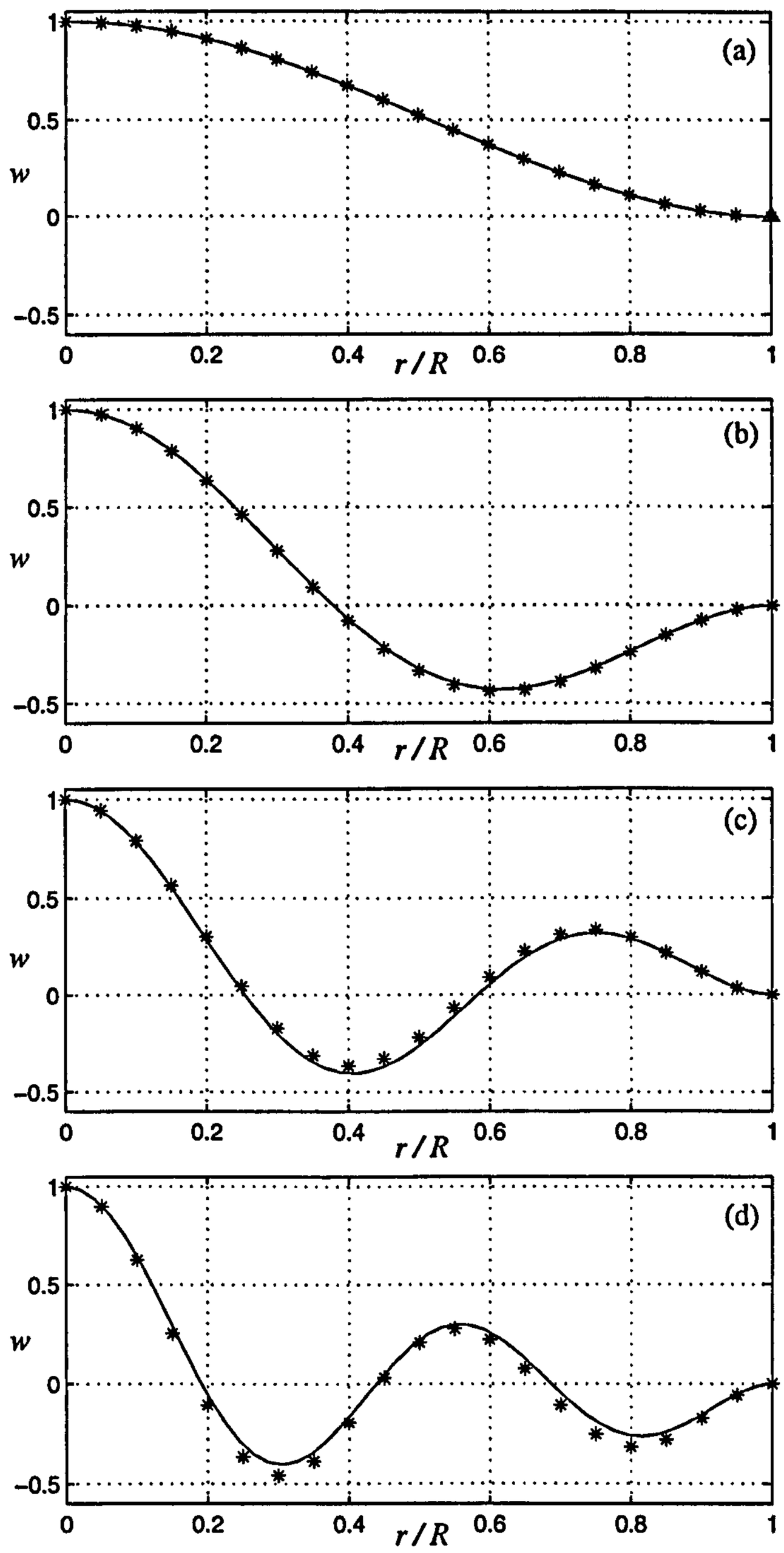

Figure 2.5: The mode shape of the ith harmonic frequency. (a) i=1, (b) i=2, (c) i=3 and (d) i=4. Comparison of the analytical solution (–) and a twenty-point finite-difference scheme (∗).

2.3 The PZT

Many diaphragm-driven jet actuators have been fabricated with a PZT adhered to their underside such as that shown in Figure 2.6. The Lead Zirconium Titanate (PZT) experiences a lateral expansion/contraction when subjected to an electric field. It is its tendency towards a new strain level, while at the same time being adhered to the diaphragm, which generates a moment, and consequently a downward acceleration of both diaphragm and PZT. The PZT also affects the overall stiffness and mass of the diaphragm, this can significantly alter the system's behaviour.

This section will firstly detail the method by which the stiffnesses of the PZT and diaphragm are combined (§2.3.1), and secondly, how the moment generated by the PZT is calculated (§2.3.2).

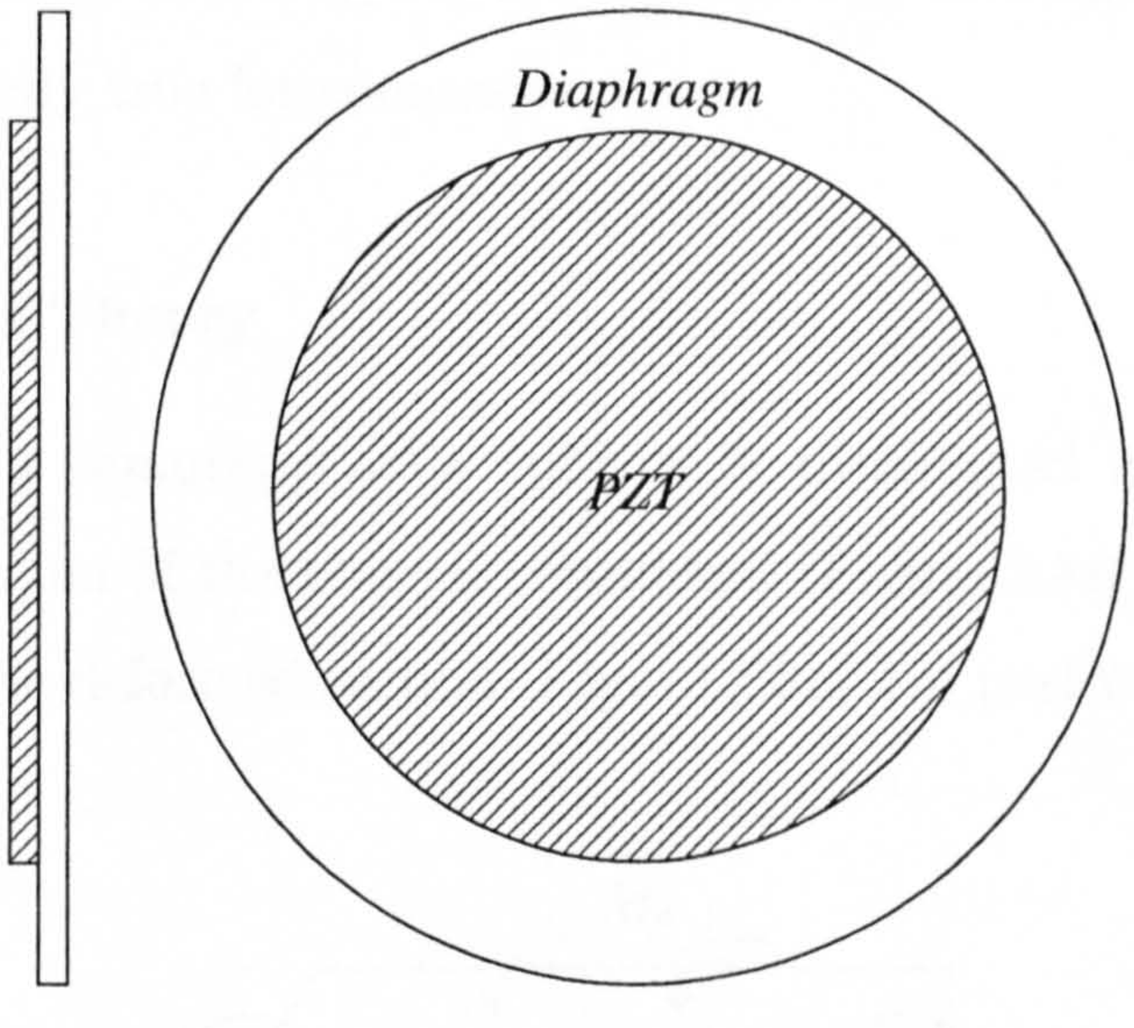

Figure 2.6: The PZT and diaphragm configuration.

2.3.1 The Composite PZT and Diaphragm

The relationship between moment and curvature is important in plate theory, since it is a direct reflection of the plate's rigidity. For homogeneous plates the curvature is related to moment by the following equations:

$$M_x = -\frac{Et^3}{12(1-\nu^2)}\left(\frac{\partial^2 w}{\partial x^2} + \nu\frac{\partial^2 w}{\partial y^2}\right)$$
$$M_y = -\frac{Et^3}{12(1-\nu^2)}\left(\frac{\partial^2 w}{\partial y^2} + \nu\frac{\partial^2 w}{\partial x^2}\right) \tag{2.22}$$

Where t is the plate's thickness, w is the deflection, E is the elastic modulus, and ν is Poisson's ratio. For composite plates, however, it is not so simple. The standard plate equations (2.22) assume that the elastic modulus is constant throughout the plate; this is not true in the composite case. As a consequence, equations (2.22) automatically assume that the neutral surface (the surface at which there is no stress or strain) lies exactly mid-way through the section; again this is not necessarily true for composite plates.

Composite Plate Theory

Figure 2.7 shows a composite plate subject to distributed moments along its edges. A small section of the plate is considered (Figure 2.8*i*) and it is assumed that the faces of the deformed section (Figure 2.8*ii*) are perfectly flat. From this

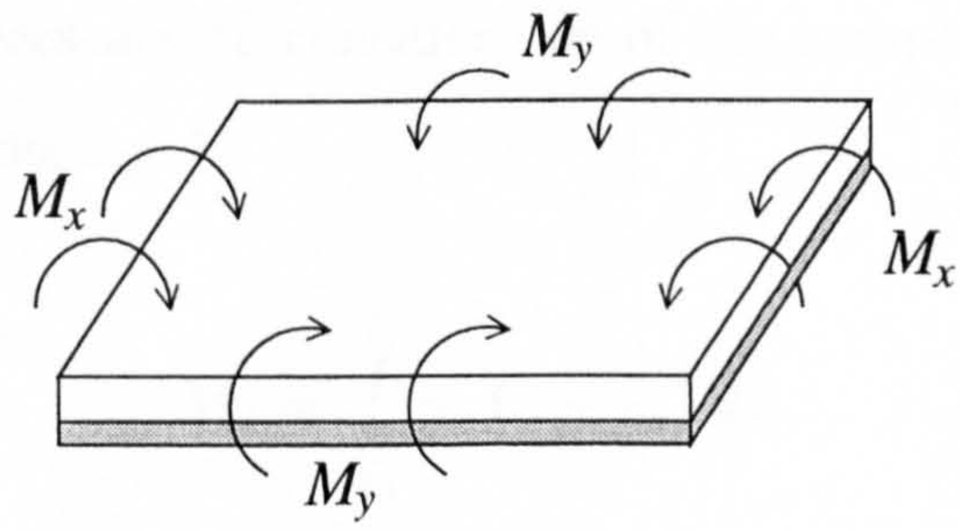

Figure 2.7: A composite plate subjected to distributed moments.

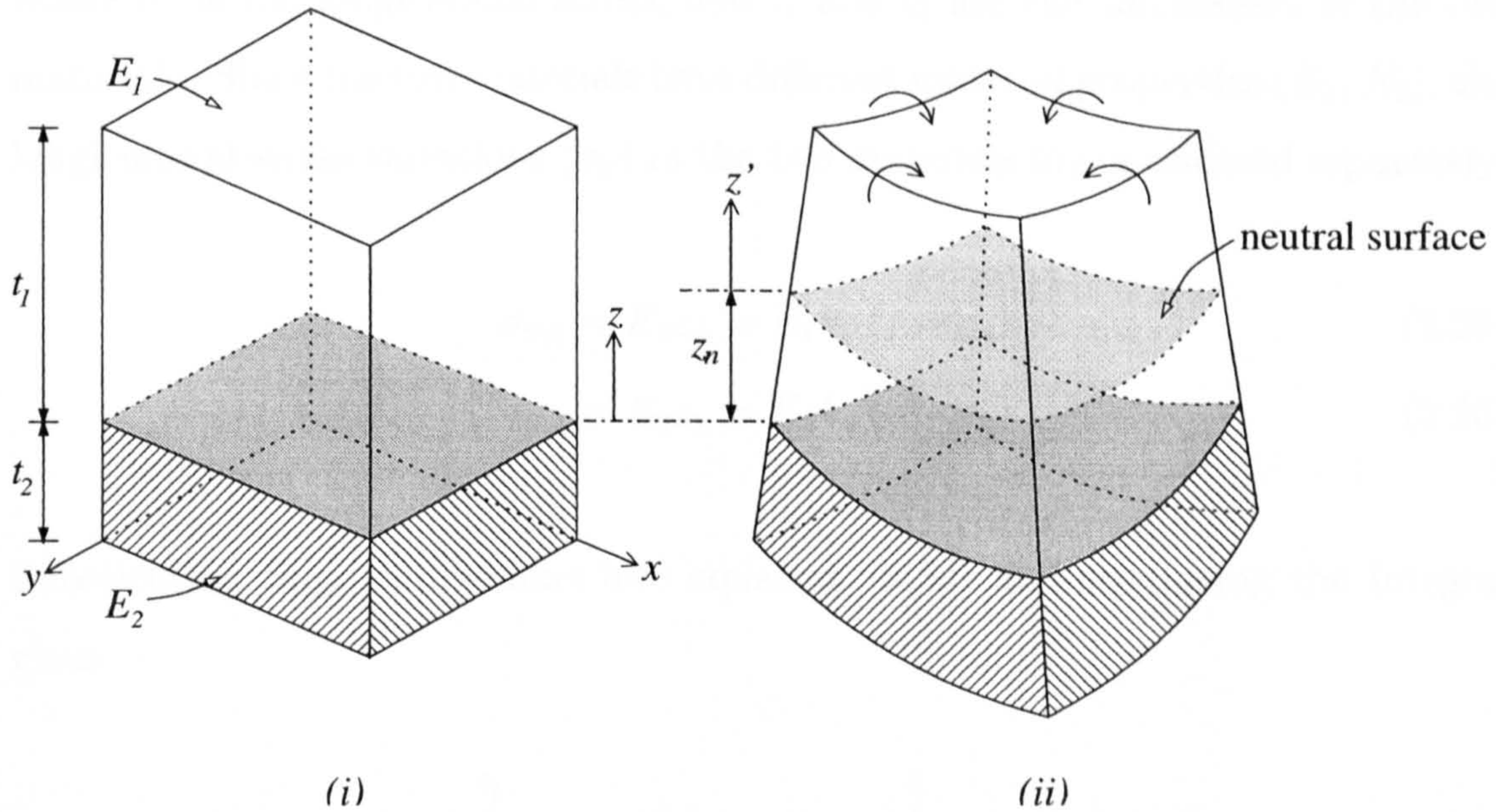

Figure 2.8: A small section of a composite plate before (i) and after (ii) bending.

assumption it can be inferred that both the x and y components of longitudinal strain are proportional to the distance from the neutral surface, z'. The linear relationship between z' and longitudinal strain is simply expressed:

$$\varepsilon_x = k_x z' = k_x \left(z - z_n\right) \tag{2.23}$$

where k_x is a constant, z is the distance from the material join, and z_n is the distance from the material join to the neutral surface (see Figure 2.8*ii*). The internal moment of resistance in the plate can be evaluated about the neutral surface: (it is only necessary to consider one of the components of moment per unit length – M_x in this case)

$$M_x = \int_{-t_2}^{t_1} \sigma_x \left(z - z_n\right) \, \mathrm{d}z \tag{2.24}$$

where σ_x is the longitudinal stress, and t_1 and t_2 are the thicknesses of the two materials. Since the two materials have different material properties (E_1, E_2), the longitudinal stress variations (σ_x) in the two materials are considered separately:

$$\sigma_{x,1} = E_1 \varepsilon_x = E_1 k_x (z - z_n) \tag{2.25}$$

$$\sigma_{x,2} = E_2 \varepsilon_x = E_2 k_x (z - z_n) \tag{2.26}$$

Substituting these expressions into equation (2.24) and separating the integral gives

$$\begin{aligned} M_x &= E_1 k_x \int_0^{t_1} (z - z_n)^2 \, \mathrm{d}z + E_2 k_x \int_{-t_2}^{0} (z - z_n)^2 \, \mathrm{d}z \\ &= \frac{k_x}{3} \left(E_1 (t_1 - z_n)^3 + E_2 (t_2 + z_n)^3 + z_n^3 (E_1 - E_2) \right) \end{aligned} \tag{2.27}$$

For thin plates the strain can be related to curvature, κ, by the following expression:

$$\frac{\varepsilon_x}{z'} \left(1 - \nu^2\right) = \kappa = -\left(\frac{\partial^2 w}{\partial x^2} + \nu \frac{\partial^2 w}{\partial y^2} \right) \tag{2.28}$$

The linear definition of strain ($\varepsilon_x = k_x z'$) can be substituted into equation (2.28) to obtain:

$$k_x = -\frac{1}{(1 - \nu^2)} \left(\frac{\partial^2 w}{\partial x^2} + \nu \frac{\partial^2 w}{\partial y^2} \right) \tag{2.29}$$

Combining equations (2.27) and (2.29) yields the relationship between moment and curvature for the composite plate:

$$M_x = -\frac{E_1 (t_1 - z_n)^3 + E_2 (t_2 + z_n)^3 + z_n^3 (E_1 - E_2)}{3 (1 - \nu^2)} \left(\frac{\partial^2 w}{\partial x^2} + \nu \frac{\partial^2 w}{\partial y^2} \right) \tag{2.30}$$

The effective flexural rigidity, B_e, can be extracted from equation (2.30):

$$B_e = \frac{E_1 (t_1 - z_n)^3 + E_2 (t_2 + z_n)^3 + z_n^3 (E_1 - E_2)}{3 (1 - \nu^2)} \tag{2.31}$$

The Position of the Neutral Surface

The position of the neutral surface, z_n, has yet to be evaluated in terms of the known variables (E_1, E_2, t_1, and t_2). This is achieved by imposing the condition of zero net horizontal force:

$$\int_{-t_2}^{t_1} \sigma_x \, \mathrm{d}z = 0 \tag{2.32}$$

The integral in equation (2.32) is separated for the two materials, with equations (2.25) and (2.26) substituted for σ_x:

$$E_1 k_x \int_0^{t_1} (z - z_n) \, \mathrm{d}z + E_2 k_x \int_{-t_2}^{0} (z - z_n) \, \mathrm{d}z = 0 \tag{2.33}$$

Equation (2.33) can be evaluated and rearranged for z_n:

$$z_n = \frac{1}{2} \left(\frac{E_1 t_1^2 - E_2 t_2^2}{E_1 t_1 + E_2 t_2} \right) \tag{2.34}$$

The Effective Poisson's Ratio

The value for Poisson's ratio, ν, must be an effective value which takes into account the different ratios of the two materials. A varying Poisson's ratio cannot exist as this would contravene the condition of zero net force in the perpendicular direction. This effective value is calculated by equating the perpendicular internal energy generated by the individual materials being allowed to adopt their own Poisson's ratio with the internal energy generated by the composite plate with

an effective Poisson's ratio. This expression takes the form:

$$\frac{E_1\nu_1^2}{2}\int_0^{t_1}\varepsilon_x^2\,\mathrm{d}z+\frac{E_2\nu_2^2}{2}\int_{-t_2}^{0}\varepsilon_x^2\,\mathrm{d}z=\frac{E_1\nu_e^2}{2}\int_0^{t_1}\varepsilon_x^2\,\mathrm{d}z+\frac{E_2\nu_e^2}{2}\int_{-t_2}^{0}\varepsilon_x^2\,\mathrm{d}z \tag{2.35}$$

Substituting equation (2.23) into equation (2.35) and then evaluating the integrals yields, after some rearrangement, an expression for the 'effective' Poisson's ratio:

$$\nu_e=\sqrt{\frac{E_1\nu_1^2\left(t_1-z_n\right)^3+E_2\nu_2^2\left(t_2+z_n\right)^3+z_n^3\left(E_1\nu_1^2-E_2\nu_2^2\right)}{E_1\left(t_1-z_n\right)^3+E_2\left(t_2+z_n\right)^3+z_n^3\left(E_1-E_2\right)}} \tag{2.36}$$

The Numerical Implications of the Composite Diaphragm

The PZT discs work most effectively when they are slightly smaller than the diaphragm (see §3.1.4). This means that at some point in the evaluation of the discretised plate equation (2.6)-(2.7), the flexural rigidity must switch between the normal and the combined effective value. This in itself, is not difficult to implement, but it does necessitate the inclusion of 'internal' boundary conditions at the interface between the composite section and the single material section (for simplicity's sake, the combined PZT and diaphragm is assumed to be a continuous material with a thickness equal to that of the single material section).

The first condition that must be satisfied is the continuity of the gradient of deflection:

$$\left.\frac{dw}{dr}\right|_1=\left.\frac{dw}{dr}\right|_2 \quad \text{when} \quad r=r_{jn} \tag{2.37}$$

where r_{jn} is the radial position of the join between materials, the subscript 1 denotes the effective material of the combined PZT and diaphragm, and the subscript 2 denotes the material of the diaphragm alone.

To include the boundary condition stated in equation (2.37) within the present

numerical scheme, dummy points are introduced either side of the material join as shown in Figure 2.9. Using these dummy points, equation (2.37) can be approximated using centred differences:

$$\left(\frac{1}{2\Delta r}\right) w_{I-1} + \left(\frac{1}{2\Delta r}\right) w_{I+1} = \left(\frac{1}{2\Delta r}\right) w_{D2} + \left(\frac{1}{2\Delta r}\right) w_{D3} \qquad (2.38)$$

where Δr is the grid spacing, and w_i are the deflections of the points as denoted in Figure 2.9.

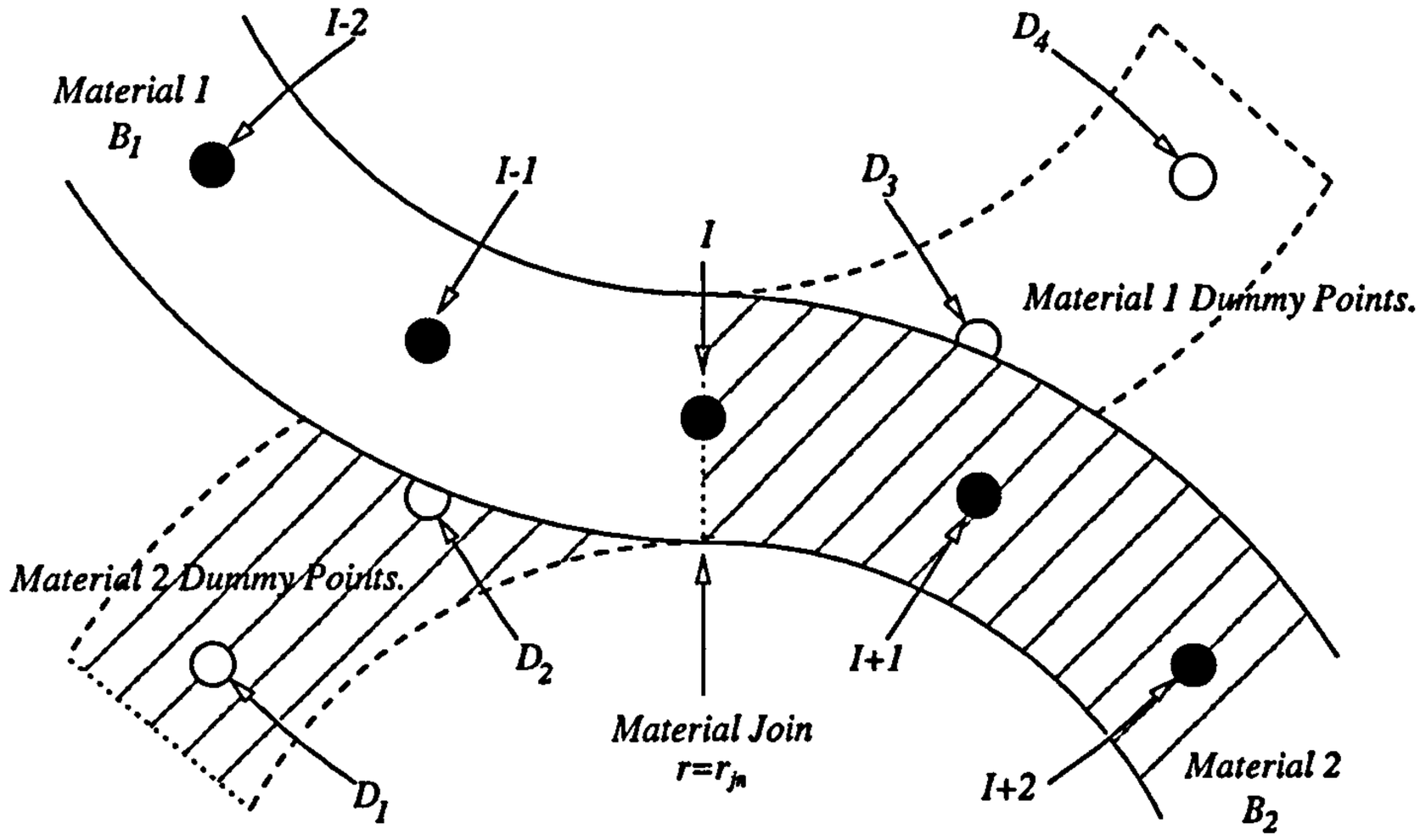

Figure 2.9: A finite-difference representation of the join of two distinct materials.

The second condition to be enforced using the dummy points is the continuity of moment, i.e. the internal moment in material 1 at the join must equal the internal moment in material 2 at the join:

$$B_1 \left(\frac{d^2w}{dr^2} + \frac{\nu_1}{r}\frac{dw}{dr}\right) = B_2 \left(\frac{d^2w}{dr^2} + \frac{\nu_2}{r}\frac{dw}{dr}\right) \quad \text{when} \quad r = r_{jn} \qquad (2.39)$$

this is also approximated using centred differences to give

$$\left(\frac{B_1\nu_1}{2r\Delta r}-\frac{B_1}{\Delta r^2}\right)w_{I-1}+\left(\frac{2B_1}{\Delta r^2}-\frac{2B_2}{\Delta r^2}\right)w_I+\left(\frac{B_2\nu_2}{2r\Delta r}+\frac{B_2}{\Delta r^2}\right)w_{I+1}+$$
$$\left(\frac{B_2}{\Delta r^2}-\frac{B_2\nu_2}{2r\Delta r}\right)w_{D2}-\left(\frac{B_1\nu_1}{2r\Delta r}+\frac{B_1}{\Delta r^2}\right)w_{D3}=0 \quad (2.40)$$

The final internal boundary condition arises from enforcing continuity of shear, i.e. the shear force experienced in material 1 at the join must equal the shear force experienced in material 2 at the join:

$$B_1\left(\frac{d^3w}{dr^3}+\frac{1}{r}\frac{d^2w}{dr^2}-\frac{1}{r^2}\frac{dw}{dr}\right)=B_2\left(\frac{d^3w}{dr^3}+\frac{1}{r}\frac{d^2w}{dr^2}-\frac{1}{r^2}\frac{dw}{dr}\right) \quad (2.41)$$

when $r=r_{jn}$. The centred-difference approximation of equation (2.41) is

$$\begin{aligned}0=&\left(\frac{2B_1}{r\Delta r^2}-\frac{2B_2}{r\Delta r^2}\right)w_I\\&-\left(\frac{B_1}{\Delta r^3}+\frac{B_1}{r\Delta r^2}+\frac{B_1}{2r^2\Delta r}\right)w_{I-1}+\left(\frac{B_1}{2\Delta r^3}\right)w_{I-2}\\&-\left(\frac{B_2}{\Delta r^3}-\frac{B_2}{r\Delta r^2}+\frac{B_2}{2r^2\Delta r}\right)w_{I+1}+\left(\frac{B_2}{2\Delta r^3}\right)w_{I+2}\\&+\left(\frac{B_2}{\Delta r^3}+\frac{B_2}{r\Delta r^2}+\frac{B_2}{2r^2\Delta r}\right)w_{D2}-\left(\frac{B_2}{2\Delta r^3}\right)w_{D1}\\&+\left(\frac{B_1}{\Delta r^3}-\frac{B_1}{r\Delta r^2}+\frac{B_1}{2r^2\Delta r}\right)w_{D3}-\left(\frac{B_1}{2\Delta r^3}\right)w_{D4}\end{aligned} \quad (2.42)$$

A Sample Calculation

To illustrate the potential differences of composite and homogeneous diaphragms, a sample simulation has been performed. Figure 2.10 shows the comparison of a statically-deflected homogeneous plate with a statically-deflected composite plate. In the simulation, the PZT, which is approximately half the size of the diaphragm, has a flexural rigidity that is sixty times greater than that for the diaphragm. The presence of the stiff PZT has, in this case, drastically altered the static mode

shape (the maximum deflection has also been seriously reduced in the composite case – the deflections in Figure 2.10 have been normalised). The relative stiffnesses used in this example, although exaggerated for illustrative purposes, may be applicable to MEMS-scale diaphragms that are purposely fabricated using materials with low stiffness in order to reduce their high natural frequency (see §3.2.1).

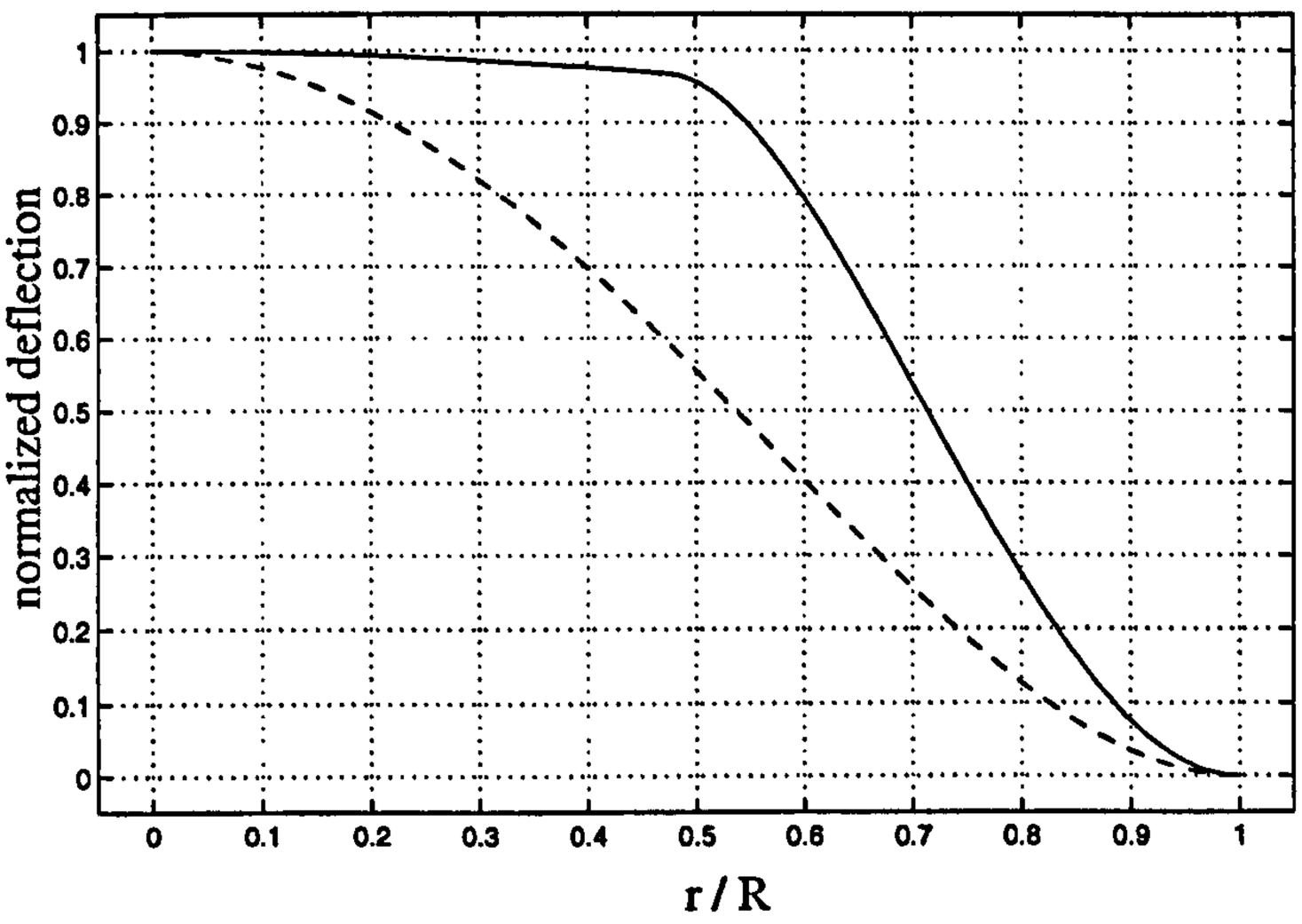

Figure 2.10: A comparison of the statically-deflected mode shapes of homogeneous (––) and composite (–) plates.

2.3.2 The PZT Force

The force that is generated by the PZT is lateral, it is therefore clear that to fully model the PZT and diaphragm system, lateral motion would need to be encorporated within the equations of motion. Such a model would be three-dimensional (2-D in symmetrical polar coordinates) and would require much greater computational effort as a consequence. Some approximations can be made to model the motion of the PZT and diaphragm using the classic plate theory described in §2.2.

The first main assumption is that any lateral motion occurs instantaneously as a response to an applied electric field. This assumes that the electrostriction effect, which is a polarisation phenomenon (Askeland 1990, p697), is immediate. Also, it assumes that the lateral response of the PZT is much faster than the induced vertical response, and can therefore be treated as being instantaneous. This can be shown to be a fair assumption by the analysis of a simpler configuration to that of the PZT and diaphragm (see Appendix §B.1).

The second main assumption that enables the use of the two-dimensional plate equations is that the vertical motion is only dependent on the moment that the quasi-instantaneous lateral deflections produce. This is a statement of linearity which is in keeping with the plate model used in §2.2.

The Lateral Deflection of the PZT and Diaphragm

If it can be accepted that the lateral (radial) deflection is instantaneous, the steady-state result can be used to calculate the generated moment. The steady-state strain that is produced in a free-standing PZT is given by

$$\varepsilon_p = \frac{d_{31} V}{t_p} \tag{2.43}$$

where d_{31} is the piezo-electric constant for strain perpendicular to polarisation, V is the applied voltage, and t_p is the PZT thickness (Askeland 1990, p697). The stress that electrostriction is responsible for is given by

$$\sigma_p = \frac{E_p d_{31} V}{t_p} \tag{2.44}$$

where E_p is the elastic modulus of the PZT. Note that the elastic stress (stress generated as a result of deformation σ_e) is equal and opposite to the PZT stress (σ_p) which means there is zero *net* stress. (Contributions from bending to net hor-

izontal force are equivalently zero and so lateral deformations can be considered independent of vertical deflection).

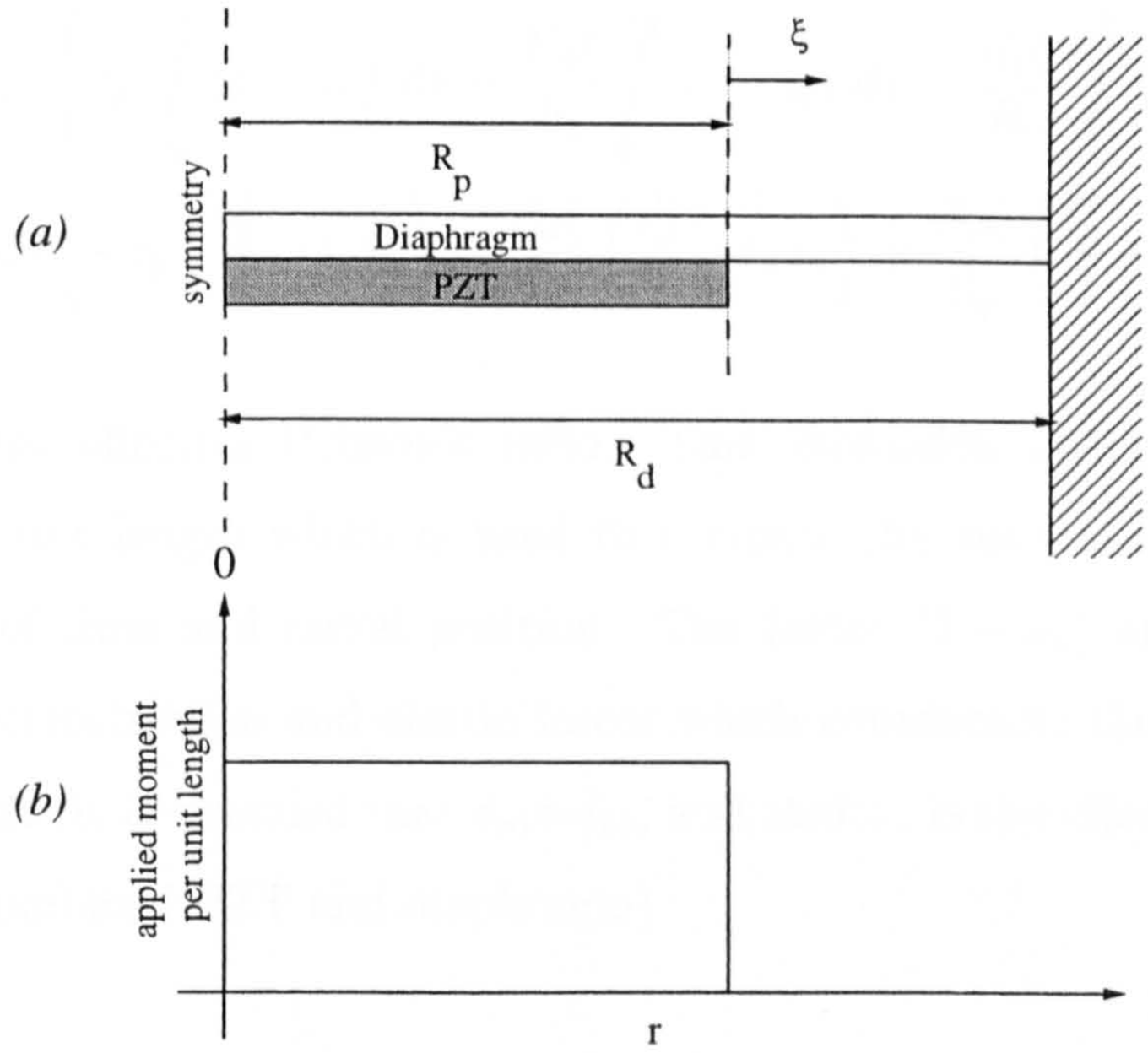

Figure 2.11: (a) A radial section of the diaphragm and PZT configuration, (b) The variation of moment per unit length applied by the PZT.

Figure 2.11 shows a radial section of the PZT and diaphragm configuration. There is only one degree of freedom laterally, and this is the deflection (ξ) at the join between composite and non-composite material. A condition of zero net force is imposed on this configuration in order to attain the steady-state solution, which when rearranged in terms of ξ (lateral deflection) gives

$$\xi = \sigma_p t_p \left(\frac{E_p t_p}{R_p} + \frac{E_d t_d}{R_p} + \frac{E_d t_d}{R_d - R_p} \right)^{-1} \tag{2.45}$$

where E_d is the elastic modulus of the diaphragm, t_d is the thickness of the diaphragm, R_d is the radius of the diaphragm, and R_p is the radius of the PZT. To estimate the generated moment from the extension ξ, the position of the neutral surface (z_n) must be known. This is dependent upon the nature of bending only,

and can be evaluated using equation (2.34). The total moment generated within the composite region, is given by

$$\begin{aligned} M_a &= (1-\nu_e)\left(\sigma_p \int_{-t_p}^{0} (z-z_n)\,\mathrm{d}z - \frac{E_d\xi}{R_p}\int_{0}^{t_d}(z-z_n)\,\mathrm{d}z - \frac{E_p\xi}{R_p}\int_{-t_p}^{0}(z-z_n)\,\mathrm{d}z\right) \\ &= (1-\nu_e)\left(-\sigma_p\left(\frac{t_p^2}{2}+t_pz_n\right) - \frac{E_d\xi}{R_p}\left(\frac{t_d^2}{2}-t_dz_n\right) + \frac{E_p\xi}{R_p}\left(\frac{t_p^2}{2}+t_pz_n\right)\right) \end{aligned} \quad (2.46)$$

where ν_e is the effective Poisson's ratio. This expression defines the applied moment per unit length which is used to evaluate the vertical response; it is independent of time and radial position. The factor $(1-\nu_e)$ arises from the azimuthal electrostriction and elastic forces which counteracts the directly generated moment (it is assumed that d_{31}=d_{32}, and that ν_e is the effective Poisson's ratio of the combined PZT and diaphragm).

Numerical Implementation

The radial variation of applied moment per unit length is constant, this is illustrated in Figure 2.11 (b). This cannot be imposed directly on the plate equations as the applied moment cannot be separated from the total bending moment; however, the applied moment can be created by a fictitious vertical forcing. To do this the relationship between the second derivative of *applied* moment per unit length (M) and force per unit area (q) is used:

$$\frac{d^2M}{dr^2} = q \quad (2.47)$$

In order for the second derivative to be calculated some approximation to the step function shown in Figure 2.11 (b) must be made. A quintic approximation is used for the applied moment over a small length δ where the value jumps from

M_a to 0:

$$M(x) = Ax^5 + Bx^4 + Cx^3 + Dx^2 + Ex + F \tag{2.48}$$

here $x = r - R_p$, and the coefficients are found by imposing the following boundary conditions:

$$\begin{aligned} M(0) = M_a \quad &\text{and} \quad M(\delta) = 0 \\ M'(0) = 0 \quad &\text{and} \quad M'(\delta) = 0 \\ M''(0) = 0 \quad &\text{and} \quad M''(\delta) = 0 \end{aligned} \tag{2.49}$$

The function including the evaluated coefficients is

$$M(x) = -\frac{6M_a x^5}{\delta^5} + \frac{15M_a x^4}{\delta^4} - \frac{10M_a x^3}{\delta^3} + M_a \tag{2.50}$$

Figure 2.12 (a)-(c) shows plots of the function and its first two derivatives. The second derivative of equation (2.50) is substituted into equation (2.47) to give the variation in vertical force that would induce the desired step in moment. This vertical forcing function is

$$q(x) = -\frac{120M_a x^3}{\delta^5} + \frac{180M_a x^2}{\delta^4} - \frac{60M_a x}{\delta^3} \tag{2.51}$$

Figure 2.12 (c) is a plot of equation (2.51), from which it is clear that the function is in the form of a forcing couple.

There is, however, a difficulty in implementing this forcing function as its accuracy depends on δ being small. This requires more grid points, and hence, increases the computational time. It is therefore in the interest of the numerical scheme to implement this couple with as few grid points as possible. An extreme case would be to apply the couple using only two grid points: the first $q_i = -F_a$, and the second $q_{i+1} = F_a$, where i denotes the grid position. The problem is

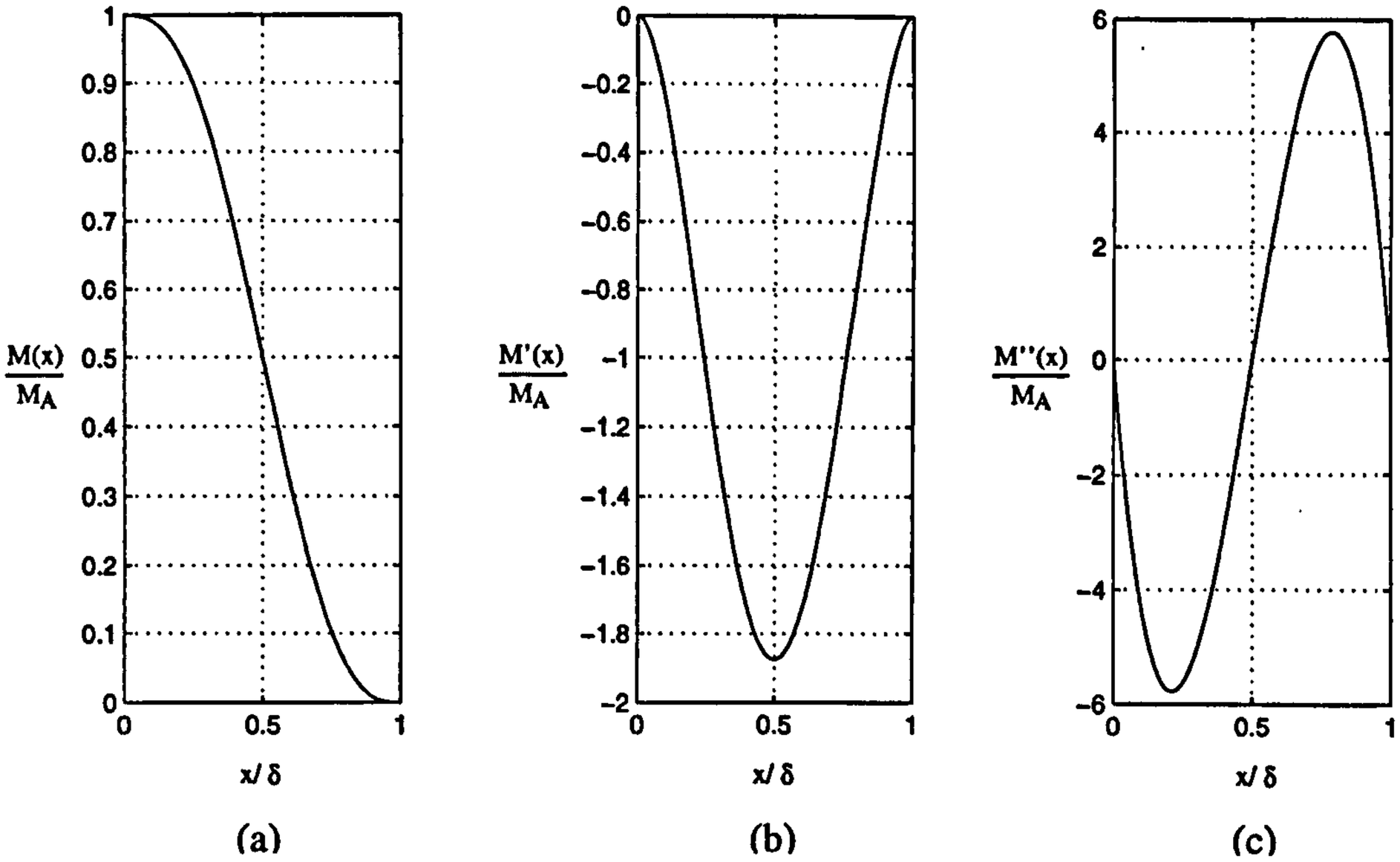

Figure 2.12: The function and first two derivatives of equation (2.50).

now, finding the value of F_a that will give the desired moment step M_a. Figure 2.13 shows the moment step that is implied by the two-grid-point couple. The values in the figure are calculated by integration of the couple using the following finite-difference approximation:

$$M'(i+1) = M'(i) + \frac{\Delta r}{2}\left(M''(i+1) + M''(i)\right)$$
$$M(i+1) = M(i) + \frac{\Delta r}{2}\left(M'(i+1) + M'(i)\right) \tag{2.52}$$

The moment step is equal to the applied moment per unit length, and therefore M_a is related to F_a by:

$$F_a = \frac{M_a}{\Delta r^2} \tag{2.53}$$

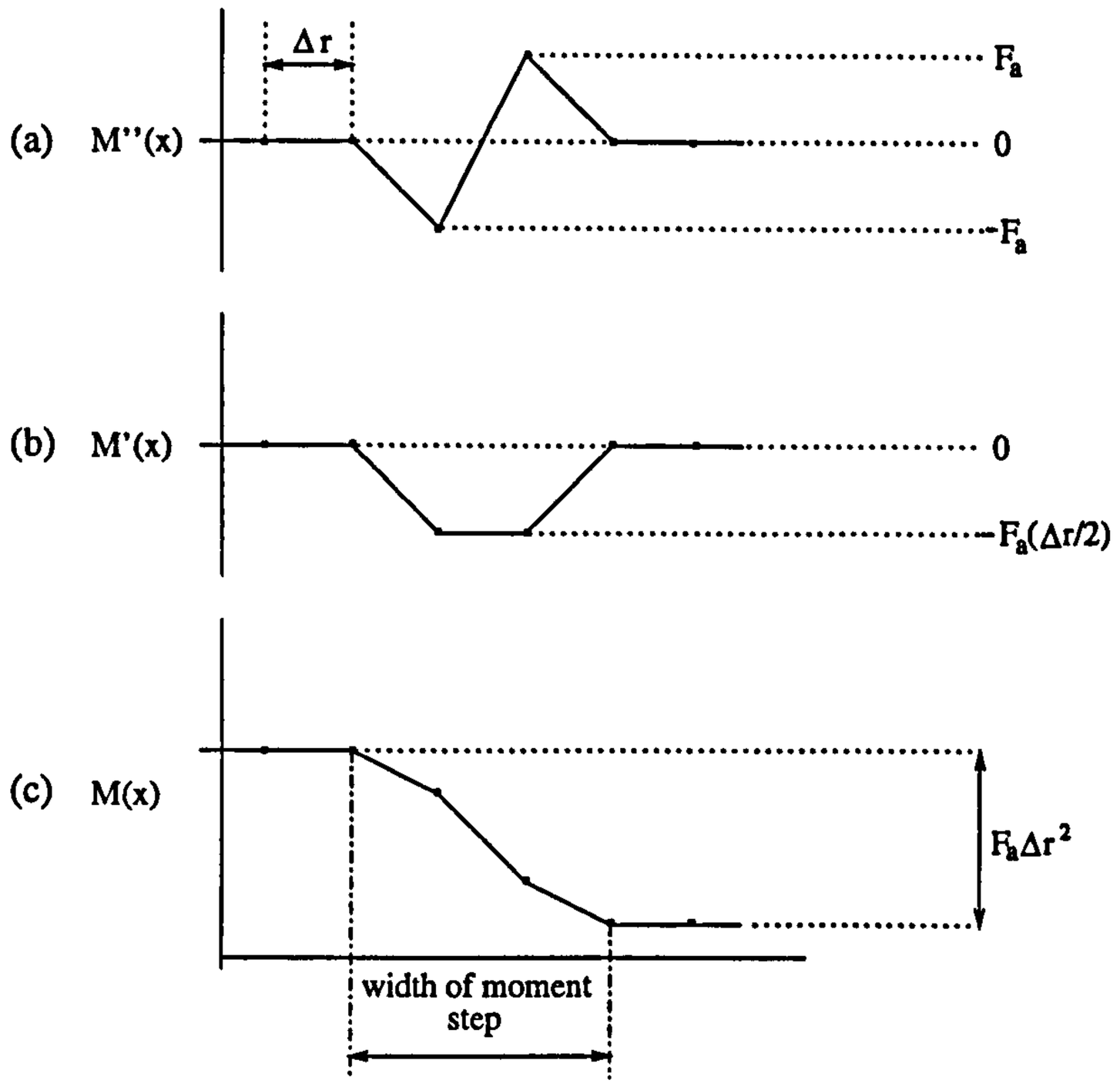

Figure 2.13: The moment step (c) implied by the integration of the two-point forcing couple (a). The integration is performed using the finite-difference equations (2.52).

Analytical Validation of the Two-Point Couple

For validation purposes, a finite-difference approximation of a cantilever beam subjected to a two-point couple, is compared against the known analytical solution with an internal moment. The analytical solution is simple as the applied moment is directly related to curvature as follows:

$$\frac{\mathrm{d}^2\eta}{\mathrm{d}x^2} = \frac{bM_a}{EI} \tag{2.54}$$

where η is the vertical deflection, x is the distance along the beam, M_a is the applied moment per unit length, b is the beam breadth, I is the second moment of area, and E is the elastic modulus. This can be integrated twice and solved

for the two boundary conditions to give the following solution:

$$\eta = \frac{bM_a x^2}{2EI} \tag{2.55}$$

The numerical solution uses a two-point couple ($F_a = M_a/\Delta x^2$) that is applied to the end of the beam. Figure 2.14 shows the comparison between the analytically- and numerically-calculated deflection. The comparison is exact which implies that the two-point couple method is sound.

For the circular plate this two-point method needs a small additional force at the centre of the diaphragm to ensure zero net vertical force, otherwise this condition is not satisfied and the applied moment will not be constant. The balancing is required because in polar coordinates a point force (per unit length) more distant from the origin provides a slightly larger total force than a nearer point force.

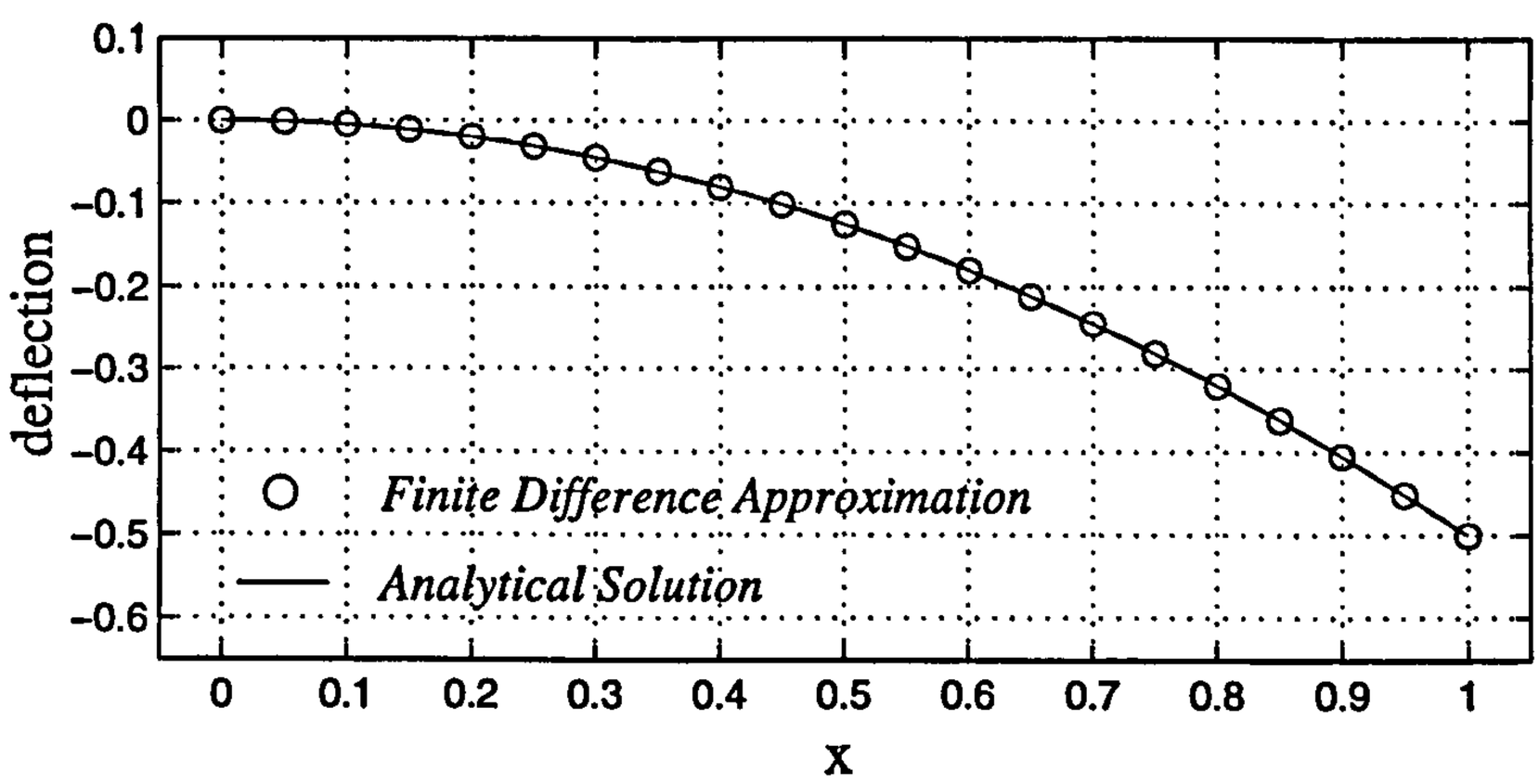

Figure 2.14: The deflection of a cantilever beam with a constant applied moment. A comparison of the analytical (–) and finite-difference approximation (o).

2.3.3 Section Summary

In this section the effects of the expanding/contracting PZT on the diaphragm have been modelled. It has been shown that, given certain assumptions, the electrostrictive force in the PZT applies a constant moment per unit length to the PZT and diaphragm section; it is this moment that drives the entire diaphragm. To model this moment a vertical-force couple is required, which can be numerically implemented using only two grid points.

2.4 The Orifice Flow

The pressure fluctuations in and outside of the cavity exert a pressure gradient across the orifice; this pressure differential drives fluid out of the orifice in the form of a jet. In the model of Rathnasingham and Breuer (1997a) the orifice flow was approximated using the one-dimensional inviscid unsteady Bernoulli equation. In contrast to this, Crook *et al.* (1999) employed a quasi-steady Poiseuille solution for the orifice flow. A 'best of both worlds' model that captures the viscous and unsteady phenomena can be found by a more general treatment of the governing equations. However, before methods of the solution of the Navier-Stokes equations can be proposed, it must be established that the continuum assumption is valid at the scale of the current MEMS application.

2.4.1 Micro-Fluidic Considerations

An increasing amount of effort is being dedicated to the research of micro-fluidic effects in the field of MEMS (Piekos and Breuer 1996, review: Gad-el-Hak 1999). The main concern for modelling purposes is whether or not the continuum approximation is valid, and if not, how does the 'rarefied' flow behave? The point at which such considerations are necessary is when the mean free path of the gas (λ) (the average distance between particle collisions) is comparable to the characteristic length of the flow (L). The degree of gas rarefaction is expressed by the Knudsen number (K_n) as the ratio of the characteristic length and the mean free path:

$$K_n = \frac{\lambda}{L} \tag{2.56}$$

The continuum assumption and the Navier-Stokes equations are valid only when $K_n < 0.01$, beyond this the 'slip flow' regime is encountered ($0.01 < K_n < 0.1$), here the no-slip condition at wall interfaces is no longer satisfied. The 'transition'

regime is when $0.1 < K_n < 3$, and then completely rarefied or 'free-molecular' flow occurs for $K_n > 3$ (Schaaf and Chambré, 1958).

The characteristic length of the flow for this application is taken as the orifice diameter, and the mean free path of air to be λ=0.065 μm. The orifice diameter need not be any smaller than one tenth of the spanwise spacing of the turbulent structures that the MEMS is to control. In a turbulent boundary layer the mean streak spacing is widely reported to be around 100 wall units, which at flight conditions is roughly equal to 100 μm. This spacing suggests an appropriate characteristic length scale (orifice diameter) of no less than 10 μm. The Knudsen number for the turbulent control application, based on equation (2.56), is in the region of $K_n = 0.0065$. This value satisfies the continuum criterion safely, which implies that the Navier-Stokes equations are indeed valid for the turbulent control application.

For strongly compressed flows it might be the case that a more accurate Knudsen number based on the gradient of density is higher than that just calculated (see Gad-el-Hak, 1999). This is, however, difficult to assess without modelling the compressible fluid dynamics of the cavity.

2.4.2 Navier-Stokes Approximations

Perhaps the most extreme numerical simulation would involve solving the complete compressible Navier-Stokes equations in the orifice as well as inside the cavity (Rizzetta *et al.* 1999). This is a very demanding computation and would not be commensurate with the effort expended on the solution of the boundary layer, with which this code will ultimately be coupled. Inevitably, some approximation to the Navier-Stokes equations must be made. The main assumption is that of parallel flow in the exit nozzle; in cylindrical coordinates this is stated as:

$$u_\theta = 0, \quad u_r = 0, \quad \text{and} \quad \frac{\partial u}{\partial \theta} = 0. \tag{2.57}$$

where u is the velocity, r is the radial coordinate, and θ is the azimuthal coordinate.

Even though flow speeds in the orifice will be much less than the speed of sound, incompressible flow is not a good assumption. The inlet and outlet of the orifice impose density, as well as pressure, boundary conditions. If there is an imposed density difference there will be an expansion/compression over the orifice; this prevents any further simplification of the two-dimensional Navier-Stokes equations. To enable a calculation of one-dimensional order, as would be the case if incompressibility were valid, it is assumed that the variations with respect to the axial coordinate (x) of density, pressure and velocity are linear. This given, the continuity and x-momentum equation are as follows:

$$\textit{continuity} \qquad \frac{\partial \rho}{\partial t} + \frac{\partial (\rho u)}{\partial x} = 0 \tag{2.58}$$

$$\textit{momentum} \qquad \frac{\partial (\rho u)}{\partial t} + \frac{\partial (\rho u^2)}{\partial x} = -\frac{\partial p}{\partial x} + \mu \nabla^2 u \tag{2.59}$$

where ρ is the density, p is the pressure, t is time, μ is the dynamic viscosity, and ∇^2 is the Laplacian operator given by:

$$\nabla^2 \equiv \left[\frac{1}{r} \frac{\partial}{\partial r} + \frac{\partial^2}{\partial r^2} \right] \tag{2.60}$$

Combining the continuity equation (2.58) and the x-momentum equation (2.59) gives

$$\rho \frac{\partial u}{\partial t} + \rho u \frac{\partial u}{\partial x} = -\frac{\partial p}{\partial x} + \mu \nabla^2 u \tag{2.61}$$

Equation (2.61) can be simplified further when linear definitions for $u, \rho,$ and p, with respect to x, are introduced:

$$u = u_1 + \frac{x}{l} (u_2 - u_1) \tag{2.62}$$

$$\rho = \rho_1 + \frac{x}{l}(\rho_2 - \rho_1) \tag{2.63}$$

$$p = p_1 + \frac{x}{l}(p_2 - p_1) \tag{2.64}$$

where l is the orifice length, the subscript 1 denotes a value inside the cavity, and the subscript 2 denotes a value outside of the cavity. Substituting equations (2.62)-(2.64) into equation (2.61), and evaluating at x=0, yields a one-dimensional equation with only two unknown variables $u_1(r,t)$ and $u_2(r,t)$: (the variables p_1, p_2, ρ_1, and ρ_2 are known boundary conditions)

$$\rho_1 \frac{\partial u_1}{\partial t} + \frac{\rho_1 u_1 (u_2 - u_1)}{l} = \frac{p_1 - p_2}{l} + \mu \nabla^2 u_1 \tag{2.65}$$

Integrating the continuity equation (2.58) with respect to x over the length of the orifice gives an expression for u_2 in terms of u_1 and the known variables:

$$u_2 = \frac{\rho_1 u_1}{\rho_2} - \frac{l}{2\rho_2}\frac{\partial \rho_1}{\partial t} \tag{2.66}$$

(There are no compressible-flow effects in the boundary layer so the density at station 2, ρ_2, is constant with respect to time). Substituting equation (2.66) into (2.65) gives a single expression for the variable u_1:

$$\underbrace{\frac{\partial u_1}{\partial t}}_{\text{I}} + \underbrace{\left(\frac{\rho_1}{\rho_2} - 1\right)\frac{u_1^2}{l}}_{\text{II}} - \underbrace{\frac{u_1}{2\rho_2}\frac{\partial \rho_1}{\partial t}}_{\text{III}} = \underbrace{\frac{p_1 - p_2}{l\rho_1}}_{\text{IV}} + \underbrace{\frac{\mu}{\rho_1}\nabla^2 u_1}_{\text{V}} \tag{2.67}$$

Equation (2.67) is the governing equation for the orifice, it has five distinct terms which contribute uniquely to the overall behaviour of the system. Term I is the inertial term and is responsible for the unsteadiness of the fluid flow; Term II is a non-linear damping term arising from the spatial expansion/compression of the fluid from station 1 to station 2; Term III is also a non-linear damping term which results from the time-dependent compression of fluid inside the cavity;

Term IV is the forcing term, which is in the form of a pressure gradient; and Term V is a linear damping term - the source of viscous resistance.

2.4.3 Numerical Solution of the Orifice Equation

When disregarding the nonlinear terms (II) and (III) from the orifice equation (2.67) an implicit solution is quite straightforward to obtain. Firstly, the equation is evaluated half way between the new and the current time step. The linear form is then as follows

$$\left(\frac{1}{\Delta t} - \frac{\mu}{2\bar{\rho}_1}\nabla^2\right) u^{n+1} = \frac{\bar{p}_1 - \bar{p}_2}{\bar{\rho}_1 l} + \left(\frac{1}{\Delta t} + \frac{\mu}{2\bar{\rho}_1}\nabla^2\right) u^n \tag{2.68}$$

where a superscript $n+1$ denotes a variable at the new time step, a superscript n at the current time step, and a bar denotes a mean value between n and $n+1$. The Laplacian operator, defined in equation (2.60), can be approximated using centred differences. The set of equations produced for each time step can be expressed in tri-diagonal form and solved using a Thomas algorithm, also known as the tri-diagonal matrix algorithm (TDMA) (see Ferziger 1998, p8).

The full orifice equation is not as easy to solve, as there are nonlinear terms preventing the organisation into the linear tri-diagonal form. This problem can be overcome by expressing the equation in Δ-form (Ferziger 1998, p 225). The values at the new time step are replaced by values at the old plus an increment, Δu:

$$u_i^{n+1} = u_i^n + \Delta u_i \tag{2.69}$$

where i refers to the radial grid point. The benefit arises from the ability to neglect terms of the order Δu^2; these are of the same order as the finite-difference scheme's truncation error. Evaluating the orifice equation at $t = t^n + (\Delta t/2)$ and

expressing in Δ-form gives the following numerical approximation:

$$\left(\frac{1}{\Delta t} - \frac{1}{4\rho_2}\frac{\overline{\partial \rho_1}}{\partial t} + \left(\frac{\bar{\rho}_1}{\bar{\rho}_2} - 1\right)\frac{u_1}{l} - \frac{\mu}{2\bar{\rho}_1}\nabla^2\right)\Delta u_i = \frac{\bar{p}_1 - \bar{p}_2}{\bar{\rho}_1 l} + \left(\frac{1}{2\bar{\rho}_2}\frac{\overline{\partial \rho_1}}{\partial t} - \left(\frac{\bar{\rho}_1}{\bar{\rho}_2} - 1\right)\frac{u_1}{l} + \frac{\mu}{\bar{\rho}_1}\nabla^2\right)u_i \quad (2.70)$$

where a bar denotes a mean value between the new and current time step. The centred finite-difference approximation for the Laplacian operator is given by

$$\nabla^2 \Delta u_i = \left(\frac{1}{r}\frac{\partial}{\partial r} + \frac{\partial^2}{\partial r^2}\right)\Delta u_i = \frac{\Delta u_{i+1} - \Delta u_{i-1}}{2r\Delta r} + \frac{\Delta u_{i+1} + \Delta u_{i-1} - 2\Delta u_i}{\Delta r^2} \quad (2.71)$$

Equations (2.70) and (2.71) can now be put into tri-diagonal form and solved using the Thomas algorithm. The Thomas algorithm is famously efficient using only an order of m operations to forward multiply an (m x m) tri-diagonal matrix.

Boundary and Initial Conditions

The boundary conditions for the system are that the velocity at the wall is zero (Dirichlet condition) and that there is radial symmetry at the centre of the orifice (von Neumann condition). To describe how these are incorporated into the tri-diagonal matrix the radial position of each grid point is defined:

$$r = \frac{(i-1)R}{(N-1)} \qquad \text{for} \qquad i = 1 \text{ to } N \quad (2.72)$$

where i is the grid point number, R is the radius of the orifice, and N is the total number of grid points.

The Dirichlet condition is easily implemented:

$$u_N = 0 \quad (2.73)$$

where the subscript denotes the grid point number. Equation 2.73 is simply an enforcement of the no-slip condition at the wall.

The second boundary condition, that of symmetry at the centre of the orifice, can be enforced using Taylor expansions. The Taylor expansions are here stated for velocities near the centre of the orifice in terms of the velocity (u) and derivatives (u',u'', and u''') at r=0:

$$u(\Delta) = u(0) + \Delta u'(0) + \frac{\Delta^2}{2}u''(0) + \frac{\Delta^3}{6}u'''(0) + \mathcal{O}(\Delta^4) \tag{2.74}$$

$$u(2\Delta) = u(0) + 2\Delta u'(0) + 2\Delta^2 u''(0) + \frac{8\Delta^3}{6}u'''(0) + \mathcal{O}(\Delta^4) \tag{2.75}$$

where Δ is the radial grid spacing. From these expansions we can immediately enforce the symmetry condition, i.e. $u'(0) = u'''(0) = 0$. Equations (2.74) and (2.75) can now be combined to give

$$u(0) = \frac{4}{3}u(\Delta) - \frac{1}{3}u(2\Delta) + \mathcal{O}(\Delta^4) \tag{2.76}$$

This can be expressed as a boundary condition on velocity:

$$u_1 - \frac{4}{3}u_2 + \frac{1}{3}u_3 = 0 \tag{2.77}$$

An additional complication arises from the need to modify the Thomas algorithm in order to deal with the non-tri-diagonal form of the boundary condition (2.77). For an example, a small matrix with a non-tri-diagonal boundary condi-

tion is shown:

$$\begin{pmatrix} -1 & \frac{4}{3} & -\frac{1}{3} & 0 \\ a & b & c & 0 \\ 0 & d & e & f \\ 0 & 0 & g & h \end{pmatrix} \begin{pmatrix} u_0 \\ u_1 \\ u_2 \\ u_3 \end{pmatrix} = \begin{pmatrix} 0 \\ R_1 \\ R_2 \\ R_3 \end{pmatrix}$$

The off tri-diagonal term is eliminated from line 1 by adding to it an appropriate factorisation of line 2. This simple modification recovers the tri-diagonal form:

$$\begin{pmatrix} \left(-1+\frac{a}{3c}\right) & \left(\frac{4}{3}+\frac{b}{3c}\right) & 0 & 0 \\ a & b & c & 0 \\ 0 & d & e & f \\ 0 & 0 & g & h \end{pmatrix} \begin{pmatrix} u_0 \\ u_1 \\ u_2 \\ u_3 \end{pmatrix} = \begin{pmatrix} \frac{R_1}{3c} \\ R_1 \\ R_2 \\ R_3 \end{pmatrix}$$

2.4.4 Integrity of the Orifice Code

Validation of the orifice code's integrity is reasonably straightforward as well-known analytical solutions to the governing equations exist. However, some of the facets of the orifice equation, namely the nonlinear ones, cannot be readily validated.

Startup Flow

The first analytical solution of the Navier-Stokes equations considered here, is that of the pipe flow resulting from a suddenly applied uniform pressure gradient (dp/dx). This classical problem was first solved by Szymanski (1932) and is known as *startup* or *starting* flow (White 1991, p133). The steady-state result,

towards which the transient solution tends, is given by:

$$u_s = -\frac{dp}{dx}\frac{1}{4\mu}\left(R^2 - r^2\right) \tag{2.78}$$

The complete solution is

$$u = u_s - \frac{1}{\mu}\frac{dp}{dx}\sum_{n=1}^{\infty}\frac{2J_0\left(\lambda_n r/R\right)}{\lambda_n^3 J_1(\lambda_n)}\exp\left(\frac{-\lambda_n^2 \nu t}{R^2}\right) \tag{2.79}$$

where J_0 and J_1 are Bessel functions of the first kind and λ_n are their roots. The velocity history of the theoretical solution and numerical code are compared in Figure (2.15). The dashed and solid lines are barely distinguishable. Figure (2.16) shows the development of the profile during startup at three different moments in time. Here again the code successfully resolves the details with only a few finite-difference grid points.

The second orifice code validation is also a celebrated analytical solution of the Navier-Stokes equations. The pipe flow resulting from an oscillating pressure gradient was first solved by Sexl (1930), and the solution consists of a potential and viscous component $u = u_p + u_v$ (Sherman 1990). The potential flow component is associated with an oscillating pressure gradient (Π_x=-Asin(ωt)) and is given by

$$u_p(t) = \frac{A}{\omega}\cos(\omega t) \tag{2.80}$$

Where ω and A are the frequency and amplitude of the pressure gradient, respectively. The second part of the solution is assumed to be harmonic:

$$u_v(\zeta, t) = \Re\{f(\zeta)e^{i\omega t}\} \tag{2.81}$$

where $\zeta = r/R$. The function f is chosen such that the no-slip condition at the

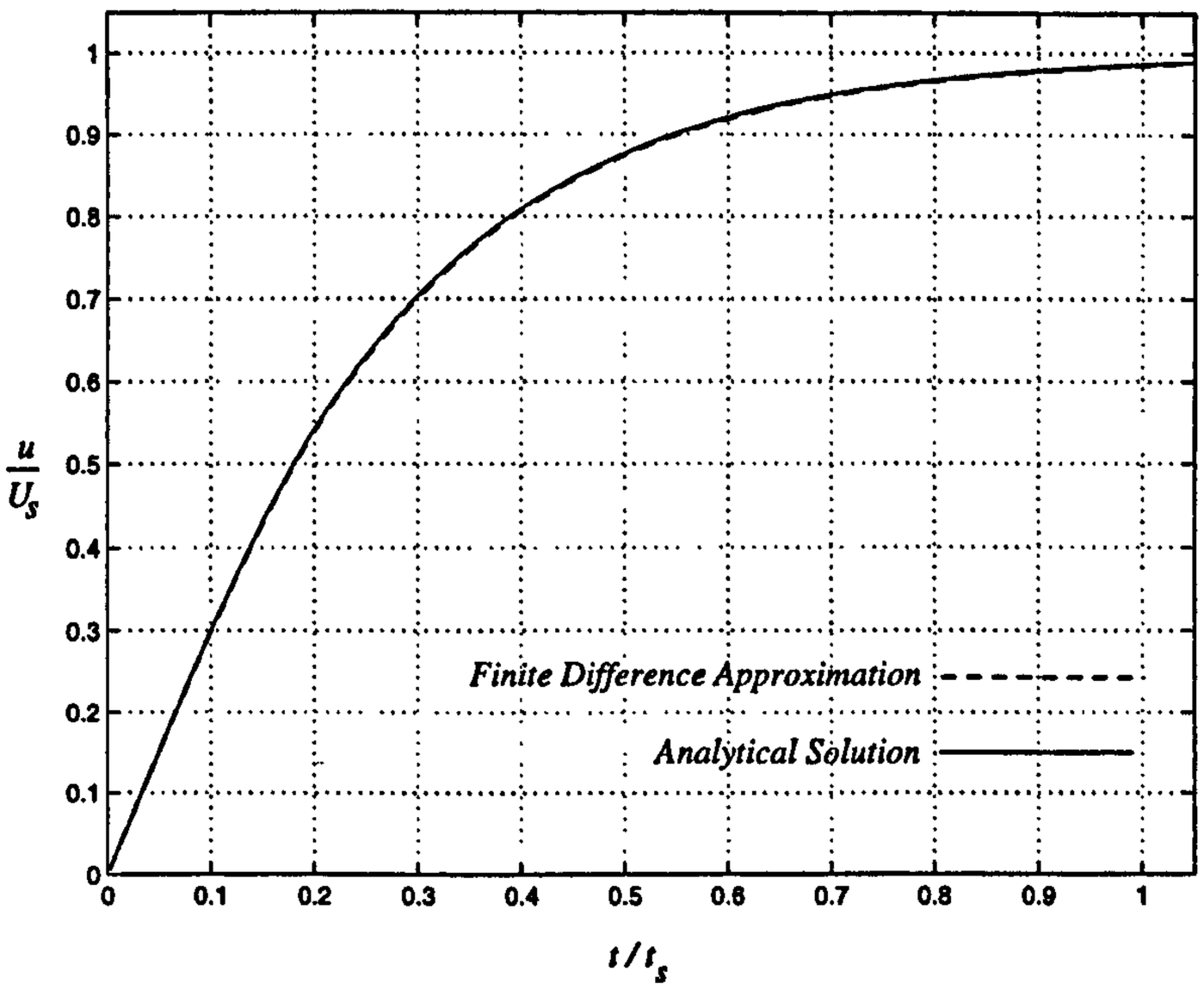

Figure 2.15: The centre-line velocity history of flow in a pipe subject to a suddenly applied, constant, pressure gradient. Comparison of analytical solution (–) with a numerical simulation (– –). The startup time, t_s, is the time taken for u/U_s to be greater then 0.99.

wall is satisfied when added to the potential component. The final solution is

$$u(\zeta,t) = -\frac{I_o\left(\zeta\sqrt{i\omega R^2/\nu}\right)}{I_o\left(\sqrt{i\omega R^2/\nu}\right)}\frac{A}{\omega}\exp(i\omega t) \tag{2.82}$$

Where I_0 is a modified Bessel function and ν is the kinematic viscosity.

Figure 2.17 shows the comparison of the analytical solution and a five-point finite-difference approximation, at different times during the flow cycle. Figure 2.18 shows the same result compared against a finite-difference scheme with a finer discretisation; convergence towards the analytical solution is clearly shown.

The results in Figures 2.17 and 2.18 exhibit 'near-wall velocity overshoot' (also known as Richardson's annular effect), which is what occurs when the point of maximum velocity does not lie on the pipe's centre-line. This phenomenon is characteristic of oscillatory pipe flows, and was first observed experimentally by Richardson and Tyler (1929).

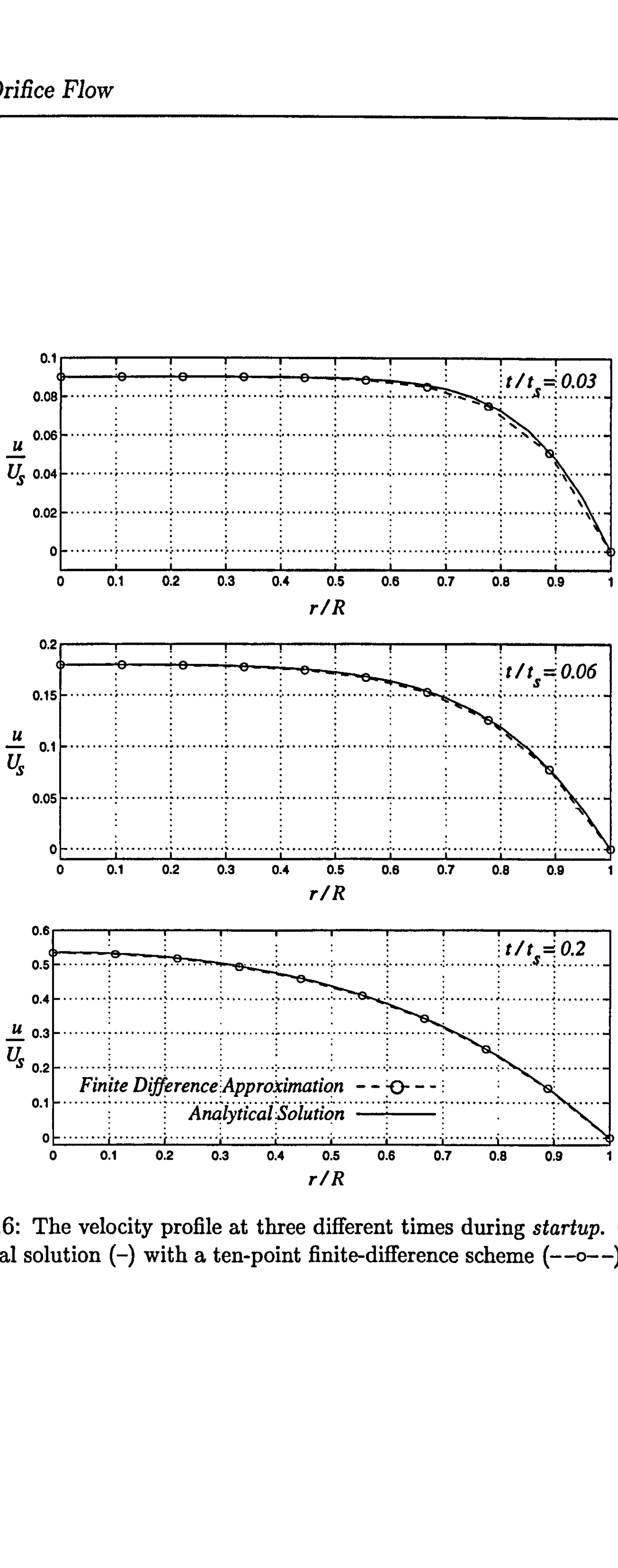

Figure 2.16: The velocity profile at three different times during *startup*. Comparison of analytical solution (–) with a ten-point finite-difference scheme (--o--).

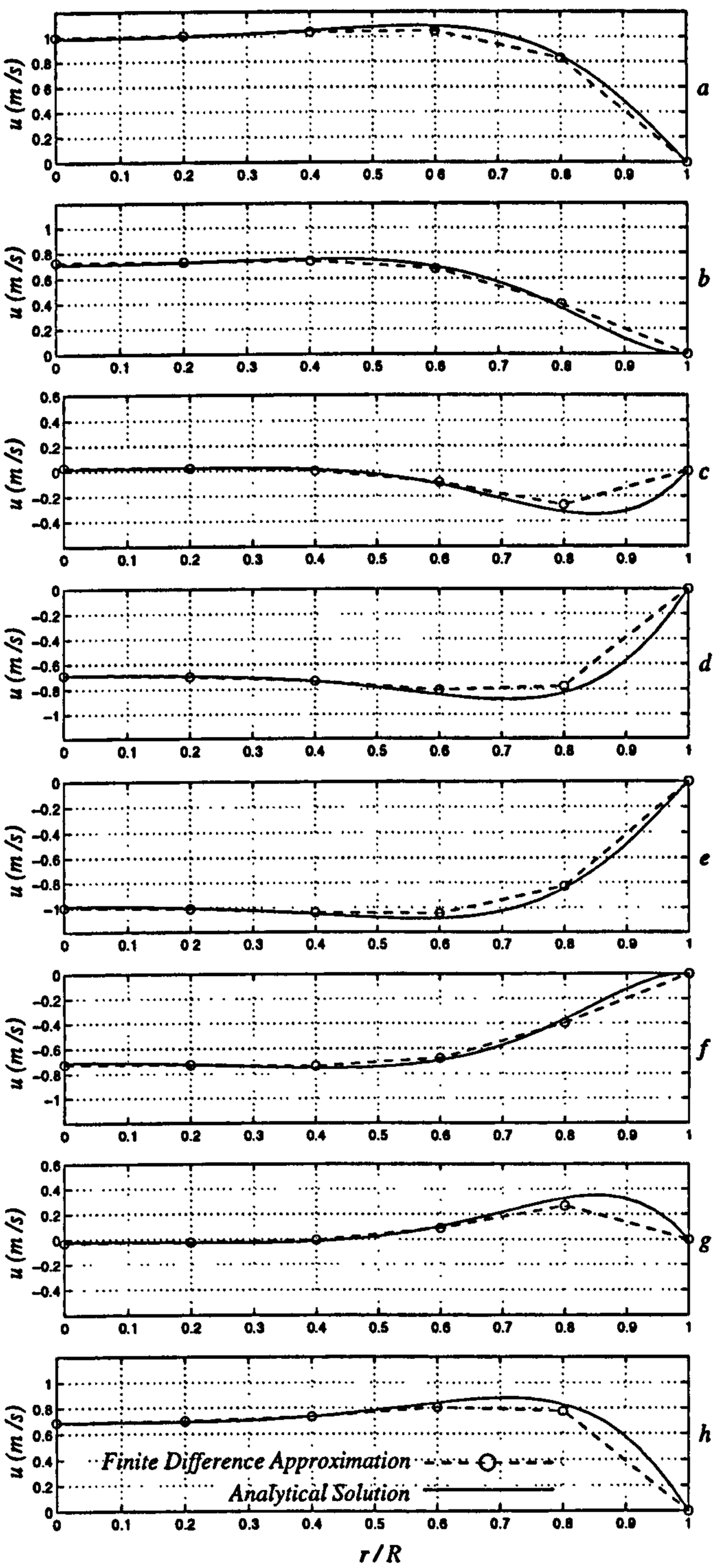

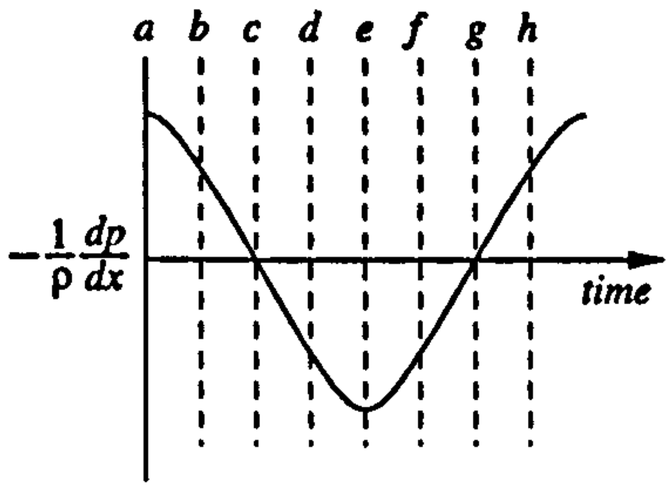

Figure 2.17: The velocity profile development of a pipe subject to an oscillating pressure gradient. Comparison of the analytical solution (–) with a five-point finite-difference scheme (– –o– –).

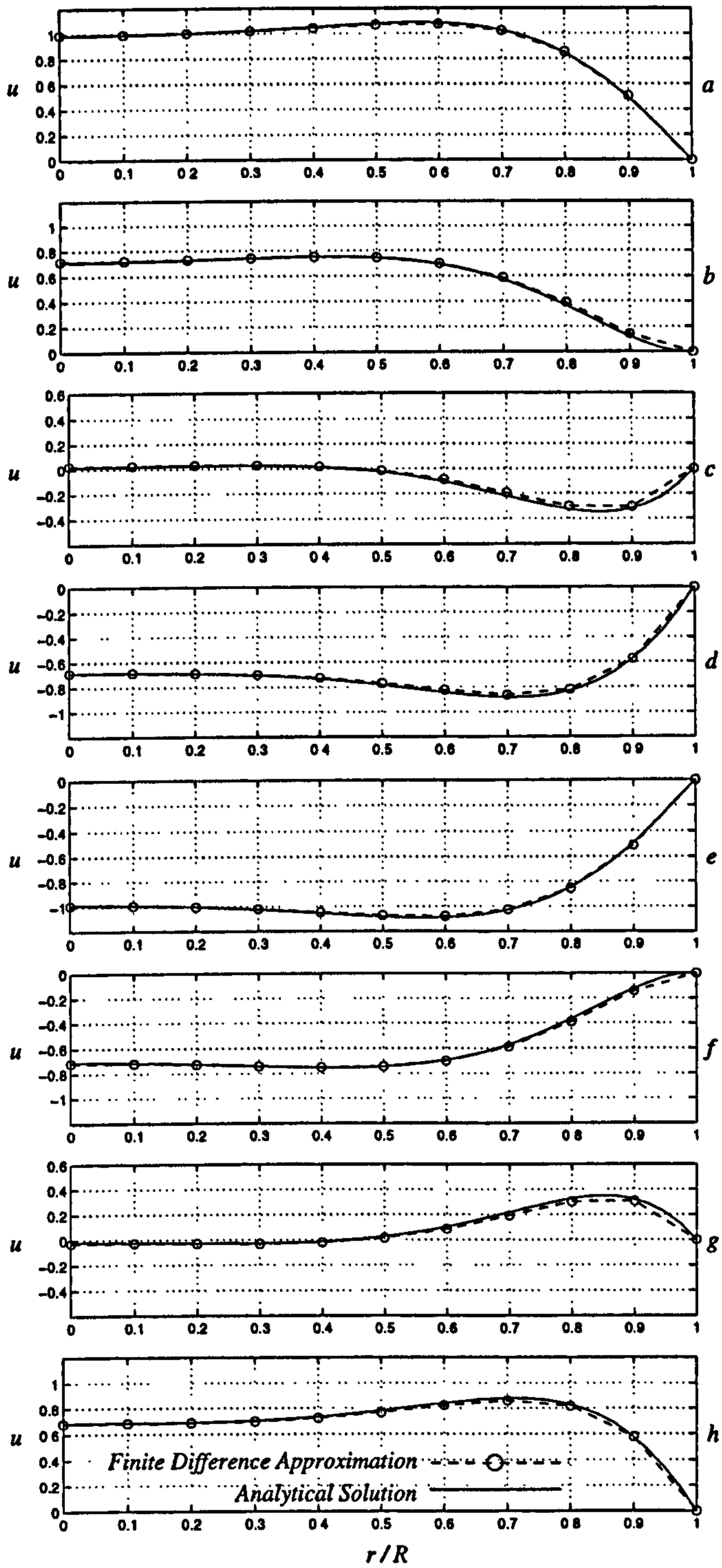

Figure 2.18: The velocity profile development of a pipe subject to an oscillating pressure gradient. Comparison of the analytical solution (–) with a ten-point finite-difference scheme (––o––).

2.5 The Cavity

2.5.1 Modelling the Cavity

The cavity is the lever between the plate motion and jet expulsion – its behaviour is central to the system. Unfortunately, accurate modelling of the cavity would be computationally extortionate, requiring the solution of the full compressible Navier-Stokes equations at every time step. Such a calculation has been performed by Rizzetta *et al.* (1999), but this is not in line with the desire to produce a solution that is numerically economical. The method used by Rathnasingham and Breuer (1997a), which has been adopted here, defines pressure variations in the cavity by density changes. This is simply achieved by the equation of state:

$$P_c = \rho_c RT \tag{2.83}$$

where R is the gas constant, T is the temperature, ρ_c is the density of fluid in the cavity, and P_c is the fluid pressure in the cavity. The density is assumed to be uniform within the cavity and any changes to it are felt instantaneously:

$$\rho_c = M_c/V_c \tag{2.84}$$

where M_c is the mass of fluid in the cavity and V_c is the volume of the cavity. The evolution of V_c is governed by the diaphragm, whereas the evolution of M_c is governed by mass conservation:

$$\frac{dM_c}{dt} = \dot{M}_{out} \tag{2.85}$$

where $\dot{M}_{out}$ is the rate of mass flow through the orifice. These equations are the hub of the MEMS model. There are, however, inherent approximations in their

use. Firstly, no account of particle motion in the cavity is taken into consideration. Rizzetta *et al.* (1999) have shown that, for some configurations, internal flow structures similar to external ones can be observed in the cavity.

To establish when it is safe to apply the approximation of a static cavity, some rules of thumb have been developed.

Limits of the Static-Compressible Approximation

When the cap area of the cavity is of comparable order to the orifice area, and incompressible fluid dynamics are assumed, the flow rates in the orifice and cavity will also be comparable. If, therefore, the cavity fluid dynamics are to be safely neglected, the orifice area must be at least an order of magnitude smaller than the area of the cavity cap. This constraint is stated algebraically:

$$\frac{A_o}{A_c} < 0.1 \tag{2.86}$$

where A_o is the orifice area, and A_c is the cap area of the cavity.

Another rule of thumb arises from comparing the static and compressible model of this chapter with an incompressible dynamic solution. The incompressible dynamic solution is very easily obtained from mass conservation; the mass flow induced by the diaphragm is equal to the mass flow out of the orifice. The average velocity in the orifice ($\bar{u}_{o,\text{inc}}$) is given by

$$\bar{u}_{o,\text{inc}} = \bar{u}_d \frac{A_d}{A_o} \tag{2.87}$$

where A_d is the diaphragm area, and $\bar{u}_d$ is the average diaphragm velocity. If in a simulation the velocity out using the static-compressible model is greater than that calculated by the dynamic-incompressible solution (equation (2.87)), it is likely that the static approximation is no longer valid. This can be inferred

on the assumption that a lesser energy solution will be preferred by the system. This limit to the static-compressible model can be expressed algebraically as:

$$\frac{A_d \bar{u}_d}{A_o \bar{u}_o} > 1 \tag{2.88}$$

Uniform and Immediate Compressibility

The second major assumption in the model, as defined by equations (2.83)-(2.85), is that all density and pressure variations are felt uniformly and instantaneously throughout the cavity. This assumes that flow inside the cavity is not dynamically compressible. This is a reasonable assumption near the diaphragm, provided that the diaphragm velocity is at least an order of magnitude less than the speed of sound; this is easily the case for the MEMS application. There may, however, be significant density variations around the orifice. In this model it is assumed that all expansion acts over the length of the orifice with complete uniformity in the cavity, this will not be true in many cases.

The Governing Equations in Differential Form

The mass and the volume of the cavity are the 'cavity variables' and to calculate them requires the expression of their evolution in differential form. Firstly, we can say that the rate of change of mass in the cavity is equal to the mass flow rate into the cavity through the orifice. This expressed algebraically is:

$$\frac{dM_c}{dt} = -\rho_1 \int_{A_o} u_1 \, dA \tag{2.89}$$

where A_o is the orifice area and the subscript 1 denotes values at the cavity orifice interface. The integration of the jet velocity profile (u_1) is performed numerically at each evaluation of equation (2.89) using the first Newton-Cotes formula - the

simple trapezoidal rule (Chapra and Canale 1990).

The other cavity variable, cavity volume, is also expressed in differential form. The rate of change of cavity volume is equal to the average velocity of the diaphragm multiplied by its area. Again, stated algebraically:

$$\frac{dV_c}{dt} = -\int_{A_d} \dot{w}\, dA \tag{2.90}$$

where A_d is the area of the diaphragm and $\dot{w}$ is the diaphragm's velocity. The numerical integration in equation (2.90) is also performed using the trapezoidal rule.

2.5.2 The Predictor-Corrector Scheme

Nomenclature used in §2.5.2

x^n = a superscript n denotes a value at the current time step

x^{n+1} = a superscript n+1 denotes a value at the next time step

M_c = total mass in the cavity (kg)

V_c = cavity volume (m^3)

u_1 = velocity at cavity-orifice interface ($m\ s^{-1}$)

$w, \dot{w}, \ddot{w}$ = deflection (m), velocity ($m\ s^{-1}$), acceleration ($m\ s^{-2}$) of diaphragm

r_o = radial distance from orifice centroid (m)

r_d = radial distance from diaphragm centroid (m)

A_o = area of the orifice (m^2)

A_d = area of the diaphragm (m^2)

F = force per unit area applied to diaphragm ($N\ m^{-2}$)

Δt = time-step incremement (s)

ρ_c = density of cavity fluid (kg m^{-3})

$f_{1,2}$ = implicit functions for the diaphragm and orifice

The cavity variables are expressed as a pair of ordinary differential equations, (2.89) and (2.90). These can be solved using a predictor-corrector scheme that is second-order accurate in time (Ferziger 1998 p109). The predictor-corrector works by evaluating the time derivative of the variable at the current time step to extrapolate a *predicted* value at the next time step. If predicted values of all the variables are known, then the time derivative at the new time step can be estimated. Finally, the two derivatives at the current and new time step are averaged and the *corrected* value is obtained by extrapolation using this mean time derivative. For clarity, the whole process has been mapped symbolically:

The Predictor Stage

Firstly the time derivatives of the cavity variables are calculated from equations (2.89) and (2.90):

$$\frac{dM_c}{dt}^n = -\rho_c^n \int_{A_o} u_1^n \, dA$$
$$\frac{dV_c}{dt}^n = -\int_{A_d} \dot{w}^n \, dA \tag{2.91}$$

By using a first-order approximation, these derivatives can be used to estimate the cavity variables at the next time step:

$$M_c^{n+1} = M_c^n + \frac{dM_c}{dt}^n \Delta t$$
$$V_c^{n+1} = V_c^n + \frac{dV_c}{dt}^n \Delta t \tag{2.92}$$

At this point the implicit functions for the orifice and diaphragm are evaluated:

$$\begin{aligned} \dot{w}(r_d)^{n+1} &= f_1\left(F(r_d)^n, F(r_d)^{n+1}, w(r_d)^n, \dot{w}(r_d)^n, \ddot{w}(r_d)^n, M_c^n, V_c^n, M_c^{n+1}, V_c^{n+1}\right) \\ u_1(r_o)^{n+1} &= f_2\left(u_1(r_o)^n, \overline{\frac{d\rho_c}{dt}}, M_c^n, V_c^n, M_c^{n+1}, V_c^{n+1}\right) \end{aligned} \tag{2.93}$$

where the bar denotes a mean value between the new and the current time step. For the predictor stage the term $\overline{d\rho_c/dt}$ is estimated as such (this is also used to predict a value for ρ_c^{n+1}):

$$\overline{\frac{d\rho_c}{dt}} = \frac{1}{2}\left(\frac{d\rho_c}{dt}^n + \frac{d\rho_c}{dt}^{n+1}\right) \approx \frac{d\rho_c}{dt}^n = \frac{1}{V_c^n}\left(\frac{dM_c}{dt}^n - \rho_c^n \frac{dV_c}{dt}^n\right) \tag{2.94}$$

At the end of this stage, values for the orifice velocity, diaphragm velocity, cavity volume,cavity-fluid density and cavity mass, have been predicted.

The Corrector Stage

The corrector stage starts by calculating the time derivatives of the cavity variables at the new time step using the predicted values.

$$\begin{aligned} \frac{dM_c}{dt}^{n+1} &= -\rho_c^{n+1} \int_{A_o} u_1^{n+1}\, dA \\ \frac{dV_c}{dt}^{n+1} &= -\int_{A_d} \dot{w}^{n+1}\, dA \end{aligned} \tag{2.95}$$

Average time derivatives are found for the cavity variables between the two time steps, using the derivatives calculated in equations (2.91) and those calculated in equations (2.95). These mean derivatives are used to calculate the *corrected*

cavity values:

$$M_c^{n+1} = M_c^n + \overline{\frac{dM_c}{dt}}\Delta t$$
$$V_c^{n+1} = V_c^n + \overline{\frac{dV_c}{dt}}\Delta t \tag{2.96}$$

The final stage of the time step is to calculate corrected orifice and diaphragm values using the implicit functions:

$$\dot{w}(r_d)^{n+1} = f_1\left(F(r_d)^n, F(r_d)^{n+1}, w(r_d)^n, \dot{w}(r_d)^n, \ddot{w}(r_d)^n, M_c^n, V_c^n, M_c^{n+1}, V_c^{n+1}\right)$$
$$u_1(r_o)^{n+1} = f_2\left(u_1(r_o)^n, \overline{\frac{d\rho_c}{dt}}, M_c^n, V_c^n, M_c^{n+1}, V_c^{n+1}\right) \tag{2.97}$$

2.6 Chapter Summary

In this chapter the modelling of the MEMS actuator has been separated into four parts; the diaphragm (§2.2), the PZT (§2.3), the orifice (§2.4), and the cavity (§2.5). For each of these, various assumptions and approximations have been made and then discussed. Some validation exercises against known analytical solutions have been performed successfully. It is fair to conclude that, although approximate methods have been employed, an accurate and economical code has been developed.

Chapter 3

Actuator Simulations

In this chapter the mathematical actuator model is tested and investigated. In §3.1 the model is compared to experimental data from a micro-scale synthetic-jet actuator. The validated model is used to explore several issues in MEMS-actuator design, including: actuator scaling (§3.2), synthetic-jet alternatives (§3.4), and the optimum actuator dimensions (§3.6).

Nomenclature

c = correction factor

d = diaphragm damping (N s m^{-3})

d_{31}, d_{32} = radial/azimuthal piezoelectric constant (m V^{-1})

E_d = elastic modulus of diaphragm material (N m^{-2})

E_p = elastic modulus of PZT material (N m^{-2})

F = constant load (N)

g = parameter used to characterise actuator scale (m)

H_c = cavity height (m)

$i = \sqrt{-1}$

k = gas constant (J kg^{-1} K^{-1})

K_e = effective spring constant (N m^{-1})

l = orifice length/cap thickness (m)

M_e = effective mass (kg)

N_d = number of grid points in diaphragm finite-difference scheme

N_o = number of grid points in orifice finite-difference scheme

P_c = cavity pressure (N m^{-2})

P_o = ambient pressure outside cavity (N m^{-2})

Q = mass flow rate (kg s^{-1})

r = radial distance from centroid (m)

R_o = orifice radius (m)

R_d = diaphragm radius (m)

R_p = PZT disc radius (m)

St = Stokes parameter

t = time (s)

t_d = diaphragm thickness (m)

t_p = PZT disc thickness (m)

T = air temperature (K)

U_c = centre-line jet velocity (m s^{-1})

$U_{c,max}$ = maximum centre-line jet velocity (m s^{-1})

$\overline{U}$ = average velocity of jet profile (m s^{-1})

$\overline{U}_{max}$ = maximum average velocity of jet profile (m s^{-1})

$\overline{U}_{min}$ = minimum average velocity of jet profile (m s^{-1})

$\overline{U}_{opt}$ = optimised average velocity (m s^{-1})

V = cavity volume (m^3) or voltage (V)

w = diaphragm deflection (m)

w_{max} = maximum diaphragm deflection (m)

$\bar{w}$ = average diaphragm deflection (m)

w_c = diaphragm deflection at central point (m)

$\Delta P = P_c - P_o$ (N m^{-2})

Δt = time step (s)

λ = decay rate (s^{-1})

μ = dynamic viscosity (kg m^{-1} s^{-1})

ν = kinematic viscosity (m^2 s^{-1})

ν_d = Poisson's ratio of the diaphragm material

ν_p = Poisson's ratio of the PZT material

Π = pressure gradient $\Delta P/\rho l$ (m s^{-2})

ρ = density (kg m^{-3})

ρ_o = ambient air density (kg m^{-3})

ρ_d = density of diaphragm material (kg m^{-3})

ρ_p = density of PZT material (kg m^{-3})

ω = frequency of orifice flow or Helmholtz frequency (rad s^{-1})

ω_d = driving frequency (s^{-1})

ω_n = natural frequency of diaphragm (s^{-1})

ω_r = resonant frequency of diaphragm (s^{-1})

3.1 Model Validation

For the purposes of separation control, Crook *et al.* (1999) fabricated an actuator based on the design of Coe *et al.* (1994). The actuator had a diaphragm of 12.7 mm in radius and produced jet velocities of up to 20 m s^{-1}. This device, referred to here as the *Manchester* actuator (the location of the experiments of Crook *et al.* 1999) produced a 'synthetic' or 'massless' jet. To generate the synthetic jet the diaphragm is driven sinusoidally, this produces an oscillatory flow which eventually generates a continuous jet away from the orifice via a mechanism similar to acoustic streaming (see Lighthill 1978).

The bulk of calculations in this thesis are for actuators with non-oscillatory forcing. However, the experimental data from Crook *et al.* (1999) are used in this section to validate the mathematical model.

The Manchester actuator differs slightly in design to that in Figure 2.1, with the diaphragm oriented on its side as shown in Figure 3.1 (this was also the case in the actuator of Rathnasingham 1997). This design maximises the size of the diaphragm while minimising spanwise spacing between actuators – a larger diaphragm improves the performance of the actuator (see §3.6.4).

The numerical model described in Chapter 2 can be applied to the Manchester actuator without any significant adjustments. The model, however, is limited by its inability to account for the fluid dynamics inside and outside the cavity; in a synthetic-jet flow this can be a serious issue. Rizzetta *et al.* (1999) have performed direct numerical simulations of the compressible Navier-Stokes equations for a synthetic-jet flow field, and have shown that during the inflow cycle a vortical recirculation occurs within the cavity; this cannot be taken into account in the current model. A second serious issue is that the synthetic-jet mechanism cannot be modelled without taking into account the fluid dynamics outside the cavity; in the simulations of this chapter the device is effectively issuing into still air. For these reasons, only rough quantitative comparison can be made between the numerical model and the experiments of Crook *et al.* (1999).

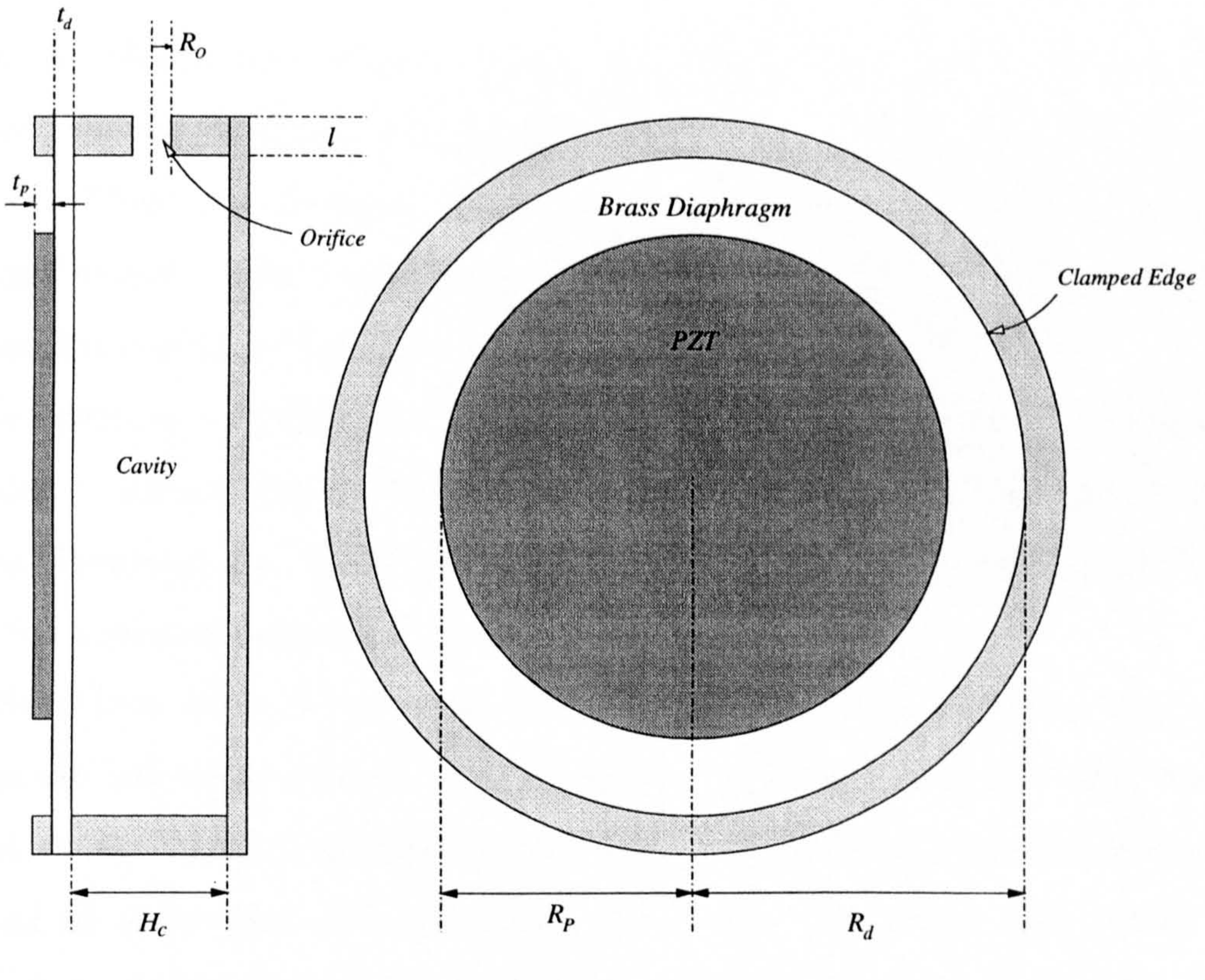

Figure 3.1: The Manchester Actuator

3.1.1 Orifice Optimisation

The system, as defined by the modelling in Chapter 2, has some general axioms of design for velocity optimisation (these will be supported in §3.6.4). Firstly, that the diaphragm should be as large as possible, and secondly, that the volume of the cavity should be as small as possible. This, generally speaking, increases the potential compression and increases the net mass flow and the volumetric flow rate.

In the Manchester actuator (Figure 3.1) these two rules can be seen to be applied; the diaphragm is oriented to maximise its size and the cavity height is shallow. There are obviously upper and lower design limits for the diaphragm size and cavity volume, such as manufacturing capabilities; however, these are not incorporated in the model.

The current modelling predicts that the orifice length, l, should be minimised in order to reduce viscous effects and to increase the pressure gradient over the orifice. However, the actual orifice and cap thickness is likely to be set by the need for a level of robustness and rigidity.

Given that there are general rules defining the overall actuator shape, the parameter left undetermined, and in need of optimisation, is the orifice radius. Crook *et al.* (1999) performed such an optimisation for the Manchester actuator and an optimum orifice radius (R_o) of 0.5 mm $\pm$ 0.05 mm was found. The dimensions of the actuator were as follows: cavity height H_c=2 mm; orifice thickness l=1.6 mm; cavity and diaphragm radius R_d=12.7 mm; diaphragm driving frequency ω_d=1366 Hz.

A numerical emulation of this optimisation experiment was performed and Figure 3.2 shows the variation of maximum centre-line velocity ($U_{c,max}$) plotted against orifice radius (R_o) (simulation parameters §A.1.1). The data show a sharp optimum around an orifice radius of 0.7 mm. This is misleading, however, as it is the optimum that would occur if flow within the cavity were negligible; for the synthetic-jet configuration this is not the case.

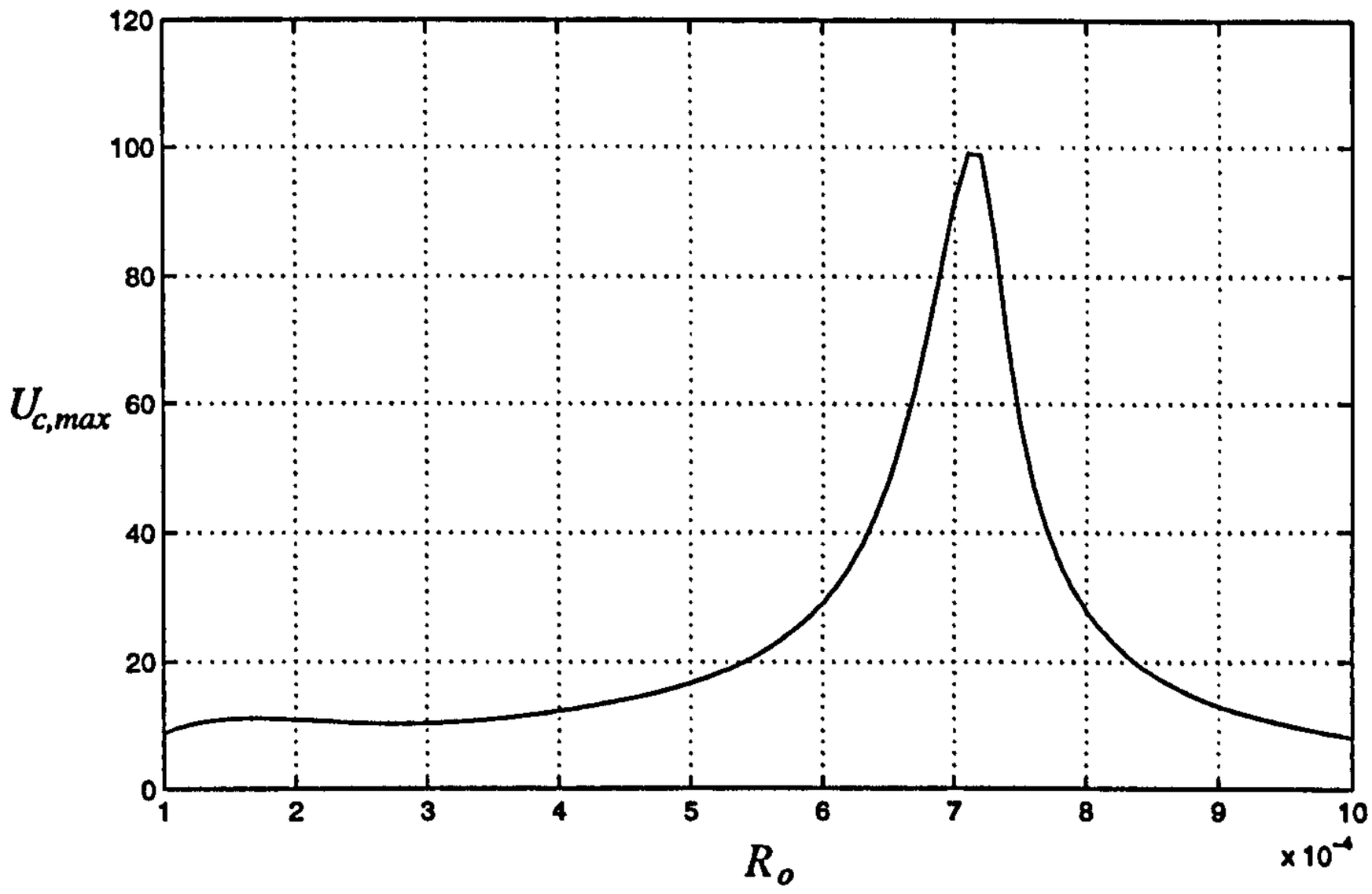

Figure 3.2: Variation of maximum centre-line velocity ($U_{c,\max}$) with orifice radius (R_o).

The result is a static-compressible solution, i.e. one that neglects the fluid dynamics in the cavity and assumes perfect compressibility. A simple dynamic-*in*compressible solution was derived in §2.5 and Figure 3.3 shows this analytical solution (−−) juxtaposed with the static-compressible results (–) (the velocity is an average of the maximum velocity profile, $\overline{U}_{\max}$ as opposed to a centre-line velocity, $U_{c,\max}$).

In reality the system is compressible *and* the cavity fluid dynamics are significant. In this case, the most accurate of the two approximate solutions, for a given R_o, will be the one that produces the lowest jet velocity (it is assumed that the least energy output will be preferred by the system). The point of maximum velocity will therefore be approximately coincident with the intersection between the compressible and dynamic solutions; this is used to provide a better estimation of the optimum orifice radius than the static-compressible model alone. (Rathnasingham and Breuer (1997a) also equate an incompressible solution with a viscous-compressible solution to successfully predict an optimum Stoke's parameter for their actuator – see §C.1).

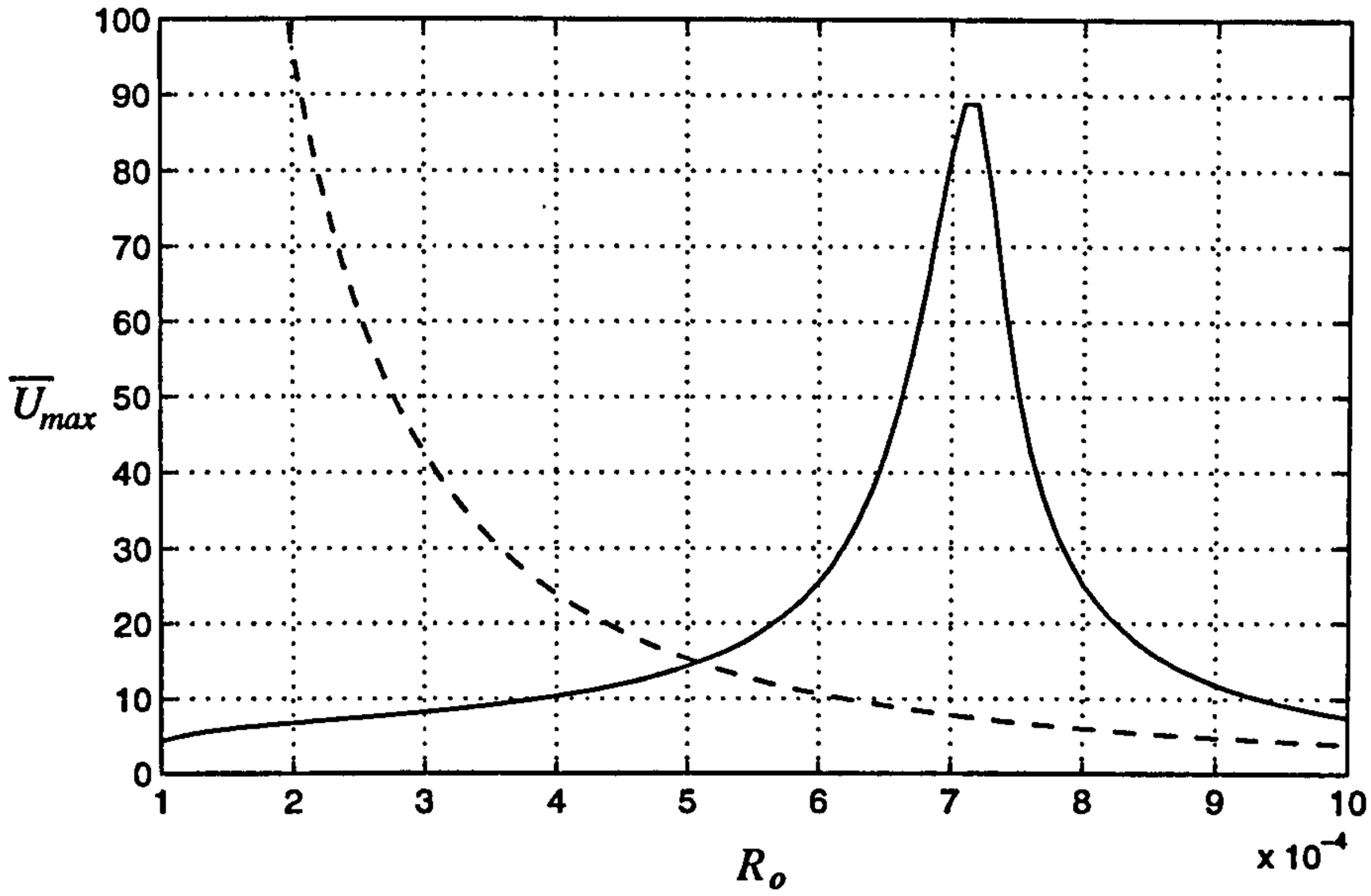

Figure 3.3: Variation of maximum average velocity ($\overline{U}_{\max}$) with orifice radius (R_o); The static-compressible solution (–); the dynamic-incompressible solution (– –).

This intersection method estimates an optimum orifice radius of 0.51 mm, which is in nearly exact agreement to that observed experimentally. Optimised velocity magnitudes cannot be compared to the numerical model as values around the optimum radius are likely to be significantly overestimated.

3.1.2 Cavity Height Optimisation

Experimental data showing the effect of varying cavity height on jet velocity have also been published (Crook *et al.* 1999). The dimensions of the device for this experiment were the same as those in §3.1.1, apart from the cavity height (H_c) was varied, and the orifice radius was fixed at R_o=0.6 mm.

Again, an emulation of this procedure was performed numerically (simulation parameters §A.1.2). Figure 3.4 shows the variation of maximum average velocity ($\overline{U}_{\max}$) with cavity height (H_c) . The solid line is the static-compressible numerical model and the dashed line is the dynamic-incompressible solution. The optimum, which is at the intersection of the two curves, occurs at H_c=2.8 mm. This compares very closely with the experimental optimum, H_c=3 mm ± 0.5

mm.

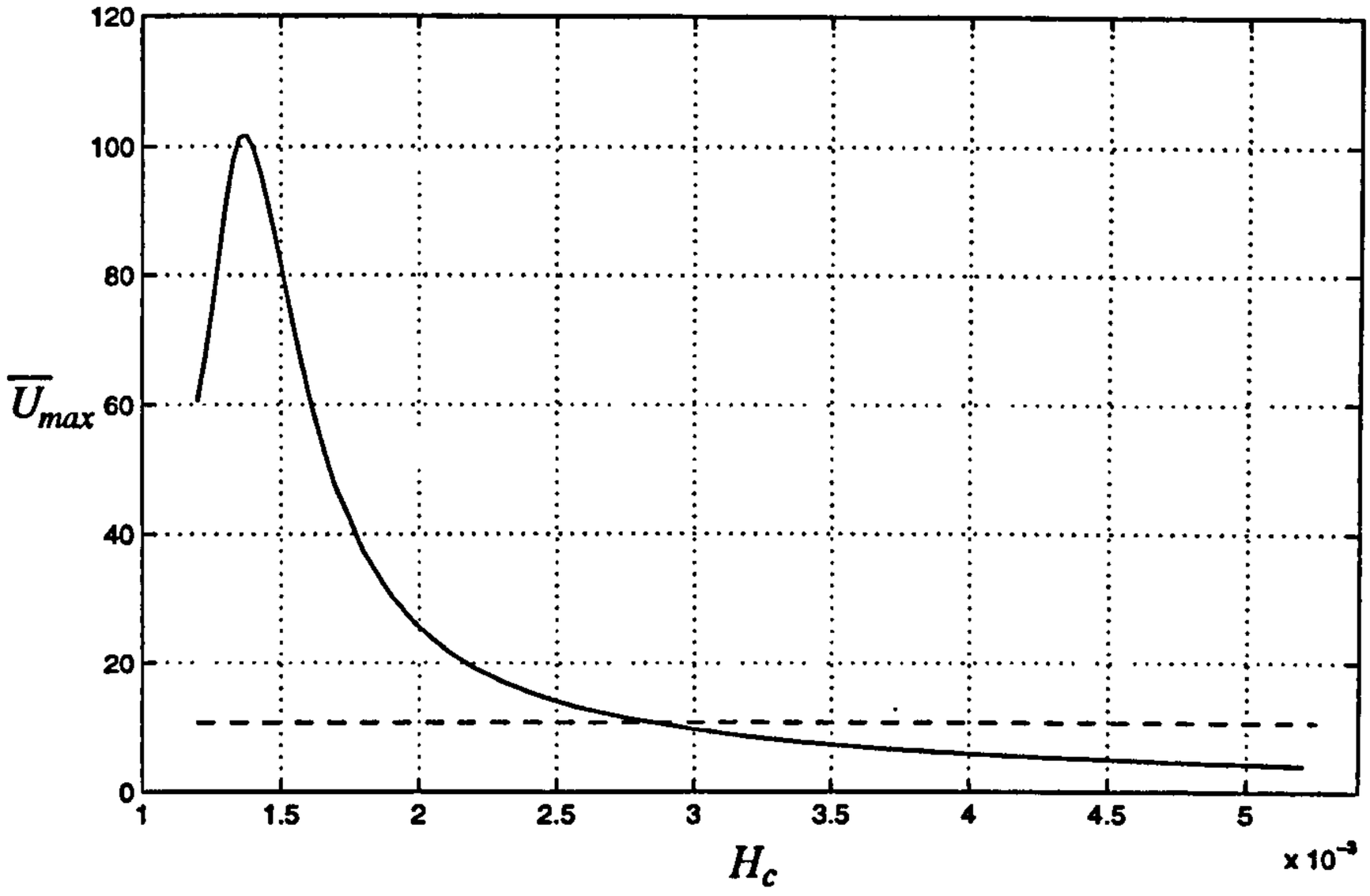

Figure 3.4: Variation of maximum average velocity ($\overline{U}_{\max}$) with cavity height (H_c); The static-compressible solution (–); the dynamic-incompressible solution (– –).

This is a one-dimensional optimisation for a specific orifice width, and not an overall optimisation. If the orifice radius were re-optimised at each distinct cavity height, the numerical model would not predict an optimum. In reality, however, an optimum cavity height would exist, when viscous forces in the cavity become comparable to those in the orifice.

3.1.3 Diaphragm Dynamics

The Manchester actuator consists of a diaphragm with a PZT attached to its underside (see Figure 3.1). Crook *et al.* (1999) performed a frequency analysis on the combined PZT and brass diaphragm; a resonant frequency of 1366 Hz was observed.

To calculate the resonant frequency of the numerical model a single pulsed force is used to excite the diaphragm and a fast Fourier transform is used to calculate the most dominant mode of vibration. The results of the spectral decomposition are shown in Figure 3.5 (simulation parameters §A.1.3). The solid

line is the numerical prediction and the dashed vertical line is the experimentally identified resonant frequency of 1366 Hz. The results agree very well with the experimental data.

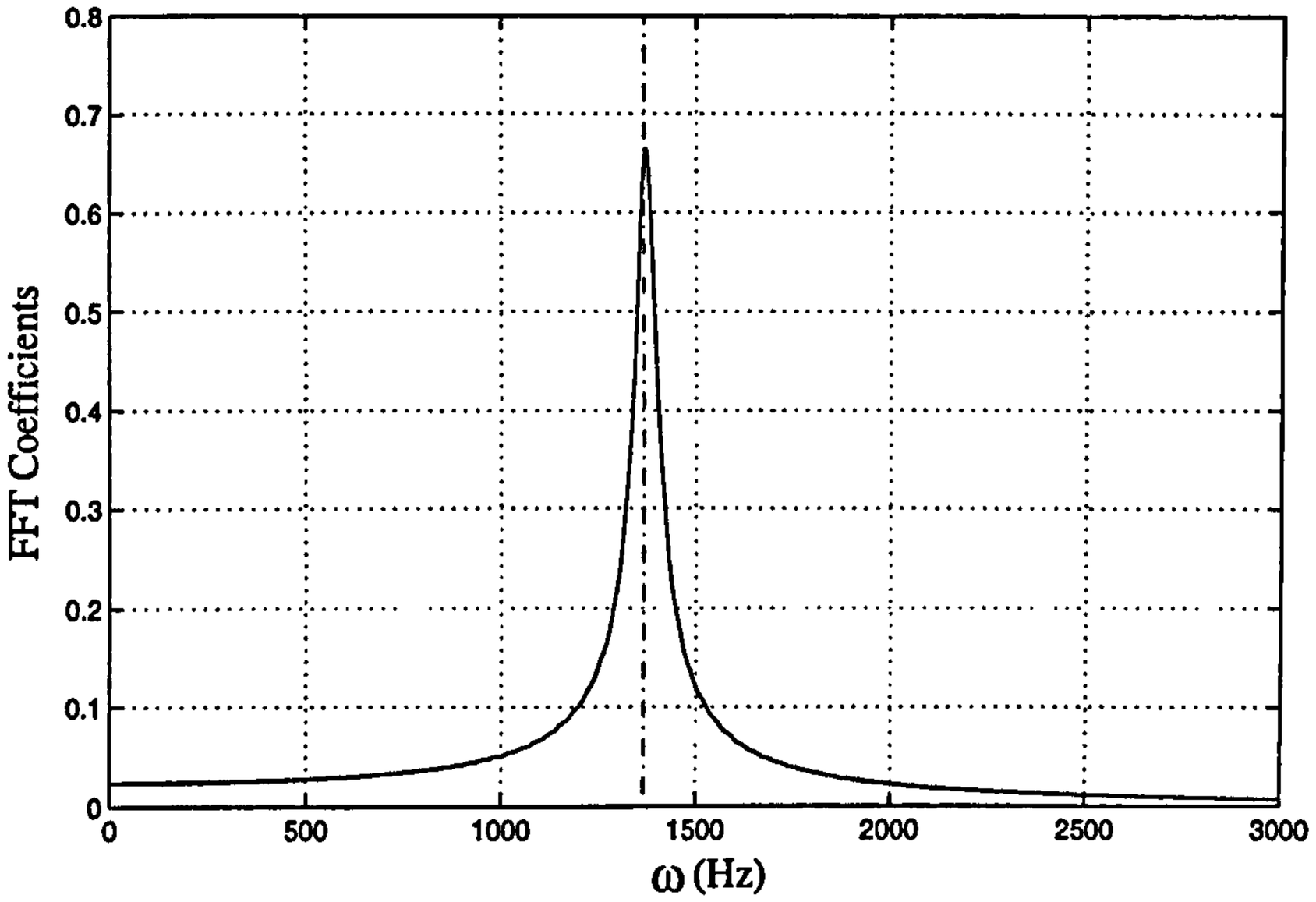

Figure 3.5: The resonant frequency of the PZT and diaphragm. Experimental data (–·–) and numerical simulation (–).

3.1.4 Diaphragm and PZT Optimisation

The relative size of the PZT to the diaphragm plays an important role in determining the overall electrostrictively induced deflection. Figure 3.6 demonstrates how varying PZT radii can seriously affect the deflected mode shape.

There is, in fact, an optimum PZT size. Here, this is defined as the PZT thickness and radius which, for a given diaphragm size, produces the greatest overall deflection. The brass diaphragms and PZT discs that were used in the Crook *et al.* (1999) experiments were factory made and presumably optimised to some extent for performance. In this section such an optimisation has been numerically replicated.

A simple iterative process has been adopted for this two-dimensional optimi-

sation. Firstly the optimum radius is found for an arbitrarily chosen thickness (here $t_p = 50$ μm), this optimum radius is then fixed and a new optimum thickness found. The procedure continues until the optimum values of radius and thickness no longer vary outside a chosen tolerance (to three significant figures in this case). Table 3.1 shows the progression of the PZT optimisation for a brass diaphragm with the following dimensions: R_d=12.7 mm, t_d=100 μm (simulation parameters §A.1.4).

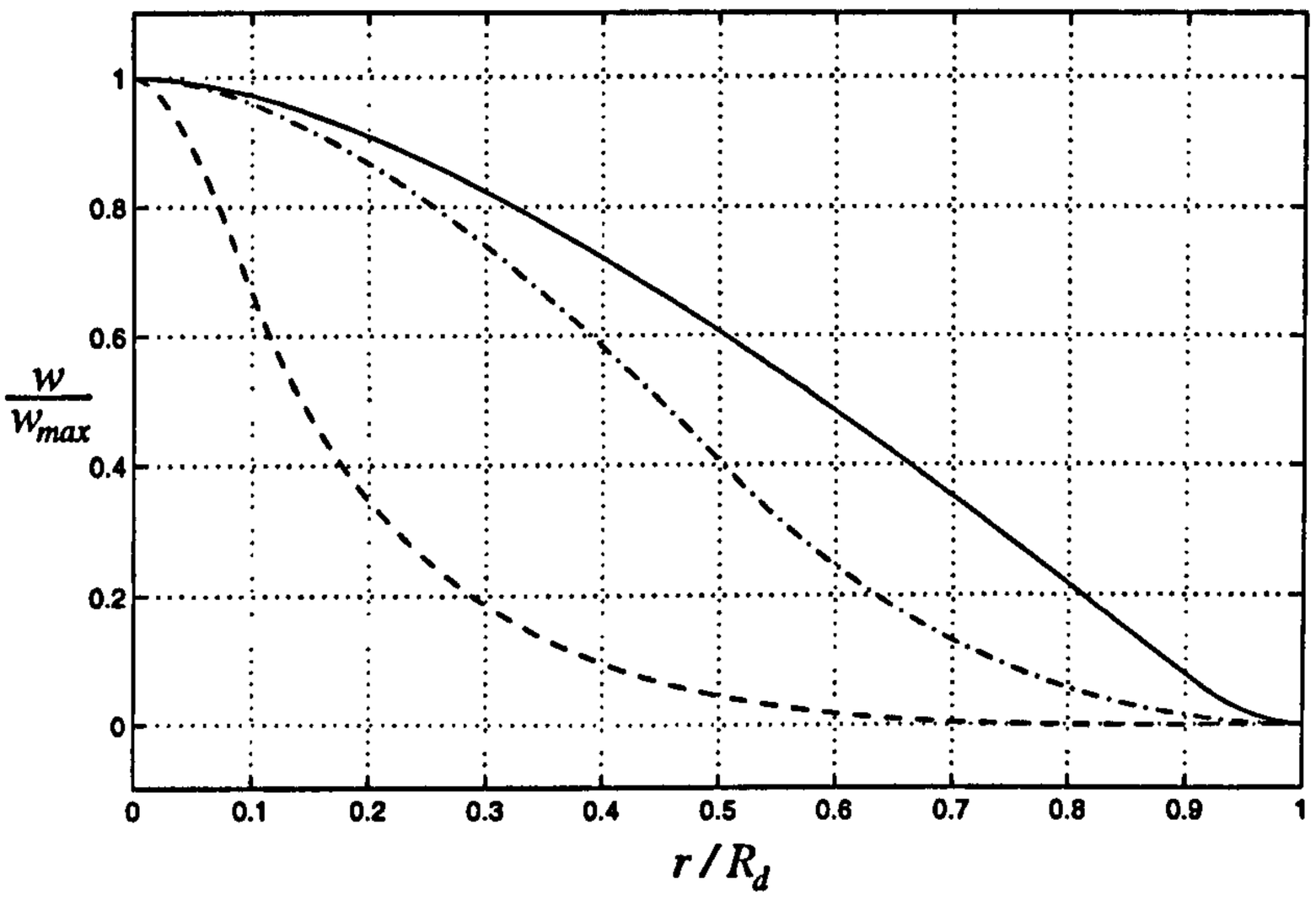

Figure 3.6: The statically deflected mode shape for diaphragms with different radii PZT discs. R_p/R_d=0.1 (– –); R_p/R_d=0.5 (– · – ·);R_p/R_d=0.9 (–)

The simulations that correspond to the sequence of optimisations (A)-(F) are shown in Figures 3.7 and 3.8 (the solid lines are polynomials that have been fitted to the data in order to produce better estimates for the next stage of optimisation).

The final optimised PZT thickness is 126 μm, this is fairly close to the thickness of 100 μm of the manufactured device. This optimal thickness occurs when the flexural rigidity of the PZT is comparable to that of the diaphragm. A balance such as this is perhaps most conducive to the production of moment from a given electric field.

The optimum PZT radius was found at 10.9 mm, this is very close to the

Optimisation Stage	t_p	R_p
A	fixed @ 50 μm	optimised - 10.2 mm
B	optimised - 113 μm	fixed @ 10.2 mm
C	fixed @ 113 μm	optimised - 10.9 mm
D	optimised - 126 μm	fixed @ 10.9 mm
E	fixed @ 126 μm	optimised - 10.9 mm
F	optimised - 126 μm	fixed @ 10.9 mm

Table 3.1: PZT optimisation

actual PZT dimension of 11 mm. The existence of this optimum is due to a trade off between increasing total moment by increasing R_p, but ensuring that R_p is not so large that it inhibits the fundamental mode shape of deflection. The mode shape of a deflected diaphragm with clamped edges has a curvature which turns from negative near the centre to positive near the edge. If the PZT radius is very big then there will be a conflict between the forcing, which asserts a constant moment, and the mode shape, which has a moment that changes sign.

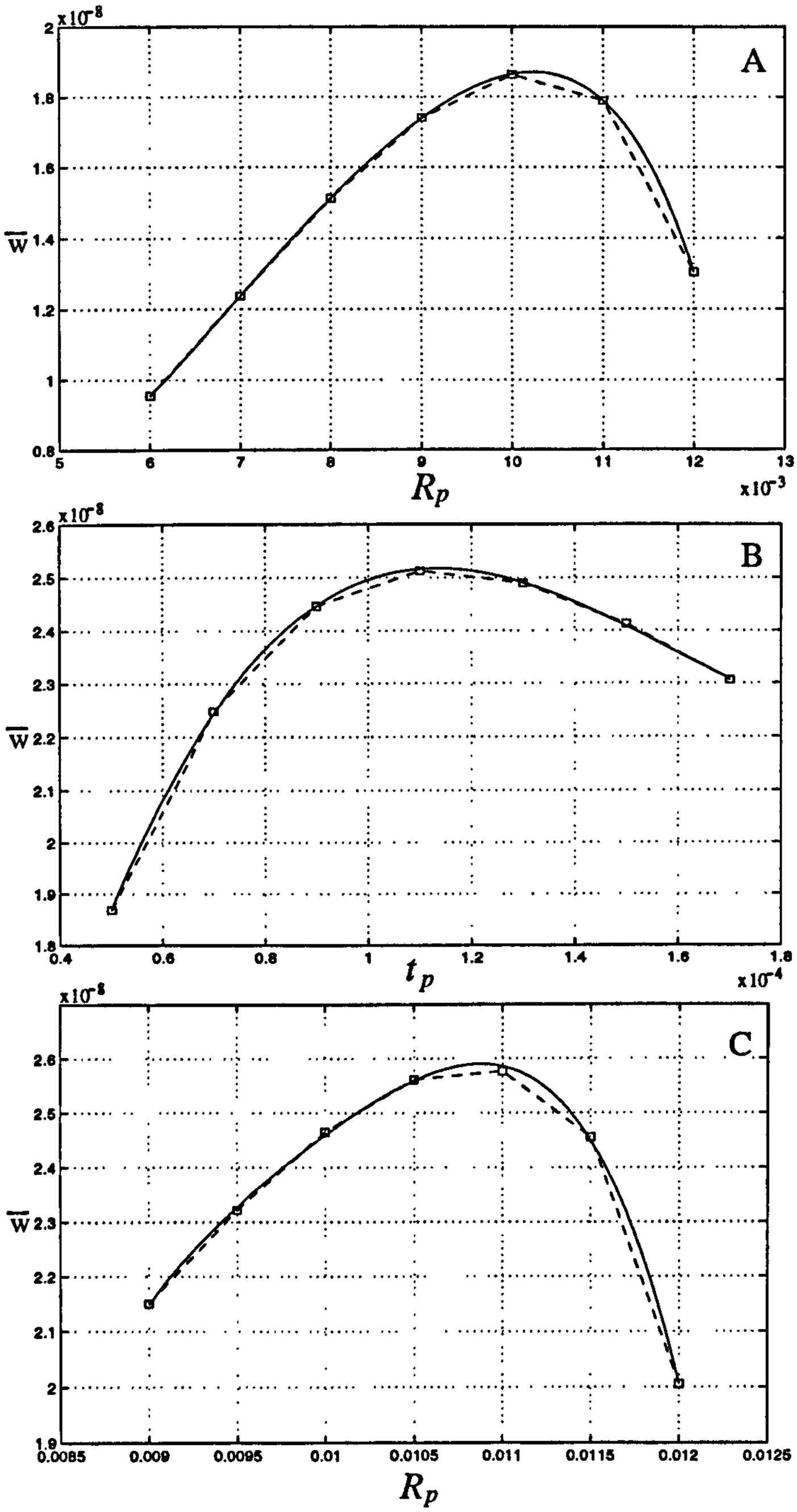

Figure 3.7: The stages (A)-(C) in the PZT optimisation procedure of Table 3.1. Plots (A) and (C) are radius (R_p) optimisations with fixed thickness (t_p); Plot (B) is a thickness optimisation with fixed radius.

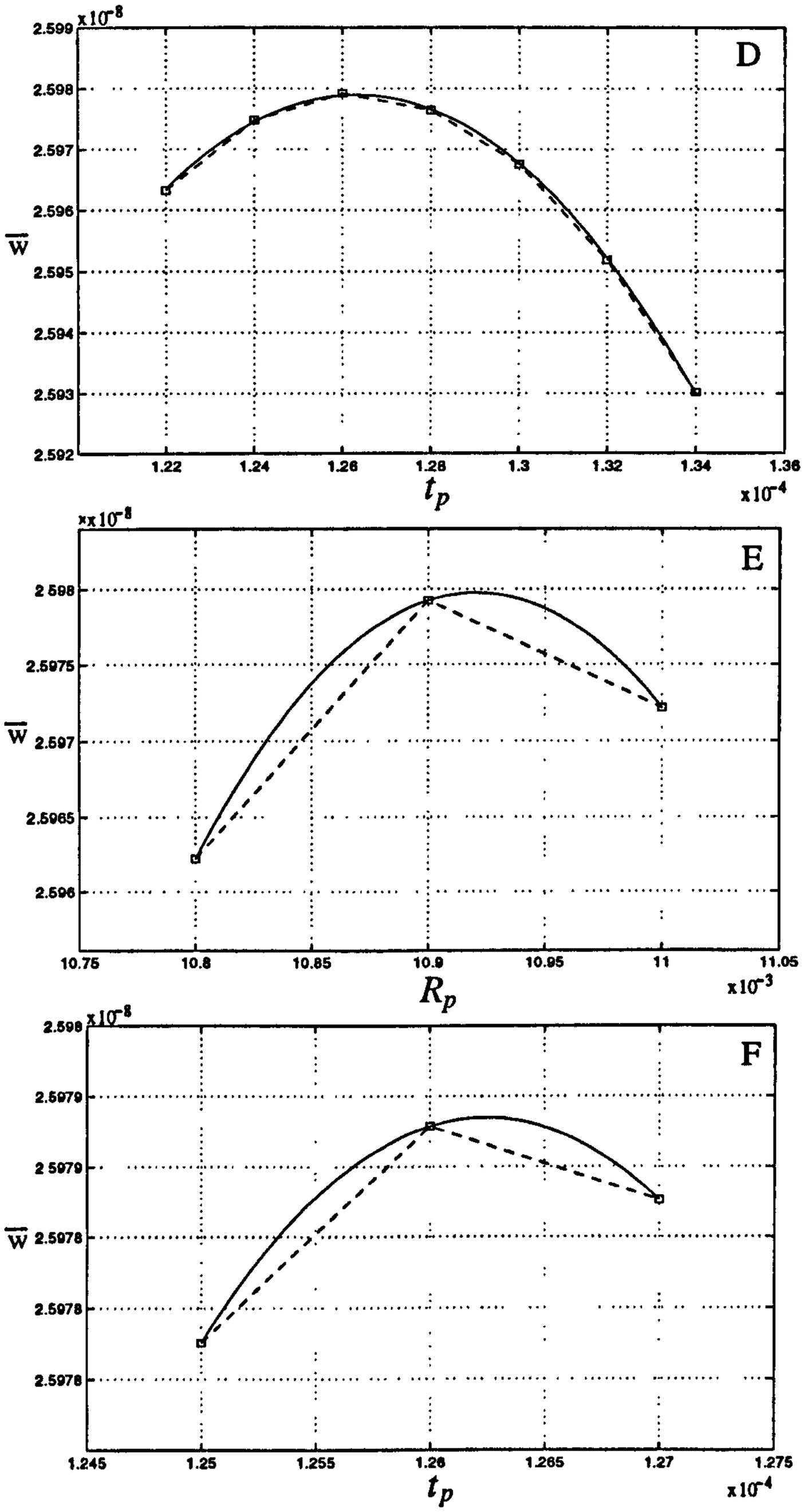

Figure 3.8: The stages (D)-(F) in the PZT optimisation procedure of Table 3.1. Plot (E) is a radius (R_p) optimisation with fixed thickness (t_p); Plots (D) and (F) are thickness optimisations with fixed radius.

3.1.5 Velocity Magnitude

In this section a comparison between the velocity magnitude observed in experiment and numerical simulation is performed. The model has been compared with experimental data using an actuator which has the following dimensions: H_c=2 mm, R_d=12.7 mm, and R_o=300 μm. In Crook *et al.* (1999) this design is reported to have produced synthetic-jet velocities of around 20 m s^{-1}. However, peak fluctuations were as much as four times larger than the synthetic mean in some cases, and so here the orifice exit velocity is estimated at around 80 m s^{-1}. An applied voltage of 40 V has been used for the numerical simulations which, if the experiment behaved linearly, would produce peak fluctuation velocities of approximately 40 m s^{-1}.

Figure 3.9(a) and 3.9(b) show the exit jet-velocity history and the plate-deflection history, respectively (simulation parameters §A.1.5). The maximum central deflection of the plate is 36 μm and the maximum centre-line velocity at the orifice is 57 m s$^-$1, which is significantly higher than the predicted peak fluctuation of 40 m s$^-$1 based on the experimental data.

The inaccuracies in the comparison come from many sources but mainly from the inability to model the fluid dynamics in or outside of the cavity. This is largely an issue because of the sinusoidal diaphragm forcing; other modes of diaphragm forcing will not tax the model so severely (see §3.4.1). Crook *et al.* (1999) also suggest the possibility of actual velocities being higher than those measured owing to the large size of the hot wire in comparison to the orifice radius; it is possible that this is a factor in the overestimation.

The deflection of the diaphragm is also likely to be inaccurate because of the model's simplified treatment of electrostriction and its inability to account for nonlinearities.

The success of the numerical and experimental comparison of velocity magnitude is only modest. However, the model is close enough for rough quantitative predictions of velocity magnitude to be made.

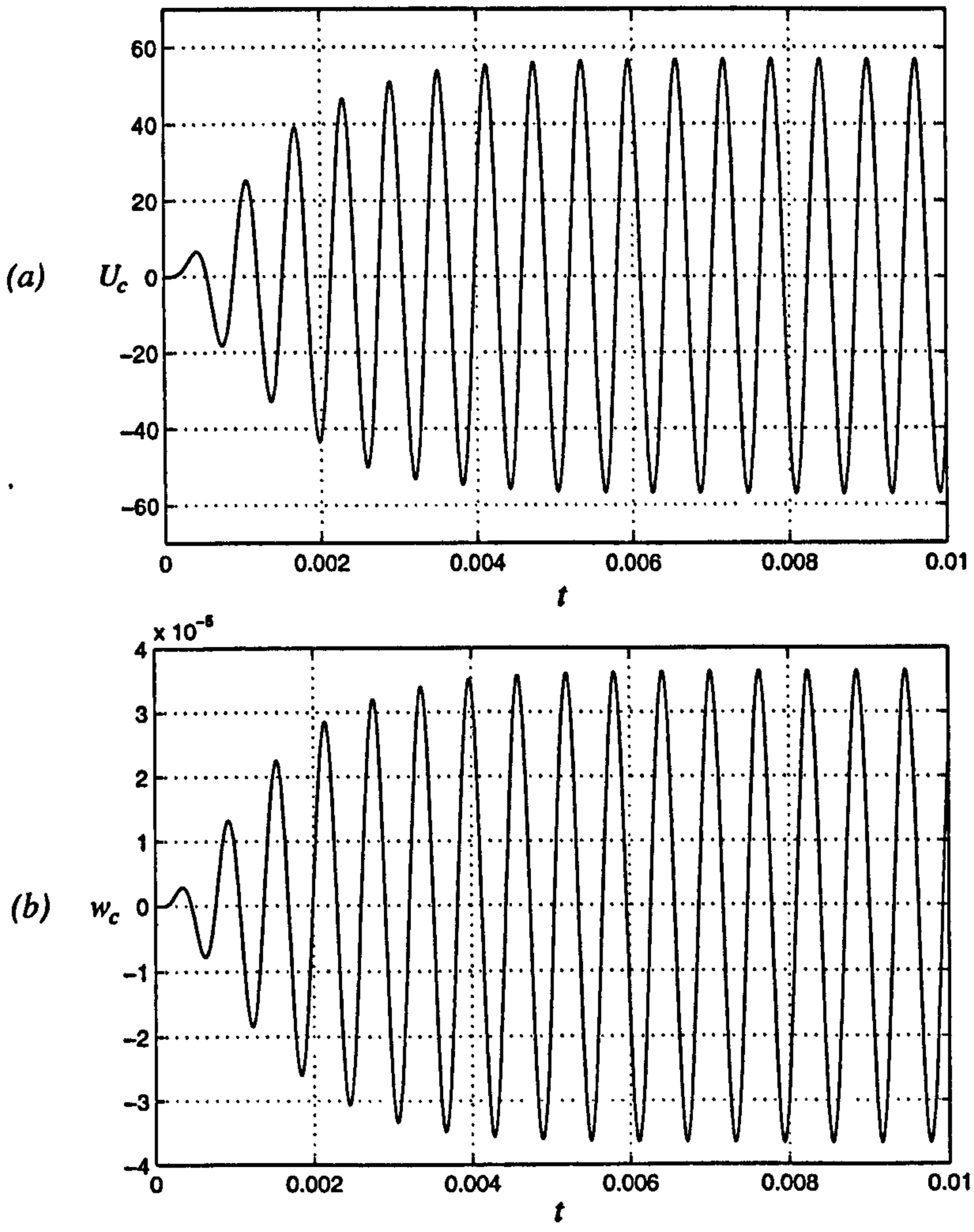

Figure 3.9: (a) Centre-line velocity history at the orifice exit; (b) deflection history of the diaphragm at its central point.

3.1.6 Section Summary

Overall, the model validation has been successful with good predictions having been made for optimum orifice radius, cavity height, and the diaphragm/PZT resonant frequency. Also, the design of the diaphragm and PZT has been emulated by an optimisation simulation that obtained an optimum R_p-to-R_d ratio of 0.858; this compares very well with the actual device ratio of 0.866.

There are, however, some areas that need to be improved to achieve a good quantitative comparison between experiment and simulation. Firstly, some account of fluid motion inside and outside the cavity must be made. Secondly,

the electrostrictive force must be modelled properly and integrated into the plate equations (including any transient effect, as this will strongly influence the maximum deflection possible in sinusoidal operation). Finally, a nonlinear plate model should be used (see Lucey *et al.* 1997); Crook *et al.* (1999) have demonstrated the nonlinearities of the plate and PZT system, with different resonant frequencies being measured for different applied voltages.

3.2 The Effects of Actuator Scaling

A micro-scale device (of the order of mm) such as the Manchester actuator, will not necessarily behave in the same way as a scaled-down version of the same design. This section investigates how different properties, such as maximum velocity and optimum orifice radius, scale with the overall size of the actuator. This is of interest as it may help to establish when it is possible to draw comparisons between large-scale prototypes and the actual MEMS devices.

3.2.1 Natural frequency

Probably the most predictable result of scaling down the actuator is on the natural frequency of the diaphragm. The following mathematical reasoning demonstrates the effect.

The first harmonic frequency of a thin circular plate, clamped at its edge, is given by:

$$\omega_n = K\sqrt{\frac{Et^2}{12(1-\nu^2)\rho R^4}} \tag{3.1}$$

where K=10.2158, t is the thickness, R is the radius, E is the elastic modulus, ν is Poisson's ratio, and ρ is the density of the plate. From equation (3.1) the following relationship can be obtained:

$$\omega_n \propto \frac{t}{R^2} \tag{3.2}$$

If the entire diaphragm is scaled equally, then t will always be a constant factor of R, therefore equation (3.2) can be simplified further:

$$\omega_n \propto \frac{1}{R} \tag{3.3}$$

This simple inverse relationship has serious ramifications for the design of MEMS-

scale synthetic jets, which require sinusoidal operation at the diaphragm's resonant frequency. For example, a diaphragm that is scaled from 50 mm to 50 μm will have a resonant frequency one thousand times greater as a result. This may prove to be an impossibly-high driving frequency.

Numerical simulations of the Manchester diaphragm and PZT have been performed at different scales using a parameter g to characterise the overall size of the device. The actuator dimensions are expressed here in terms of g: diaphragm radius R_d=12.7g; diaphragm thickness t_d=0.1g, PZT radius R_p=11g; PZT thickness t_p=0.1g. (for the Manchester actuator g=1 mm).

Figure 3.10 shows the variation of natural frequency with g, which clearly exhibits the inversely proportional relationship of equation (3.3), and shows a natural frequency in excess of 100 kHz for g=10 μm (simulation parameters §A.1.6)

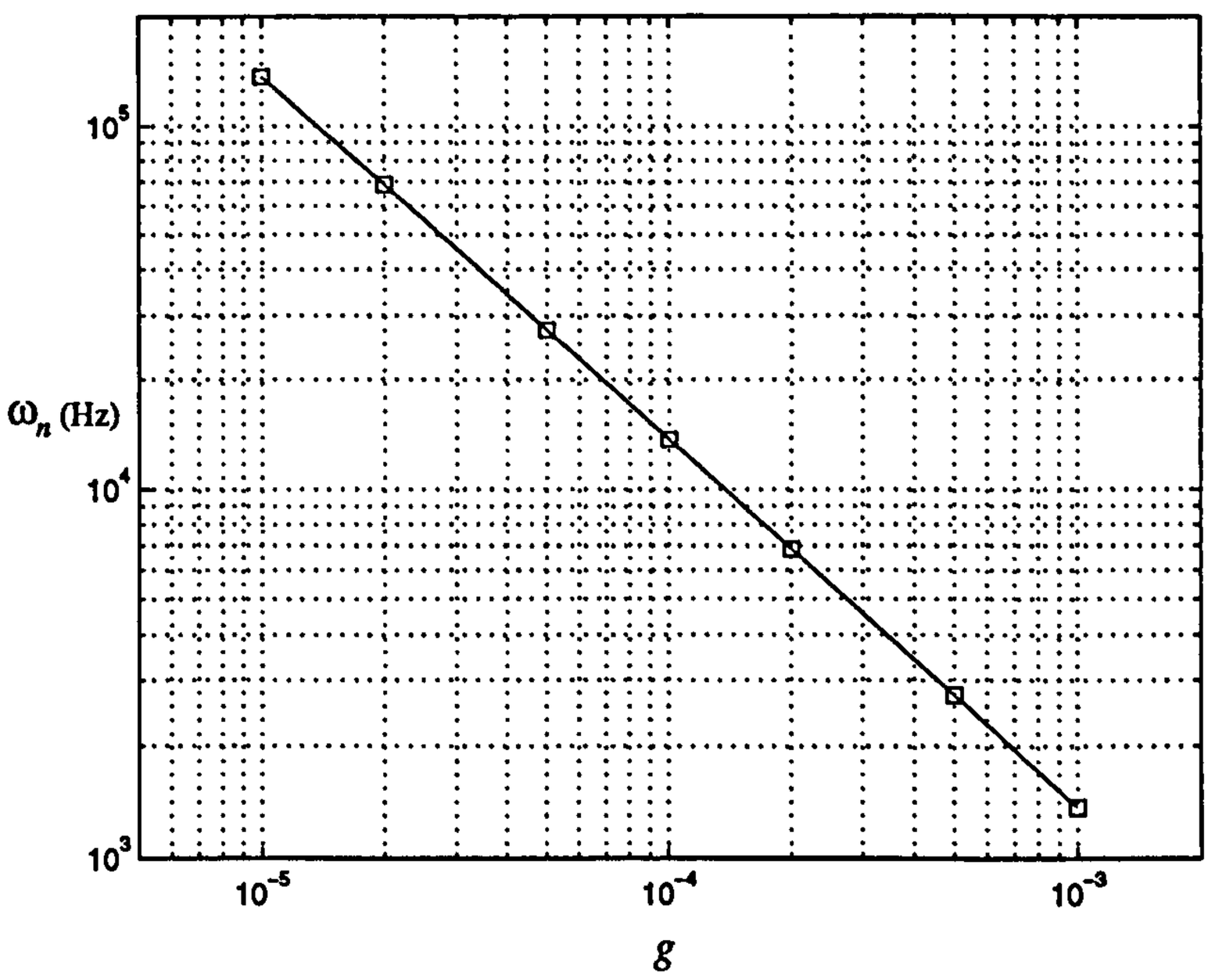

Figure 3.10: The effect of scale (g) on natural frequency (ω_n)

3.2.2 Velocity Magnitude

The effect that scaling an actuator has on the jet velocity attainable, is of serious interest when considering the feasibility of MEMS jets for turbulence control. If the viscous effects at micron scale are so severe that only minimal velocities can be achieved, then the success of a turbulent control scheme would seem less likely.

In order to investigate the variation of velocity magnitude with scale, the design dimensions that have been used in §3.1.5 are expressed in terms of g – the scale parameter. The actuator dimensions are: R_d=12.7g; t_p=0.1g; R_p=11g; t_p=0.1g; R_o=0.3g; and H=2g. Simulations have been performed at seven scales, between g=10 μm and g=1 mm. In each case the electric field strength is held constant, and the driving frequency is adjusted to maximise the diaphragm's deflection (simulation parameters §A.1.7).

Figure 3.11 shows the variation of maximum diaphragm deflection with the scale parameter g (□); the fitted solid line is the function w_{max}=0.0365g. These results demonstrate the proportionality of the diaphragm deflection, w_{max}, with scale, g.

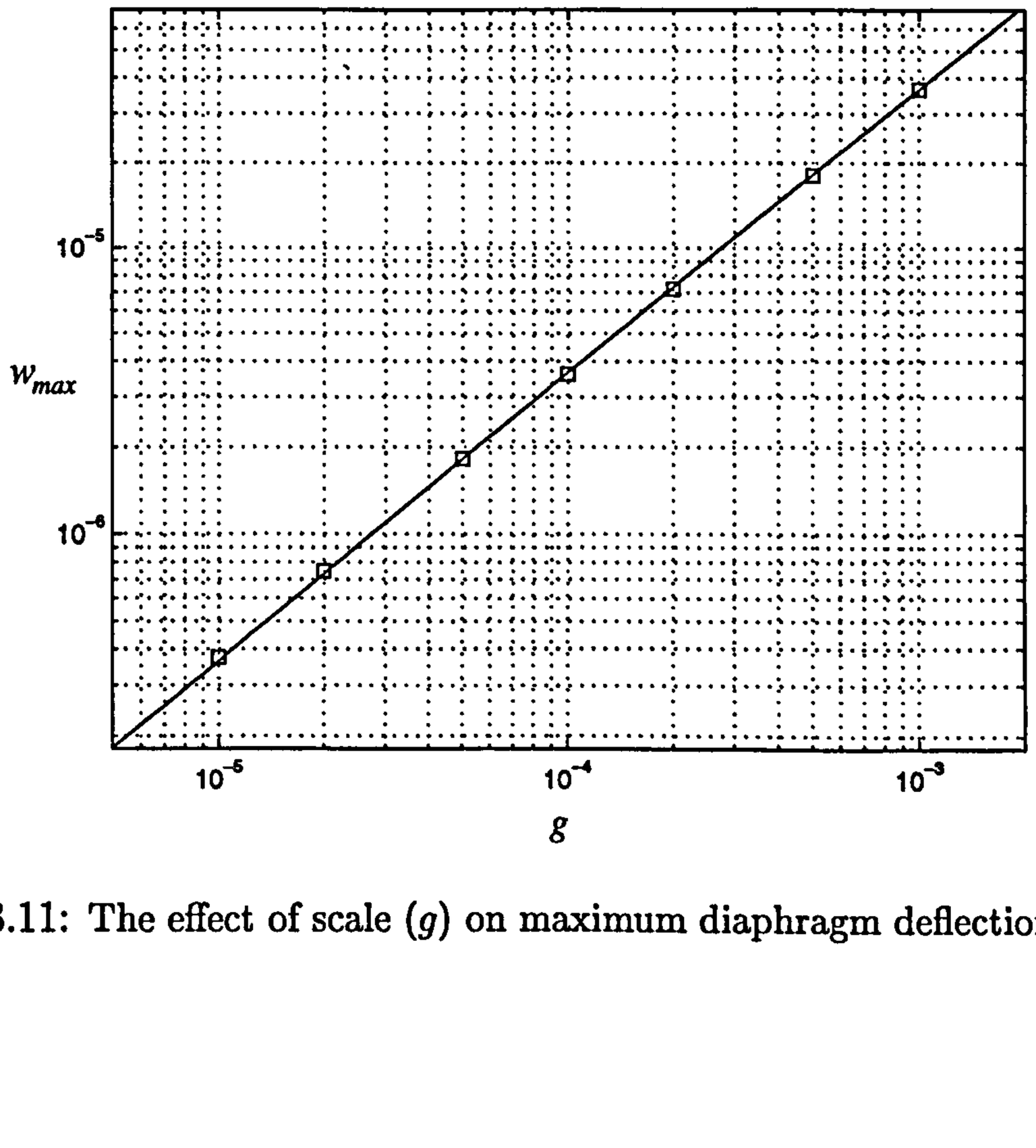

Figure 3.11: The effect of scale (g) on maximum diaphragm deflection (w_{max}).

Figure 3.12 shows the variation of resonant frequency with the scale parameter g; The fitted solid line is the function $\omega_r = 10.25/g$. These results are different to those presented in §3.2.1, as here the diaphragm is coupled with the cavity pressure. The results demonstrate that the inversely proportional relationship between resonant frequency and scale predicted by equation (3.3) is maintained regardless of the significant pressure feedback.

Figure 3.13 shows the variation of maximum center-line velocity magnitude with the scale parameter g. A general trend appears to be a reduced velocity at smaller scales; the large-scale magnitudes are at least five times greater than those at MEMS scale. What is also noticeable from Figure 3.13 is that there is an optimum scale g for the design being considered. If this were a plot of average velocity (as opposed to centre-line) the graph would tend to an asymptotic value and no optimum would occur (see Figure 3.22). The optimum exists because the ratio of centre-line to average velocity falls at larger scales, and hence the centre-line velocity falls.

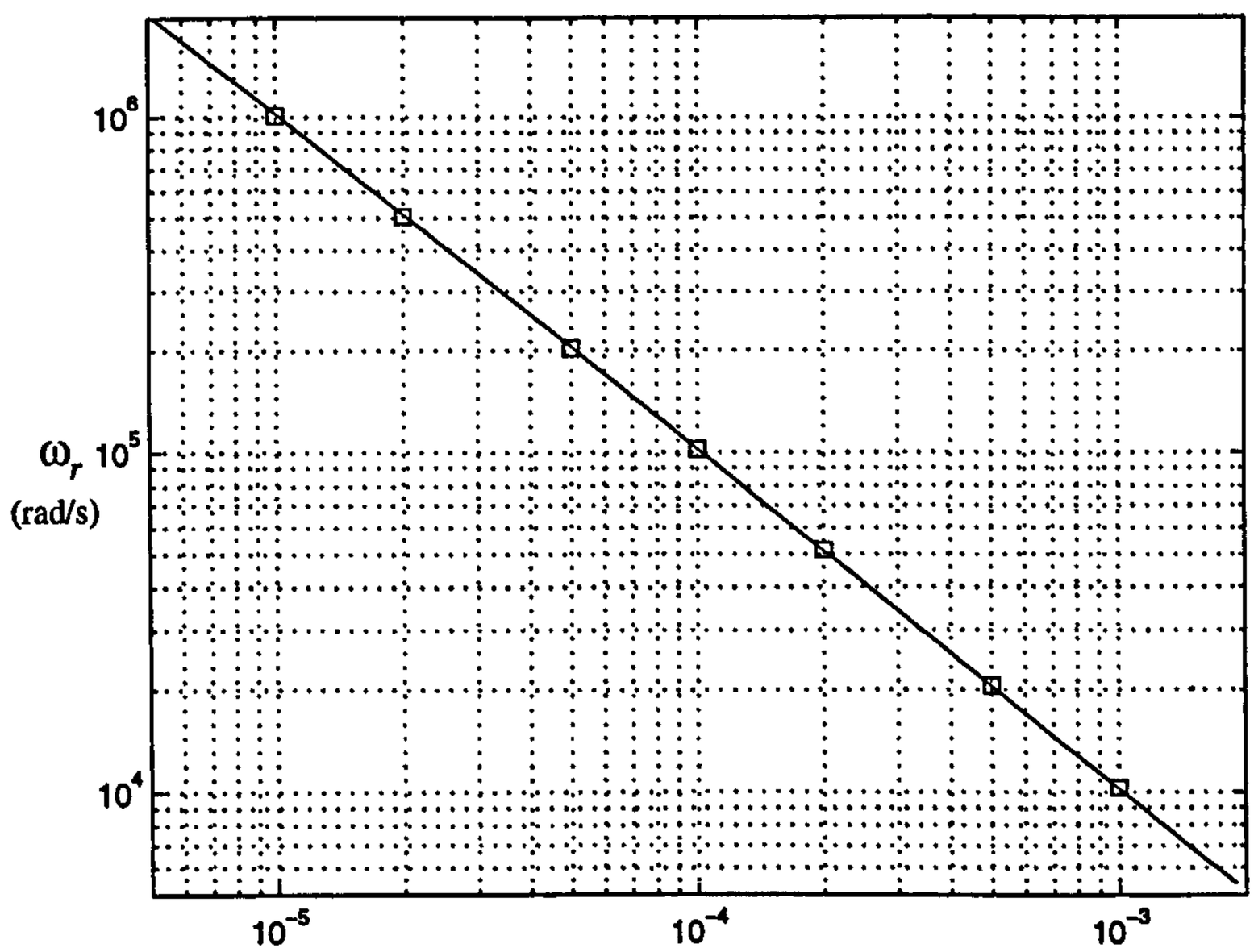

Figure 3.12: The effect of scale (g) on resonant frequency (ω_r).

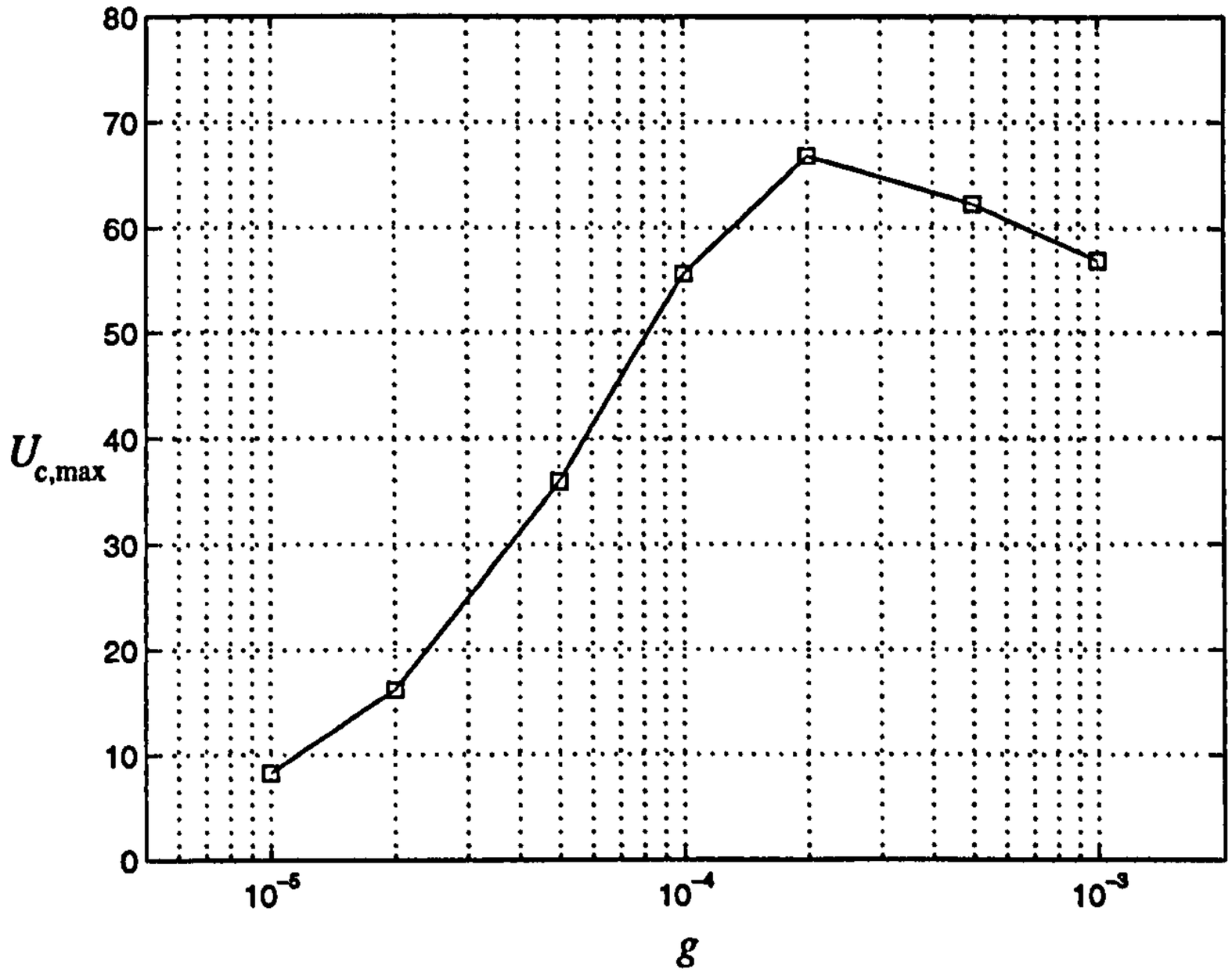

Figure 3.13: The effect of scale (g) on jet velocity ($U_{c,max}$).

The results shown in this section suggest that the velocities produced by MEMS-scale devices are likely to be less than predictions based on large-scale prototypes. This is due to the larger surface-to-volume ratio, and hence stronger viscous effects in the smaller devices.

It is, however, important to remember that maximum velocity may not be the most important feature of an actuator's output (see Chapter 5). If, for example, the mass flow rate of the jet was more important than average velocity for providing effective flow control, the MEMS would be at a severe disadvantage. If you compare the design at scale g= 1 mm with that of g=10μm, the maximum mass flow rate of the larger design is roughly 70,000 times greater than that of the smaller design. Also, in synthetic operation the stroke length, (defined by Smith and Glezer (1998) as half the period of oscillation), is much reduced at MEMS scale because of the large natural frequency of the diaphragm. If there is any correlation between the overall effectiveness of the synthetic jet, and the mass or energy imparted to the boundary layer over the period of one stroke length, then again, MEMS are at a disadvantage as the stroke length is so much shorter.

It may, however, not be so important to generate large velocities or mass flow rates if the actuation is sufficiently sophisticated so as to only excite (or suppress) the structures in a turbulent boundary layer that are responsible for turbulent reproduction.

3.2.3 Optimum PZT Design

A lot of MEMS prototyping is performed at larger than MEMS scale, it is therefore essential to know whether a large-scale optimum is the same, or similar, to the MEMS-scale optimum. Numerical simulations have been performed to investigate how optimum dimensions are altered by scaling.

The effect of scale on optimum PZT dimensions is investigated by simulations similar to those in §3.1.4. The same optimisation procedure has been performed but at MEMS scale and with different diaphragm proportions and material properties. The diaphragm thickness and radius are set at 1 μm and 254 μm, respectively.

The results for the optimisation of PZT thickness and radius are shown in Table 3.2, and the individual one-dimensional stages of the optimisation can be seen in Figures 3.14–3.16 (simulation parameters §A.1.8). The optimum PZT radius is found at 218 μm, which is a PZT-to-diaphragm radius ratio of 0.858, this is exactly equal to the optimum ratio found in the larger device. This result shows that the optimum is independent of scale, device proportions, and material properties. It was suggested in §3.1.4 that the optimum PZT radius was influenced by the mode shape of deflection, this is constant, and therefore an invariant optimum PZT radius is not unexpected.

The optimum value of PZT thickness at this small scale is 1.1 μm, which means that the PZT-to-diaphragm thickness ratio has changed from 1.26 to 1.1. In order to establish what one of the three variants (properties, proportion or scale) has caused this change, the same simulation has been performed, but with

Optimisation Stage	t_p	R_p
A	fixed @ 0.5 μm	optimised - 205 μm
B	optimised - 1.01 μm	fixed @ 205 μm
C	fixed @ 1.01 μm	optimised - 217 μm
D	optimised - 1.09 μm	fixed @ 217 μm
E	fixed @ 1.09 μm	optimised - 218 μm
F	optimised - 1.1 μm	fixed @ 218 μm
G	fixed @ 1.1 μm	optimised - 218 μm

Table 3.2: PZT optimisation

constant material properties. In this simulation the optimum radius remained unchanged, whereas the optimum PZT thickness changed to 126 μm - the same thickness (relative to the diaphragm thickness) as the large-scale device. This implies that the optimum PZT thickness is scale and proportion invariant, but not independent of material property.

It was suggested in §3.1.4 that the optimum thickness occurs when the diaphragm and PZT have similar flexural rigidities. It follows then, that a change in material property would alter the PZT thickness that achieves this balance. This varying optimum PZT thickness is an important consideration for MEMS designs that might employ less rigid materials in order to reduce the natural frequency of the diaphragm.

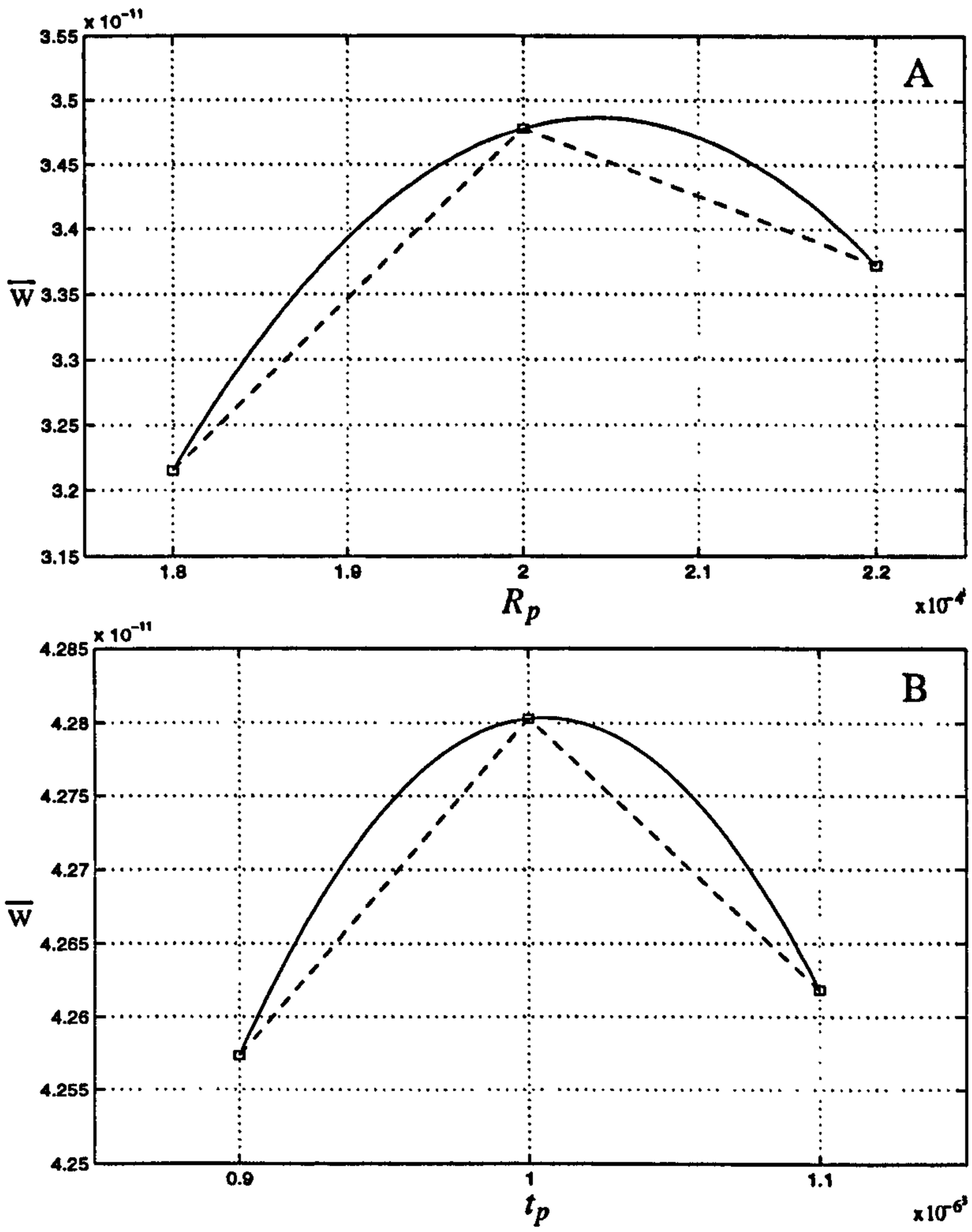

Figure 3.14: The stages (A)-(B) in the PZT optimisation procedure of Table 3.2. Plot (A) is a radius (R_p) optimisation with fixed thickness (t_p); Plot (B) is a thickness optimisation with fixed radius.

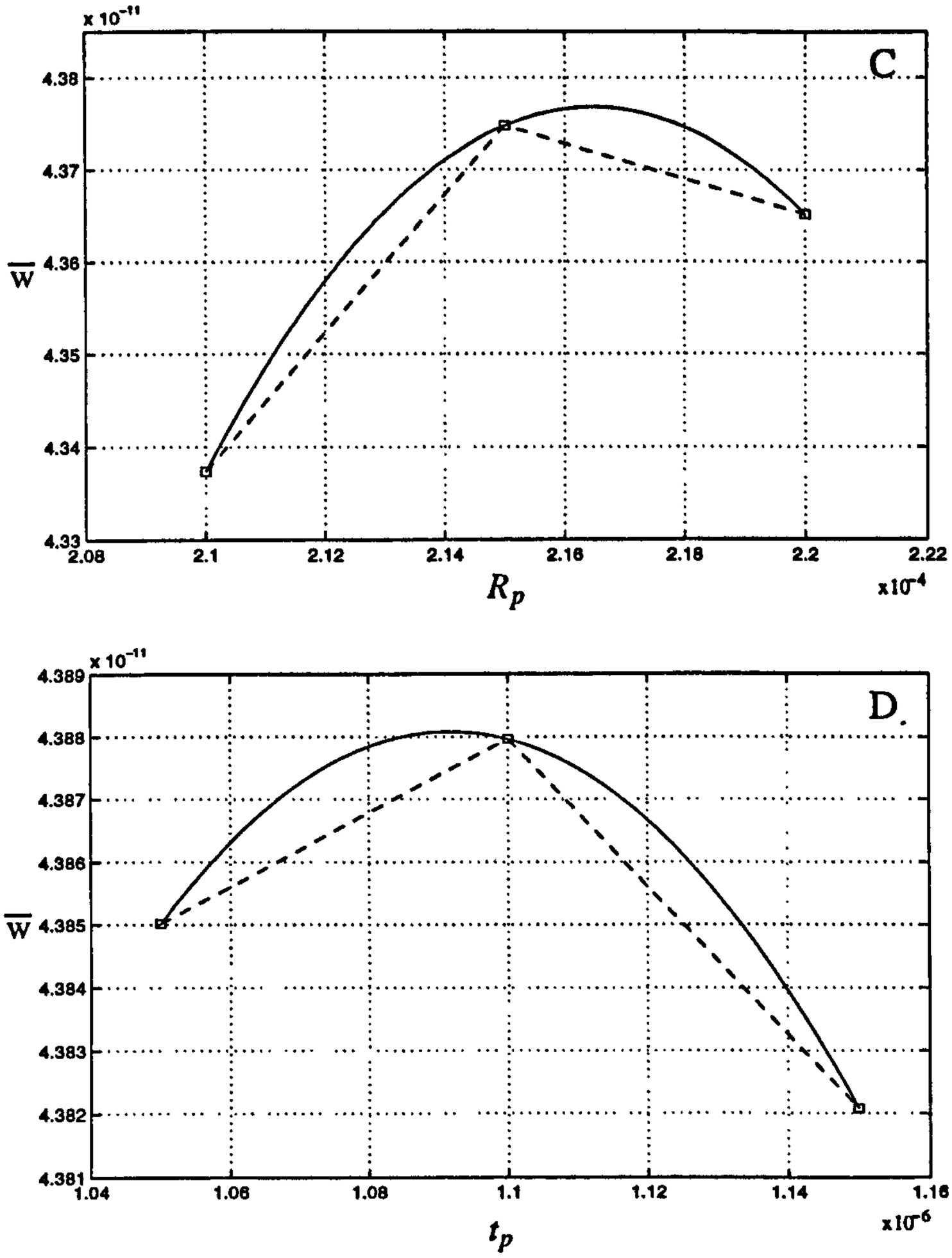

Figure 3.15: The stages (C)-(D) in the PZT optimisation procedure of Table 3.2. Plot (C) is a radius (R_p) optimisation with fixed thickness (t_p); Plot (D) is a thickness optimisation with fixed radius.

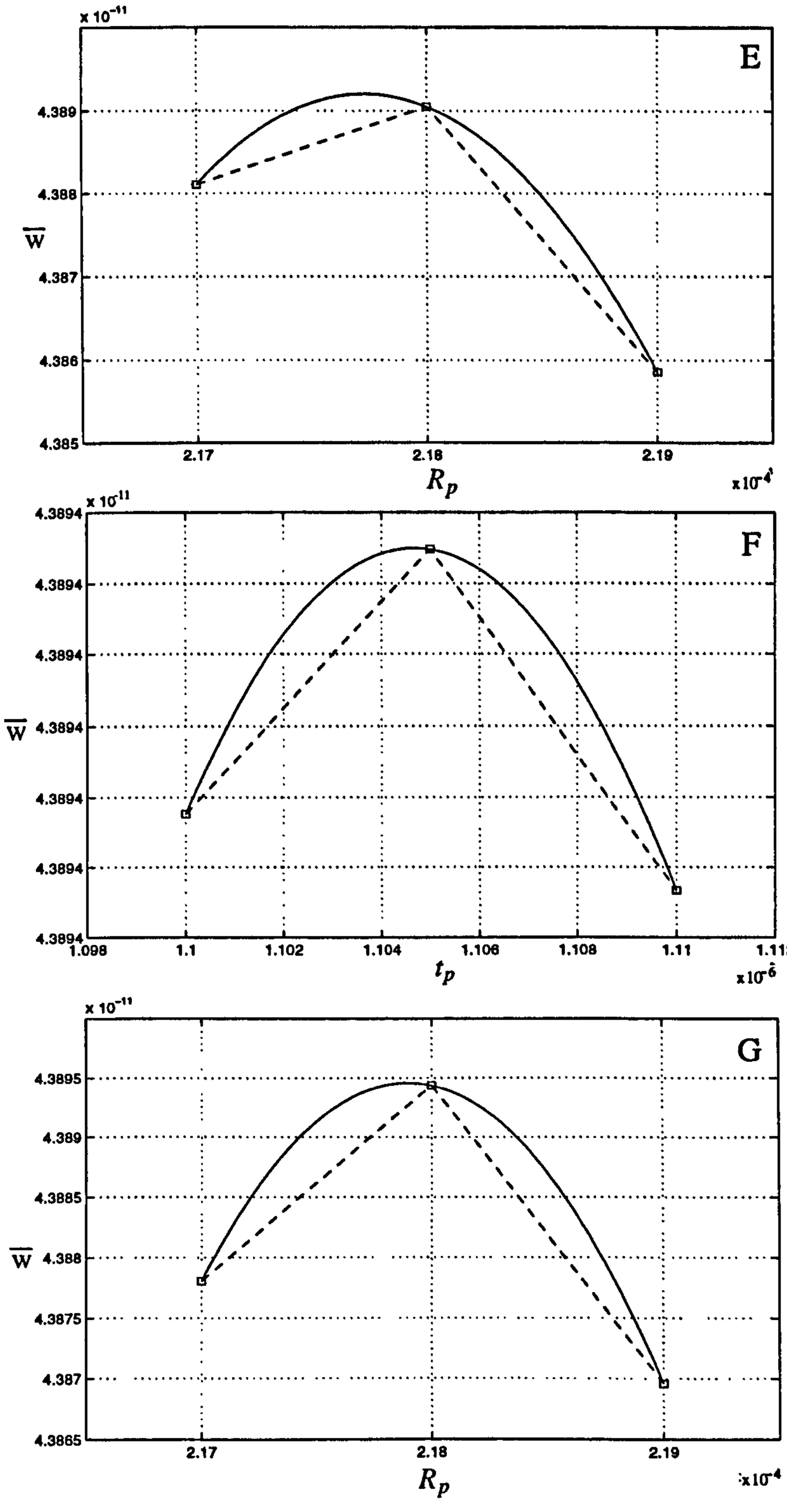

Figure 3.16: The stages (E)-(G) in the PZT optimisation procedure of Table 3.2. Plots (E) and (G) are radius (R_p) optimisations with fixed thickness (t_p); Plot (F) is a thickness optimisation with fixed radius.

3.2.4 Optimum Orifice Radius

An investigation into the effect of scale on optimum orifice radius (R_o) has also been made. The parameter g is again used to characterise the overall scale of the device. In terms of g, the dimensions of the device are as follows: H_c=$2g$, l=$1.6g$, and R_d=$12.7g$ (for the Manchester actuator g=1 mm).

For these optimisation runs the diaphragm's deflection has been prescribed proportionally to scale (the results in §3.2.2 have shown this to be a reasonable estimation) and the driving frequency is set at resonance for each simulation (see Figure 3.10).

Figure 3.17 shows the optimum orifice radius R_o (non-dimensionalised with respect to half the cavity height), against the scale parameter g. The individual optimisations at the seven different scales can be seen in Figure 3.18 (simulation parameters §A.1.9).

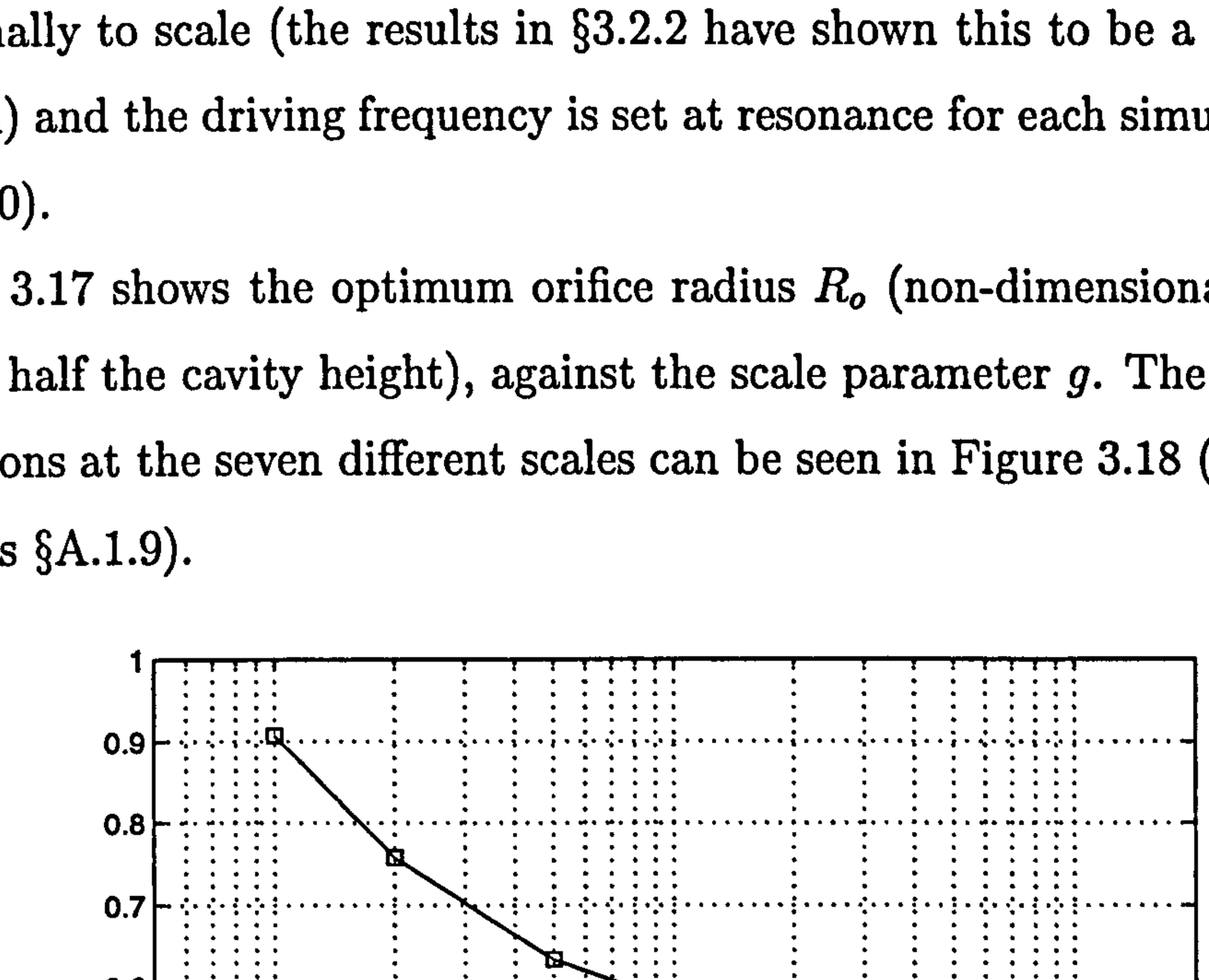

Figure 3.17: Variation of non-dimensionalised optimum orifice radius ($2R_o/H$) with the scale parameter g (–□–).

It is clear from the results that, unlike the optimum PZT radius, the optimum orifice size (relative to the characteristic length of the device) is dependent on

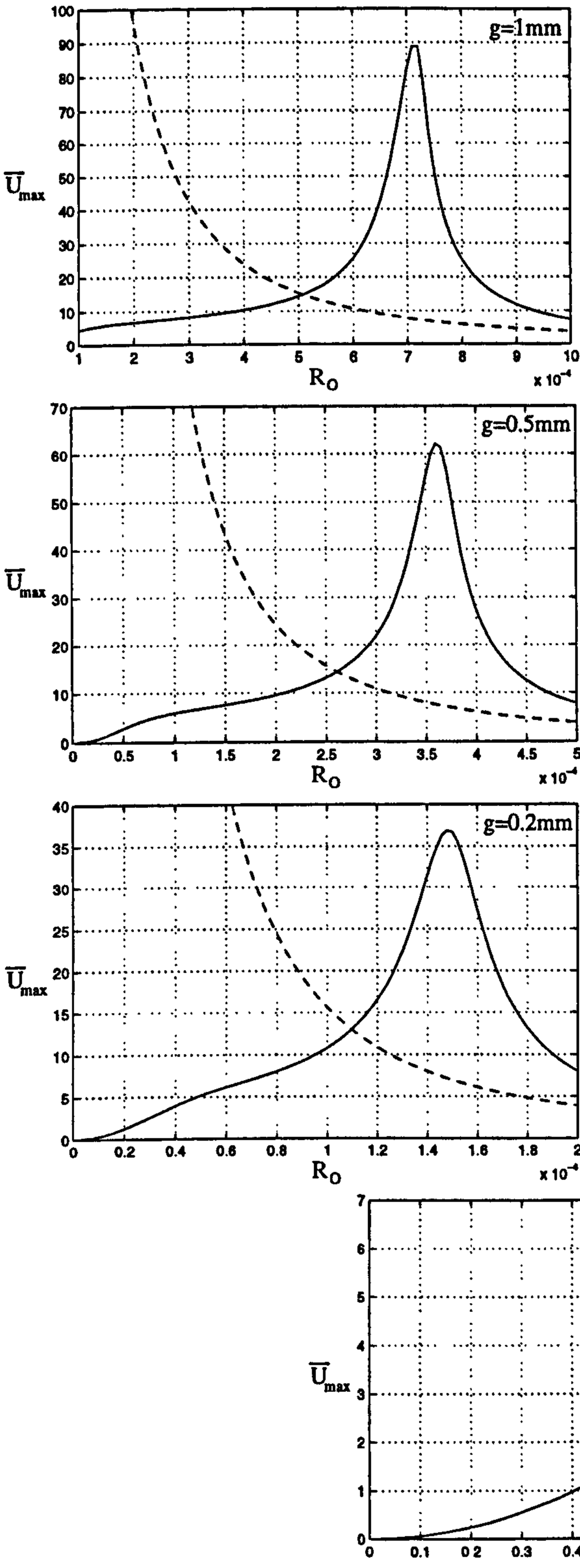

Figure 3.18: The individual orifice radius optimisations in Figure 3.17. The static-compressible simulation (–) and the dynamic-incompressible solution (– –)

scale. At MEMS scale (g=10 μm) the optimum orifice diameter is over 90% of the cavity height, as opposed to just 50% at micro scale (g=1 mm). (The ratio of cavity cap area (A_c) to orifice area (πR_o^2) is greater than ten in all cases and is therefore within the limits of the model defined in §2.5 – in the Manchester configuration $A_c \approx R_d H$).

This variation in optimum radius with g, is due to the increased presence of viscosity at the smaller scales. To further this discussion and understanding of the system, the Stokes parameter (St) is introduced, this characterises the level of viscosity in an oscillating orifice flow:

$$St = 2\sqrt{\frac{\omega R_o^2}{\nu}} \tag{3.4}$$

where R_o is the orifice radius, ω is the frequency of oscillation, and ν is the kinematic viscosity.

Simulations have been performed to demonstrate the effect of varying the Stokes parameter on the orifice flow. Figure 3.19(a) shows the variation of the ratio of maximum centre-line velocity to maximum average velocity, with the Stokes parameter. This ratio, $U_{c,\max}/\overline{U}_{\max}$, reflects how much viscous retardation exists in the flow.

Figures 3.19 (b) to (d) show the velocity profiles (at the maximum point in their cycles) for Stokes parameters of 5, 10, and 20, as indicated on Figure 3.19(a). Figure 3.19(b) is a viscous-dominated flow, whereas 3.19(d) is mainly inviscid with thin boundary layers at the orifice walls. Using Figure 3.19(a), general regimes can be quantified; St< 5 viscous dominated; 5 <St< 20 viscous-unsteady; St> 20 effectively inviscid.

The effect of scaling the Manchester actuator on the Stokes parameter is investigated, this can demonstrate whether the flow regime in the miniaturised devices will be typically viscous or inviscid.

Figure 3.20 shows the variation of the Stokes parameter with the scale pa-

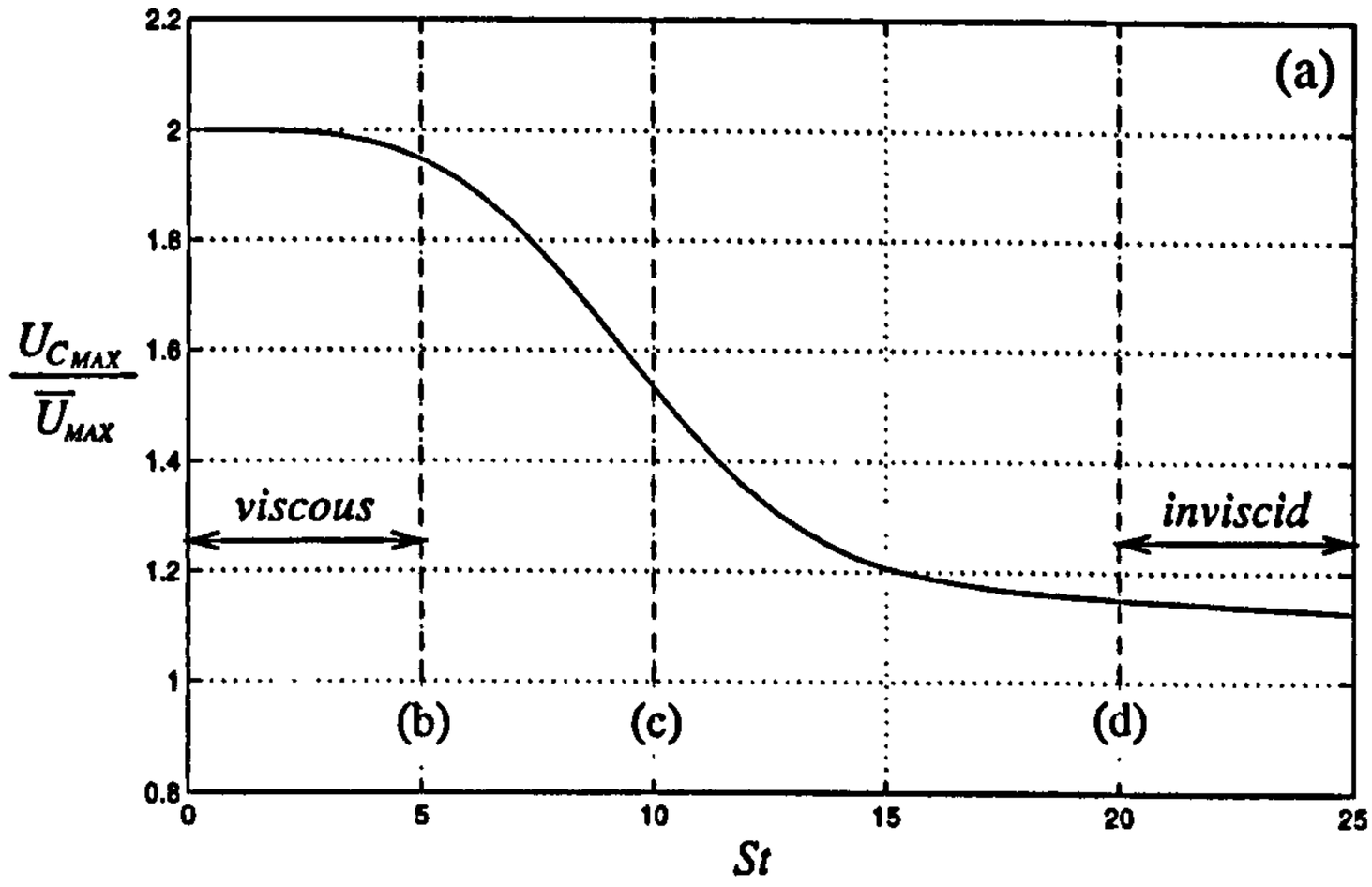

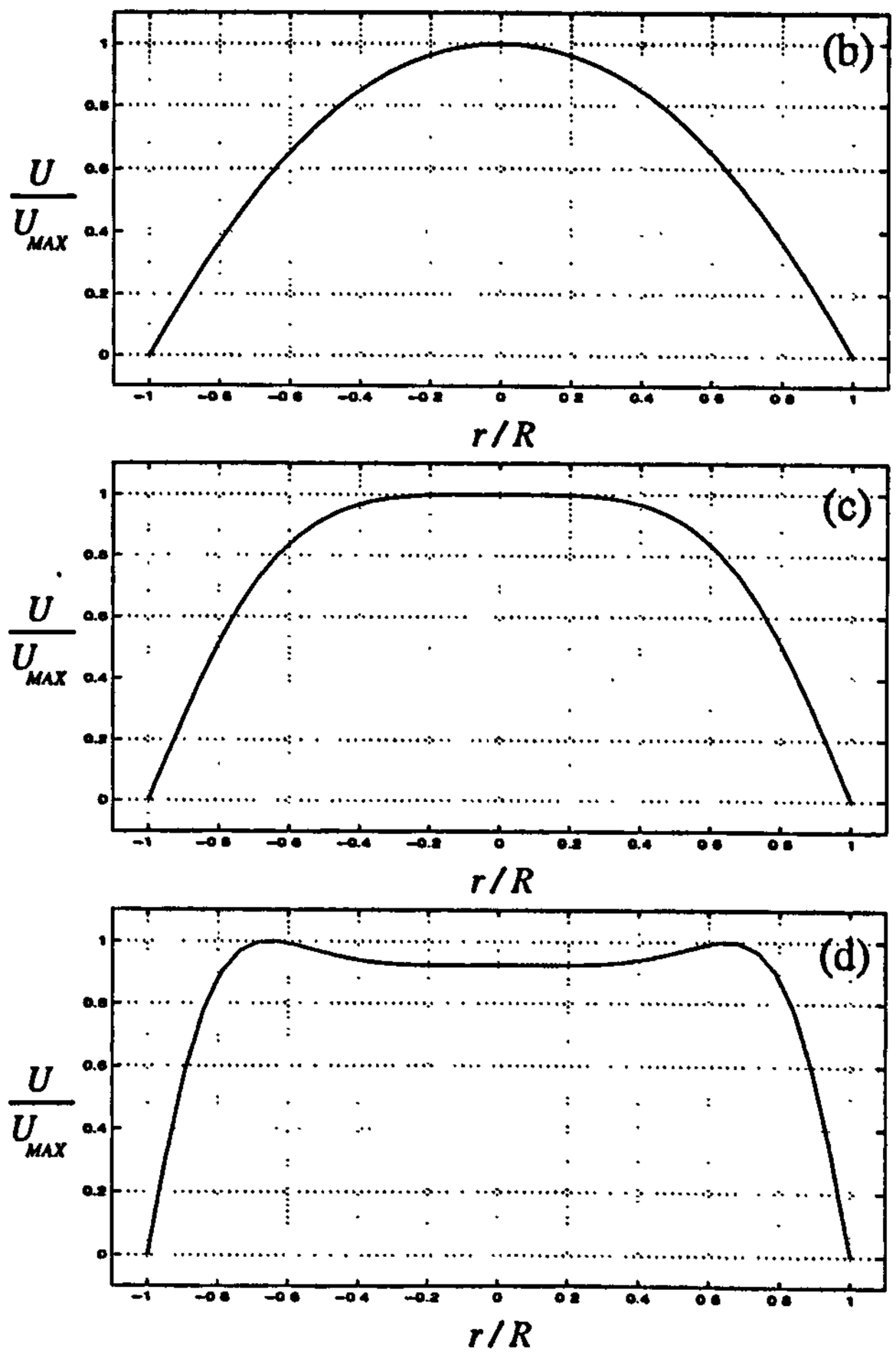

Figure 3.19: (a) The variation of $U_{c,\max}/\overline{U}_{\max}$ with the Stokes parameter. (b)-(d) Velocity profiles at varying Stokes parameters; (b) St=5; (c) St=10; (d) St=20.

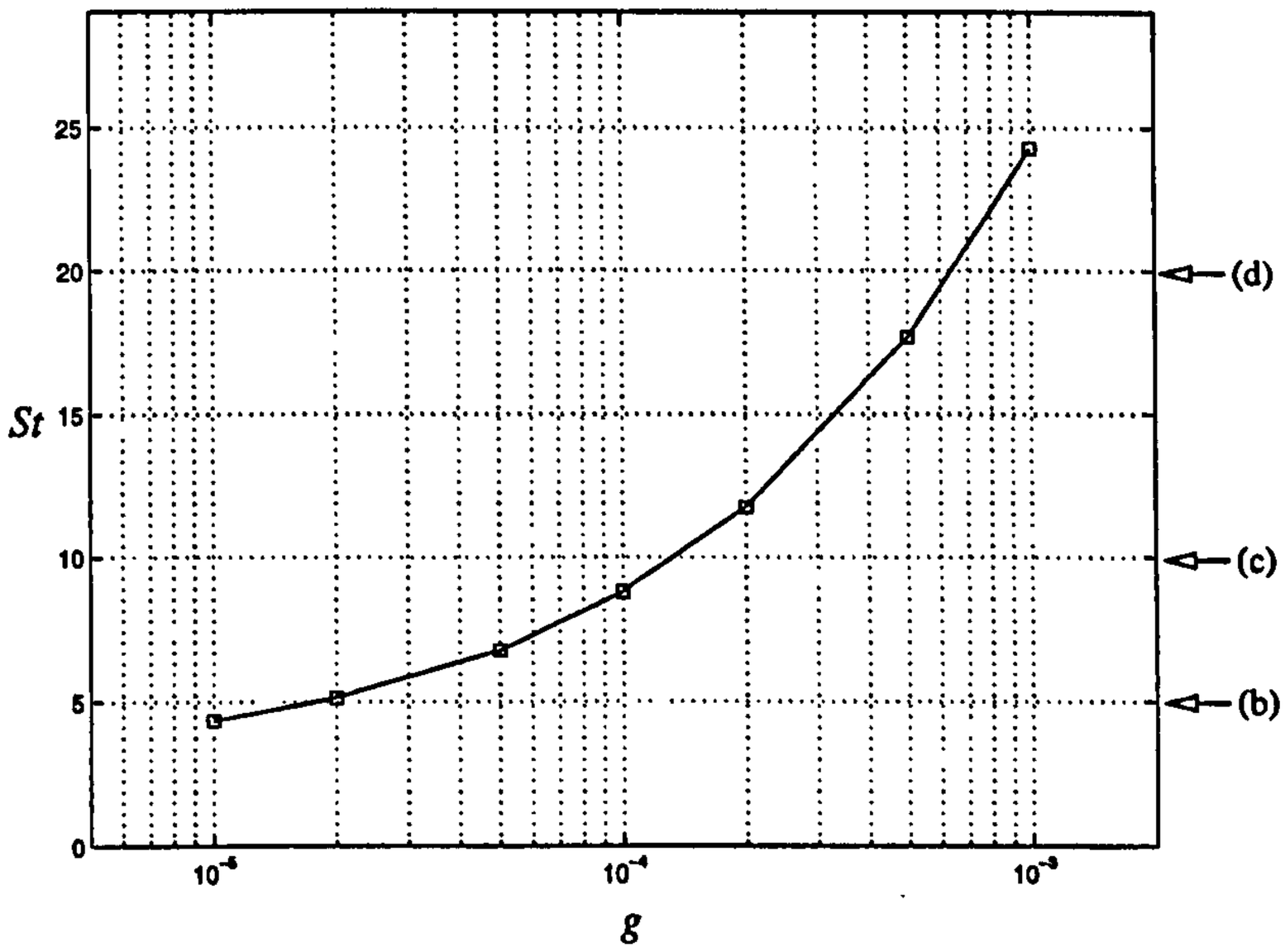

Figure 3.20: The Stokes parameter for the Manchester design at a scale g.

rameter g; the profile shapes shown in Figure 3.19 (b)-(d) are referenced on the St scale. It can be seen that the Manchester actuator at micro-scale is in the inviscid regime, whereas the actuator at MEMS scale is viscous dominated.

Analytical Optimisation

Rathnasingham and Breuer (1998) proposed a method by which the optimum Stokes parameter could be predicted analytically. It involved equating a viscous-dominated static-compressible solution with a dynamic-incompressible solution. By making some approximations to the system, an expression was found for the optimum Stokes parameter: (derived here for optimum orifice radius - see §C.1)

$$R_o = \left(\frac{8\mu\omega_d l R_d^2 H_c}{P_o} \right)^{\frac{1}{4}} \tag{3.5}$$

where H_c is the cavity height, R_d is the radius of the diaphragm and cavity, l is the orifice length, μ is the dynamic viscosity, ω_d is the driving frequency, and P_o is the ambient pressure.

Figure 3.21 shows the value of optimum orifice radius calculated from equation (3.5) compared with the numerical simulations from §3.2.4. The values compare well with the numerical results at MEMS scale, but not at larger values of g. This is because the quasi-steady flow solution used in the analytical solution is only valid for Stokes parameters of less than 5. Figure 3.20 shows that the Stokes parameter exceeds 5 at scales greater than g=20μm, therefore the analytical optimum radius is only applicable for g <20μm.

The closest agreement in Figure 3.21, occurs when g=20μm and not at g=10μm. This unexpected divergence at the MEMS scales arises because the constant mass approximation in the analytical solution begins to break down at large orifice-to-cavity area ratios (see §C.1).

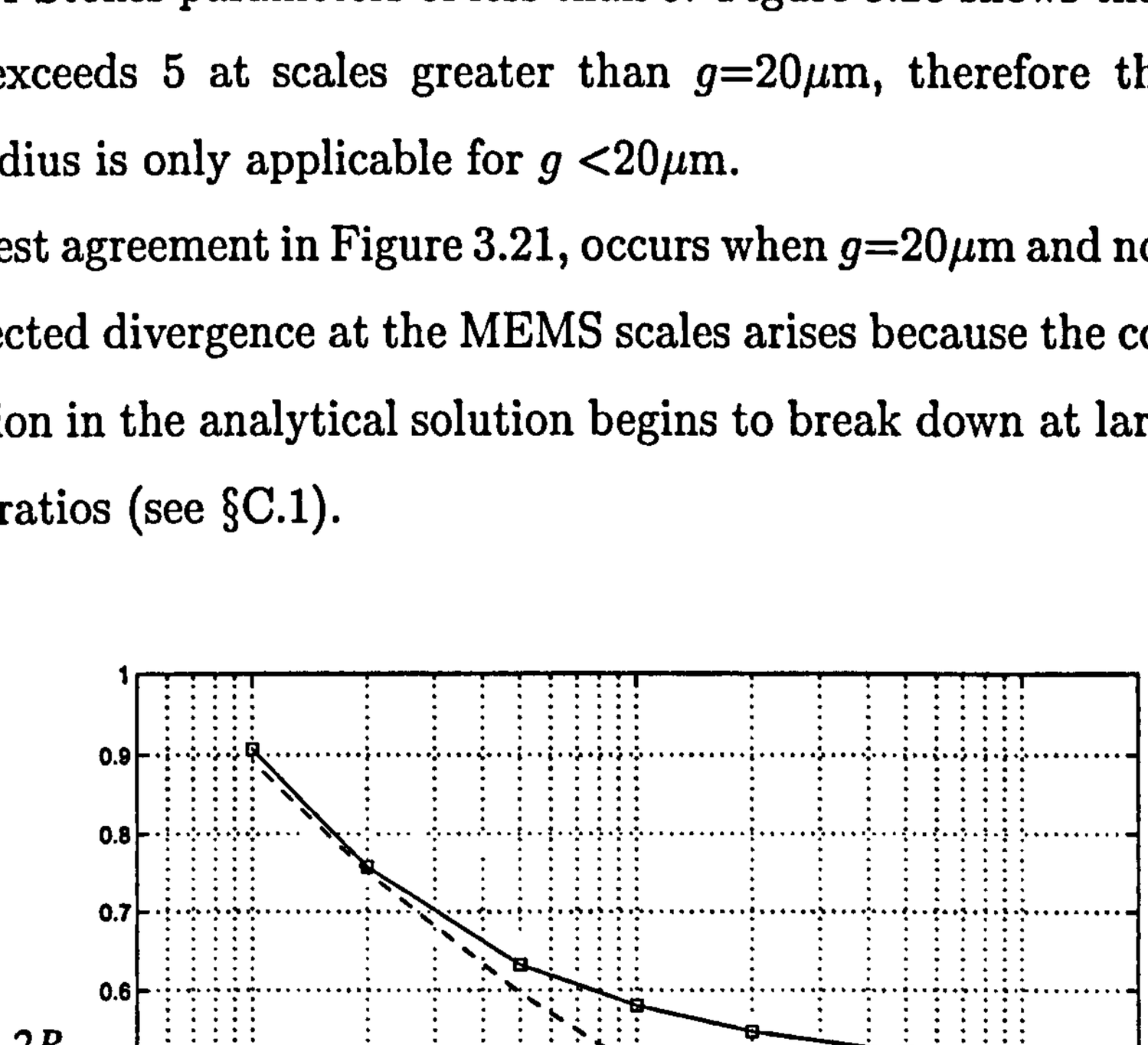

Figure 3.21: Variation of non-dimensionalised optimum orifice radius ($2R_o/H$) with the scale parameter g; numerical results (–□–); analytical solution (– –).

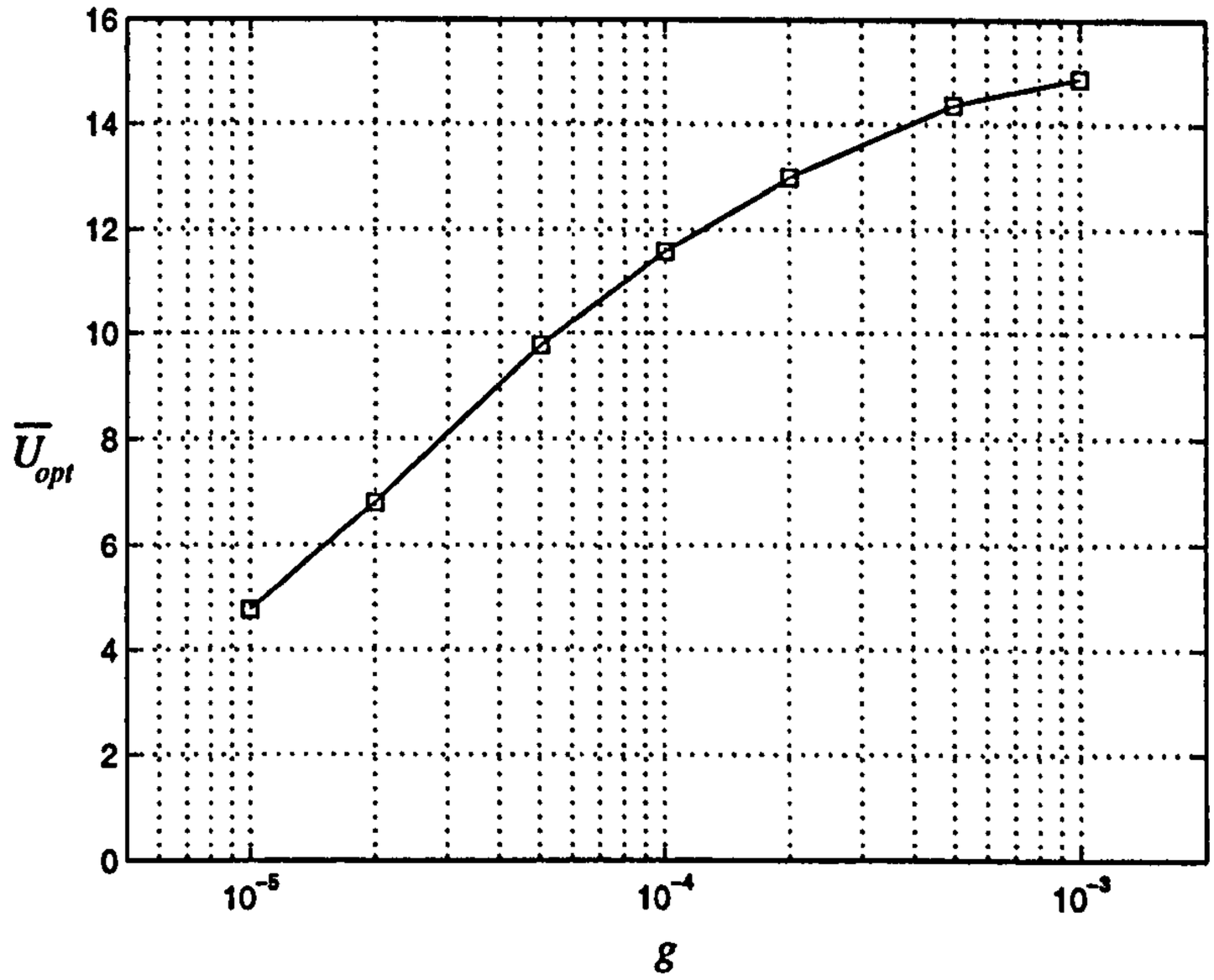

Figure 3.22: Variation of optimised average velocity ($\overline{U}_{opt}$) with the scale parameter g.

3.2.5 Optimised Velocity

Even though the predicted optimised velocity magnitudes are not precise, the variation of the optimised velocity with scale is at least qualitatively accurate. In §3.2.2, Figure 3.13 showed the general decrease in velocity magnitude that is attainable when all design dimensions are scaled-down equally. The results in the current section are obtained from the simulations in §3.2.4, which have been optimised at each scale by varying the orifice radius. The results show that at larger scales, larger average velocities can be achieved; however, even with optimisation an upper limit seems to exist.

3.2.6 Section Summary

In section §3.2.1 it was demonstrated analytically and numerically that miniaturisation results in very large diaphragm and PZT natural frequencies. This presents a major difficulty for synthetic-jet operation at MEMS scale. In section §3.2.3 it was shown that the optimum size of the PZT, relative to the diaphragm,

is independent of scale. Conversely, section §3.2.4 showed that the optimum orifice radius (relative to the scale of the device) is *not* independent of scale. In sections §3.2.2 and §3.2.5 it has been illustrated that at smaller scales lower maximum velocities are achievable. It has also been observed that potentially crucial jet features such as maximum mass flow rate are seriously reduced in a MEMS device. The miniaturisation effects discussed in this section suggest that any control scheme must be highly sophisticated and possess the ability to enhance or negate turbulent structures with minimal mass flow.

3.3 Diaphragm-Cavity Interaction

Pressure changes in the cavity directly influence the motion of the diaphragm. The extent to which the diaphragm's motion is affected is investigated in this section.

3.3.1 A Closed Cavity

The natural frequency of the diaphragm is quite sensitive to cavity-pressure feedback. Numerical simulations have been performed using the Manchester actuator design (§3.2.1) inside a *closed* cavity (R_o=0) of varying height (simulation parameters §A.1.10). Figure 3.23 shows how the resonant frequency (ω_n) of the diaphragm is increased when within a cavity of height (H_c); the isolated diaphragm's resonant frequency is indicated by the dashed line.

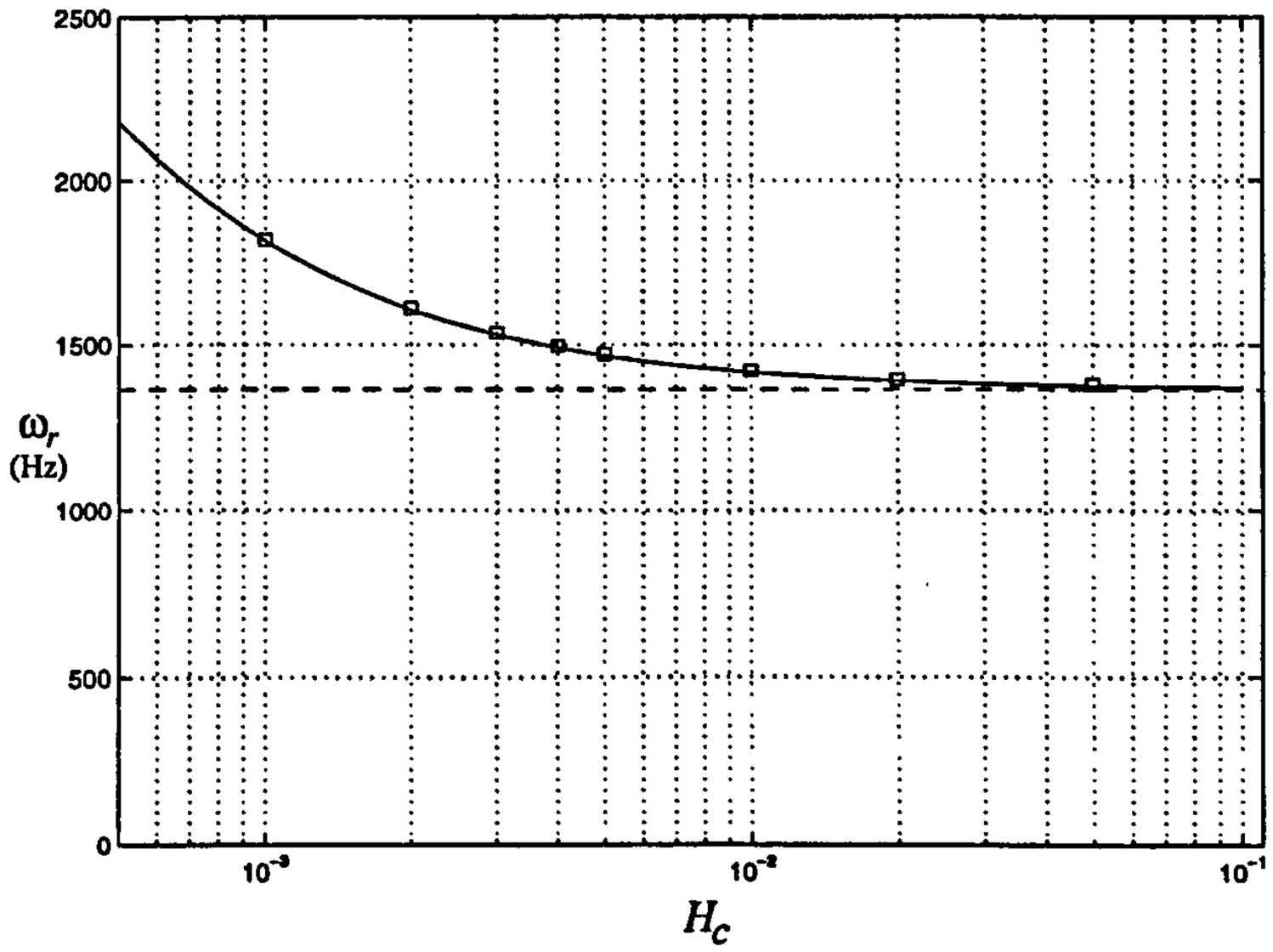

Figure 3.23: The resonant frequency of the Manchester diaphragm and PZT set inside a closed cavity of height H_c; the analytical model (–); the numerical simulations (□); the isolated diaphragm's natural frequency (– –).

Rathnasingham and Breuer (1997a) derived a simple analytical expression to predict the effect on natural frequency of a diaphragm within a closed cavity.

The diaphragm was modelled as a piston, with an effective spring stiffness (K_e), and an effective mass (M_e). The resonant frequency (ω_r) of the piston model in a closed cavity was given by:

$$\omega_r = \sqrt{\frac{K_e + P_o A_d / H_c}{M_e}} \tag{3.6}$$

where P_o is the ambient pressure, A_d is the area of the diaphragm, and H_c is the height of the cavity.

Values for K_e and M_e have been obtained from the numerical model by applying a constant load (F) and using the average deflection ($\overline{w}$) to calculate the effective stiffness:

$$K_e = \frac{F}{\overline{w}} \tag{3.7}$$

M_e is obtained from:

$$M_e = \frac{K_e}{{\omega_n}^2} \tag{3.8}$$

where ω_n=1366 Hz for the Manchester actuator. The solid line in Figure 3.12 is calculated from equation (3.6). Exact agreement between the model and analytical expression is found; however, this is only the case for closed cavities.

3.3.2 A Cavity with an Orifice

The resonant frequency is also dependent upon the orifice radius. Figure 3.24 illustrates how a small orifice radius can increase the resonant frequency of the diaphragm (simulation parameters §A.1.11). This is due to the fact that for small orifice radii, the outflow lags at least 90 degrees out of phase with the velocity of the diaphragm. This means that the maximum rate of change of cavity density

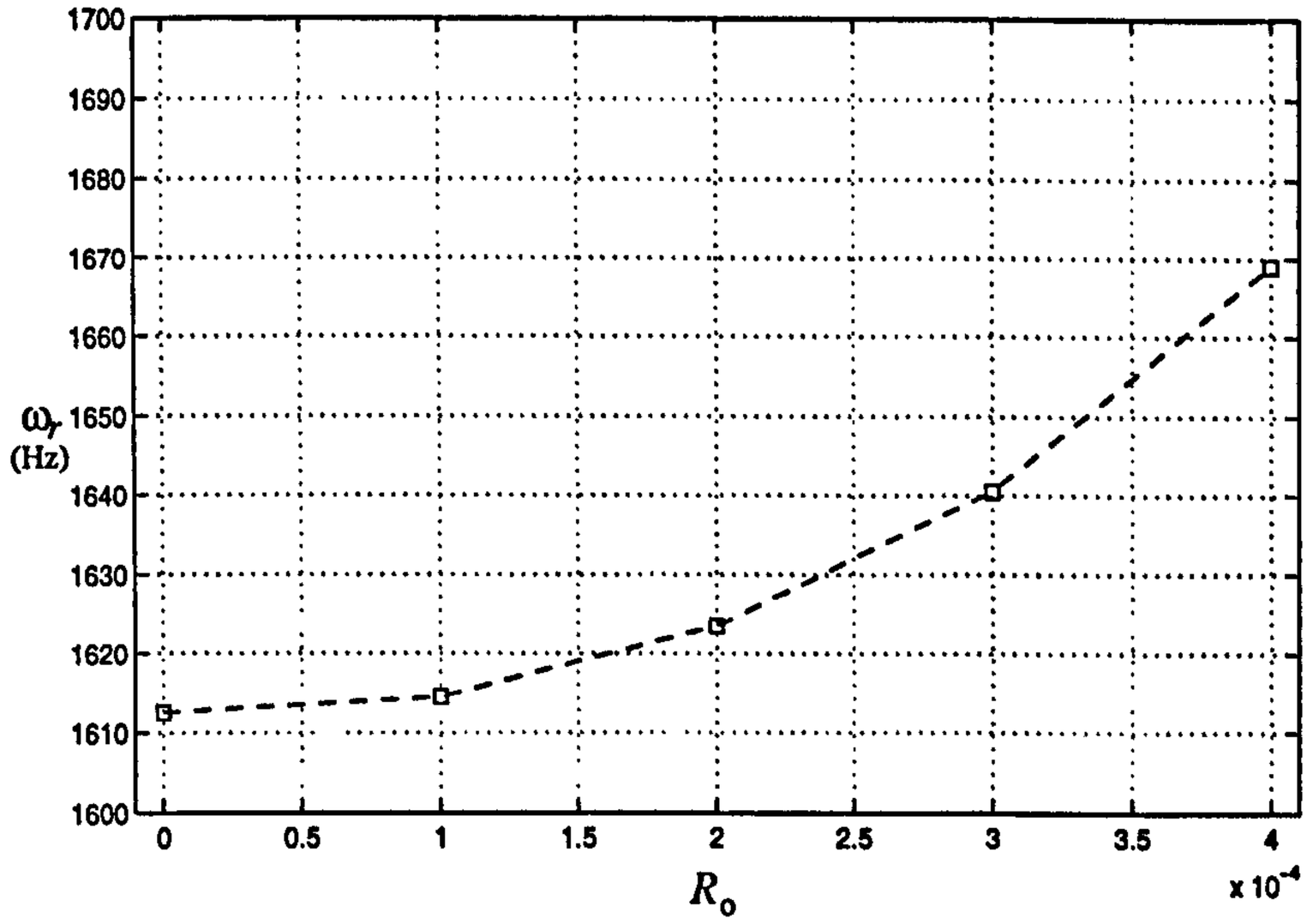

Figure 3.24: The resonant frequency (ω_n) of the Manchester diaphragm and PZT set inside a cavity with a small orifice radius, R_o.

and pressure are actually increased when there is a small orifice.

Only small orifices are considered here, since the current model overestimates pressure fluctuations when the orifice radius is large relative to the cavity area; at larger radii the pressure fluctuations can be expected to fall.

3.3.3 Deflected Diaphragms

The effect of cavity pressure on the diaphragm operated at resonance is significant. When, however, a constant force or couple is applied, very little effect is observed. This is because the cavity pressure can only affect the dynamic response of the diaphragm and not the steady-state deflection. Figure 3.25 shows the comparison of responses for an isolated diaphragm and one within a cavity (simulation parameters §A.1.12).

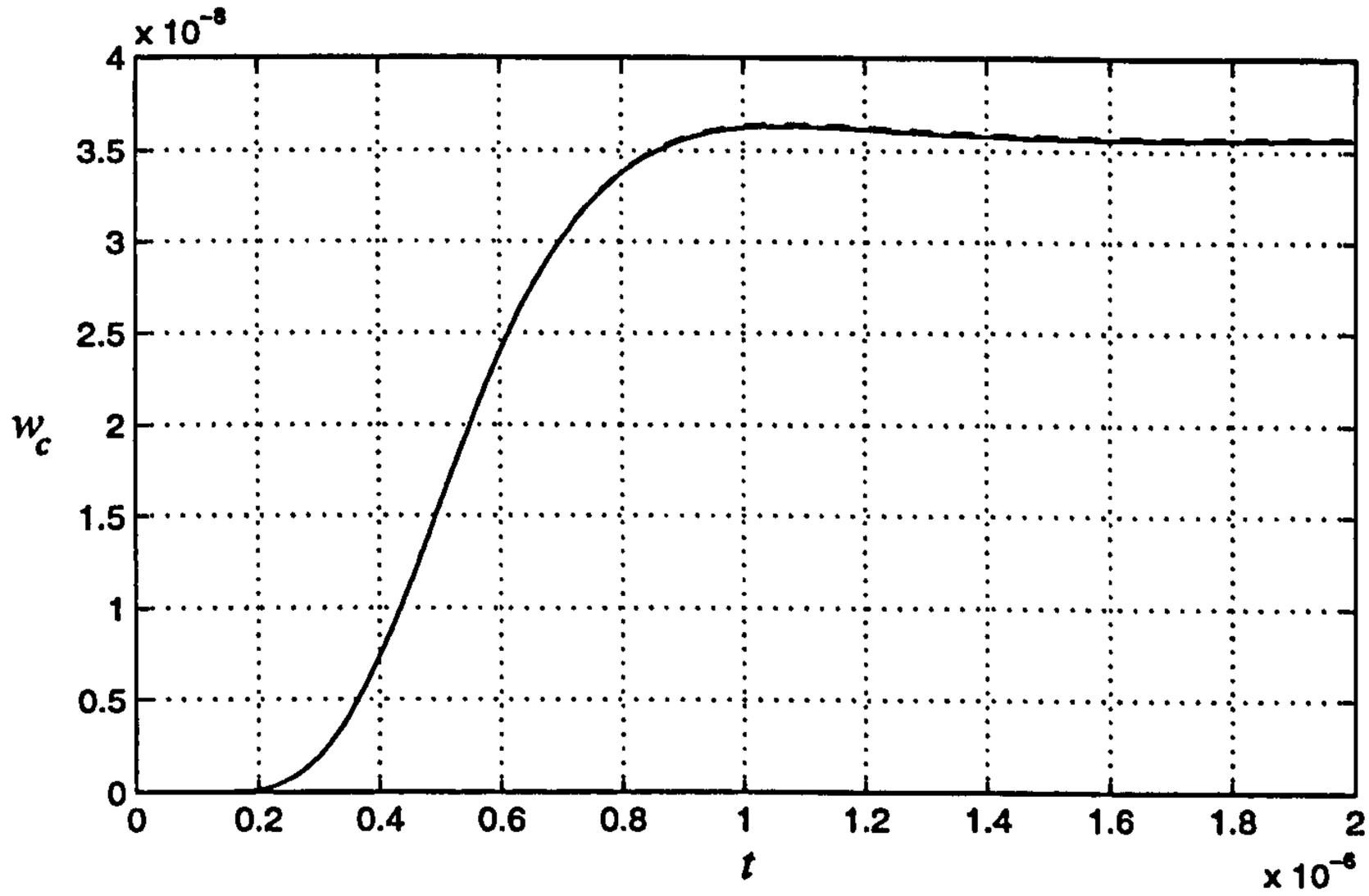

Figure 3.25: The response of a damped diaphragm subjected to a constant load. Central deflection (w_c) against time (t) for an isolated diaphragm (– –) and for a cavity-set diaphragm (–)

3.3.4 Section Summary

The results in §3.3.1 have demonstrated that the cavity increases the resonant frequency of the diaphragm. For closed cavities, numerical simulations have been compared with a semi-analytical calibrated solution, and good agreement found. In §3.3.2 it has also been illustrated that the existence of a small orifice can increase the resonant frequency further. Finally, in §3.3.3 it has been shown that the cavity pressure feedback only has an effect on the dynamic behaviour of the diaphragm and not the steady-state deflection.

3.4 Pressure-Jump Actuators

Synthetic jets have received significant attention for their potential as flow controllers. There are, however, many drawbacks with this configuration, especially for the turbulent-control application. Firstly, resonance of the diaphragm may not be feasible at the high natural frequencies found at MEMS scale (see §3.2.1). Secondly, aircraft manufacturers are loathe to contemplate a cavity actuator with a strong inflow cycle for fear of ingesting dust. And finally, the synthetic jet may not be suitable for targeting coherent structures since they need to be controlled quickly and selectively. For these reasons an alternative style of actuator has been sought.

A rapidly-deflecting diaphragm can produce a sudden jump in the cavity pressure. Such a pressure jump will, in some cases, produce a single puff of fluid out through the orifice. Such a response does not have the drawbacks of the synthetic-jet configuration, and this is investigated in the current section.

3.4.1 The Step Force

To generate a rapid deflection a step force (or voltage), is applied to the diaphragm (after the actuation the diaphragm can be relaxed back slowly to its non-deflected state). In an undamped diaphragm this causes strong oscillation at many frequencies. Figure 3.26 (a) shows the response to a step force of three diaphragms with different damping factors (simulation parameters §A.1.13). Figure 3.26 (b) shows, for a given actuator, the velocities produced in each case. To generate the most suitable jet actuation (one with a high velocity and with no oscillation) a damping that only just suppresses the diaphragm oscillation appears to be most desirable.

3.4.2 The Pressure-Jump Actuator Design

The pressure-jump actuator's dimensions are expressed here in terms of the scale parameter g: height of the cavity H_c=50g, radius of the diaphragm R_d=50g, thickness of the diaphragm t_d=1g, optimum PZT radius R_p=43g, optimum PZT thickness t_p=1.22g, and orifice length l=10g. The diaphragm is made of single-crystal silicon, a popular material in MEMS fabrication (see §A.1.14 for a full parameter list).

Figure 3.27 shows velocity outputs from a pressure-pulse actuator (g=1 μm) with varying orifice radii (a)-(d). The strong viscous forces developed in a small orifice (Figure 3.27 (a) R_d=3.8 μm) reduce the maximum velocity and lengthen the period of actuation. A large orifice (Figure 3.27 (d) R_d=9.8 μm) produces a greater velocity but also exhibits an oscillation that is not generated by diaphragm motion. The oscillation is a Helmholtz-resonance effect and will be discussed in §3.5.

3.4.3 Pressure Valves

Pressure-jump actuators, as described in this section, do not necessarily have to be driven by a rapidly-deflecting diaphragm. A micro valve, for example, could raise the cavity pressure rapidly by introducing pressurised air.

The micro-valve input can be modelled as an instantaneous pressure rise in the cavity (this pressure is only imposed as an initial condition, and not continuously). Figure 3.28 shows the variation of maximum jet velocity with an input ΔP, where ΔP is the initial difference between ambient and cavity pressure (the actuator parameters are the same as for the diaphragm-driven pressure-jump device with R_o=7.8g and g=1 μm – simulation parameters §A.1.15).

Figure 3.28 shows a linear relationship between applied pressure and maximum velocity up until average velocities of 30-40 m s^{-1}, at which point nonlinear terms in the orifice equation (2.67) start to have an effect.

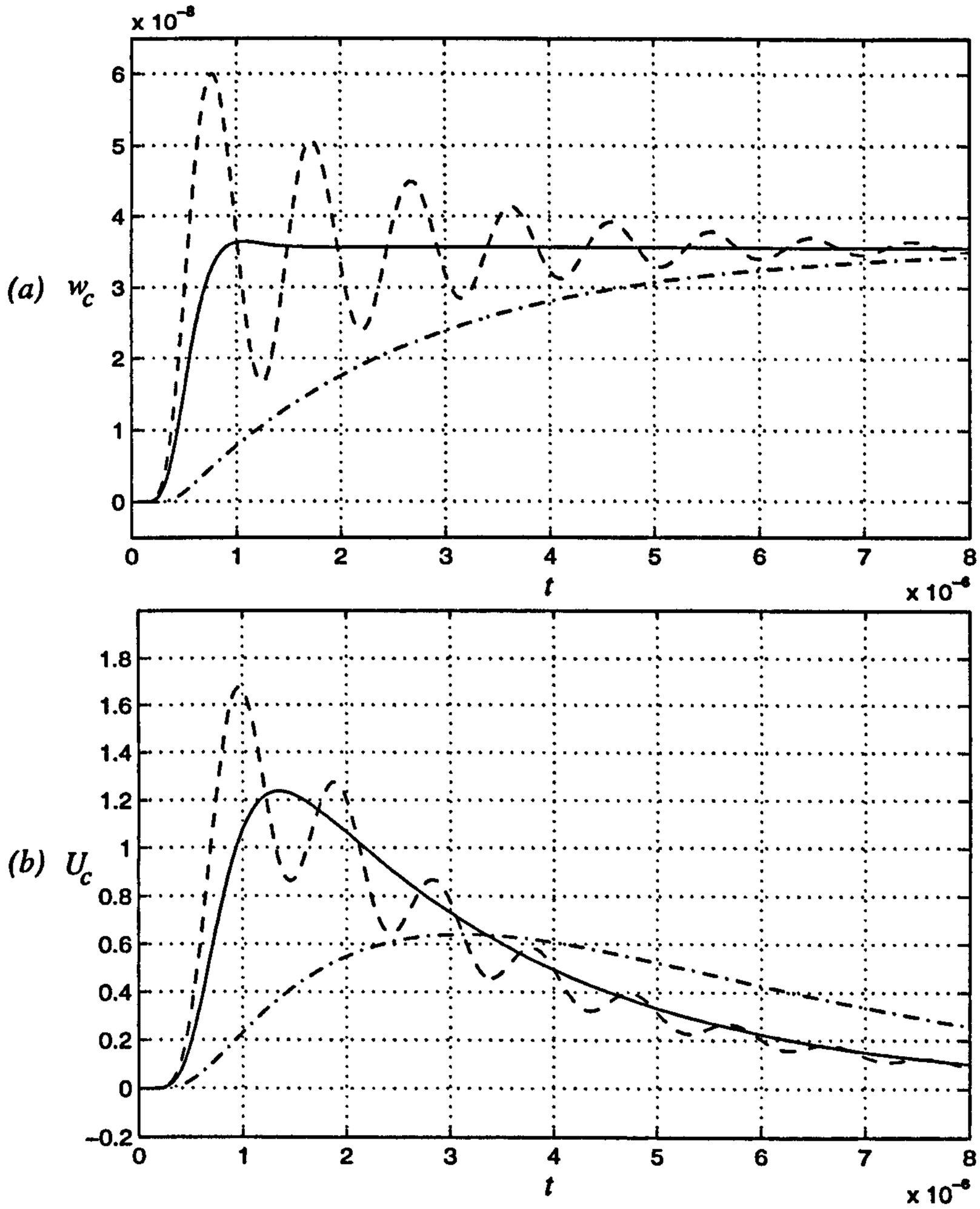

Figure 3.26: (a) The response of a diaphragm (w_c) subjected to a constant load, with varying levels of damping: d=10 kN s m^{-3} (--), d=100 kN s m^{-3} (-), d=1000 kN s m^{-3} (-·-). (b) The corresponding jet velocity responses resulting from the diaphragm motion.

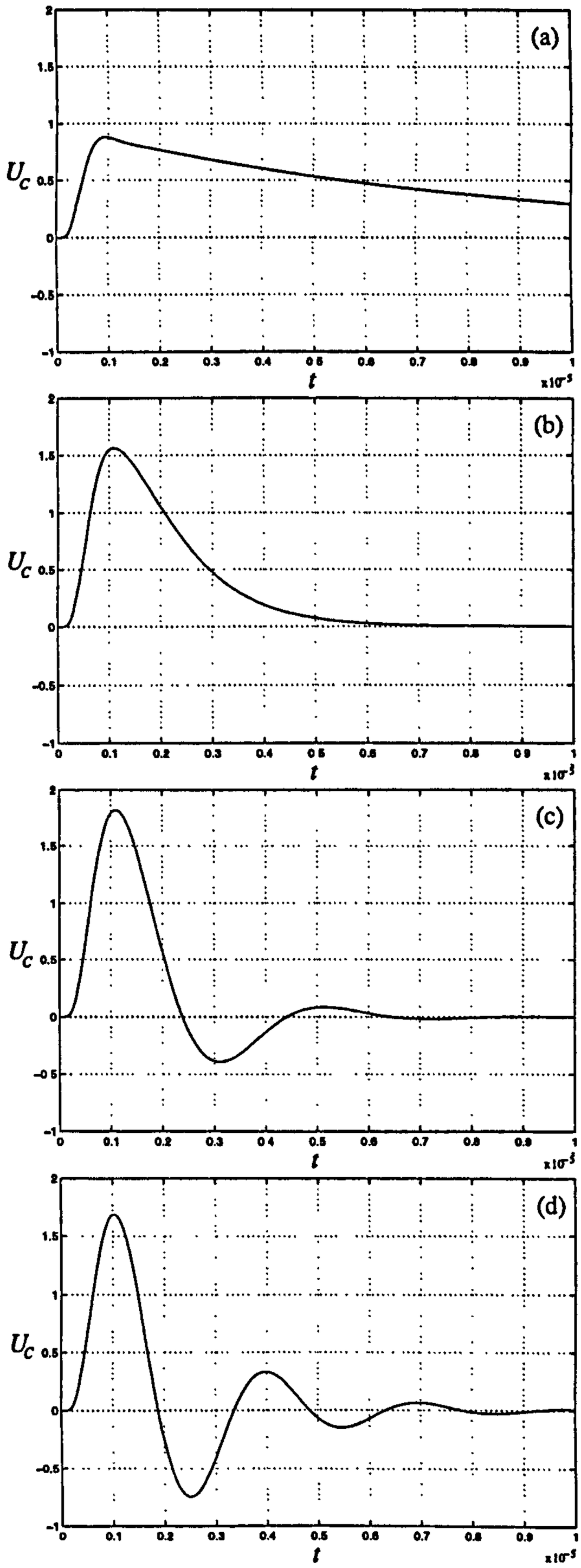

Figure 3.27: The velocity output from a pressure-jump actuator with varying orifice radii: (a) R_o=3.8μm; (b) R_o=5.8μm; (c) R_o=7.8μm, (d) R_o=9.8μm.

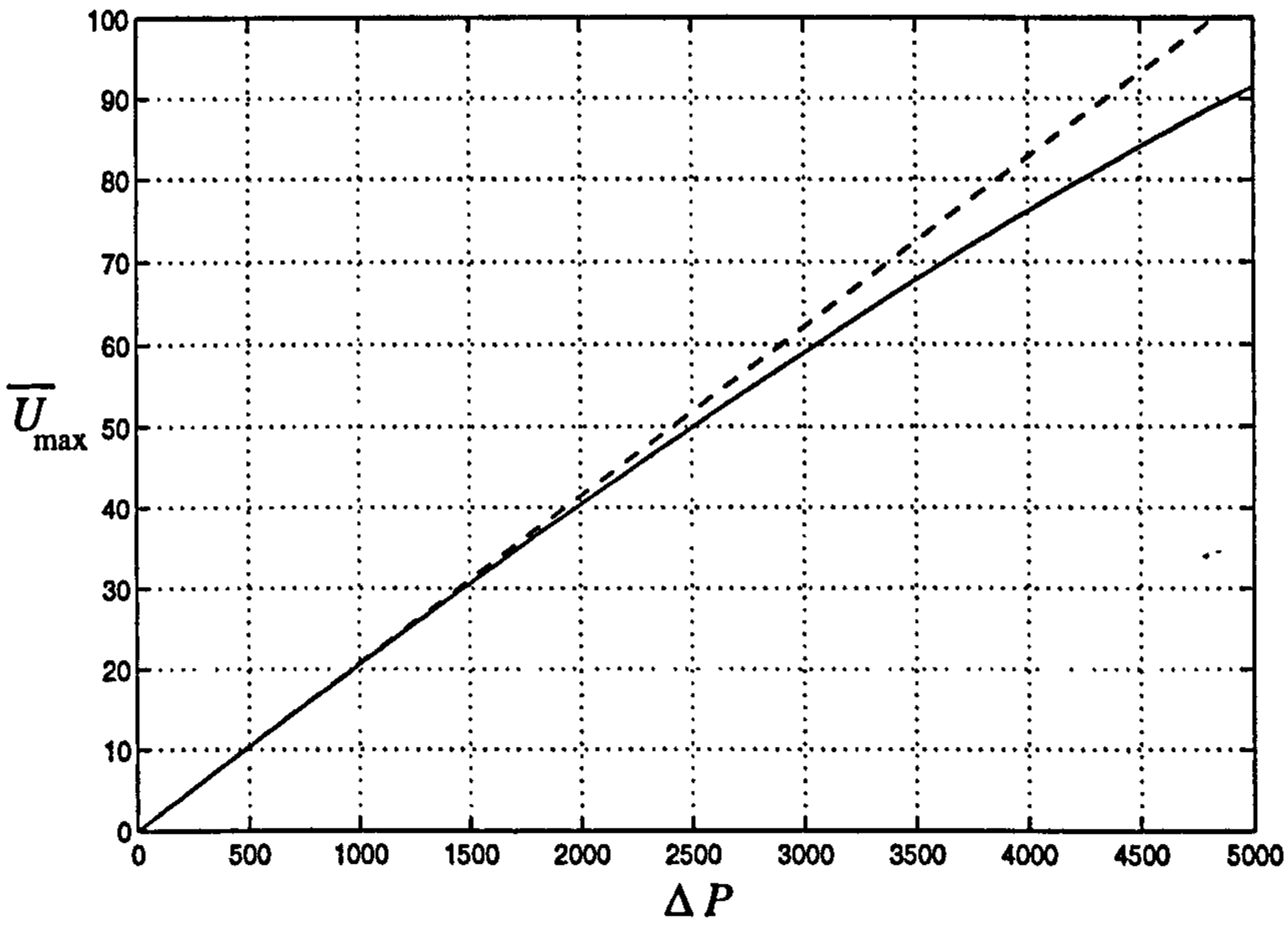

Figure 3.28: Variation of maximum average velocity ($\overline{U}_{max}$) with pressure pulse ΔP (–); $\overline{U}_{max} \propto \Delta P$ (– –).

3.5 Helmholtz Oscillation

In the results of the previous section a pressure-jump actuator was shown to produce an oscillating jet (see Figure 3.27(d)). The oscillation, which is not a consequence of diaphragm motion, can be predicted using simple analytical reasoning. The following analysis is similar to that in Dowling and Ffowcs Williams (1983).

3.5.1 Calculating the Helmholtz Frequency

If the diaphragm is ignored and the flow through the orifice is simplified (treated inviscidly), then it is possible to obtain a single equation to describe the temporal variation of pressure in the cavity.

For inviscid flows the relationship between the cavity pressure (P_c) and the mass flow rate out of the cavity (Q) is:

$$P_c = \left(\frac{l}{\pi R_o^2}\right)\frac{\mathrm{d}Q}{\mathrm{d}t} + P_o \tag{3.9}$$

where l is the orifice length, R_o is the orifice radius, and P_o is the ambient pressure outside the cavity. The rate of change of cavity density ($\mathrm{d}\rho/\mathrm{d}t$) and the mass flow rate (Q) are related by:

$$Q = -V\frac{\mathrm{d}\rho}{\mathrm{d}t} - \rho\frac{\mathrm{d}V}{\mathrm{d}t} \tag{3.10}$$

where V is the volume of the cavity, and ρ is the density of the cavity fluid. Since the diaphragm's deflection is ignored the volume of the cavity is constant, and so equation (3.10) can be simplified to:

$$\frac{\mathrm{d}\rho}{\mathrm{d}t} = -\frac{Q}{V} \tag{3.11}$$

Substituting the equation of state into equation (3.11), and assuming an isothermal process, yields:

$$\frac{\mathrm{d}P_c}{\mathrm{d}t} = -\frac{QkT}{V} \tag{3.12}$$

where k is the gas constant for air and T is the air temperature. If equation (3.12) is differentiated with respect to t, then the resulting $\mathrm{d}Q/\mathrm{d}t$ term can be substituted with a rearranged version of equation (3.9). This leaves a single second-order differential equation for the cavity pressure:

$$\frac{\mathrm{d}^2P_c}{\mathrm{d}t^2} = \frac{\pi R_o^2 kT}{lV}(P_o - P_c) \tag{3.13}$$

This has a solution in the form of

$$P_c = P_o + Ae^{i\omega t} \tag{3.14}$$

where A is a constant of integration and ω is the preferred or fundamental frequency at which the pressure oscillates – the *Helmholtz frequency.* The Helmholtz frequency can be found by substituting equation (3.14) into (3.13):

$$\omega = \sqrt{\frac{\pi R_o^2 kT}{lV}} \tag{3.15}$$

Unforced pressure fluctuation at this frequency, such as that demonstrated in Figure 3.27 (c)-(d), will be referred to as *Helmholtz oscillation.*

3.5.2 The Helmholtz Condition

Figures 3.27 (a)-(b) are examples of when viscous forces introduced by the orifice dampen the system sufficiently to prevent Helmholtz oscillation. The viscous threshold after which Helmholtz can occur, is important to quantify for two reasons. Firstly, if strong Helmholtz oscillation occurs, there will be a significant flow into the cavity. This is undesirable because of the increased risk of inhaled dust clogging the system. The second concern is that the device would have the potential for *Helmholtz resonance.* This phenomenon occurs when imposed pressure variations, perhaps from the boundary layer, coincide with the Helmholtz frequency causing large mass flow rates in and out of the cavity (see Chapter 6).

The analysis here is similar to that performed in §3.5.1 apart from the treatment of the orifice flow. At the viscous threshold, the flow will be fully developed but will also have the potential for unsteadiness. This flow regime can be described by unsteady Poiseuille flow (this equation can be derived from equation (2.67) if compressible effects are neglected and a parabolic velocity profile is assumed)

$$\frac{\mathrm{d}U_c}{\mathrm{d}t} = \frac{3\Pi}{2} - \frac{6\nu U_c}{R_o^2} \tag{3.16}$$

where U_c is the center-line velocity, Π is the unsteady pressure gradient, and ν is the kinematic viscosity. Equation (3.16) can be expressed in terms of mass flow rate and pressure inside and outside the cavity.

$$\frac{\mathrm{d}Q}{\mathrm{d}t} = \frac{3\pi R_o^2}{4l}(P_c - P_o) - \frac{6\nu Q}{R_o^2} \tag{3.17}$$

As in §3.5.1, the relationship between cavity pressure and the mass flow rate is

given by

$$\frac{\mathrm{d}P_c}{\mathrm{d}t} = -\frac{QkT}{V} \tag{3.18}$$

Equation (3.18), and its derivative with respect to t, can be substituted into equation (3.17) to obtain a second-order differential equation describing the temporal variation in cavity pressure:

$$\frac{\mathrm{d}^2P_c}{\mathrm{d}t^2} = -\frac{3\pi R_o^2 kT}{4lV}(P_c - P_o) - \frac{6\nu}{R_o^2}\frac{\mathrm{d}P_c}{\mathrm{d}t} \tag{3.19}$$

which has a solution in the form of

$$P_c = P_o + Ae^{i\omega t} \tag{3.20}$$

Substituting equation (3.20) into (3.19) yields the auxiliary equation:

$$\omega^2 - \frac{6\nu}{R_o^2}i\omega - \frac{3\pi R_o^2 kT}{4lV} = 0 \tag{3.21}$$

and the roots of equation (3.21) are

$$\omega_{1,2} = \frac{3\nu}{R_o^2}i \pm \sqrt{\frac{3\pi R_o^2 kT}{4lV} - \frac{9\nu^2}{R_o^4}} \tag{3.22}$$

Helmholtz oscillation can only occur when the roots of equation (3.21) have a real component, i.e when

$$\frac{3\pi R_o^2 kT}{4lV} > \frac{9\nu^2}{R_o^4} \tag{3.23}$$

This can be rearranged in terms of R_o:

$$R_o > \left(\frac{12\nu^2 lV}{\pi kT}\right)^{\frac{1}{6}} \tag{3.24}$$

This is the *Helmholtz condition.* If this condition is satisfied then the Helmholtz frequency at the threshold is given by:

$$\alpha = \sqrt{\frac{3\pi R_o^2 kT}{4lV} - \frac{9\nu^2}{R_o^4}} \tag{3.25}$$

and the decay rate is

$$\lambda = \frac{3\nu}{R_o^2} \tag{3.26}$$

where the solution is in the form

$$P_c = P_o + Ae^{-\lambda t}e^{i\alpha t} \tag{3.27}$$

(initial conditions must be satisfied for a complete solution).

A series of numerical simulations have been performed to check the prediction of the Helmholtz condition given by equation (3.24). This was achieved by varying the orifice radius and measuring the minimum velocity output over the actuation period. If a negative minimum velocity was obtained it could be assumed that Helmholtz oscillation was occurring. Figure 3.29 shows the variation of minimum average velocity with orifice radius, for g=625μm. The numerical results (–□–) suggest that the Helmholtz condition is satisfied at R_o=430μm – the analytically obtained value (–··–) is in exact agreement with this.

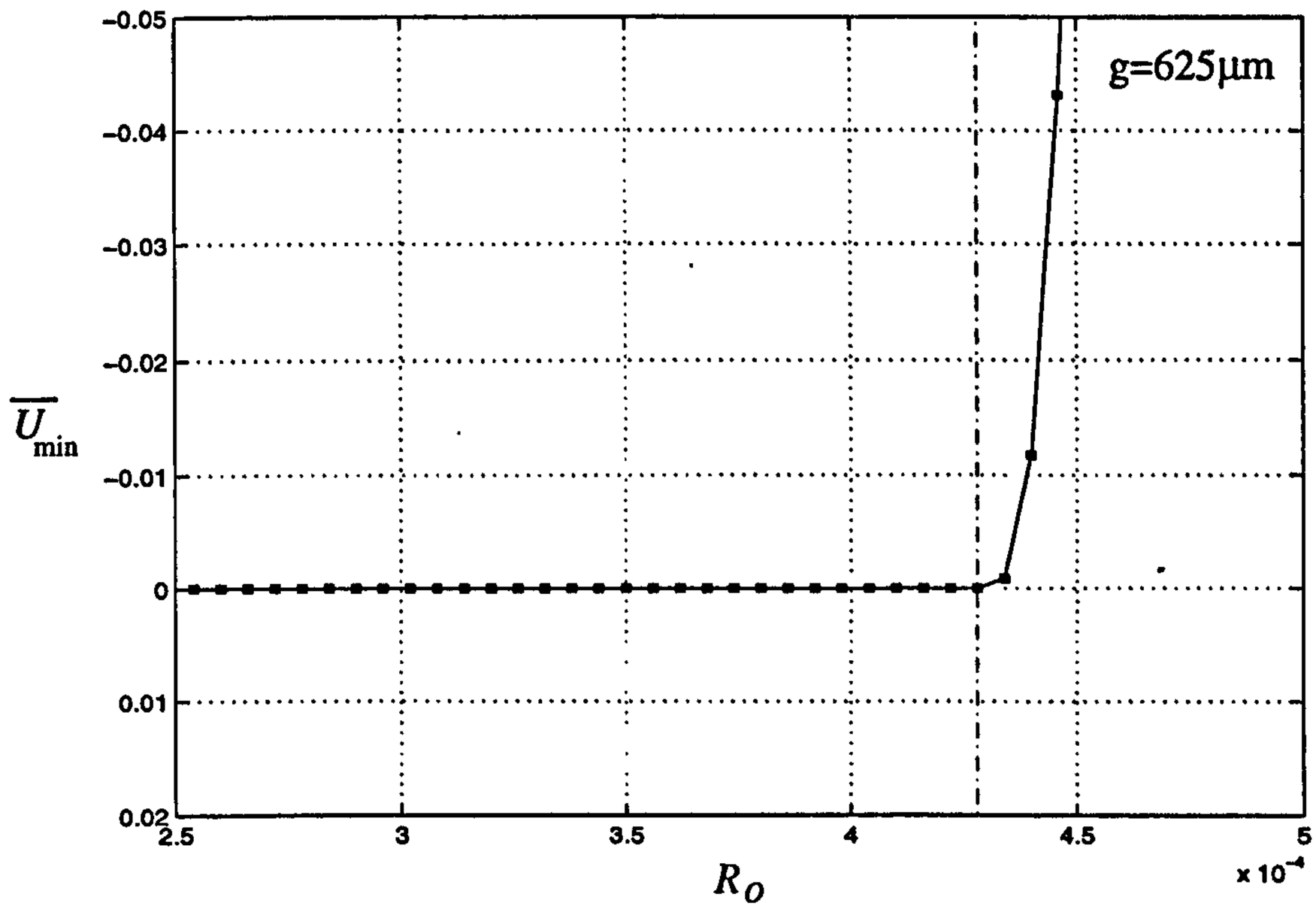

Figure 3.29: The minimum average velocity $\overline{U}_{min}$ obtained from a pressure-jump actuator (g=625μm) with varying orifice radius R_o (-□-); the analytically obtained Helmholtz condition (–·–).

3.6 Velocity Optimisation

In Chapter 5 it will be demonstrated that for pressure-jump devices the most important jet characteristic, in terms of its ability to affect the boundary layer, is the total mass outflow during the actuation period (net mass flow). This is maximised by making the net volume displacement of the diaphragm or pressure valve as large as possible. This section details how the remaining design parameters, such as orifice radius, can be set to achieve maximum velocity for the given mass flux. The optimisation in this section is relevant to both diaphragm-driven and microvalve-driven pressure-jump actuators.

3.6.1 Optimum Orifice Radius

In this section orifice-radius optimisation is performed for the pressure-jump design (see §3.4.2) at varying scales. Figure 3.30 shows the optimisation for different scale parameters, g; in all cases the optimum occurs within the static-compressible limit for the model (§2.5). Figure 3.31 shows the variation of optimum orifice radius with scale (g) in which there are two main points of interest. Firstly, the orifice radius when optimised for maximum average velocity is greater than when it is optimised for maximum centre-line velocity. Secondly, there seems to be a clear power-law relationship between optimum orifice radius and scale.

3.6.2 Optimisation for a Generalised Design

Some simplifications to the system can be made to derive an analytical expression for optimum orifice radius (R_o) for a generalised pressure-jump actuator design. The method is similar to the analytical optimisation described in Rathnasingham and Breuer (1997a) (see §C.1). The pressure jump (ΔP) can induce one of two extreme flow regimes; for small R_o a viscous-dominated flow, and for large R_o an inviscid Helmholtz oscillation. The unsimplified flow is a combination

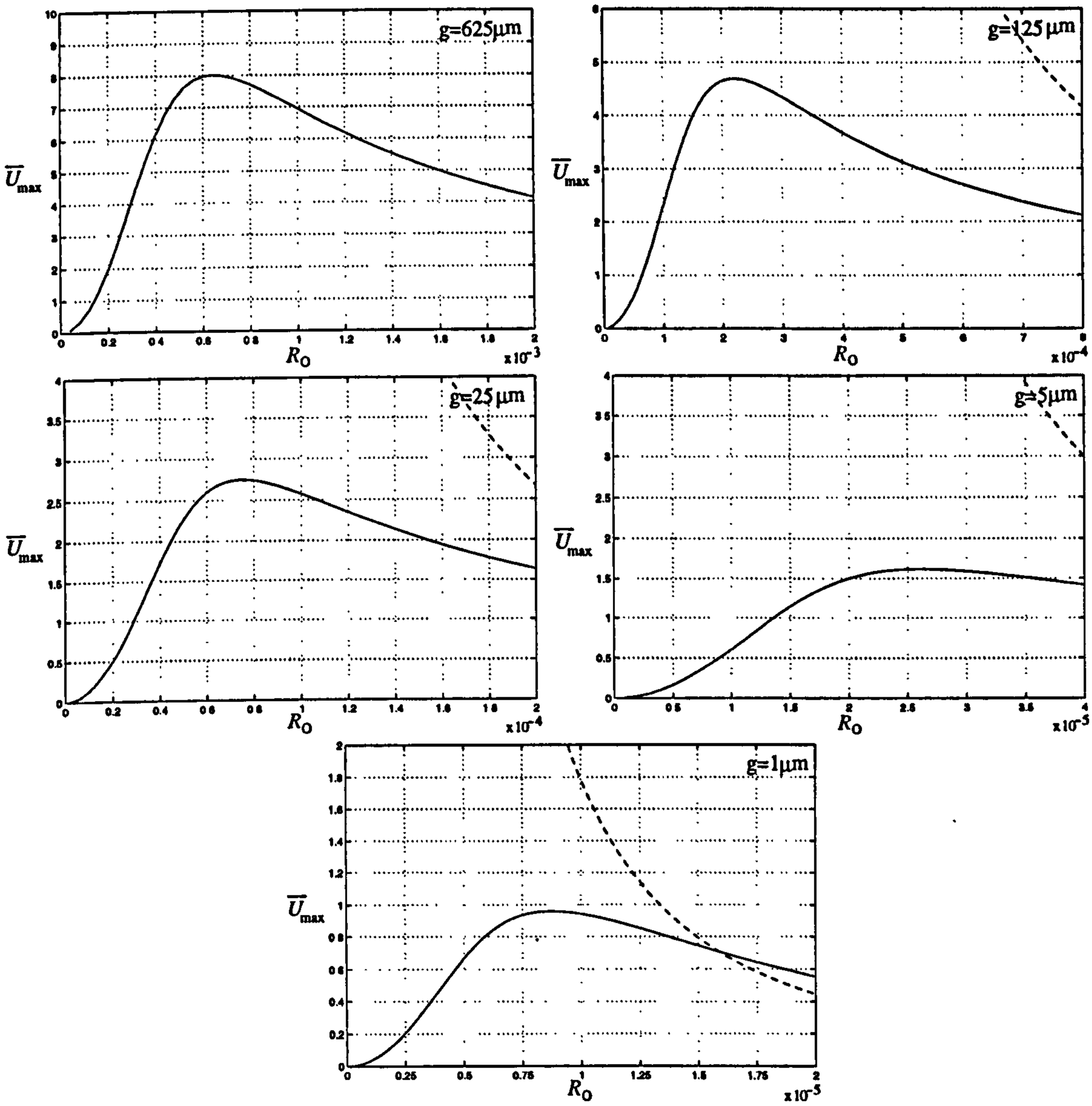

Figure 3.30: The variation of maximum average velocity ($\overline{U}_{max}$) with orifice radius (R_o) at different scales; g=1–625μm. The static-compressible simulation (–) and the dynamic-incompressible solution (– –)

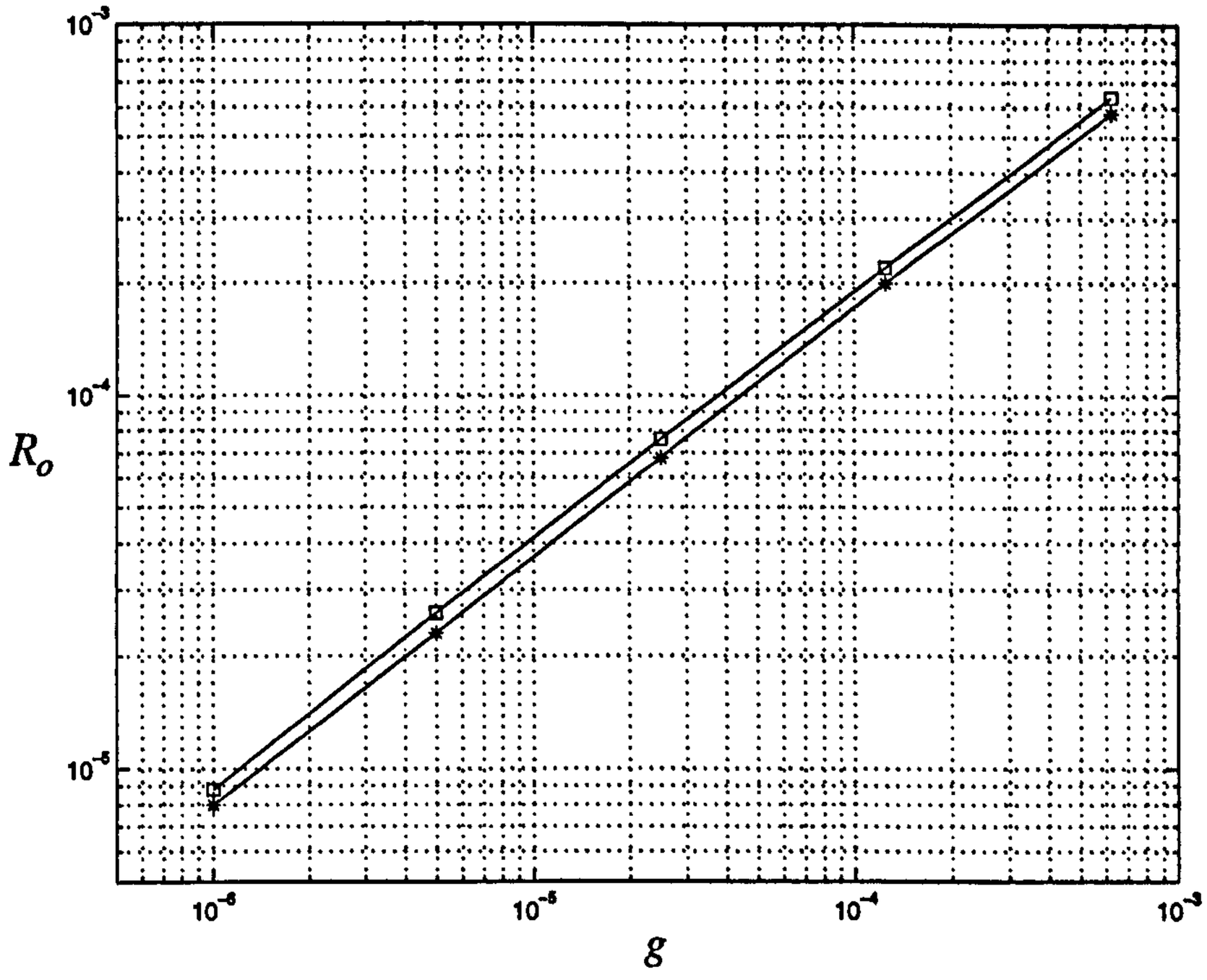

Figure 3.31: The variation of optimum orifice radius (R_o) with scale (g); optimised for maximum average velocity (–□–), optimised for maximum centre-line velocity (–∗–)

of both regimes. However, a good estimate for optimum orifice radius can be obtained if it is assumed that the flow switches abruptly between regimes at some intermediate R_o. The regime that is chosen at a particular R_o is that which produces the minimum energy/velocity output, therefore the maximum velocity of the combined flow occurs when the regimes intersect. The equations defining the velocity output from each regime are equated in order to find the optimum orifice radius.

The Inviscid Regime

The maximum average velocity in the inviscid regime can be obtained by firstly stating the inviscid and unsteady flow equation:

$$\frac{\mathrm{d}\overline{U}}{\mathrm{d}t} = \Pi \tag{3.28}$$

where $\overline{U}$ is the average velocity and Π is the pressure gradient. If a sinusoidal Helmholtz oscillation is assumed, the variation of cavity pressure (P_c) will be in the form given by equation (3.14):

$$P_c = P_o + Ae^{i\omega t} \tag{3.29}$$

where P_o is the ambient pressure, A is a constant of integration, and ω is the Helmholtz frequency. The constant A can be found by enforcing the pressure jump (ΔP) at time zero:

$$P_c - P_o = A = \Delta P \qquad \text{at } t{=}0 \tag{3.30}$$

The solution equation (3.29) can be substituted into equation (3.28) to give

$$\frac{\mathrm{d}\overline{U}}{\mathrm{d}t} = \frac{\Delta P}{\rho_o l} e^{i\omega t} \tag{3.31}$$

where l is the orifice length and ρ_o is the ambient density. The solution for average velocity, $\overline{U}$, will also be in harmonic form:

$$\overline{U} = \frac{\overline{U}_{max}}{i} e^{i\omega t} \tag{3.32}$$

Equation (3.32) can be substituted into equation (3.31) to obtain a relationship between initial pressure jump (ΔP) and maximum average velocity ($\overline{U}_{max}$):

$$\overline{U}_{max} = \frac{\Delta P}{\rho_o l \omega} \tag{3.33}$$

In the inviscid regime the Helmholtz frequency, ω, is defined by equation (3.15) and can be substituted into (3.33):

$$\overline{U}_{max} = \frac{\Delta P}{\rho_o l}\sqrt{\frac{V}{kT\pi R_o^2}} \tag{3.34}$$

where V is the volume of the cavity, T is the air temperature, k is the gas constant for air, and R_o is the orifice radius.

The Viscous-Dominated Regime

In the viscous-dominated regime, flow is governed by the quasi-steady Poiseuille equation:

$$\overline{U} = \frac{\Pi R_o^2}{8\nu} \tag{3.35}$$

where ν is the kinematic viscosity. The pressure variation following the initial jump, ΔP, will be 'over damped'. This means that the pressure, and the average velocity, will be greatest at time zero – the point of pressure-jump application. Equation (3.21) can be evaluated at t=0 to obtain a relationship between ΔP and maximum average velocity, $\overline{U}_{max}$:

$$\overline{U}_{max} = \frac{R_o^2 \Delta P}{8\rho_o \nu l} \tag{3.36}$$

The maximum velocity in both inviscid and viscous regimes (given by equations (3.34) and (3.36)) can be equated and rearranged to provide an estimate for the optimum orifice radius:

$$R_o = \left(\frac{64\nu^2 l V}{\pi k T}\right)^{\frac{1}{6}} \tag{3.37}$$

Figure 3.32 shows the comparison between the analytically-obtained optimum orifice radius and the numerical optimisation results from §3.6.1. Good agreement is found for all scales (g); the analytical prediction for optimum R_o under-estimates by 14% at all values.

A correction factor (c=1.14) is introduced into equation (3.37) in order to obtain an exact agreement at all scales: (In §C.2 it is verified that c=1.14 is effectively design independent)

$$R_o = c\left(\frac{64\nu^2 lV}{\pi kT}\right)^{\frac{1}{6}} \tag{3.38}$$

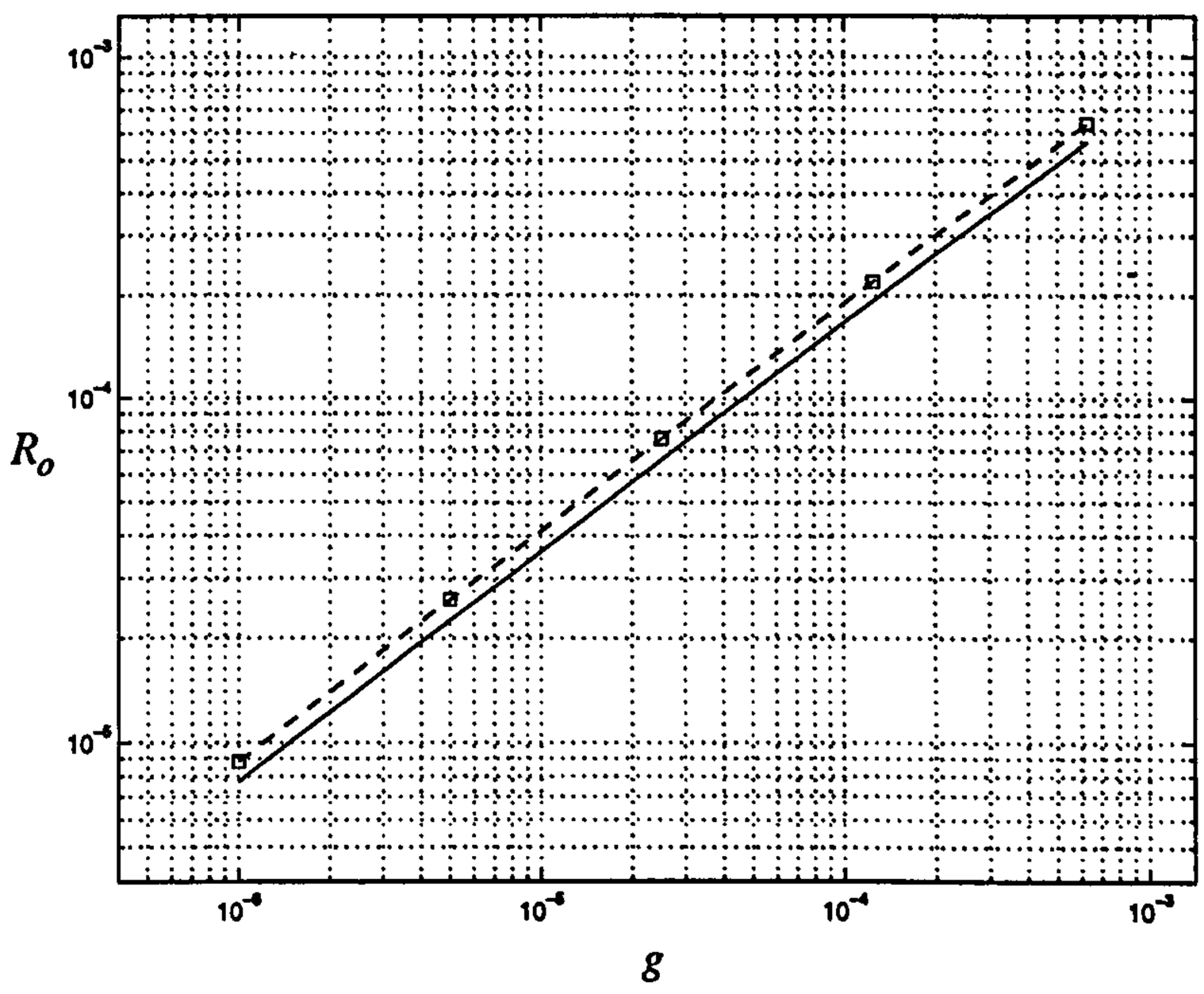

Figure 3.32: The variation of optimum R_o (optimised for maximum average velocity) with the scale parameter g. Comparison of optimum from numerical simulations (–□– –) and analytically obtained optimum (–)

3.6.3 Optimised Velocity

After having established the optimum orifice radius for a given design, it is of interest to calculate the magnitude of the optimised velocity. Figure 3.33 shows the variation of optimised average velocity with the scale parameter g (□). The solid line is the function $\overline{U}_{opt} \propto g^{\frac{1}{3}}$; this cube-root relationship between optimised velocity and scale can be predicted analytically.

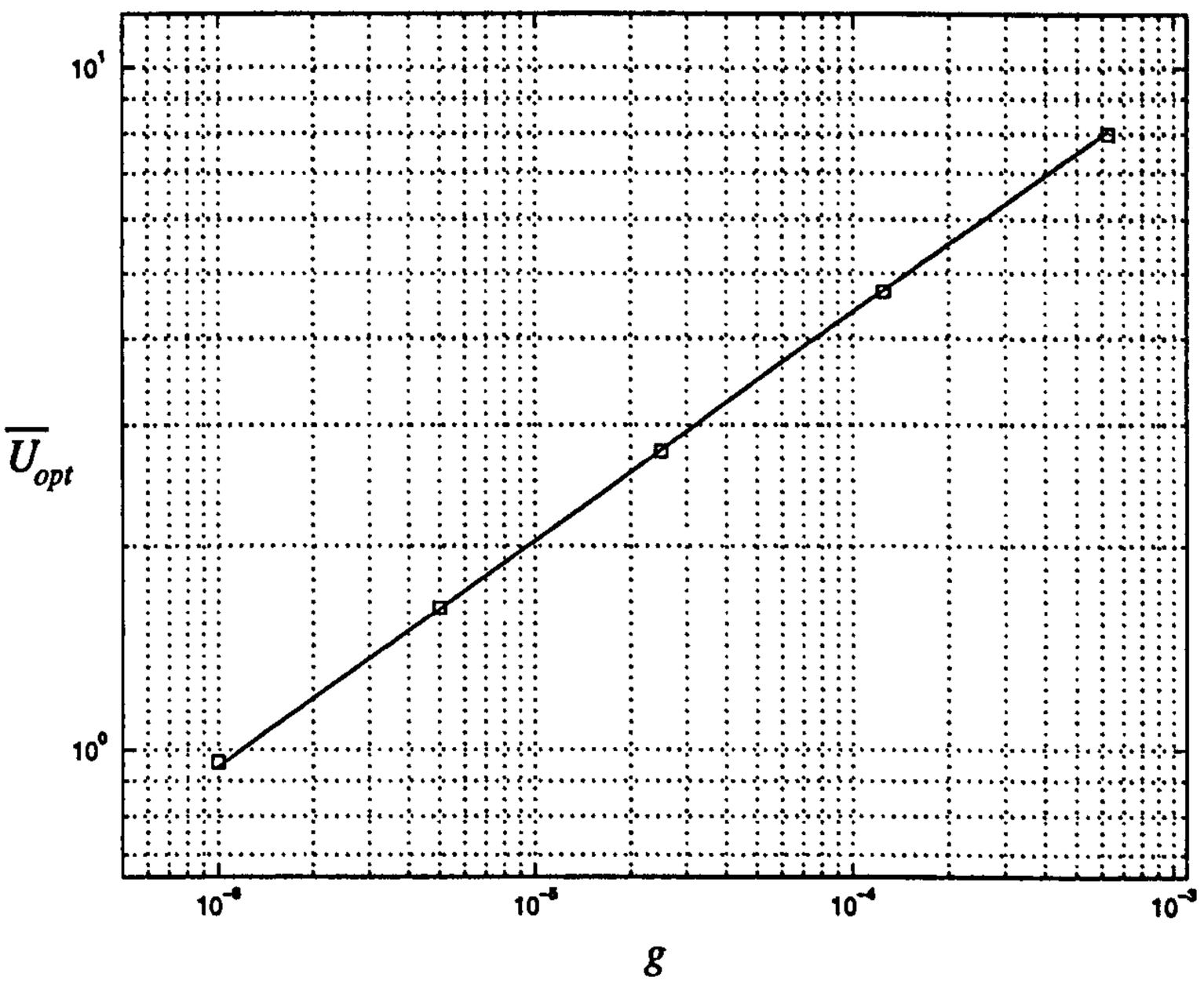

Figure 3.33: Variation of optimised average velocity ($\overline{U}_{\mathrm{opt}}$) with scale ($g$).

If the analytically evaluated optimum R_o (equation 3.38), is substituted into the maximum velocity from the quasi-steady flow solution (equation 3.35) the following expression for optimised velocity can be obtained:

$$\overline{U}_{opt} \propto \Delta P \left(\frac{V}{l^2}\right)^{\frac{1}{3}} \tag{3.39}$$

(note that, a quantitatively accurate analytical expression cannot be derived in this way). The most obvious conclusion to be drawn from equation (3.39) is that the maximum velocity obtainable (average and centre-line) is proportional to the

pressure jump (ΔP). This linear relationship has already been demonstrated in the non-optimised pressure-valve simulations presented in §3.4.3.

If the diaphragm is approximated as being instantaneously deflected, the pressure jump can be given by:

$$\Delta P = \frac{P_o \overline{w}_{max}}{H_c} \tag{3.40}$$

where $\overline{w}_{max}$ is the maximum mean deflection of the diaphragm, and H_c is the cavity height. Equation (3.40) can be substituted into equation (3.39) to obtain the optimised velocity solely in terms of $\overline{w}_{max}$ and the actuator dimensions: cavity height H_c, orifice length l, and cavity and diaphragm radius R_d:

$$\overline{U}_{opt} \propto \overline{w}_{max} \left(\frac{R_d}{lH}\right)^{\frac{2}{3}} \tag{3.41}$$

(an identical expression is obtained for maximum centre-line velocity). If all the dimensions of the actutator and the deflection are re-expressed in terms of g and substituted into equation (3.41), a relationship between the optimised velocity and the scale parameter can be obtained: (note that for a fixed applied pressure the steaddy-state deflection is linearly related to scale - see equation (2.20))

$$\overline{U}_{opt} \propto (g)^{\frac{1}{3}} \tag{3.42}$$

The cube-root relationship between optimised velocity and scale observed in Figure 3.33 is predicted by equation (3.42).

3.6.4 Actuator Design

Equation (3.41) is particularly insightful and corroborates the general guidelines of design described at the beginning of this chapter, §3.1.1. Firstly, it is clear

that a linear relationship between maximum diaphragm deflection and maximum velocity exists. Therefore a primary design objective is to make the diaphragm's deflection as large as possible for a given diaphragm size. This is also a primary objective for net-mass-flow optimisation, which will be discussed in Chapter 5. Secondly, it can be inferred that maximisation of diaphragm size (R_d) should also be sought to maximise the velocity and the net mass flow. This principle can be seen in the design of Manchester's actuator which has the diaphragm oriented on its side (see Figure 3.1). The maximum-diaphragm design precept is reinforced by the fact that if the diaphragm's radius (R_d) is increased, then the potential deflection ($\overline{w}_{max}$) will also be greater. There is, however, a limit to the optimisation of design in this way; nonlinearities obviously prohibit the indefinite increase of maximum velocity with diaphragm deflection, and maximum deflection with input voltage.

It was also suggested in §3.1.1 that the cavity volume should be minimised in order to achieve maximum potential compression from a given deflection. Equation 3.41 shows this to be true provided that the minimisation of volume is not at the expense of diaphragm size. In other words, the cavity height (H_c) should be minimised, but not the diaphragm radius (R_d). This principle can also be seen in the Manchester design which has a very shallow cavity in comparison to the diaphragm's radius. An optimum must occur at some small cavity height H, when increased cavity viscous effects and compressive nonlinearities start to become significant.

Finally, from equation (3.41), the minimisation of orifice length (l) is suggested, in order to maximise the pressure gradient for a given pressure jump. This design rule is slightly misleading because at small orifice lengths ($l < 2R_o$) the pipe theory used in the derivation of equation (3.41) becomes inappropriate. It is also probable that this design parameter will be fixed by the need to have a robust actuator cap.

3.6.5 Satisfying the Helmholtz Condition

In §3.5.2 an expression was derived to evaluate the orifice radius at which Helmholtz oscillation could occur:

$$R_o > \left(\frac{12\nu^2 lV}{\pi kT}\right)^{\frac{1}{6}} \tag{3.43}$$

Equation (3.43), the Helmholtz condition, is of serious interest as it provides information as to whether or not undesirable phenomena, such as Helmholtz resonance, are possible for a chosen design.

Substituting the optimum-R_o solution (equation 3.38) into the Helmholtz condition (equation 3.43) can determine whether Helmholtz oscillation will occur for velocity-optimised actuators:

$$c\left(\frac{64\nu^2 lV}{\pi kT}\right)^{\frac{1}{6}} > \left(\frac{12\nu^2 lV}{\pi kT}\right)^{\frac{1}{6}}$$

$$1.5 > 1 \tag{3.44}$$

The condition is clearly satisfied and therefore Helmholtz oscillation *will* occur in velocity-optimised devices, and potentially, Helmholtz resonance also. It may be more appropriate to optimise net mass flow via diaphragm maximisation, as suggested earlier, but to optimise velocity only up until the Helmholtz condition is met. These measures would dictate an orifice radius of 1.5 times less than the velocity-optimised orifice radius.

3.6.6 Section Summary

In sections §3.6.1 and §3.6.2 an analytical solution has been calibrated to numerical simulations using a linear correction factor c. This equation provides a means

of accurately estimating the optimum orifice radius for any given pressure-jump actuator design. In section §3.6.3, numerical and analytical investigation has shown that the attainable optimised velocity is proportional to the cube root of scale (g). General actuator design guidelines have been discussed in section §3.6.4 and finally, in section §3.6.5 it has been demonstrated that Helmholtz oscillation will occur in velocity-optimised pressure-jump actuators.

3.7 Chapter Summary

In section §3.1 the mathematical model described in Chapter 2 has been validated against experimental data for a synthetic jet (Crook *et al.* 1999). In section §3.2 the device dimensions that were used in section §3.1 have been scaled down to investigate the differences between MEMS-scale and micro-scale actuators. In section §3.3 the effect of cavity pressure on the diaphragm's motion is considered. In section §3.4 a more suitable operating mode is suggested for the turbulence-control application – the pressure-jump actuator. The phenomenon of Helmholtz oscillation that is resident in some pressure-jump actuators, and the potential for any cavity actuator to experience Helmholtz resonance, is investigated in section §3.5. The optimal pressure-jump actuator design is discussed in section §3.6.

Chapter 4

Modelling the Dynamics of Boundary-Layer Disturbances

This chapter describes the numerical modelling of the dynamics of boundary-layer disturbances. The mathematical method is described in §4.1 and the numerical strategy detailed in §4.2. Simulations from the computer code are compared to results from linear stability theory (§4.3.1) and results from the experiments of Klebanoff (§4.3.2).

Nomenclature for Chapter 4

Unless otherwise indicated, lengths and velocities have been non-dimensionalised using δ^* and U_∞, respectively.

$\bar{}$ = an over bar denotes a dimensional quantity

a, b = forcing function constants

$\bar{F}_y = F_y \, U_\infty^2/\delta^*$ = spanwise body force per unit mass (m s^{-2})

$\bar{G} = G \, U_\infty^2/\delta^{*2}$ = magnitude of vorticity forcing function (s^{-2})

i = complex variable

L = dimensionless mapped-domain stretching factor

N_c = number of Chebyshev polynomials

$\mathbf{N} = (N_x, N_y, N_z)$ = convective terms in the vorticity transport equations

$R = U_\infty \delta^* / \nu$ = Reynolds number

$\bar{T} = T\ \delta^* / U_\infty$ = total simulation time (s)

U_∞ = free-stream velocity (m s^{-1})

$\mathbf{u} = (u, v, w)$ = dimensionless perturbation velocity

$\mathbf{U} = (U, 0, 0)$ = dimensionless undisturbed-flow velocity (mean flow)

V_m = maximum jet-actuator velocity (m s^{-1})

x, y, z = dimensionless streamwise, spanwise and wall-normal directions

x_f, z_f = dimensionless streamwise and wall-normal position of body force

X_d = dimensionless streamwise domain length

X_b, X_e = dimensionless streamwise position of actuator

$\bar{\alpha}_x = \alpha_x / \delta^*$ = streamwise wave number (m^{-1})

$\bar{\beta} = \beta / \delta^*$ = spanwise wave number (m^{-1})

δ^* = boundary layer thickness (m)

$\bar{\Delta} t = \Delta t\ \delta^* / U_\infty$ = time step (s)

Δx = dimensionless streamwise grid spacing

ζ = mapped variable

ν = kinematic viscosity (m^2 s^{-1})

$\bar{\omega}_f = \omega_f\ U_\infty / \delta^*$ = actuator forcing frequency (s^{-1})

$\bar{\boldsymbol{\omega}} = (\omega_x, \omega_y, \omega_z)\ U_\infty / \delta^*$ = perturbation vorticity (s^{-1})

$\bar{\boldsymbol{\Omega}} = (0, 0, \Omega_z)\ U_\infty / \delta^*$ = undisturbed flow vorticity (s^{-1})

4.1 The Novel Velocity-Vorticity Formulation

In order to determine the effect a jet actuator will have on a boundary layer, the fluid dynamics of the flow must be modelled accurately. To do this the Navier-Stokes equations must be solved in some form.

The method that has been adopted here, originally described by Davies and Carpenter (1997), solves the Navier-Stokes equations in velocity-vorticity form. This method is specifically designed for the simulation of the evolution of disturbances in a boundary layer, and is also capable of solving interactive and elliptic flow problems such as that presented by the MEMS application.

The novel velocity-vorticity formulation of the Navier-Stokes equations is fully detailed in Davies and Carpenter (1997) and (1999). What follows is an overview of the technique, and details of how it has been applied to the MEMS application.

4.1.1 Variables and the Co-ordinate System

One of the advantages of this velocity-vorticity method is that it can use simplified undisturbed states that are not strictly solutions of the Navier-Stokes equations. This can allow simplifications that make the simulations less computationally demanding. For example, in this thesis, the boundary layer is modelled as a constant-thickness, incompressible shear flow, with an undisturbed-flow solution (mean flow) with the following vorticity and velocity fields:

$$\mathbf{U} = (U\ ,\ 0\ ,\ 0) \qquad \mathbf{\Omega} = (0\ ,\ 0\ ,\ \Omega_z). \tag{4.2}$$

If it is assumed that the undisturbed solution is known, such as the Blasius profile, only perturbations away from this mean need to be calculated. Hence, the total solution is decomposed into the specified undisturbed flow and a perturbation:

$$\mathbf{U}_T = \mathbf{U} + \mathbf{u}, \qquad \mathbf{\Omega}_T = \mathbf{\Omega} + \boldsymbol{\omega} \tag{4.3}$$

where the perturbations fields are

$$\mathbf{u} = (u,\, v,\, w), \qquad \boldsymbol{\omega} = (\omega_x, \omega_y, \omega_z). \tag{4.4}$$

The co-ordinate system (x,y,z) corresponds respectively to the streamwise, spanwise and wall-normal directions - see Figure 4.1.

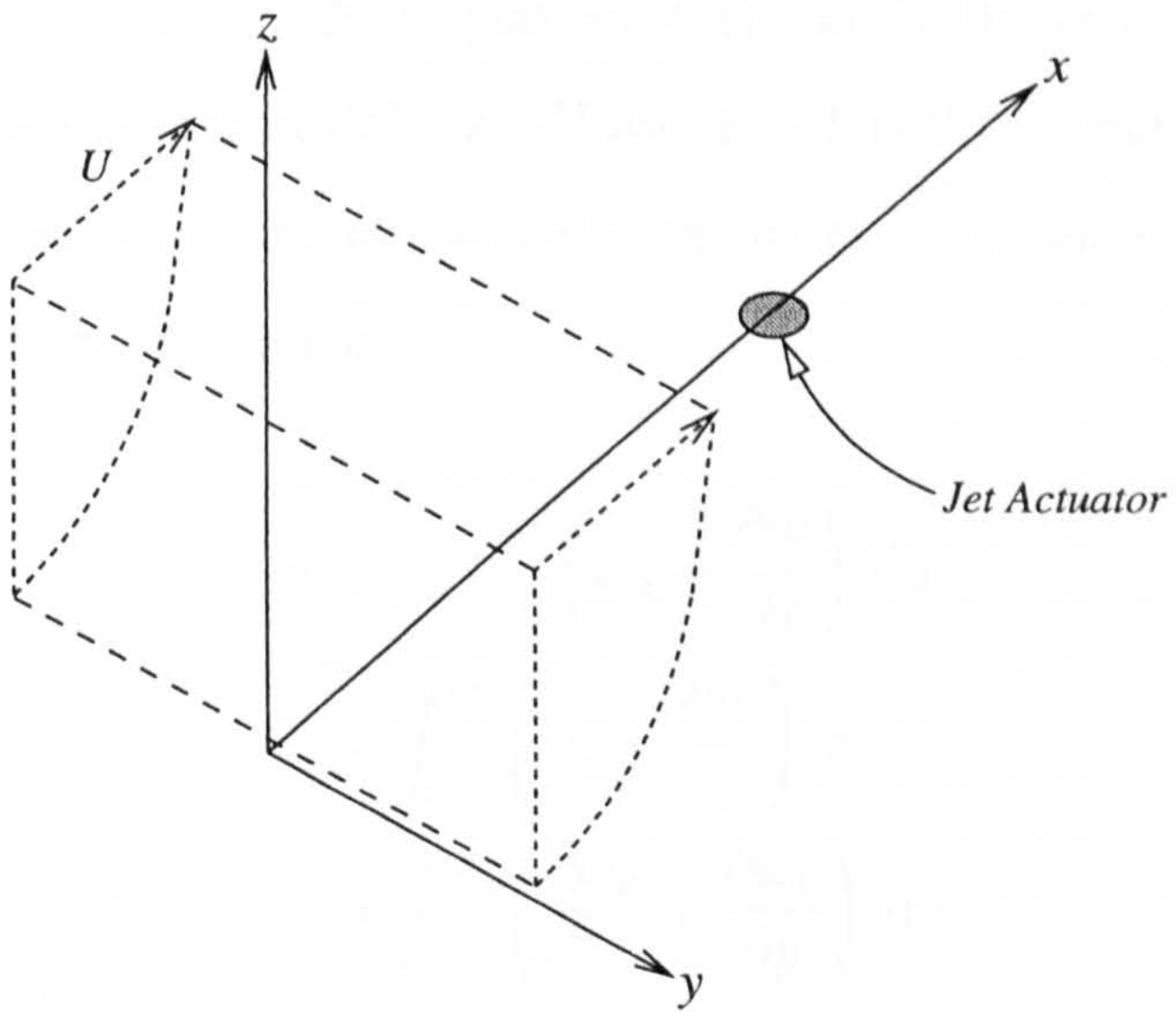

Figure 4.1: The boundary-layer co-ordinate system.

4.1.2 Governing Equations

In the velocity-vorticity formulation used here, the variables are divided into two sets; the *primary* variables $\{\omega_x,\omega_y,w\}$ and the *secondary* variables $\{\omega_z,u,v\}$. Davies and Carpenter (1997, 1999) have shown that the evolution of the primary variables is governed by the following three equations only:

$$\frac{\partial \omega_x}{\partial t} + \frac{\partial N_z}{\partial y} - \frac{\partial N_y}{\partial z} = \frac{1}{R}\nabla^2 \omega_x \tag{4.5}$$

$$\frac{\partial \omega_y}{\partial t} + \frac{\partial N_x}{\partial z} - \frac{\partial N_z}{\partial x} = \frac{1}{R}\nabla^2 \omega_y \tag{4.6}$$

$$\nabla^2 w = \frac{\partial \omega_x}{\partial y} - \frac{\partial \omega_y}{\partial x} \tag{4.7}$$

$$\text{where} \qquad \mathbf{N} = \bar{\Omega} \times \mathbf{u} + \omega \times \bar{\mathbf{U}} + \omega \times \mathbf{u} \tag{4.8}$$

The Reynolds number is given by $R = U_\infty \delta^* / \nu$, and the freestream flow speed (U_∞) and the displacement thickness (δ^*) are used as reference values for non-dimensionalisation. Equations (4.5) and (4.6) are referred to as the vorticity transport equations, and equation (4.7) is the Poisson equation.

The convective quantity N (equation 4.8) can only be evaluated by firstly calculating the secondary variables. However, if rather general conditions are satisfied as $z \to \infty$ (namely u=v=0) the secondary variables can be defined in terms of the primary variables:

$$u = -\int_z^\infty \left(\omega_y + \frac{\partial w}{\partial x} \right) \mathrm{d}z \tag{4.9}$$

$$v = \int_z^\infty \left(\omega_x - \frac{\partial w}{\partial y} \right) \mathrm{d}z \tag{4.10}$$

$$\omega_z = \int_z^\infty \left(\frac{\partial \omega_x}{\partial x} + \frac{\partial \omega_y}{\partial y} \right) \mathrm{d}z \tag{4.11}$$

Equations (4.9) and (4.10) are obtained directly from the definition of vorticity, and equation (4.11) is derived from the solenoidal condition of the vorticity field. These definitions can be used to express N explicitly in terms of the primary variables, therefore the governing equations (4.5)-(4.7) can be viewed as a system of three equations for three primary variables; all reference to the secondary variables is eliminated. The reduction in governing equations from six to three affords significant reduction in computational expense. This and other advantages over existing velocity-vorticity methods are fully detailed in Davies and Carpenter (1997) and (1999).

For the simulations presented in this thesis the governing equations are linearised in order to make the simulation times more manageable. Linearisation can be achieved by neglecting the nonlinear convective terms in equation (4.8) ($\omega \times \mathbf{u}$). Strictly then, this approach is only valid for perturbations and jet veloc-

ities of small amplitude.

4.1.3 Boundary Conditions

The boundary conditions at the wall (z=0) take the form:

$$u(x, y, 0, t) = 0 \tag{4.12}$$

$$v(x, y, 0, t) = 0 \tag{4.13}$$

$$w(x, y, 0, t) = f(x, y, t) \tag{4.14}$$

where f=0, except at the actuator exit where it equals the instantaneous velocity profile. Substituting the secondary-variable boundary-conditions (4.12)-(4.13) into equations (4.9)-(4.10) yields equivalent integral conditions in terms of primary variables:

$$\int_0^\infty \omega_y \, \mathrm{d}z = -\int_0^\infty \frac{\partial w}{\partial x} \, \mathrm{d}z \tag{4.15}$$

$$\int_0^\infty \omega_x \, \mathrm{d}z = \int_0^\infty \frac{\partial w}{\partial y} \, \mathrm{d}z \tag{4.16}$$

These equations may be viewed as constraints on the evolution of the primary variables ω_x and ω_y, respectively, and each constraint may be associated with one of the vorticity transport equations (4.5)-(4.6) to provide a way of satisfying the no-slip conditions (4.12)-(4.13). This ensures that the problem remains well-posed even though non-parallel and non-linear terms are neglected from the vorticity transport equations.

The inflow boundary conditions take the form of undisturbed flow so that the perturbations at x=0 are null. The computational domains in this thesis are sufficiently large so that flow perturbations at the downstream boundary are negligible and can therefore also be treated as null.

In Davies and Carpenter (1999) the system (4.5)-(4.7) is shown to be fully equivalent to the Navier-Stokes equations provided that fairly weak conditions are satisfied as $z \rightarrow \infty$ (u=v=0, as mentioned earlier). These conditions pose no practical difficulty for the present application and explicit enforcement can be circumvented by making a judicious choice of co-ordinate mapping in the z direction.

4.2 Numerical Scheme

A full description of the numerical method for an application in cylindrical co-ordinates is given in Davies and Carpenter (1999). The details of the present numerical scheme are similar, and are summarised in this section.

4.2.1 Spatial Discretisation

A hybrid spectral and finite-difference scheme has been employed to discretise the governing equations; streamwise variations are discretised using a second-order centred-difference scheme; spanwise variations are discretised using Fourier expansions; and wall-normal variations are discretised using Chebyshev polynomials.

The wall-normal domain is semi-infinite with the solid boundary and actuator surface at $z = 0$. A co-ordinate transformation of the form

$$\zeta = \frac{L}{z + L} \tag{4.17}$$

is used to map the semi-infinite physical domain $z \in [0, \infty)$ on to the finite computational domain $\zeta \in (0, 1]$ (the parameter L is a stretching factor). The vorticity transport equations (4.5)-(4.6) and the Poisson equation (4.7) are integrated twice with respect to the mapped variable ζ. This removes the z-derivative operators and replaces them with ζ-integral operators. The resulting equations are pentadiagonal in form which facilitates the use of efficient line iteration schemes, and hence, spectral accuracy is achieved without a computational penalty.

4.2.2 Temporal Discretisation

The convective terms (N) in the transport equations (4.5)-(4.6) are calculated explicitly using a predictor-corrector scheme. This uses an Adams-Bashforth

time stepping for the predictor stage and a Crank-Nicolson time stepping for the corrector stage. In order to calculate the convective terms the secondary variables must be evaluated, and therefore some wall-normal integration of the primary variables performed (see equations (4.9)-(4.11) for secondary variable definitions). This integration of the Chebyshev polynomials produces a tri-diagonal set of equations which can be solved using the highly efficient Thomas algorithm.

To calculate the product terms in equation (4.8), an FFT is used to convert the primary perturbations into the spatial domain. Here the multiplication with the mean flow can be performed efficiently, and then the FFT can be re-applied to convert the product back to the spectral domain.

The wall-normal viscous components in the transport equations ($\partial^2\omega/\partial z^2$) are solved implicitly, whereas the spanwise and streamwise viscous terms are treated explicitly.

The updated velocity field is calculated in between the predictor and corrector stage by the solution of the Poisson equation (4.7). The viscous terms of the Poisson equation are all solved implicitly with values of vorticity from the predictor stage being used to calculate the velocity field at the new time step. The streamwise viscous component ($\partial^2 w/\partial x^2$) is evaluated by iterative solution.

4.2.3 Interactive Simulations

A major interest of the research is to investigate the interaction between the boundary layer and the MEMS device. Interactive calculations can be performed by coupling the boundary-layer code with the actuator code. This coupling is achieved by enforcing continuity of pressure and velocity at the boundary-layer and actuator interface. The actuator code is introduced as a velocity boundary condition within the Poisson equation, and the pressure distribution over the actuator is calculated by integrating the linearised z-momentum component of the Navier-Stokes equations (see Davies and Carpenter 1999, p 17). As the

Poisson equation is solved iteratively, a mechanism for the convergence of a pressure/velocity coupling is already in place. However, slightly more iterations are required than when non-interactive prescribed velocities are used.

4.2.4 Parallelisation

The spanwise variations are discretised using a series of Fourier modes which, in linear calculations such as these, can be decoupled and calculated separately. This enables a highly efficient parallelisation scheme to be implemented relatively simply. When non-interactive calculations are performed the modes (or groups of modes) can be ascribed to individual processors and run completely independently. The modes only need to be combined when an output is required. When interactive simulations are performed, however, the individual modes need to be combined in order to calculate the pressure distribution over the actuator. Fortunately, the FFT required to convert the Fourier modes into physical space, need only be performed over the small area of the complete domain that the actuator occupies.

4.3 Code Validation

In this section the integrity of the numerical boundary-layer code is tested. In order to do this, simulations have been performed and compared against equivalent results from linear stability theory (values obtained from Fasel *et al.* 1990) and Klebanoff's transitional boundary-layer investigations (data obtained from Bertolotti 1997). For all the results in this section a Blasius velocity profile has been used (see §5.1 for details).

4.3.1 Linear Stability Theory

For a given Reynolds number and forcing frequency, the form of disturbance propagating from an oscillatory point force (Tollmien-Schlichting wave) can be determined via solution of the Orr-Sommerfeld equations (also known as linear stability theory). Such solutions can be used to test the current boundary-layer code.

For these numerical simulations an oscillating jet actuator has been prescribed at the wall to excite a single spanwise Fourier mode. This forcing produces a Tollmien-Schlichting wave train emanating downstream from the actuator. Figure 4.2 shows contours at y=0 of the three components of velocity perturbation after several periods of the actuator's cycle (the computational domain extends further than that shown).

The streamwise wave number of the generated wave train can be compared to that predicted by linear stability theory. Figure 4.3 shows a comparison for two-dimensional and three-dimensional Tollmien-Schlichting waves at varying Reynolds numbers (simulation parameters §A.2.2). The streamwise wavelengths obtained in the numerical simulations are in all cases within 0.5% of the values predicted by linear stability theory.

The velocity profiles of the three velocity components are also used to compare simulation with theory. Figure 4.4 shows a very close agreement for each of the

velocity components (simulation parameters §A.2.1). In Figure 4.4 maximum magnitudes over a streamwise wavelength have been gathered at each normal position in order to compensate for the phase shifting in the wave train.

4.3.2 The Klebanoff Mode

The Klebanoff mode is associated with the streaks observed in a transitional boundary layer. The streaks are discernible owing to the spanwise modulation of streamwise velocity and these velocity variations are thought to be caused by low-frequency free-stream vortical disturbances to which the boundary layer responds in a large-scale motion. Although Klebanoff's work on the subject is mainly unpublished, the phenomenon has been investigated by many other researchers since (see for example Westin *et al.* 1994, Kendall 1985, Andersson *et al.* 1999, and Leib *et al.* 1999).

The method by which excitation of the Klebanoff mode has been numerically replicated was inspired by the work of Meitz (1996). In this reference a free-stream spanwise body force was used to generate streamwise vorticity, and as a result, streamwise velocity streaks. A similar method is employed here; however, the forcing function differs slightly.

Implementing the Body Force

The spanwise body force can be introduced directly into the Navier-Stokes momentum equations. To include them in the vorticity transport equations, the curl of the forcing components is taken. In the case of solely spanwise forcing this is relatively simple and leaves the transport equations as follows:

$$\frac{\partial \omega_x}{\partial t} + \frac{\partial N_z}{\partial y} - \frac{\partial N_y}{\partial z} = \frac{1}{R}\nabla^2 \omega_x - \frac{\partial F_y}{\partial z} \tag{4.18}$$

$$\frac{\partial \omega_y}{\partial t} + \frac{\partial N_x}{\partial z} - \frac{\partial N_z}{\partial x} = \frac{1}{R}\nabla^2 \omega_y \tag{4.19}$$

$$\frac{\partial \omega_z}{\partial t} + \frac{\partial N_y}{\partial x} - \frac{\partial N_x}{\partial y} = \frac{1}{R}\nabla^2 \omega_z + \frac{\partial F_y}{\partial x} \tag{4.20}$$

where $\mathbf{N} = \bar{\mathbf{\Omega}} \times \mathbf{u} + \boldsymbol{\omega} \times \bar{\mathbf{U}} + \boldsymbol{\omega} \times \mathbf{u}$. In the current formulation, equation (4.20) is not calculated directly, which leaves one component of the body force seemingly unaccounted for. This is not the case and it can be shown that the augmented wall-normal transport equation (4.20) can be derived explicitly from the *primary* transport equations (4.18)-(4.19). Firstly, equations (4.18) and (4.19) are differentiated with respect to x and y respectively and then summed together:

$$\frac{\partial}{\partial t}\left(\frac{\partial \omega_x}{\partial x} + \frac{\partial \omega_y}{\partial y}\right) + \frac{\partial^2 N_x}{\partial y \partial z} - \frac{\partial^2 N_y}{\partial x \partial z} = \frac{1}{R}\nabla^2\left(\frac{\partial \omega_x}{\partial x} + \frac{\partial \omega_y}{\partial y}\right) - \frac{\partial^2 F_y}{\partial x \partial z} \tag{4.21}$$

The solenoidal property of the vorticity pertubation field requires that

$$\frac{\partial \omega_x}{\partial x} + \frac{\partial \omega_y}{\partial y} = -\frac{\partial \omega_z}{\partial z} \tag{4.22}$$

which when substituted into equation (4.21) gives

$$\frac{\partial^2 \omega_z}{\partial t \partial z} - \frac{\partial^2 N_x}{\partial y \partial z} + \frac{\partial^2 N_y}{\partial x \partial z} = \frac{1}{R}\nabla^2 \frac{\partial \omega_z}{\partial z} + \frac{\partial^2 F_y}{\partial x \partial z} \tag{4.23}$$

After integration with respect to z the wall-normal vorticity transport is obtained with the additional body force component:

$$\frac{\partial \omega_z}{\partial t} + \frac{\partial N_y}{\partial x} - \frac{\partial N_x}{\partial y} = \frac{1}{R}\nabla^2 \omega_z + \frac{\partial F_y}{\partial x} \tag{4.24}$$

The Body Forcing Function

In these simulations the body force is continuous and hence only spatial variation is described by the forcing function. The forcing chosen produces a spanwise array

of counter rotating streamwise vortices that are terminated by spanwise vortices downstream and upstream of the disturbance. This type of forcing produces cleaner streaks than a single-point body force which would create counter-rotating vortices in the streamwise and wall-normal directions. The function is in the form

$$F_y = \int G \exp\{-a\,(x - x_f)^2 + i\beta y - b\,(z - z_f)^2\}\,dz \tag{4.25}$$

where G is the magnitude, x_f is the streamwise position of the body force, z_f is the normal position of the body force, β is the spanwise wave number, and a and b determine the sharpness of the numerically-approximated streamwise and wall-normal delta functions, respectively. A body forcing in the form of equation (4.25) results in a delta-type streamwise vorticity production:

$$\frac{\partial F_y}{\partial z} = G \exp\{-a\,(x - x_f)^2 + i\beta y - b\,(z - z_f)^2\} \tag{4.26}$$

Streak Generation

Simulations have been performed with body forces as described by equation (4.25). Some time after the application of the time-invariant force the perturbations reach a steady-state; Figure 4.5 shows a typical streamwise-velocity streak that is generated (simulation parameters A.2.3).

In experiments a dominant spanwise vortical mode is observed, and for the Blasius boundary layer this is the Klebanoff mode. A series of simulations have been performed to calculate the dominant mode in the numerical boundary layer. This is assumed to be the spanwise forcing that generates streaks most receptively (simulation parameters A.2.4). Figure 4.6 shows the results of the simulations; they identify a dominant spanwise wave number (β) that is very close to the spanwise mode observed by Klebanoff (value reported in Herbert and Lin 1993 and Bertolotti 1997).

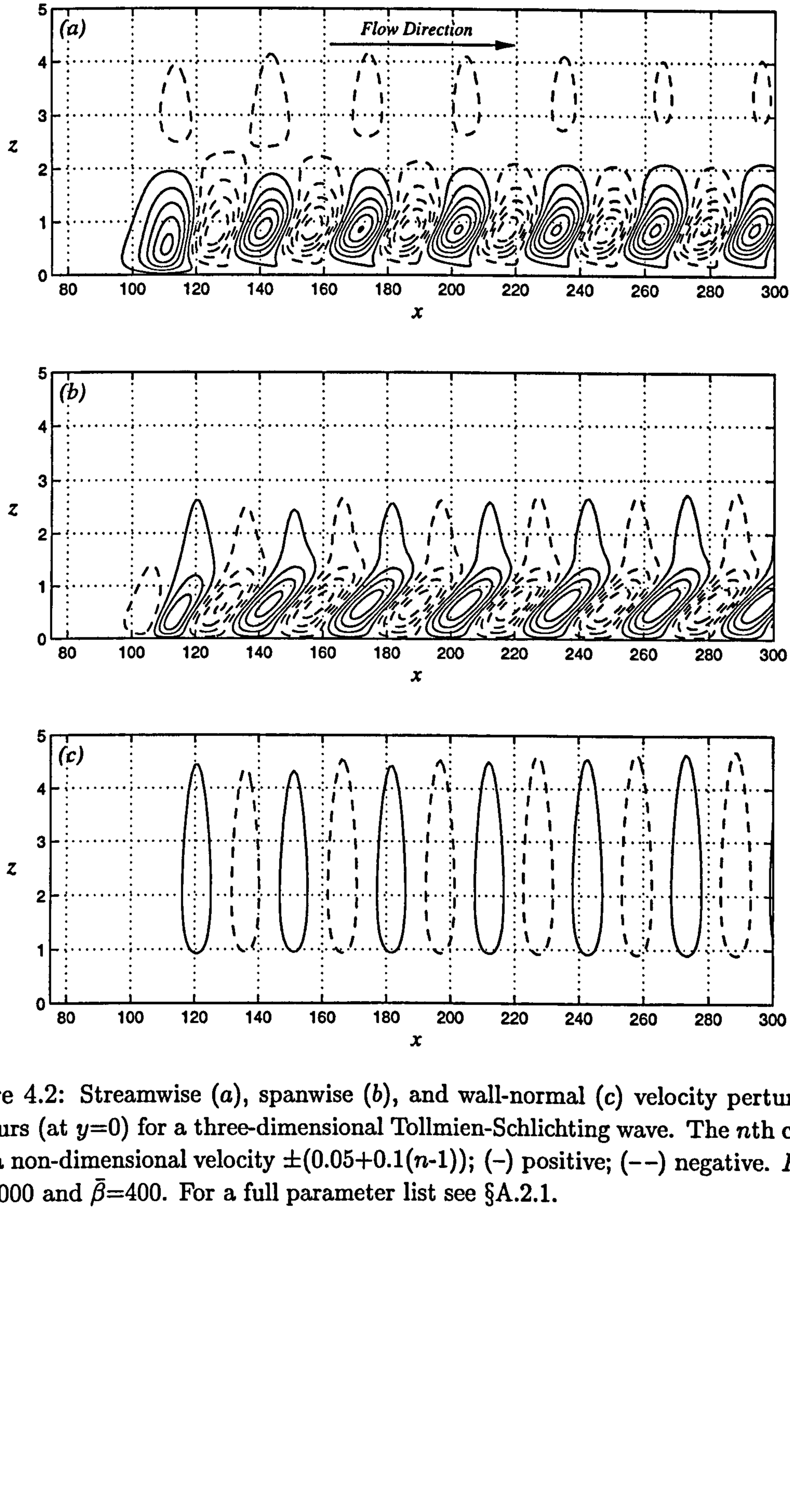

Figure 4.2: Streamwise (a), spanwise (b), and wall-normal (c) velocity perturbation contours (at y=0) for a three-dimensional Tollmien-Schlichting wave. The nth contour is at a non-dimensional velocity $\pm(0.05+0.1(n\text{-}1))$; (–) positive; (– –) negative. R=770, $\bar{\omega}_f$=6000 and $\bar{\beta}$=400. For a full parameter list see §A.2.1.

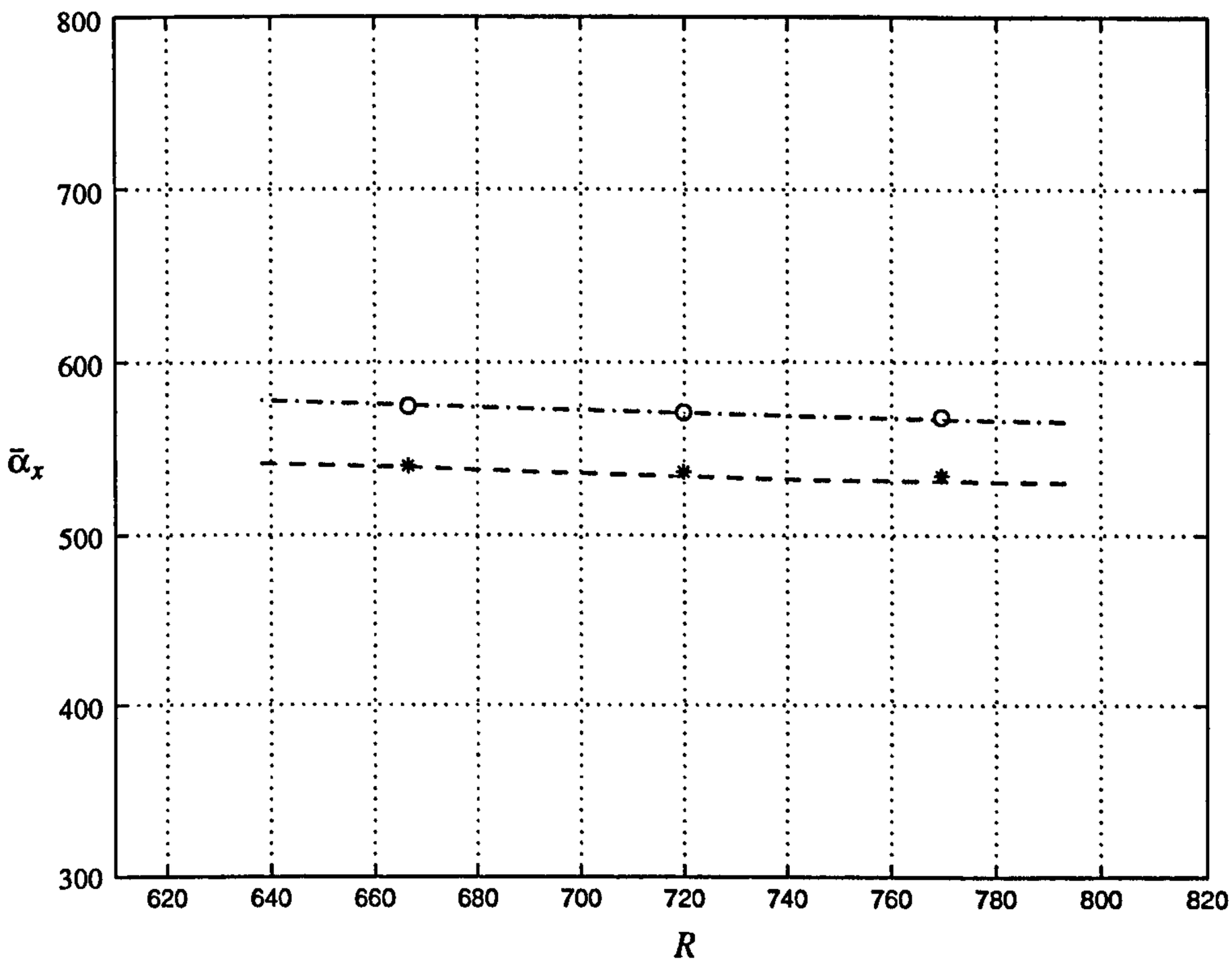

Figure 4.3: Streamwise wave number, $\bar{\alpha}_x$, of a Tollmien-Schlichting wave train for varying Reynolds numbers, R. Spanwise wave number $\bar{\beta}$=0 (-·-, o), $\bar{\beta}$=400 (--,*); linear stability theory (-·- , --); numerical simulations (o, *). $\bar{\omega}_f$=6000. For a full parameter list see §A.2.2.

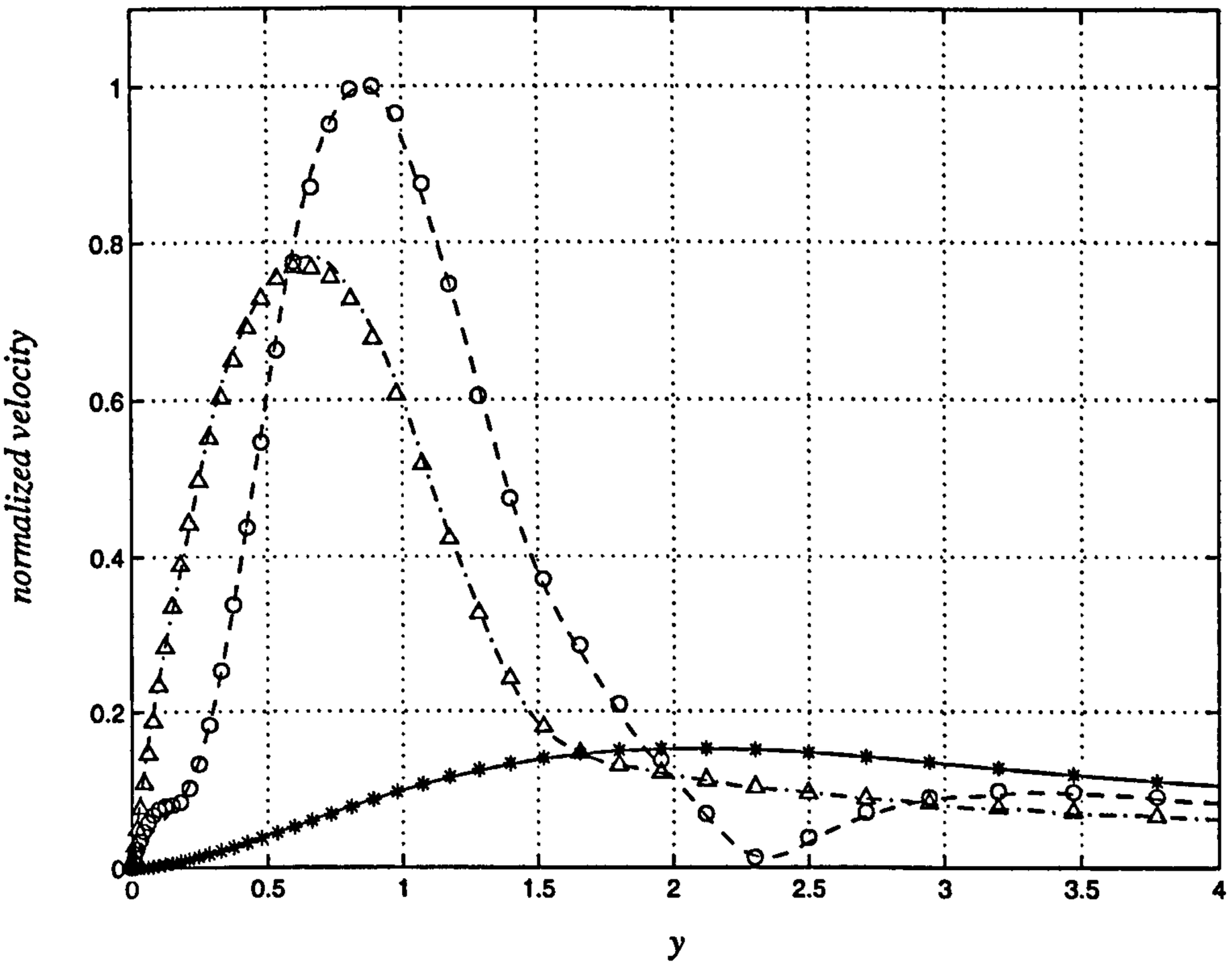

Figure 4.4: Streamwise (−−, ∘), spanwise (−·−, △) and normal (−, ∗) velocity perturbation profiles for a three-dimensional Tollmien-Schlichting wave train; linear stability theory (−−, −·−, −); numerical simulations (∘, △, ∗). All components have been normalised with maximum streamwise velocity. R=770, $\bar{\omega}$=6000, $\bar{\beta}$=400. For a full parameter list see §A.2.1.

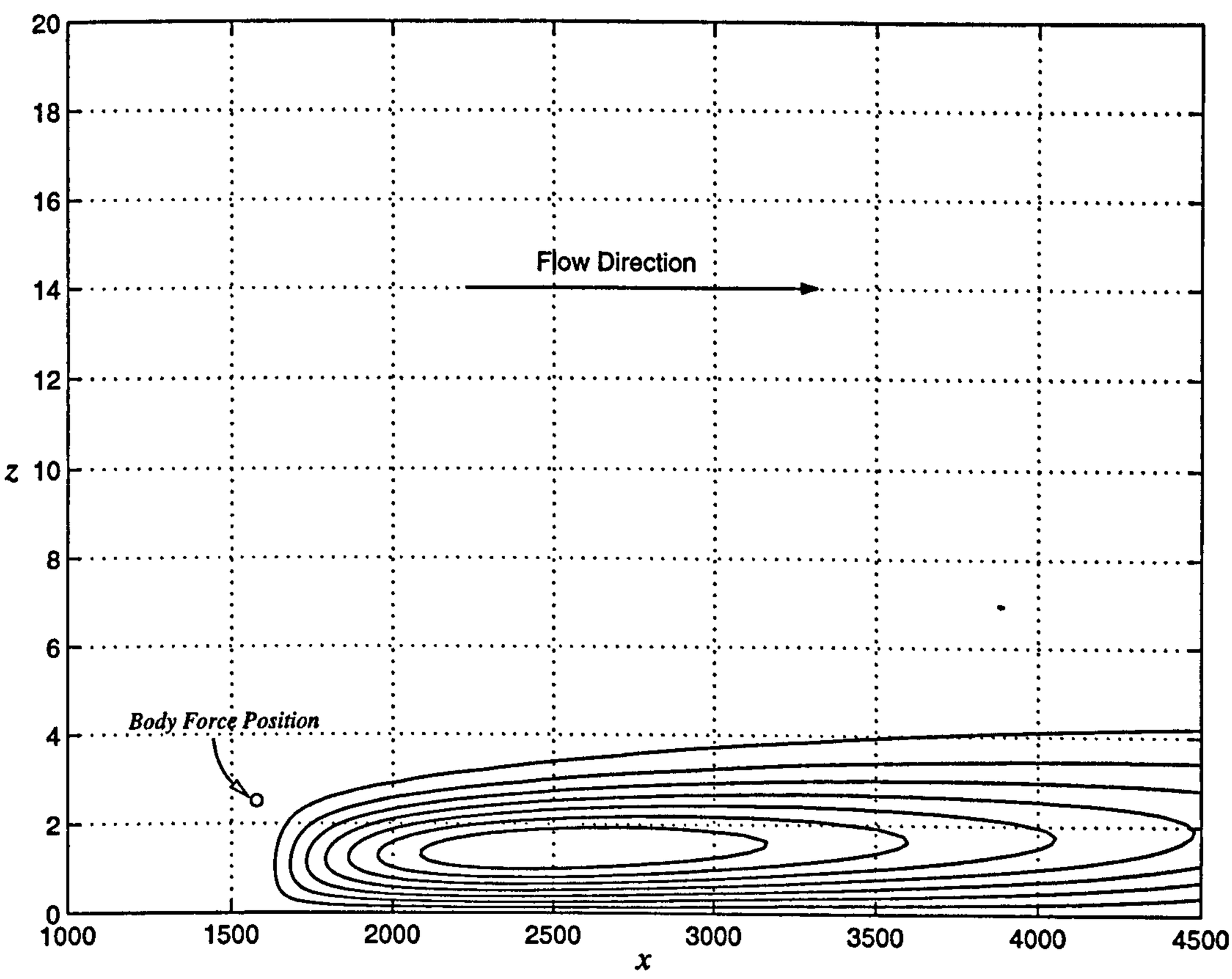

Figure 4.5: The steady-state streak generated by a body forcing function as described by equation (4.25). Contours of streamwise velocity; R=1720.7 and β=0.4. For a full parameter list see §A.2.3.

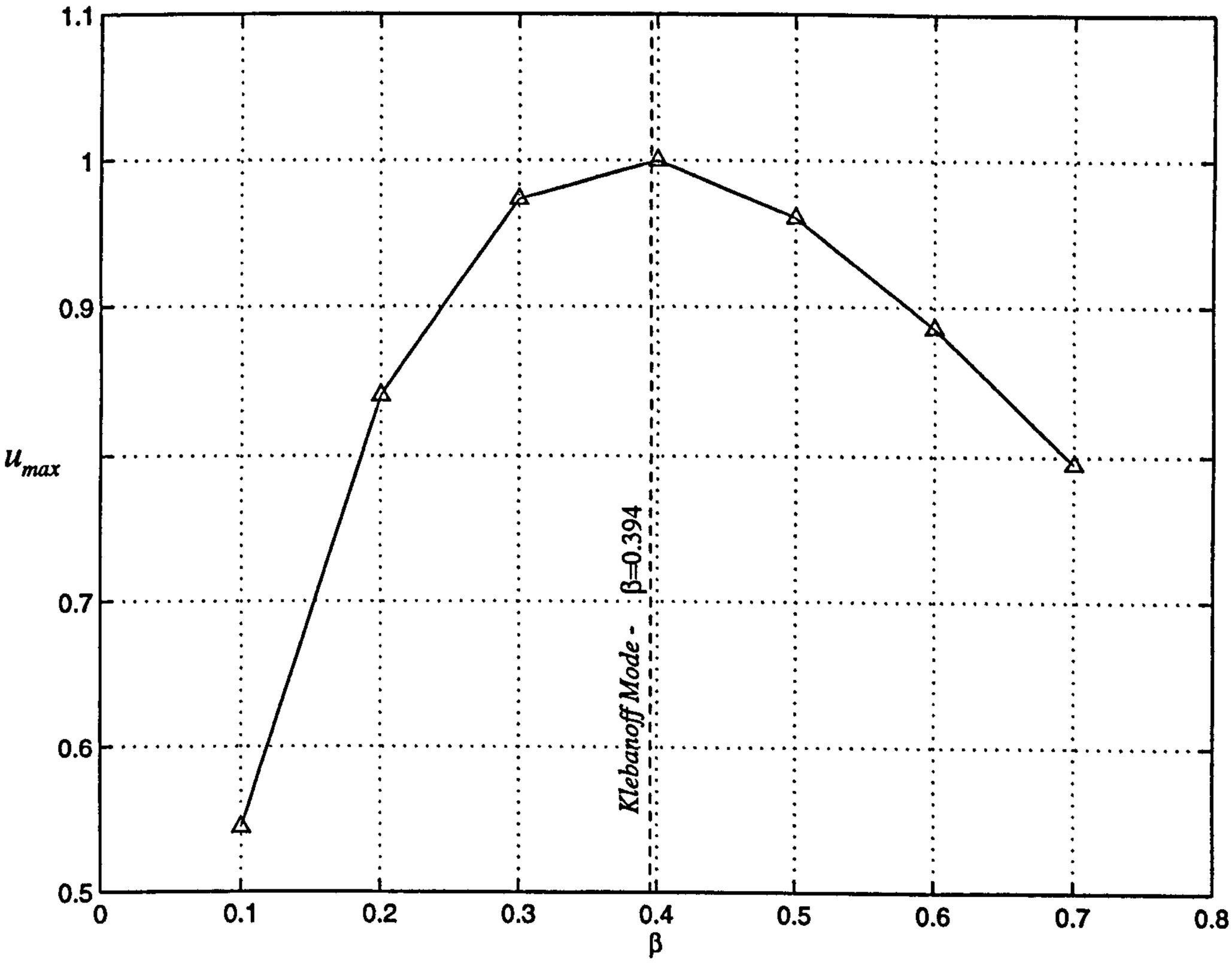

Figure 4.6: Maximum streak velocity (u_{max}) as a function of spanwise wavenumber (β). The vertical dashed line from the Klebanoff experiments as reported in Herbert and Lin (1993) and Bertolotti (1997); R=1720.7. For a full parameter list see §A.2.4.

4.4 Chapter Summary

In this chapter the method by which the Navier-Stokes equations have been numerically solved has been described. A velocity-vorticity formulation, pioneered by Davies and Carpenter (1997), has been adopted and details of the scheme are given in §4.1. This method is particularly suited to the MEMS application as it can deal with the interactive and elliptic nature of the flow problem, as well as allowing economical linearised simulations. The numerical implementation of this method is summarised in §4.2, and details of the parallelisation and the coupling of the MEMS code are also described. To test the integrity of the computer code, simulations have been compared to linear stability theory and experiment in §4.3 – very close agreement was found in both cases.

Chapter 5

Prescribed-Jet Simulations

In this chapter, boundary-layer simulations are performed that use prescribed velocity boundary-conditions as a simplified means of modelling the impact of a jet actuator. This allows cheaper computations and can help answer generalised questions about the MEMS disturbance.

In §5.2 the qualitative differences between MEMS- and micro-scale disturbances are investigated within a Blasius boundary layer. In §5.3 the investigation is continued, but with a turbulent mean-flow profile as an undisturbed flow solution. Then, in §5.4 the prescribed-jet simulations are used as a means of judging the performance of different jet designs. Lastly, §5.5 attempts to establish if MEMS can have a macro-scale impact.

Results from the coupled boundary-layer and MEMS actuator code are shown in Chapter 6.

Nomenclature

Unless otherwise indicated, lengths and velocities have been non-dimensionalised using δ^* and U_∞, respectively. A superscript '+' denotes non-dimensionalisation

using the friction velocity, v^*, and the viscous length scale, ν/v^*.

$^-$ = an over bar denotes a dimensional quantity

A_j = area of orifice (m^2) or slot width (m) in 2D simulations

B = turbulent velocity-profile constant

f' = Blasius velocity profile

L = mapped domain stretching factor (non dim.)

N_c = number of Chebyshev polynomials

N_y = number of spanwise Fourier modes

r = radial distance from jet centre (m)

r_j = radius of jet or half slot width (m)

$R = U_\infty \delta^*/\nu$ = Reynolds number

$\bar{t}$ = time (s)

t_j = duration of jet (s)

$\bar{T} = T\ \delta^*/U_\infty = T^+\ \nu/v^{*2}$ = total simulation time (s)

u^+ = streamwise velocity of turbulent profile (non dim.)

U_∞ = free-stream velocity ($m\ s^{-1}$)

v^* = friction velocity ($m\ s^{-1}$)

V = instantaneous jet velocity ($m\ s^{-1}$)

V_m = maximum jet-actuator velocity ($m\ s^{-1}$)

x, y, z = streamwise, spanwise, and wall-normal directions (non dim.)

X_d = streamwise domain length (non dim.)

X_b, X_e = streamwise position of actuator (non dim.)

Y_d = extent of spanwise domain (non dim.)

δ^* = boundary layer thickness (m)

$\bar{\Delta}t = \Delta t\ \delta^*/U_\infty = \Delta t^+\ \nu/v^{*2}$ = time step (s)

Δx = streamwise grid spacing (non dim.)

η = wall-normal coordinate for Blasius equation (non dim.)

ζ = mapped variable (non dim.)

κ = turbulent velocity-profile constant

ν = kinematic viscosity ($m^2\ s^{-1}$)

ρ = density ($kg\ m^{-3}$)

$\bar{\omega}_y = \omega_y U_\infty/\delta^* = \omega_y^+ v^{*2}/\nu$ = spanwise vorticity perturbation (s^{-1})

5.1 The Blasius Velocity Profile

As research into MEMS for boundary-layer control is still at a preliminary stage, this thesis firstly investigates the effect of MEMS-jet actuation on a *laminar* boundary layer. The undisturbed-flow solution that is used in the boundary-layer code can be chosen freely (see §4.1.1); for much of these calculations a Blasius velocity profile has been used.

In order to generate the velocity profile the Blasius equation is solved numerically:

$$f''' + f\,f'' = 0 \tag{5.2}$$

with the boundary conditions $f(0)=f'(0)=0$ and $f(\infty)=1$. (equation 5.2 is with respect to the Blasius coordinate η, this can be transformed into the z domain using a simple factorisation). Figure 5.1 shows plots of the Blasius velocity profile (against z) and its first two z-derivatives.

5.2 MEMS- and Micro-Scale Comparison

Describing the scale of a device is not straightforward, as characteristic lengths can be chosen arbitrarily and clear definitions of scales, such as 'MEMS' and 'micro', are somewhat illusive. Gad-el-Hak (1999, p 6, fig.1) defines MEMS-scale devices to be in the range of 10^{-6} m to 10^{-4} m, compared to typical man-made devices 10^{-2} m to 10^{2} m. The range in between these two is here defined as *micro* scale (10^{-4} to 10^{-2}). In this thesis the characteristic length scale of an actuator is chosen to be the orifice radius.

Rathnasingham and Breuer (1997b), Jacobson and Reynolds (1998), Crook *et al.* (1999) and Wood *et al.* (2000), have all demonstrated some form of boundary-layer manipulation using micro-scale jet actuators ($10^{-4}<R_o<10^{-2}$).

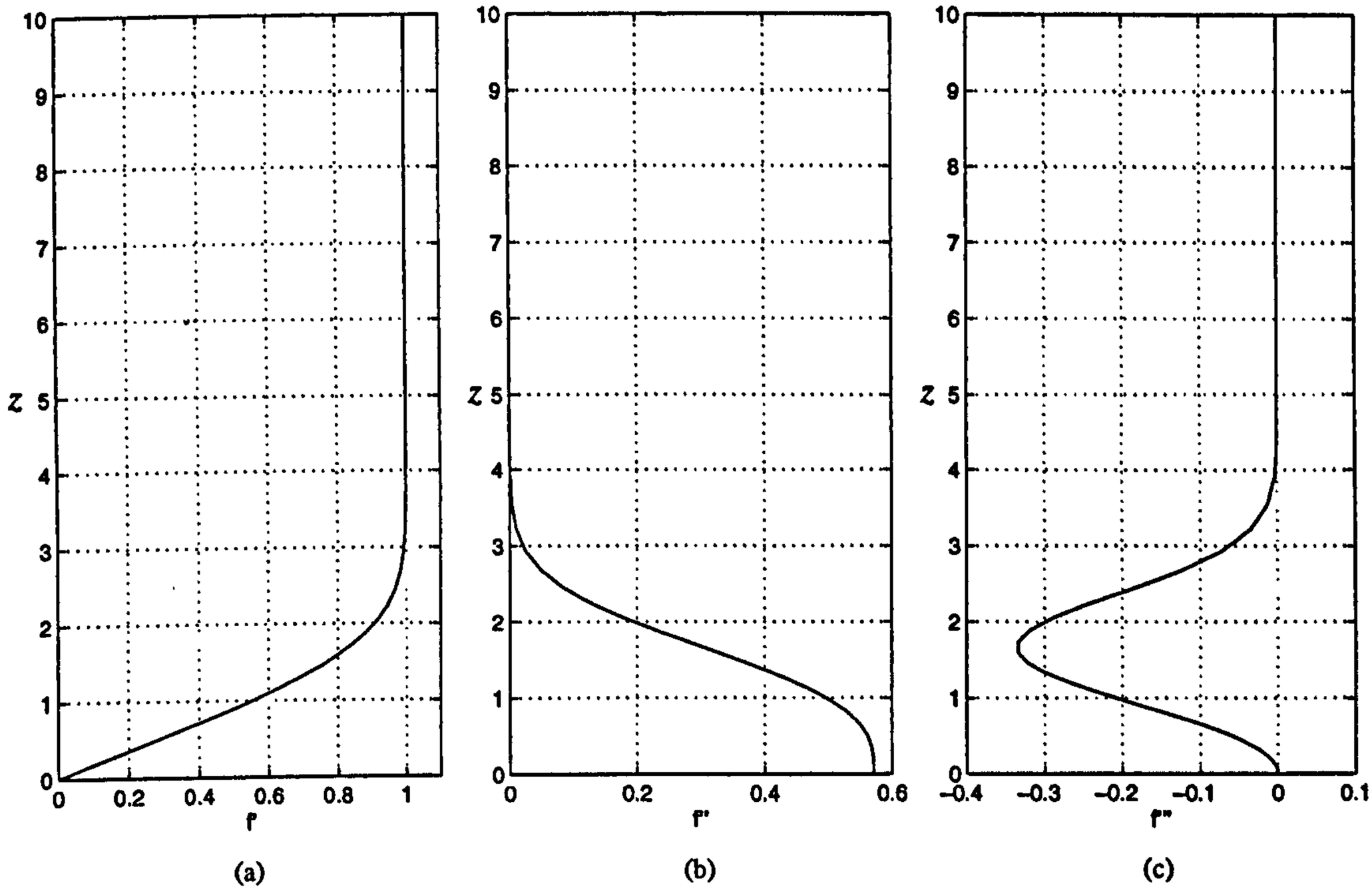

Figure 5.1: The mean-flow profile as generated from the Blasius equation (5.2). The velocity profile (a), and its first two derivatives with respect to z (b)-(c). The z-coordinate has been non-dimensionalised with δ^* and velocities non-dimensionalised with U_∞.

It is important, therefore, to establish when comparisons between these devices and MEMS can be made. The simulations of this section aim to investigate the scalability of Blasius boundary-layer disturbances caused by a jet actuator.

5.2.1 The Prescribed Jet

So that the scaled jet can be standardised, a prescribed actuation has been used. The chosen function resembles the jet responses from the pressure-jump actuators of Chapter 3, §3.4 (without Helmholtz oscillation). The temporal and spatial jet variations are described by:

$$V(r,\bar{t}) = V_m\,(1 - r^2/r_j^2)\,\sin\left(\frac{\bar{t}\pi}{t_j}\right) \tag{5.3}$$

where r is the radial distance from the jet centre, r_j is the radius of the jet, $\bar{t}$ is time, t_j is the duration of the jet actuation, and V_m is the maximum velocity of the jet. The shape of the velocity profile is parabolic at all times, and the variation of jet velocity with time is shown in Figure 5.2.

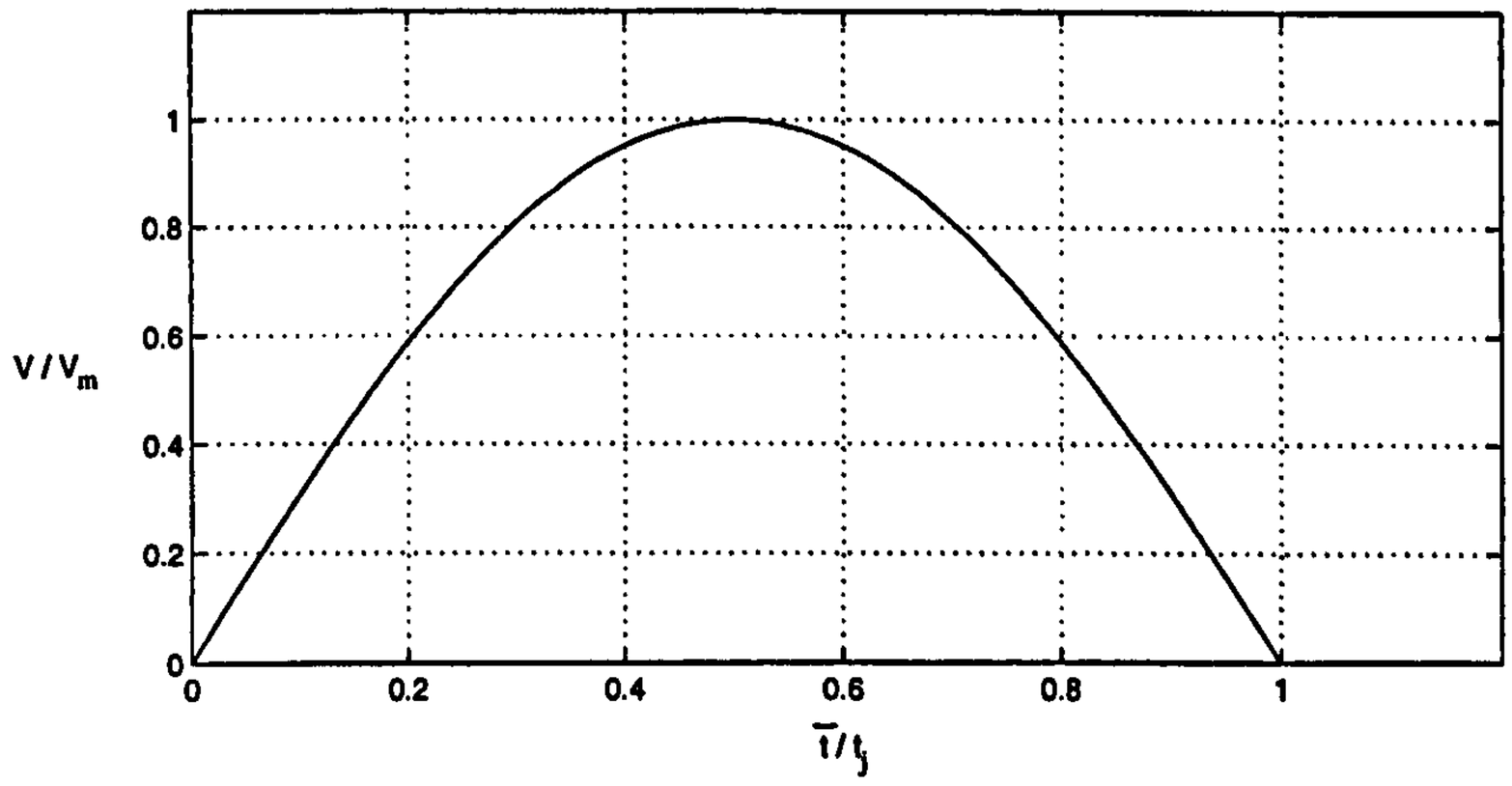

Figure 5.2: The variation of velocity (at r=0) with time for the prescribed jet.

5.2.2 Results

Figure 5.3 shows contour plots of spanwise vorticity perturbation generated within a Blasius boundary layer (R=2000, U_∞=30 m s^{-1}, δ^*=1 mm) from a three-dimensional jet as described by equation (5.3). The contour plots on the left-hand side of Figure 5.3 are for a MEMS-scale device at different times during its actuation period (r_j=8 μm, t_j=3.33 μs). The times (A)-(D) are referenced on a jet-history sketch at the bottom of the figure. The contour plots on the right-hand side of Figure 5.3 are for a micro-scale device (r_j=8 mm, t_j=3.33 ms) at times also referenced on the jet-history sketch. The time between successive contour plots, non-dimensionalised with respect to the jet duration, is the same for both the MEMS- and the micro-scale simulation.

The qualitative difference in the results is obvious, with little or no resemblance between the MEMS and micro disturbances. The MEMS disturbance

begins with a pair of counter-rotating vortices seemingly unaffected by the shear flow. This structure persists until the jet velocity decelerates, beginning the detachment of this vortex pair from the wall. When the jet has finished the original vortex pair is replaced by a pair with opposite polarity.

The micro-scale jet produces disturbances that are strikingly different at every stage. At time A (referenced on Figure 5.3) only negative vorticity is produced at the wall by the action of the jet. The positive vorticity that would have been present in a slower boundary layer has been absorbed by the negative vorticity that has swept downstream. The negative vorticity moves downstream and produces the start of a Tollmien-Schlichting wave packet.

Figure 5.4 shows a continuation of the simulations presented in Figure 5.3, with the calculations being extended to longer times. The results demonstrate further divergence between the MEMS and micro-scale disturbances. The MEMS-scale disturbance diffuses and is not greatly affected by the shear flow. This is because of the slow velocity of the Blasius profile near the wall and the short time scale of the MEMS simulation. On the other hand, the micro-scale disturbance continues to travel downstream and grow in magnitude at the head of the Tollmien-Schlichting wave packet. It would be expected, in accordance with the classic theoretical and experimental study of Gaster (1975) and Gaster and Grant (1975), that the MEMS-scale disturbance would also generate a Tollmien-Schlichting wave, eventually. This is considered further in §5.5.

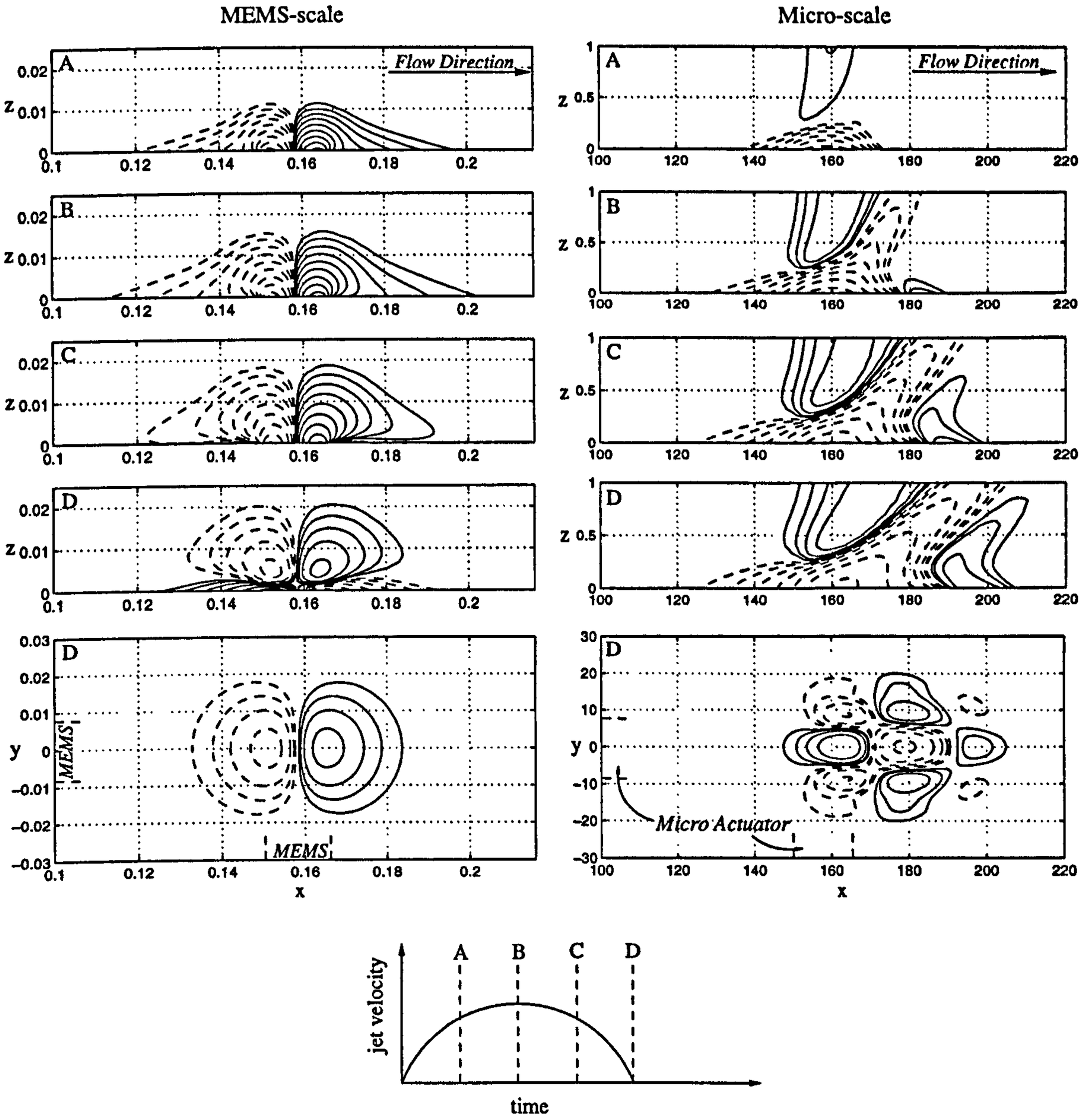

Figure 5.3: A comparison between the evolution of boundary-layer perturbations caused by a MEMS and a micro actuator. For the MEMS-scale simulations r_j=0.008δ^*, and for the micro-scale simulations, r_j=8δ^*. In both cases V_m=0.1U_∞ and t_j=12.5r_j/U_∞. The plots are of spanwise vorticity perturbation (ω_y) and the nth contour is at $\pm$ 0.2^{n-1} where the solid lines indicate positive values and the dashed lines indicate negative values. The labels (A)-(D) refer to the following non-dimensional times: $\bar{t}/t_j$=0.25 at A; $\bar{t}/t_j$=0.5 at B; $\bar{t}/t_j$=0.75 at C; and $\bar{t}/t_j$=1 at D. The plan-view contours at time D are at z=0.01δ^* for the MEMS-scale and at z=0.49δ^* for the micro-scale. R =2000; U_∞=30 m s^{-1}; δ^*=1 mm. For a full parameter list see §A.3.1.

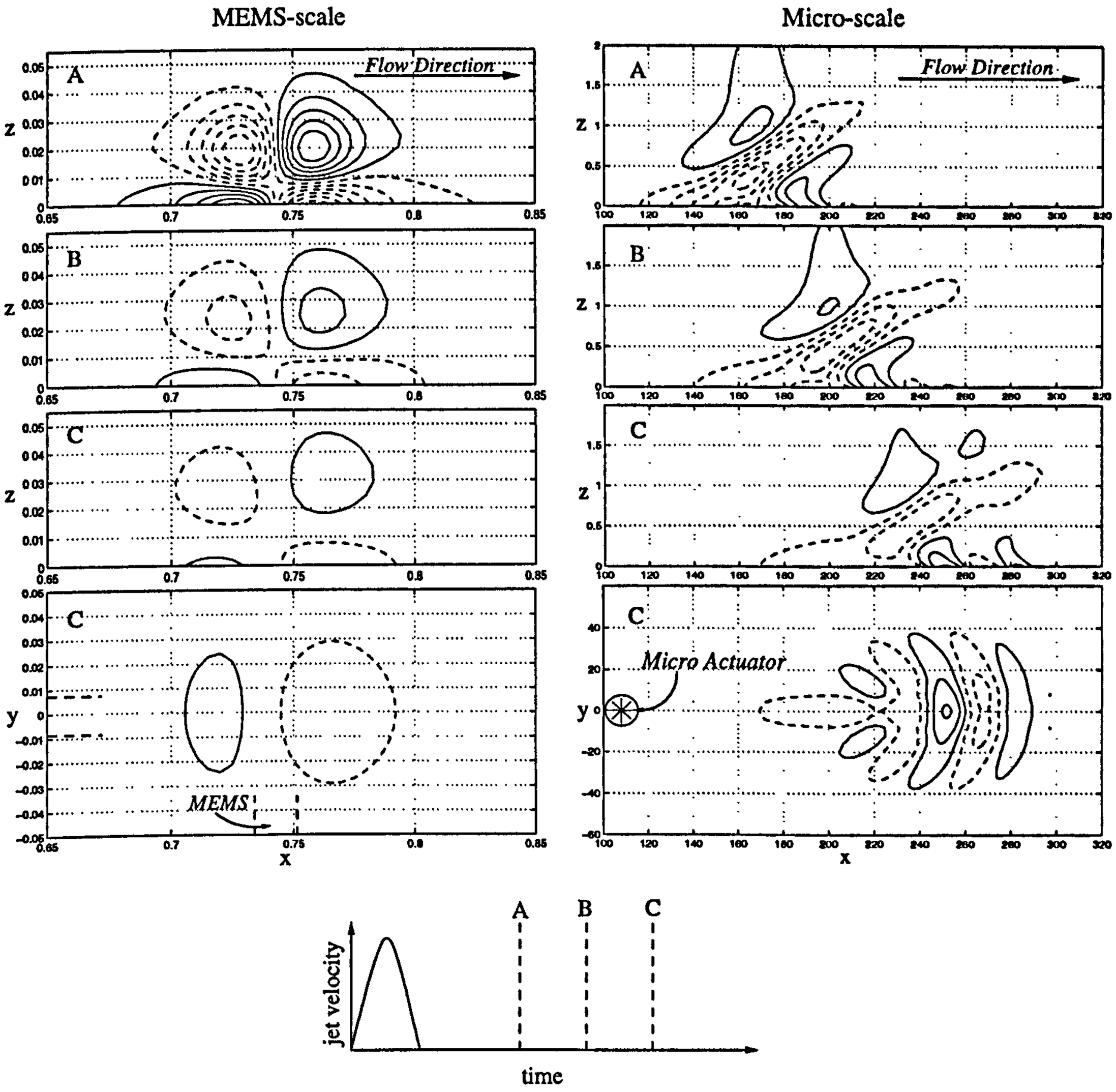

Figure 5.4: A comparison between the evolution of boundary-layer perturbations caused by a MEMS and a micro actuator. For the MEMS-scale simulations r_j=0.008δ^*, and for the micro-scale simulations r_j=8δ^*. In both cases V_m=0.1U_∞ and t_j=12.5r_j/U_∞. The plots are of spanwise vorticity perturbation (ω_y). For the micro-scale simulations the nth contour is at $\pm$ 0.5 + (n-1) and for the MEMS-scale the nth contour is at $\pm$ (2.5 + 5(n-1))$\times 10^{-3}$; the solid lines indicate positive values and the dashed lines indicate negative values. The labels (A)-(C) refer to the following non-dimensional times: $\bar{t}/t_j$=2.5 at A; $\bar{t}/t_j$=3.5 at B; and $\bar{t}/t_j$=4.5 at C. The plan-view contours at time C are at z=0 for both MEMS and micro scale. R =2000; U_∞=30 m s^{-1}; δ^*=1 mm. For a full parameter list see §A.3.2

5.2.3 Comparing Simulations of Different Scale

In §5.2.2, Figures 5.3 and 5.4 have clearly shown that a large-scale device cannot be directly compared to a smaller device within the same boundary layer. These results highlight the importance of knowing how to draw safe comparisons between simulations or experiments of different scales. This is particularly relevant to experimentalists who use large-scale models to investigate the impact of MEMS-scale devices on a boundary layer.

The non-dimensionalisation of the Navier-Stokes equations provides sufficient insight into the general applicability of any single simulation or experiment. Provided that the length and time scales of the jet are non-dimensionalised with boundary-layer characteristics (δ^*, U_∞, δ^*/U_∞) the results for a simulation or experiment are valid for any combination of δ^* and U_∞ that keep $R = \delta^* U_\infty/\nu$ invariant (where R is the Reynolds number for the simulation/experiment).

In the simulations of §5.2.2 the radius of the two jets were different proportions of the boundary-layer length scale (r_j=8δ^* and r_j=0.008δ^*) and were therefore not directly comparable. The following values need to be held constant if dynamic similarity is to be maintained:

$$R = \frac{\delta^* U_\infty}{\nu} = \text{Reynolds number} \tag{5.4}$$

$$\frac{r_j}{\delta^*} = \text{non-dimensional jet radius.} \tag{5.5}$$

$$\frac{t_j U_\infty}{\delta^*} = \text{non-dimensional jet duration.} \tag{5.6}$$

$$\frac{V_m}{U_\infty} = \text{non-dimensional jet velocity.} \tag{5.7}$$

(In linearised simulations, equation (5.7) does not act as a restriction on the general applicability of a solution). If these four non-dimensional parameters are held constant between simulations or experiments of different scales, then the results are fully equivalent. For an example, the MEMS-scale results in §5.2.2 can be related to a micro-scale simulation having the following parameters: The jet

- r_j=8 mm, t_j = 33.3 s, V_m=4 mm s^{-1}; The boundary layer - R=2000, U_∞=300 mm s^{-1}, δ^*=1m. This suggests that to model a MEMS-scale device using a micro-scale device, a particularly large boundary layer would be required.

To summarise, this means that any non-dimensional simulation is equivalent to an infinite number of dimensional simulations, but valid for only one relative jet radius, jet velocity, and jet duration with respect to the boundary-layer scales.

Although the method described in this section provides a good guide as to how safe comparisons should be performed, many more dimensionless parameters would need to be fixed if a non-prescribed actuation were considered.

5.3 The Turbulent Boundary Layer

So far in this thesis only the Blasius velocity profile has been used as an undisturbed-flow solution. In this section a turbulent velocity profile is introduced.

The eddies and random fluctuations that exist in turbulent flows cannot be modelled using a mean-flow profile. However, valuable information can be obtained regarding the qualitative behaviour of MEMS in the near-wall region of the boundary layer; here the turbulent non-deterministic nature of the boundary layer is less predominant. In fact, all the attention in this thesis is focused on the near-wall region, as it is generally believed that this is where the building blocks of turbulence reside.

5.3.1 The Semi-Empirical Velocity Profile

The inner regions of the turbulent boundary layer have been modelled using Spalding's law of the wall (Spalding 1961). Using this method the viscous, buffer, and log layers, can all be expressed with a single formula:

$$z^+ = u^+ + e^{-\kappa B}\left[e^{\kappa u^+} - 1 - \kappa u^+ - \frac{(\kappa u^+)^2}{2} - \frac{(\kappa u^+)^3}{6}\right] \tag{5.8}$$

where z^+ is the distance from the wall, u^+ is the streamwise velocity, and κ (=0.4) and B (=5.5) are near-universal constants for turbulent flow past smooth walls. The superscript '+' denotes non-dimensionalisation in terms of wall variables. Namely, friction velocity, v^*, and the viscous length scale (the wall unit), ν/v^*. The wall layers (or inner regions) of the velocity profile can be seen in Figure 5.5. This is where all the disturbances considered in this thesis are generated.

For completeness sake, the outer layer of the boundary layer is modelled using Coles' law of the wake (Coles 1956). The entire flow profile can be seen in the logarithmic plot of Figure 5.6; the boundary-layer thickness is approximately 1000 wall units.

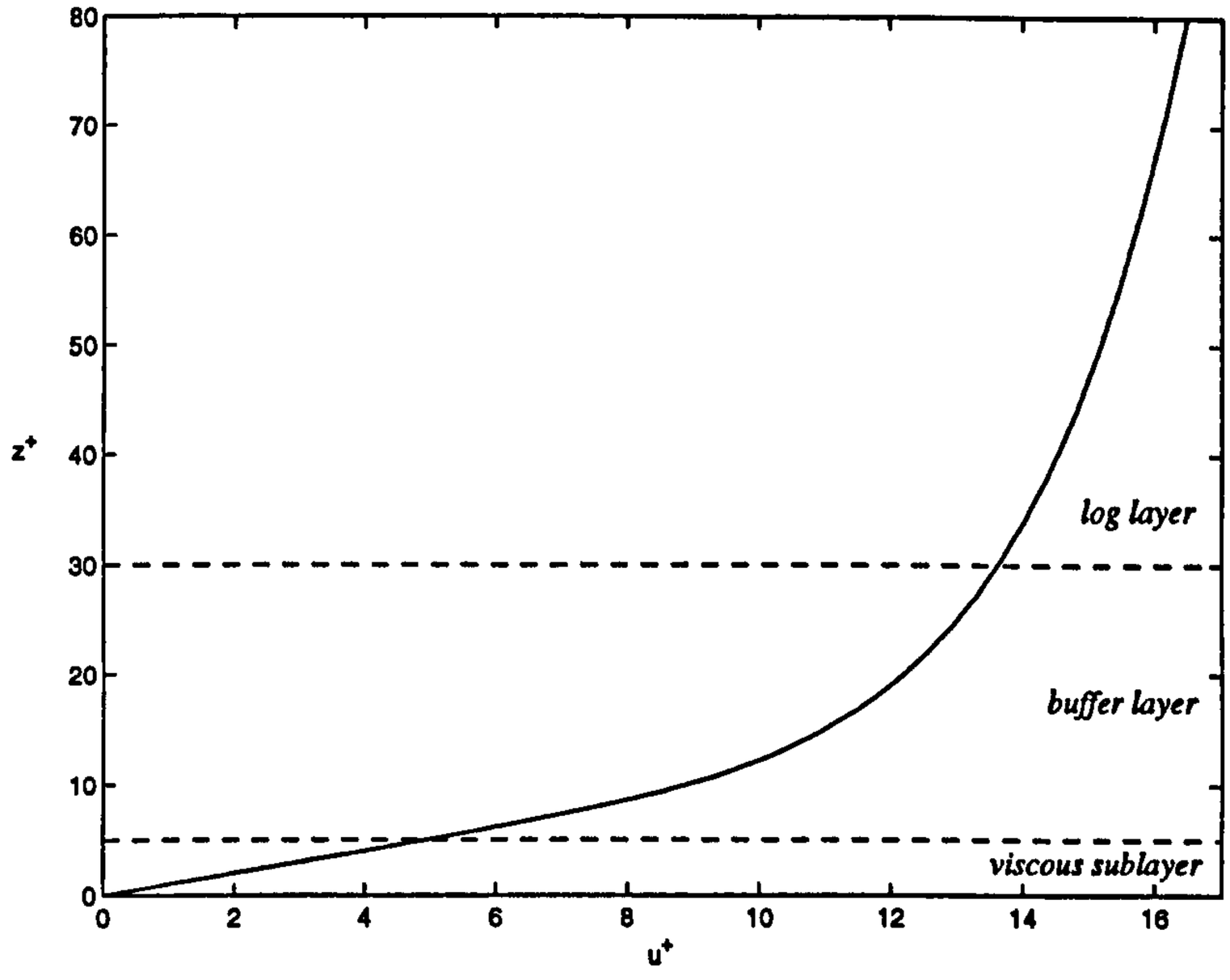

Figure 5.5: The wall layers of the turbulent velocity profile as described by Spalding's equation (5.8).

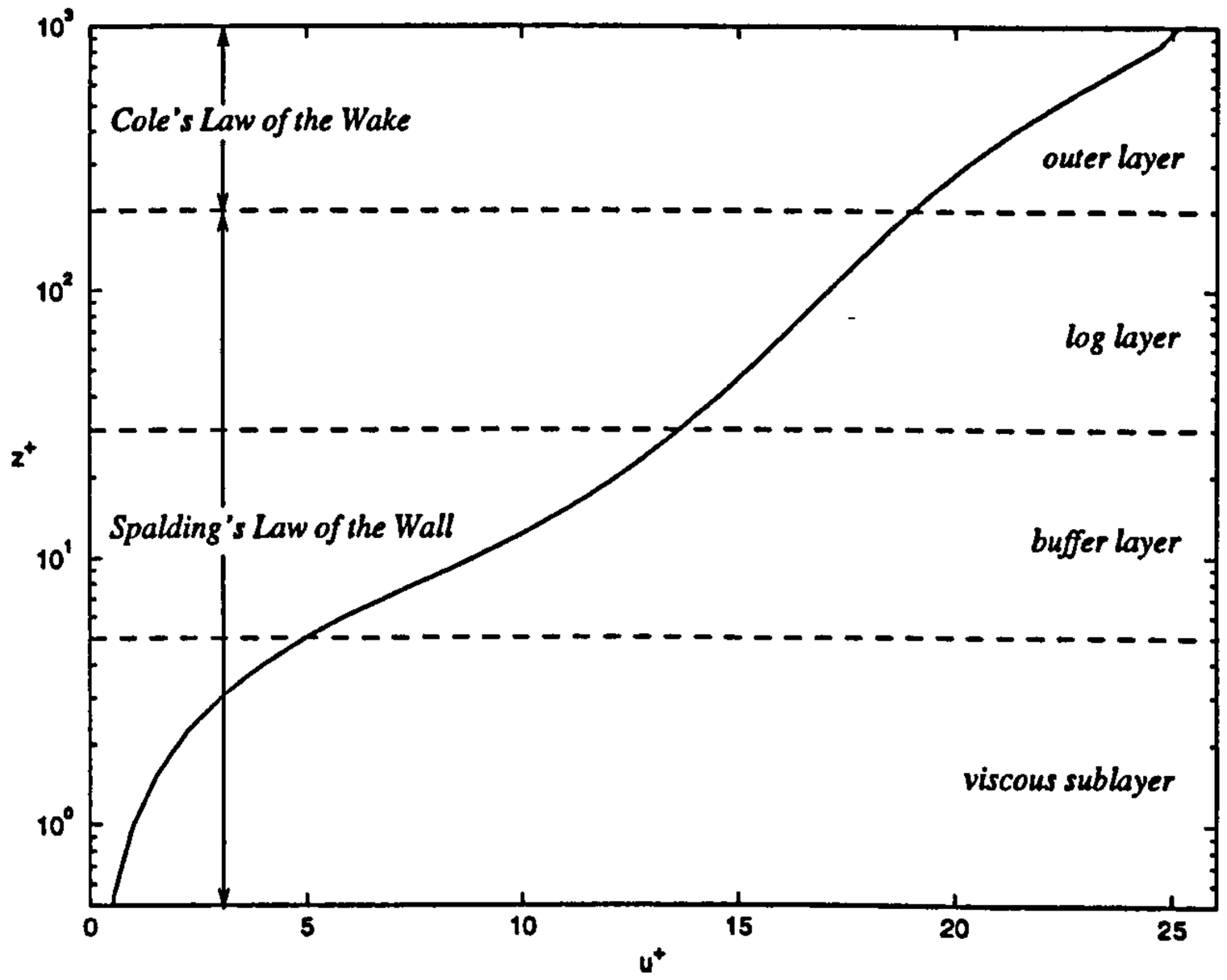

Figure 5.6: The entire turbulent velocity profile.

5.3.2 Results

In this section the same simulation as presented in Figure 5.3 (§5.2.2) is performed using the turbulent velocity profile as the undisturbed flow solution.

Figure 5.7 shows contour plots of spanwise vorticity perturbation generated within the turbulent boundary layer for MEMS- and micro-scale jet actuators (v^*=1.186 m s^{-1}). The dimensions and characteristics of the prescribed MEMS- and micro-scale jets are identical to those in Figure 5.3.

The results show that, as with the Blasius boundary layer, the MEMS and micro actuators produce significantly different disturbances. Also, it is shown that at MEMS scale the Blasius and turbulent simulations are quite similar. The reason for the differences in the micro-scale simulations is that, unlike the Blasius case, the turbulent boundary layer is not susceptible to Tollmien-Schlichting wave instabilities.

5.3.3 Scale Comparison

The results in Figure 5.3 have shown that drawing comparison between simulations of different scale can be as problematic for the turbulent boundary layer as it is for the Blasius boundary layer.

As in §5.2.3 a non-dimensionalisation method is used to ensure valid comparison between results of different scales. Here, friction velocities and the viscous length scale are used for non-dimensionalisation (rather than displacement thickness and free-stream velocity). Also, owing to interest only in the inner regions (see Figure 5.5), the Reynolds number based on outer variables (R=$\delta^* U_\infty/\nu$) does not need to be constant in order for simulations or experiments to be compared. The non-dimensional parameters to be held constant between equivalent simulations are as follows:

$$\frac{r_j v^*}{\nu} = \text{non-dimensional jet radius.} \tag{5.9}$$

$$\frac{t_j v^{*2}}{\nu} = \text{non-dimensional jet duration.} \tag{5.10}$$

$$\frac{V_m}{v*} = \text{non-dimensional jet velocity.} \tag{5.11}$$

(In linearised simulations, equation (5.11) does not act as a restriction on the general applicability of a solution). The dimensional parameters used in the simulations of Figure 5.7 can be altered so that the calculation is equivalent to one at flight-scale. If the results are dimensionalised using a flight-scale friction velocity ($v^*\approx$10 m s^{-1}) the micro-scale simulation in the slow boundary layer can be shown to be equivalent to a smaller, shorter, and faster jet at flight scale: v^*=10 m s^{-1}, r_j=950 μm, t_j=46.9 μs, and V_m=25.3 m s^{-1}.

Being able to draw a comparison in this way, between large-scale jets in slow boundary layers and small-scale jets in fast boundary layers, is particularly useful for experimentalists who find it more practical to use large-scale prototypes in low-speed turbulent wind tunnels. However, this method is only applicable when the disturbance is well within the wall layers of the turbulent profile (z^+<100).

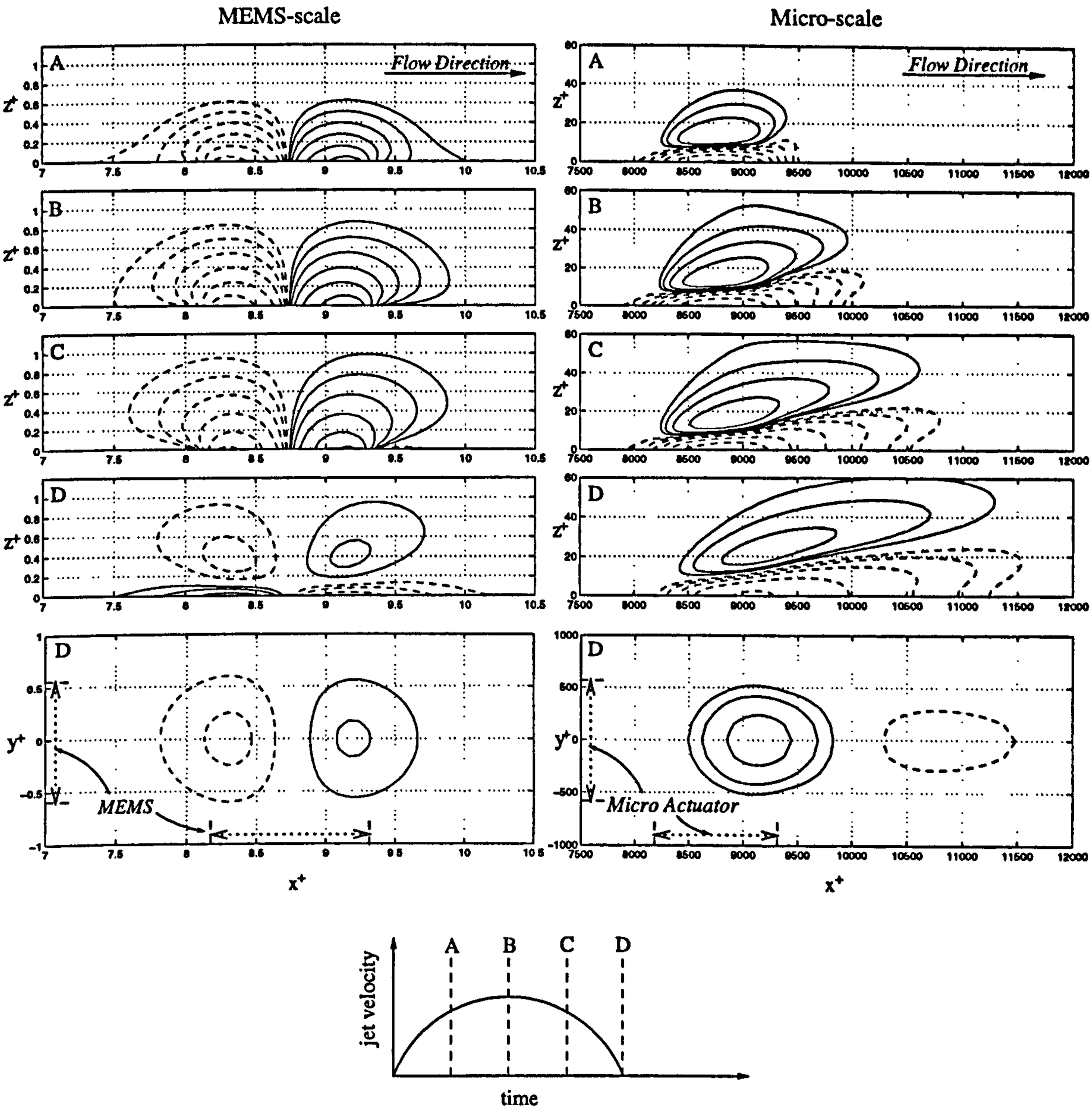

Figure 5.7: A comparison between the evolution of perturbations caused by a MEMS and a micro actuator in a turbulent boundary layer. The plots are of spanwise vorticity perturbation (ω_y^+), and the nth contour is at $\pm\ 0.248{\times}2^{n-1}$; the solid lines indicate positive values and the dashed lines indicate negative values. The labels (A)-(D) refer to the following non-dimensional times: $\bar{t}/t_j$=0.25 at A; $\bar{t}/t_j$=0.5 at B; $\bar{t}/t_j$=0.75 at C; and $\bar{t}/t_j$=1 at D. The plan-view contours at time D are at z^+=0.49 for the MEMS-scale and at z^+=21 for the micro-scale. v^*=1.186 m s^{-1}, U_∞=30 m s^{-1}, $\delta^* \approx$ 2.6 mm. For a full parameter list see §A.3.3

5.4 Optimal Jet Actuation

The jet that an actuator produces can be characterised by any number of quantities, such as maximum velocity, total momentum, or energy. It has not yet been established which such quality makes for efficient actuation in terms of the disturbance generated in the boundary layer. In Chapter 2 it has been implied that maximum velocity (V_m) is the most important jet characteristic. The results in the current section show that this is not necessarily the case. It will, however, be shown that the velocity optimisation in Chapter 2 is still relevant.

In this section different designs of jet are tested and their performance judged in terms of their ability to generate Tollmien-Schlichting wave instabilities in the Blasius boundary layer. Although the Blasius boundary layer is not the intended operating environment for the MEMS jet, it serves as a good starting point for evaluating jet-design guidelines.

5.4.1 Jet Characteristics

The prescribed jet (see equation 5.3) has been used so that different jet characteristics can be carefully controlled - these can be directly calculated from equation (5.3):

Instantaneous Quantities

$$V_m = \text{maximum velocity} \tag{5.12}$$

$$\rho A_j V_m = \text{maximum mass flow rate} \tag{5.13}$$

$$\rho A_j V_m^2 = \text{maximum impulse} \tag{5.14}$$

$$\rho A_j V_m^3 = \text{maximum power} \tag{5.15}$$

Net-Flow/Flux Quantities

$$\rho A_j V_m \int_0^{t_j} \sin\left(\frac{\bar{t}\pi}{t_j}\right) \mathrm{d}\bar{t} = \rho A_j V_m t_j/\pi = \text{net mass flow/flux} \tag{5.16}$$

$$\rho A_j V_m^2 \int_0^{t_j} \sin^2\left(\frac{\bar{t}\pi}{t_j}\right) \mathrm{d}\bar{t} = \rho A_j V_m^2 t_j/2 = \text{net momentum flux} \tag{5.17}$$

$$\frac{1}{2}\rho A_j V_m^3 \int_0^{t_j} \sin^3\left(\frac{\bar{t}\pi}{t_j}\right) \mathrm{d}\bar{t} = \rho A_j V_m^3 t_j 2/3\pi = \text{net kinetic-energy flux} \tag{5.18}$$

where A_j is the area of the jet (or the slot width in the two-dimensional case).

At first sight, all of these quantities seem reasonable goals for optimisation. However, here it is assumed that only one of these quantities is most appropriate as a performance criterion for characterizing overall actuator effectiveness - finding which one is the objective of this section.

5.4.2 Tollmien-Schlichting Wave Receptivity

As previously mentioned, the potential for the generation of Tollmien- Schlichting waves is used here to gauge the performance of the jet design. The receptivity mechanism for Tollmien-Schlichting waves is not directly applicable to the turbulence-control application. However, the method is still valid in general terms, since the jet is being rated on its ability to generate a disturbance in a boundary layer.

To measure this potential, the temporal evolution of total wall enstrophy has been calculated after the jet actuation has been completed. The level of enstrophy at which the Tollmien-Schlichting wave begins to grow is used to quantify performance. Figure 5.8 shows a typical evolution of total wall enstrophy for a prescribed actuation (see simulation parameters §A.3.4). These simulations are for a two-dimensional slot-type actuator; however, the principle and qualitative findings are transferable to the three-dimensional jet.

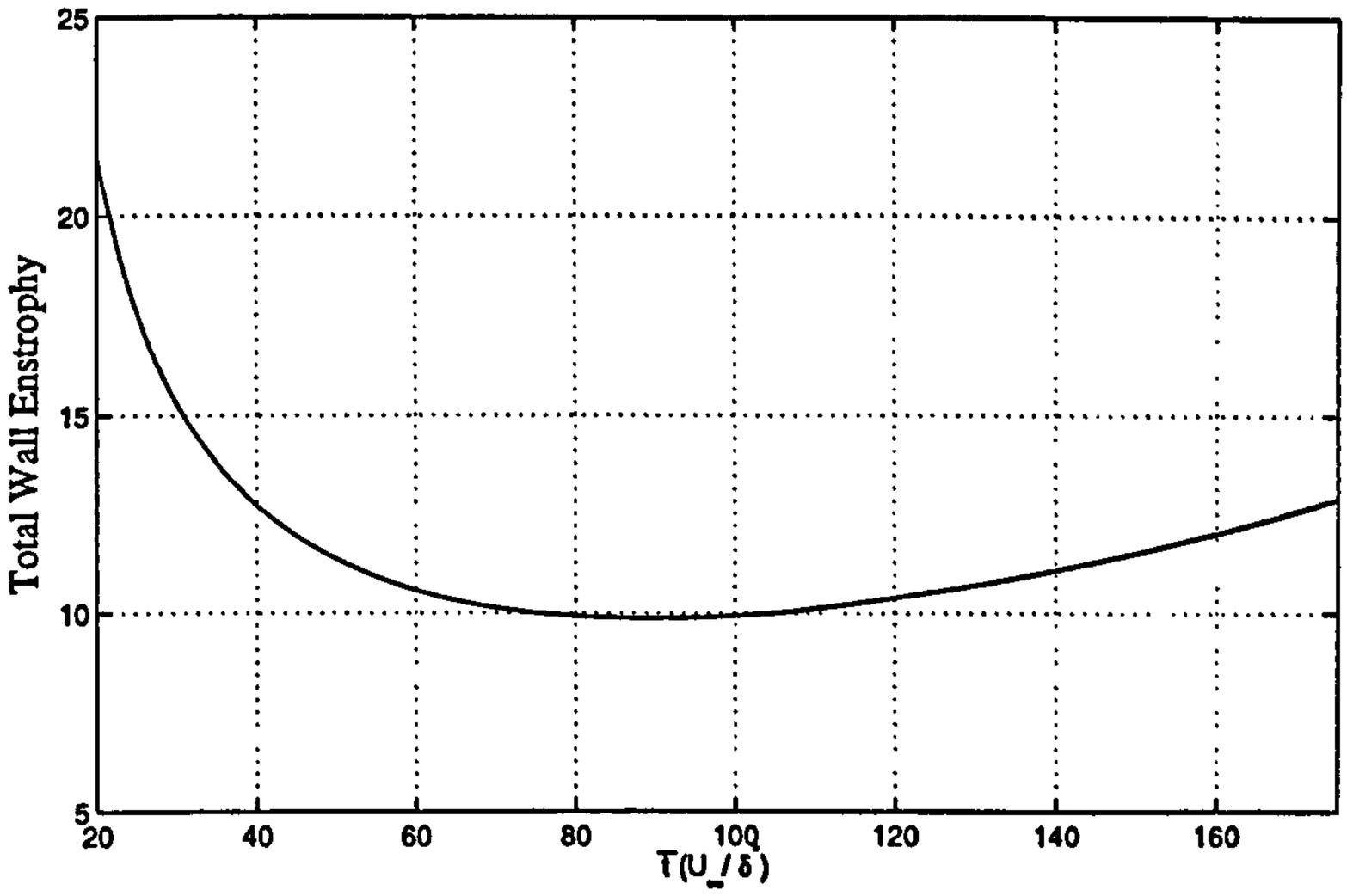

Figure 5.8: Evolution of total wall enstrophy resulting from a prescribed jet. R=2000; t_j=10 δ^*/U_∞; V_m=0.1 U_∞ ; A_j=10δ^*. See §A.3.4 for a full parameter list.

5.4.3 Results

It has been assumed that only one of the previously-identified quantities is an appropriate performance criterion. This allows a simple process of deduction to be applied. For example, if a comparison is made between two jets that have the same maximum impulse, and one of the jets produces a much stronger enstrophy evolution, it can be inferred that maximum impulse is not an appropriate performance criterion.

The results in Figure 5.8 are used as a control in the deduction process, with the velocity and duration of the jet (V_m, t_j) varied for comparison (the width of the slot, A_j, is held constant). The elimination starts with the instantaneous quantities (equations 5.12 to 5.15). Figure 5.9 shows the wall-enstrophy evolution for the control and the design variant. The maximum velocity of both jets are the same, and therefore all of the quantities described by equations (5.12)-(5.15) are held constant. What is apparent from the results is that, even though the instantaneous quantities are held constant, the disturbances in the boundary layer are significantly different. Hence, none of the instantaneous quantities would

make a good choice of performance criterion.

The deduction process now continues with the net-flow/flux quantities described in equations (5.16)-(5.18); these are the instantaneous quantities integrated over the actuation period. Figure 5.10 shows three different simulations against the control (–). In each of the three new simulations the velocity (V_m) and the jet duration (t_j) have been varied so as to keep one of the three net-flux quantities constant (mass, momentum, energy). The results indicate that only when net mass flow is held constant does the enstrophy growth remain relatively unaffected. It is therefore the net mass flow out of the actuator that is the key quantity in terms of efficient Tollmien-Schlichting wave generation, and the parameter that should be the focus of optimisation.

In Chapter 3 (§3.6) a velocity optimisation was performed for similar puff-type jet actuators. The results from that study are still relevant as they assumed a constant net mass flow (dictated by the diaphragm's deflection), and so can be thought of as a complementary, or a secondary, optimisation.

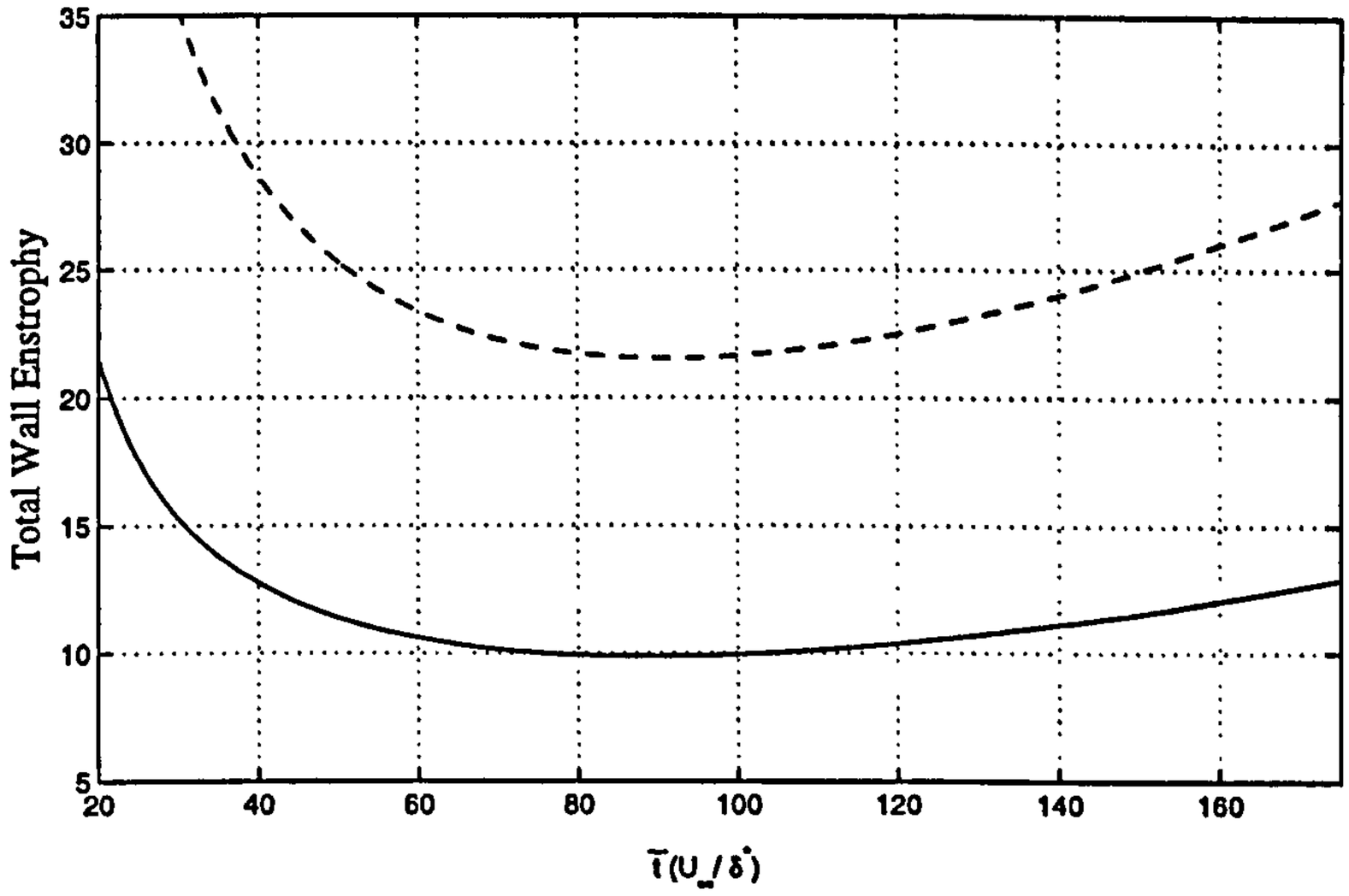

Figure 5.9: A comparison of the evolutions of total wall enstrophy resulting from prescribed jets of different design. For the control case (–) t_j=10 δ^*/U_∞ and V_m=0.1 U_∞. For the design variation (– –) t_j=15 δ^*/U_∞ and V_m=0.1 U_∞. In both simulations A_j=10δ^* and R=2000. See §A.3.5 for a full parameter list.

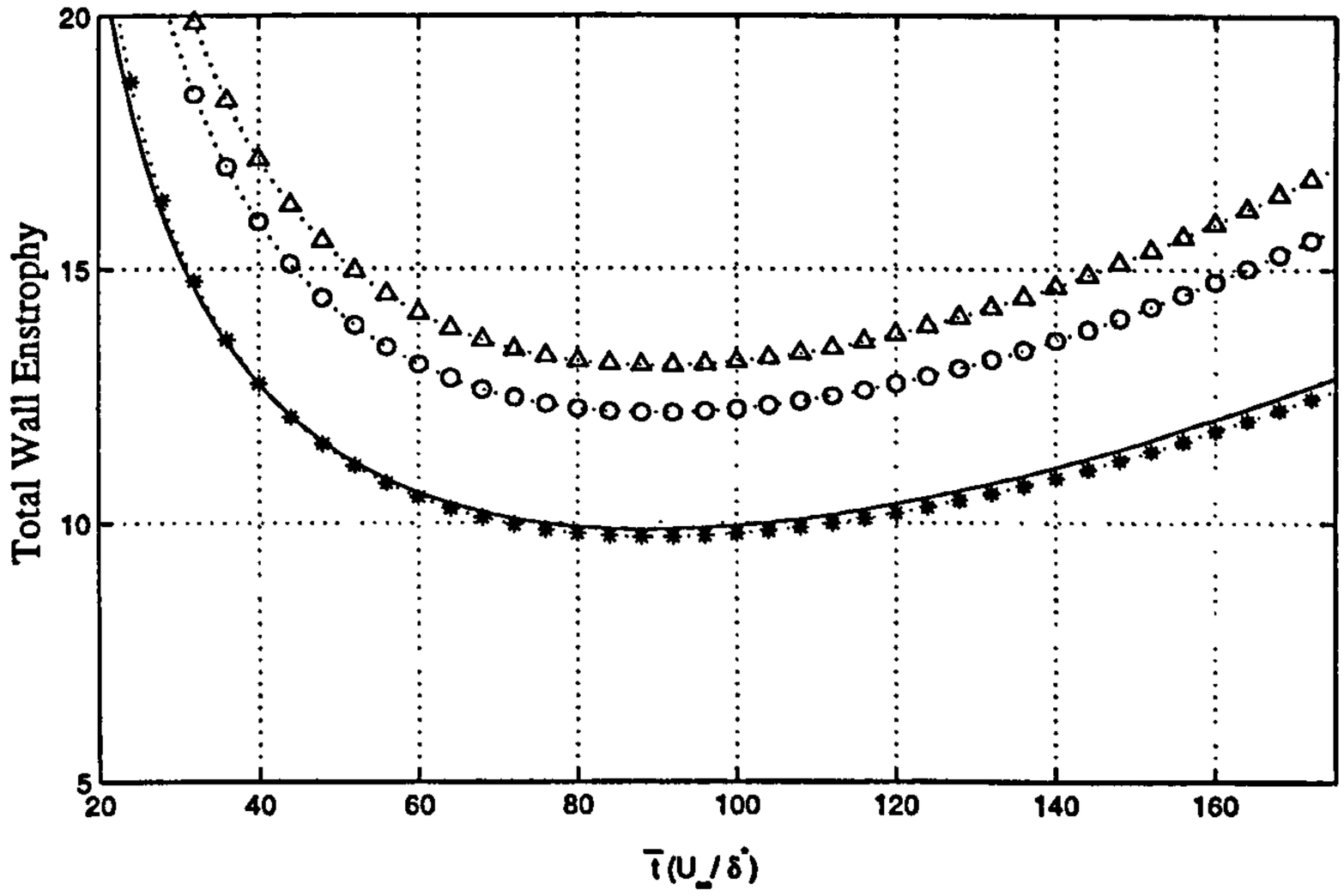

Figure 5.10: A comparison of the evolutions of total wall enstrophy resulting from prescribed jets of different design. The control design (–) (t_d=10 δ^*/U_∞, V_m=0.1 U_∞) is used for comparison. The following quantities have been held constant between the control and the design variation: net mass flow (∗) t_j=12.5 δ^*/U_∞, V_m=0.08 U_∞; net momentum flux (○) t_j=12.5 δ^*/U_∞, V_m=0.0894 U_∞; and net kinetic-energy flux (△) t_j=12.5 δ^*/U_∞, V_m=0.0928 U_∞. In all simulations A_j=10δ^* and R=2000. See §A.3.6 for a full parameter list.

5.5 Macro-Scale Impact of MEMS

Any proposed MEMS-based turbulence control scheme must assume that MEMS-scale disturbances have the ability to have macro-scale impact. If this were not the case potentially advantageous effects such as reduced skin friction or delayed separation would not be a possibility. It is therefore important that the aforementioned assumption is justified; attempts are made in this section to demonstrate some macro-scale boundary-layer control using a MEMS jet. As yet, no experimental research has shown any form of boundary-layer control using a truly MEMS-scale device.

5.5.1 Grid Scaling

The main calculation of §5.5.2 is a simulation of a MEMS slot issuing a two-dimensional jet into a Blasius boundary layer. An inherent problem with such simulations is the vast range of temporal and spatial scales that need to be resolved at different stages of the disturbance evolution. At the beginning of the calculation very fine grid resolution is required. The disturbance then disperses and the detail is diffused. Later in the calculation large-scale structures evolve over large time scales (Tollmien-Schlichting waves). To avoid the phenomenally expensive computations that would otherwise be required, the grid and time step are scaled at several stages during the simulation to track the disturbance. This takes advantage of the fact that that only fine grid resolution and time stepping are required at early times, and not for the entire calculation.

The sketch in Figure 5.11 illustrates the method of interpolating the small domain of a fine grid onto the coarse grid of a larger domain. The scaling in the wall-normal direction is performed by re-mapping the z-domain onto the ζ-domain using a coordinate transformation with a larger stretching factor, L (see §4.2.1 for details of the co-ordinate transformation). Spanwise scaling has also been attempted, but in some calculations this produces a numerical inac-

curacy leading to a non-physical solution. The results presented in §5.5.2 are two-dimensional and are not prone to such instabilities.

The calculation of the disturbance produced by a prescribed MEMS jet has been performed using the grid-scaling method. These results are compared to those from a simulation using a large fine grid throughout the calculation. Figure 5.12 shows the comparison of the grid-scaling method (–) with the straightforward method (––). The results show close agreement despite the grid-scaling method having used half the number of time steps and half the number of grid points, for half of the calculation. This means that the saving in computational time from the grid scaling has not been at the expense of an accurate solution.

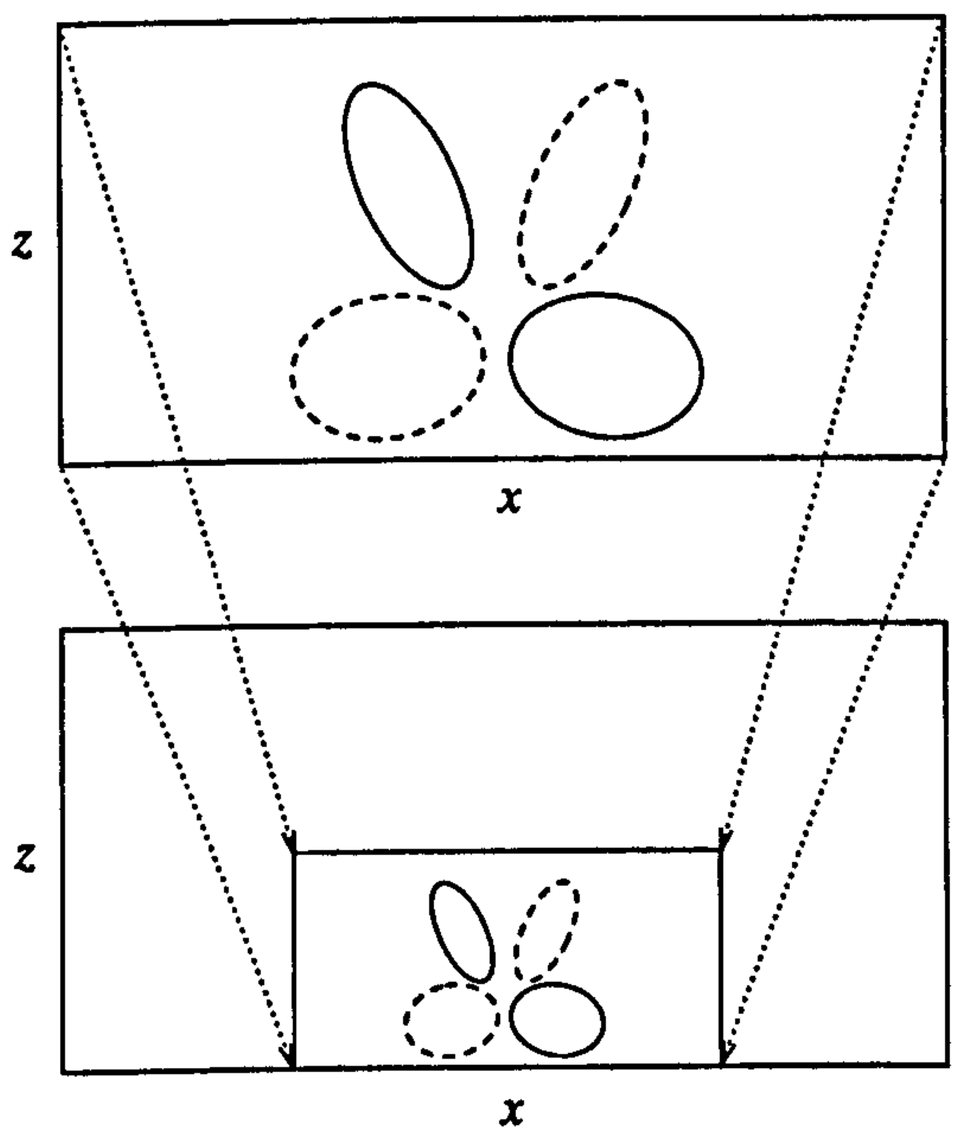

Small Domain - Fine Discretization.

Large Domain - Coarse Discretization.

Figure 5.11: The method of grid scaling.

5.5.2 Tracking MEMS- to Micro-Scale Disturbances

The grid-scaling method described in the previous section has been used to track the disturbance produced from a MEMS slot in a Blasius boundary layer from MEMS to micro scale. This would not have been possible on a single grid. In this simulation approximately twenty gradual grid scalings have been performed - the

more often the grid adapts the more accurate the solution at each stage. Figures 5.13 and 5.14 show contour plots of spanwise vorticity (ω_y) at different scales and times. The position of the MEMS is marked on each plot by the dashed lines immediately beneath the x-axis; the temporal and spatial variation of the jet is described using equation 5.3 (in the 2D case, r is the distance from the slot centre, and $2r_j$ is the slot width). The results show that after the 10 μm slot has finished its actuation ($\bar{t}$=t_j) an initial double vortex pair is generated very close to the wall. This disturbance spreads and becomes progressively weaker; the magnitude of the contours are different for each time, and the exact values of which are given in the figure caption. After a period of 21 jet durations the disturbance that had previously been unaffected by the mean flow, begins to become sheared at points furthest from the wall. After approximately 100 jet durations the centre of the disturbance has traveled 70 slot widths ($0.7\delta^*$) downstream from the slot location, and a pool of negative vorticity is gathered at the back end of the disturbance. This negative vorticity continues to become larger and stronger relative to the initial disturbance structure, and after 600 jet durations completely dominates. Eventually a Tollmien-Schlichting wave packet is formed; in a non-linear simulation this disturbance would eventually initiate laminar-to-turbulent transition. This is a crucial result as it affirms the assumption that MEMS-scale devices can, and in this case will, have macro-scale impact.

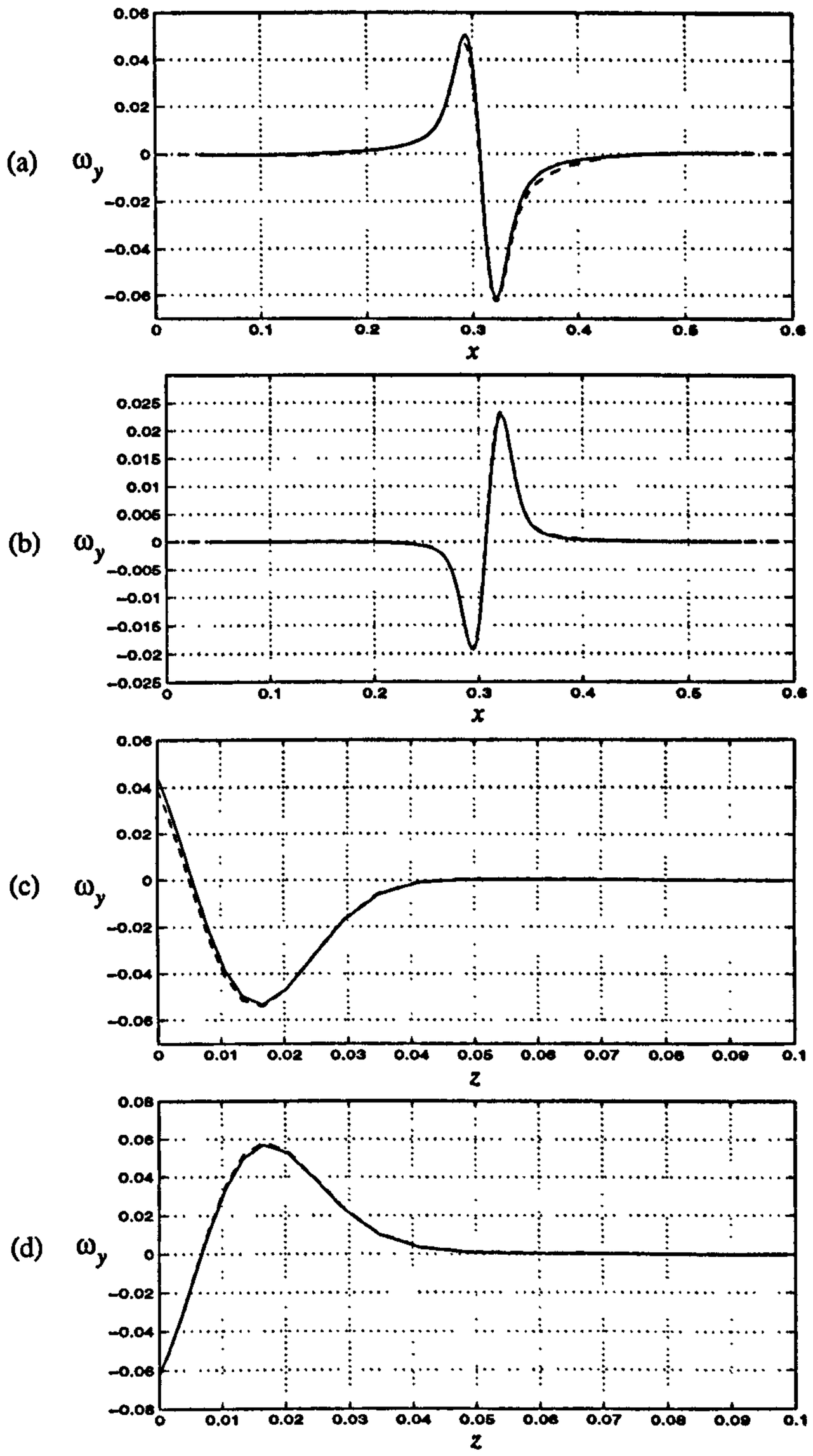

Figure 5.12: The spanwise vorticity perturbation (ω_y) produced by a prescribed three-dimensional MEMS jet. The continuous lines are for a simulation that has employed grid scaling to reduce computational time; the broken lines are for a simulation that has used a large fine grid. The MEMS devices issues from x=0.3 to 0.316 and begins at t=0; the plots here are at a time $\bar{t}$=$2t_j$. (a) streamwise variation of ω_y at $z = 0$ and y=0; (b) streamwise variation of ω_y at z=0.03 and y=0; (c) wall-normal variation of ω_y at x=0.3 and y=0; (d) wall-normal variation of ω_y at x=0.323 and y=0. R=2000, U_∞=30 m s^{-1}, and δ^*=1 mm. See §A.3.7 for a full parameter list.

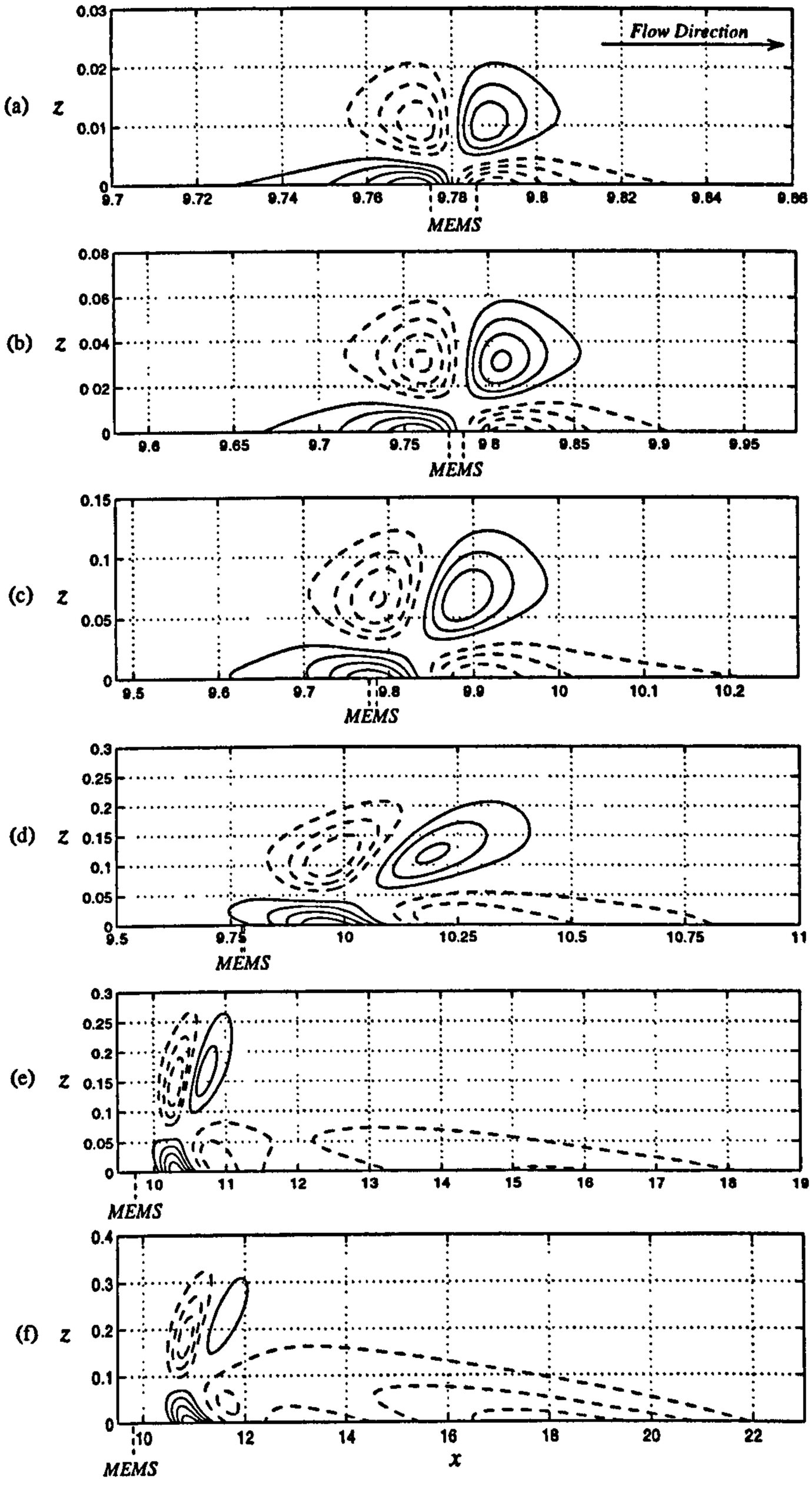

Figure 5.13: The disturbance produced by a two-dimensional MEMS slot actuator: early stages. Plots are of spanwise vorticity (ω_y), and the nth contour is at $\pm An$: (a) A=4.73×10^{-2}; (b) A=8.4×10^{-4}; (c) A=4.05×10^{-5}; (d) A=3.52×10^{-6}; (e) A=9.52×10^{-7}; (f) A=2.53×10^{-7}. The continuous and broken lines denote positive and negative values respectively. R=2000, U_∞=30 m s^{-1}, δ^*=1 mm, V_m=0.1U_∞, $2r_j$=0.01δ^*, and t_j=0.1δ^*/U_∞. See §A.3.8 for a full parameter list.

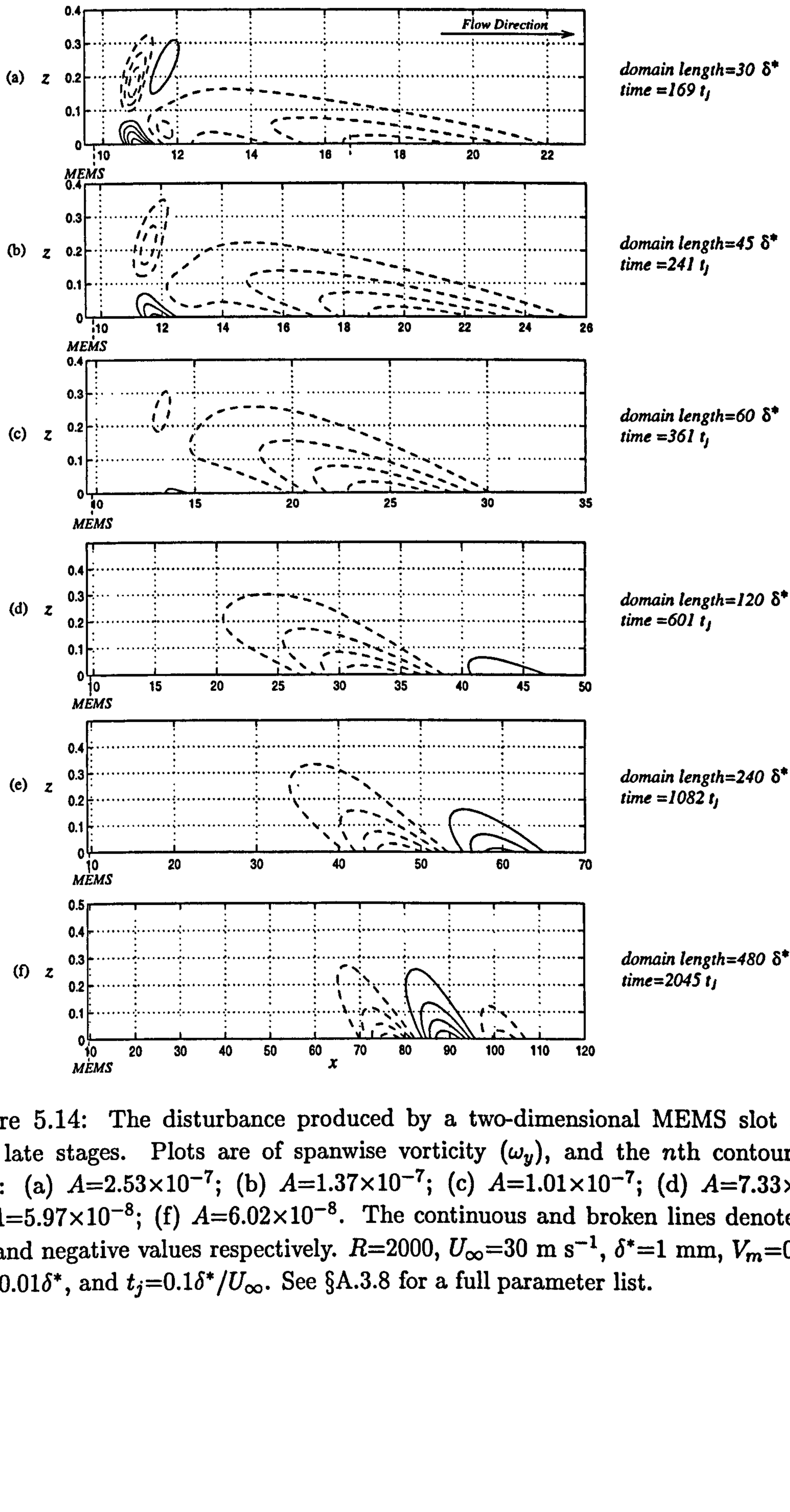

Figure 5.14: The disturbance produced by a two-dimensional MEMS slot actuator: late stages. Plots are of spanwise vorticity (ω_y), and the nth contour is at $\pm An$: (a) A=2.53×10^{-7}; (b) A=1.37×10^{-7}; (c) A=1.01×10^{-7}; (d) A=7.33×10^{-8}; (e) A=5.97×10^{-8}; (f) A=6.02×10^{-8}. The continuous and broken lines denote positive and negative values respectively. R=2000, U_∞=30 m s^{-1}, δ^*=1 mm, V_m=0.1U_∞, $2r_j$=0.01δ^*, and t_j=0.1δ^*/U_∞. See §A.3.8 for a full parameter list.

5.6 Chapter Summary

The numerical simulations of this chapter have all been performed using a prescribed boundary condition to model the jet-actuator. This enables relatively cheap computations and allows investigations into boundary-layer disturbances generated from standardised inputs. Using these simulations, issues of practical interest have been investigated and general qualitative solutions have been suggested for some of the problems that face designers and experimentalists in the field of MEMS for boundary-layer control.

Specifically, in §5.4 and §5.7, the difference between MEMS- and micro-scale disturbances are investigated in both a Blasius and a turbulent boundary layer. Striking differences were present in the results, and a method was suggested in §5.2.3 and §5.3.3 to avoid making similar erroneous comparisons. This is especially relevant to preliminary experimental investigations that use large-scale MEMS models in low-speed wind tunnels.

In §5.4 efficient actuation is defined as that which can produce a strong total disturbances in the boundary layer, and in the context of the Blasius case, an actuation which can most effectively generate a Tollmien-Schlichting wave instability. By a deductive process it has been shown that the net mass flow from a jet actuator is the most appropriate design criterion, and it is this that should be the focus of a design optimisation.

Finally in §5.5 a numerical method is described that can calculate disturbances that exhibit a wide range of time and length scales during their evolution. This method is used to demonstrate how a MEMS slot actuator is capable of producing a Tollmien-Schlichting wave train.

Chapter 6

Interactive Simulations

In Chapter 5, prescribed boundary conditions were used to model the effect of the jet actuator on the boundary layer. This was also the approach of Carlson and Lumley (1996a,b), Kral *et al.* (1997), Hofmann and Herbert (1997, 1998), who modelled similar actuators. The simulations in this chapter represent the first time the interactive behaviour of an actuator and a boundary layer has been investigated. This is performed by coupling the actuator code of Chapter 2 with the boundary-layer code of Chapter 4.

Note that Rizzetta *et al.* (1999), who modelled the fluid dynamics inside and outside of the cavity, and therefore the interaction between the two, did not investigate the actuation within a boundary layer. Also, in their simulations, the plate motion was prescribed and not 'compliant' to pressure changes in the cavity as it is here (see Chapter 3 §3.3).

Nomenclature

Unless otherwise indicated, lengths and velocities have been non-dimensionalised using δ^* and U_∞, respectively. A superscript '+' denotes non-dimensionalisation

using the friction velocity, v^*, and the viscous length scale, ν/v^*.

$\bar{}$ = an over bar denotes a dimensional quantity

d = diaphragm damping (N s m^{-3})

d_{31}, d_{32} = radial/azimuthal piezoelectric constant (m V^{-1})

E_d = elastic modulus of diaphragm material (N m^{-2})

E_p = elastic modulus of PZT material (N m^{-2})

g = parameter used to characterise actuator scale (m)

H_c = cavity height (m)

l = orifice length (m)

L = mapped domain stretching factor (non dim.)

N_c = number of Chebyshev polynomials

N_d = number of grid points in diaphragm finite-difference scheme

N_o = number of grid points in orifice finite-difference scheme

N_y = number of spanwise Fourier modes

R_o = radius of orifice or half slot width (m)

R_d = diaphragm radius (m)

R_p = PZT disc radius (m)

$R = U_\infty \delta^*/\nu$ = Reynolds number

t = time (s)

t_d = diaphragm thickness (m)

t_p = PZT disc thickness (m)

$\bar{T} = T\ \delta^*/U_\infty = T^+\ \nu/v^{*2}$ = total simulation time (s)

U_c = centre-line jet velocity(m s^{-1})

$U_{c,\max}$ = maximum centre-line jet velocity (m s^{-1})

U_∞ = free-stream velocity (m s^{-1})

v^* = friction velocity (m s^{-1})

V = voltage (V)

x, y, z = streamwise, spanwise and wall-normal directions (non dim.)

X_d = streamwise domain length (non dim.)

X_b, X_e = streamwise position of actuator (non dim.)

Y_d = extent of spanwise domain (non dim.)

δ^* = boundary layer thickness (m)

$\bar{\Delta}t = \Delta t\ \delta^*/U_\infty = \Delta t^+\ \nu/v^{*2}$ = time step (s)

Δx = streamwise grid spacing (non dim.)

ν = kinematic viscosity (m^2 s^{-1})

ν/v^* = the wall unit (m)

ν_d = Poisson's ratio of the diaphragm material

ν_p = Poisson's ratio of the PZT material

ρ = density (kg m^{-3})

ρ_d = density of diaphragm material (kg m^{-3})

ρ_p = density of PZT material (kg m^{-3})

$\bar{\omega}_{ts} = \omega_{ts} U_\infty/\delta^*$ = Tollmien-Schlichting wave excitation frequency (s^{-1})

$\bar{\omega}_x = \omega_x U_\infty/\delta^* = \omega_x^+ v^{*2}/\nu$ = streamwise vorticity perturbation (s^{-1})

$\bar{\omega}_y = \omega_y U_\infty/\delta^* = \omega_y^+ v^{*2}/\nu$ = spanwise vorticity perturbation (s^{-1})

6.1 The Damping Effect

In this section the interaction of a MEMS actuator with a Blasius boundary layer is investigated. Figure 6.1 shows the variation of exit velocity with time for pressure-jump actuators (g=1 μm – see Chapter 3 §3.4.2 for specification of actuator design) with varying orifice radii acting within a Blasius boundary layer (R=2000, δ^*=1 mm, U_∞=30 m s^{-1}). The dashed lines are the velocities that would occur if the MEMS were issuing into still air (at all times). The continuous lines, on the other hand, are the velocities that are generated in the presence of a boundary layer. There is clearly a damping effect caused by the interaction of the jet and the boundary-layer disturbance it produces. In Figure 6.1(c) Helmholtz oscillation occurs (see Chapter 3 §3.5) and in the interactive case, the damping effect has caused the velocity to oscillate almost ninety degrees out of phase with the non-interactive velocity.

To further investigate the damping effect, a number of simulations are performed at different scales of actuator (g=1 μm, g=25 μm, and g=625 μm). The velocity optimisations at these scales (Chapter 3 §3.6) have been used to determine how the damping might affect optimised velocity magnitude. Figure 6.2 shows the results from the interactive simulations (–∗–) compared with the non-interactive equivalents (–). The damping at MEMS scale (Figure 6.2(a), g=1 μm) has reduced the optimised velocity magnitude by more than ten percent, whereas at micro scale (Figure 6.2(c), g=625 μm) the damping is much weaker.

The presence of the damping might arise from the viscous dissipation of the disturbance in the boundary layer. The increased damping in the MEMS case would therefore be explained by the comparatively stronger viscous forces that exist at smaller scales. Regardless of the reason, the presence of this MEMS-scale damping is important to be aware of when extrapolating from micro-scale models to flight-scale devices.

6.1.1 Numerical Dependency Tests

In this section the dependency of the results in Figures 6.1-6.2 on numerical factors is investigated. Firstly, the number of iterations that are involved in solving the Poisson equation (equation (4.7)) and converging the coupled codes is varied (see Chapter 4, §4.2). This makes sure that the chosen iteration number is sufficient for code convergence. Figure 6.3 shows the same simulations of MEMS and boundary layer with different number of Poisson-equation iterations. The results of the three runs are nearly identical which indicates that convergence is achieved at early iteration numbers.

The results of Figures 6.1-6.2 are obtained on fairly coarse grids and small domains to keep computational costs low. Here, parameters such as grid spacing and domain length are varied to check that these computationally-cheap simulations are not significantly less accurate than simulations on finer grids with longer domains. Figures (6.4)-(6.7) show the results of such dependency studies, and there is little or no discernible difference between the simulations of each group, demonstrating conclusively that simulations of this type are grid- and domain-size independent.

The very satisfactory results of this section are largely owing to the nature of the numerical scheme, which tends to produce a numerical instability before any significant error. The discretisation is therefore set by stability requirements, and at such a level that is more than sufficient for an accurate solution. Also, the boundary conditions, which are effectively null, are robust enough to deal with small perturbations upstream and downstream, allowing reasonably small domain lengths and finer discretisations.

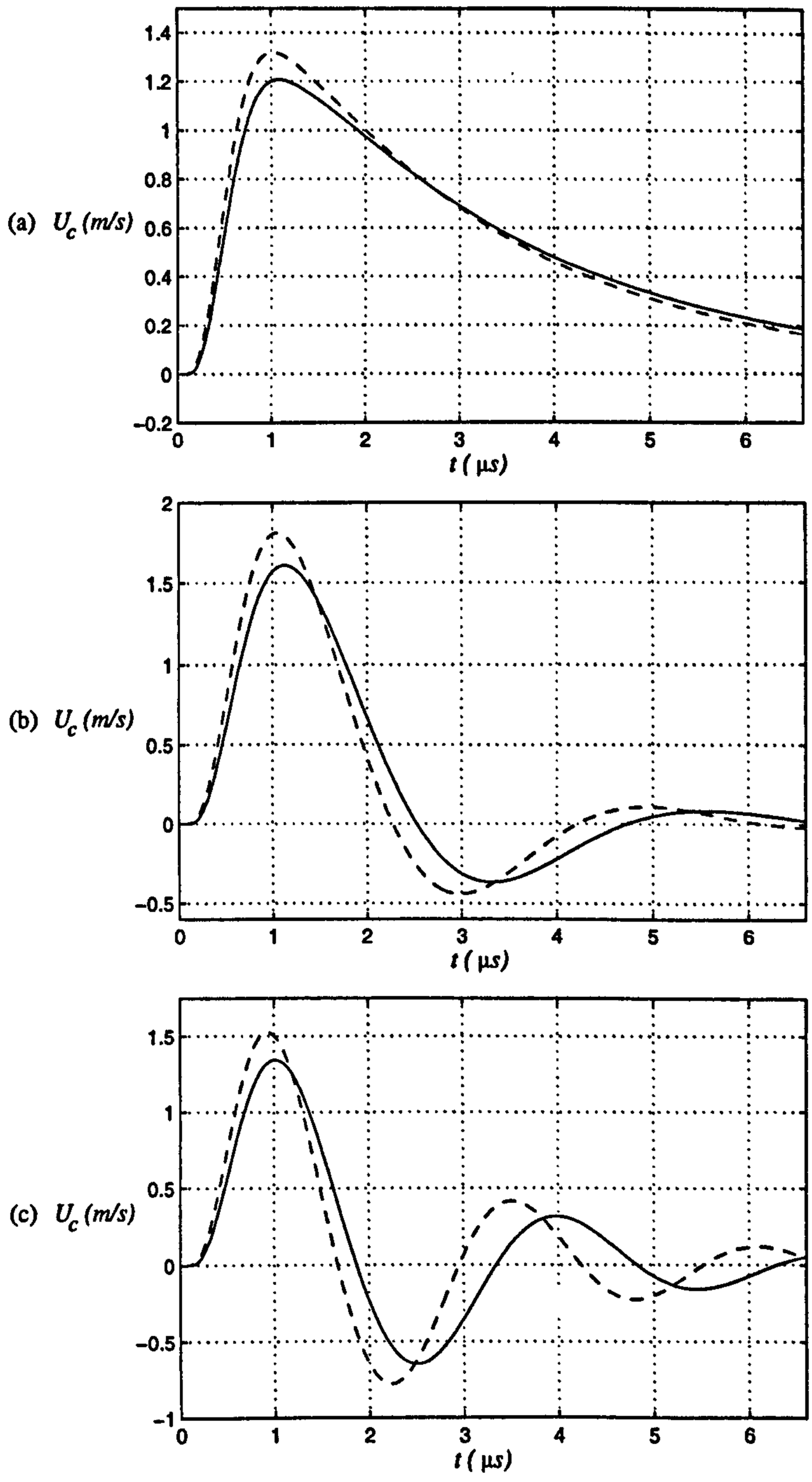

Figure 6.1: Time-history plots of centre-line velocity (U_c) produced from a MEMS-scale pressure-jump actuator. Interactive (–) and non-interactive (– –) simulations. (a) R_o=5 μm, (b) R_o=8 μm, (c) R_o=11 μm. Boundary-layer characteristics: R=2000, U_∞=30 m s^{-1}, δ^* =1 mm. See §A.4.1 for a full parameter list.

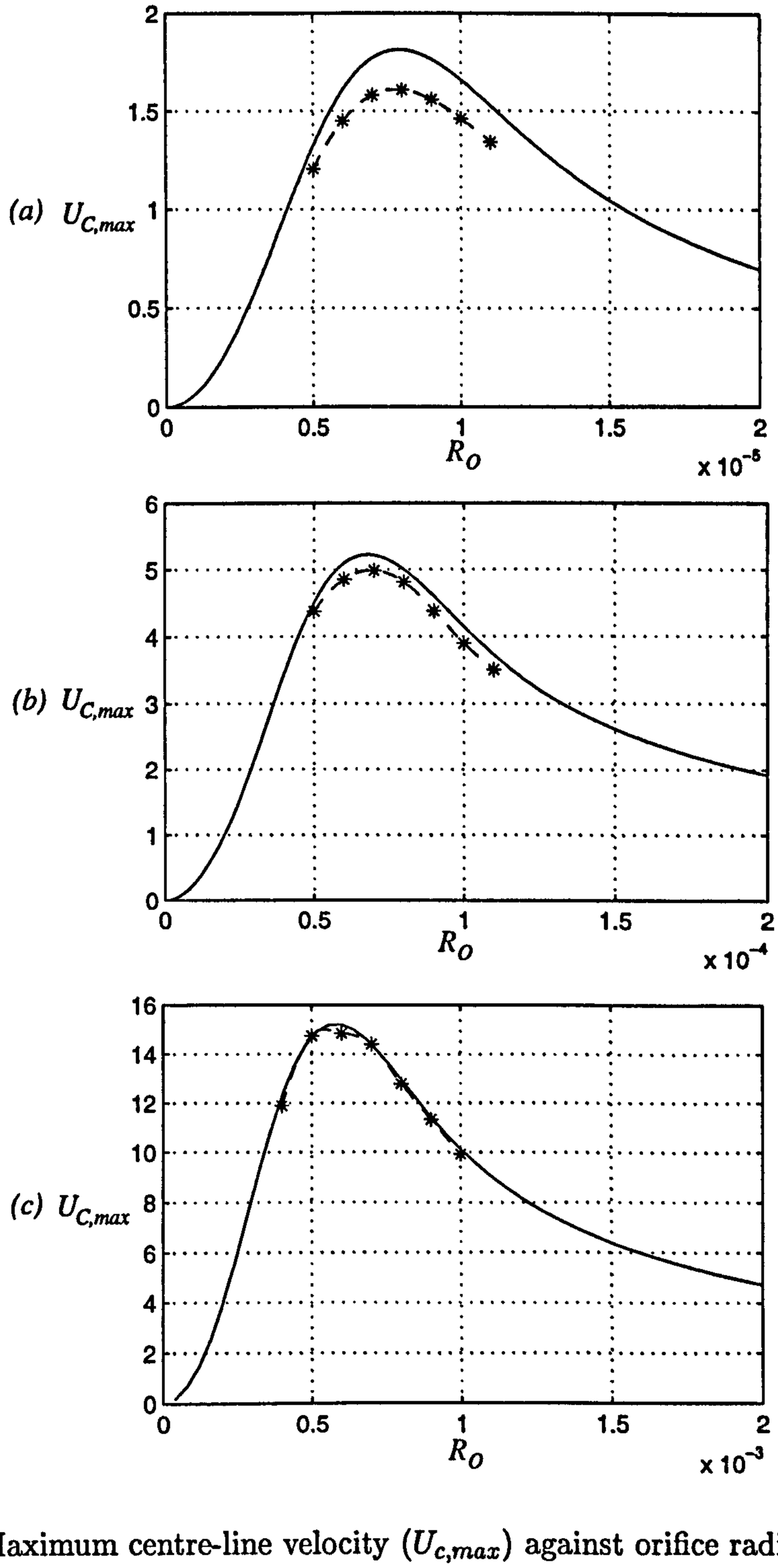

Figure 6.2: Maximum centre-line velocity ($U_{c,max}$) against orifice radius (R_o) for different size MEMS actuators. Interactive (−∗−) and non-interactive (−) simulations. (a) a small MEMS actuator, g=1 μm; (b) a large MEMS actuator, g=25 μm (c) a micro actuator, g= 625 μm. Boundary-layer characteristics: R=2000, U_∞=30 m s^{-1}, δ^* =1 mm. See §A.4.2 for a full parameter list.

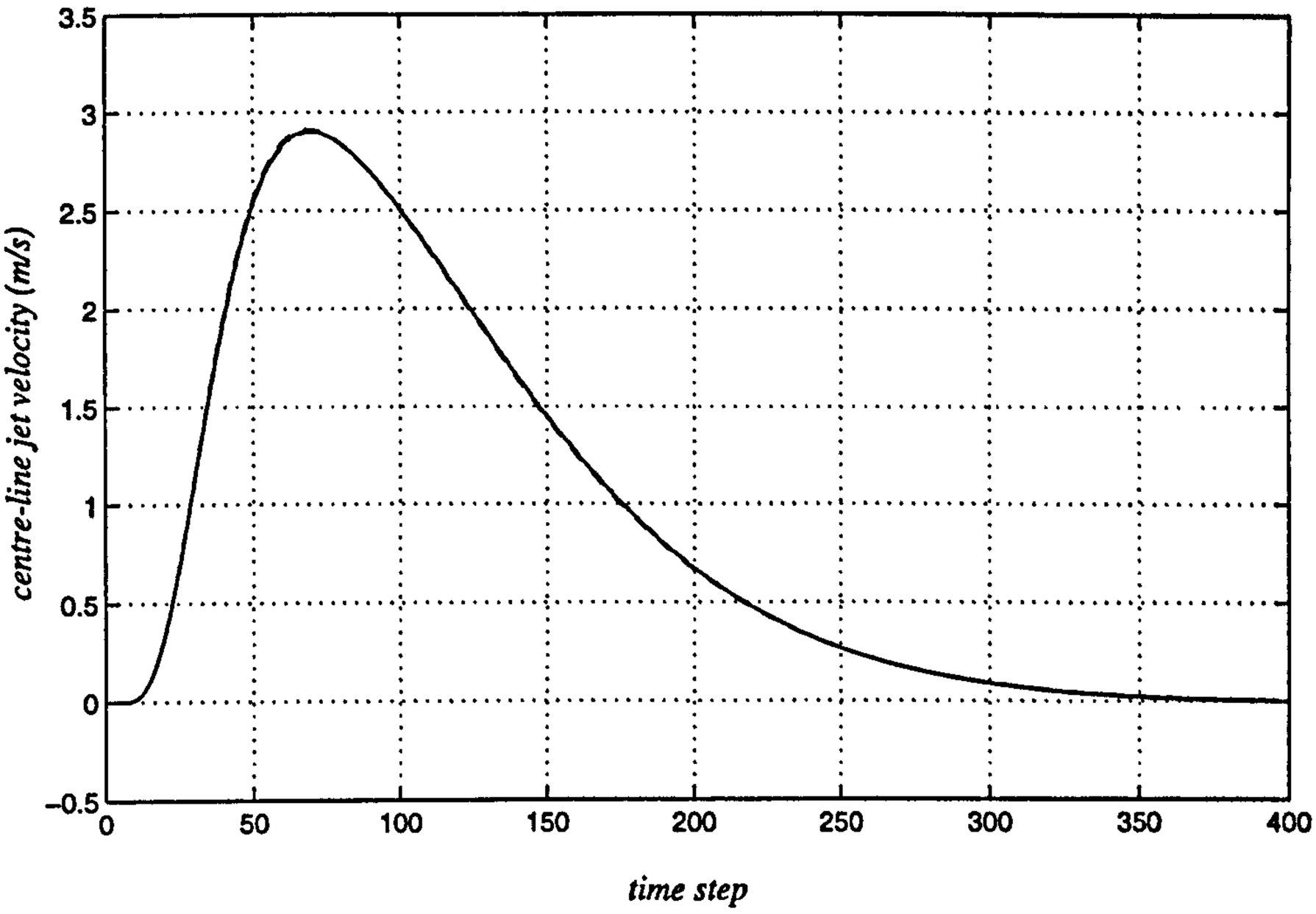

Figure 6.3: The effect of the number of Poisson-equation iterations on jet velocity. Number of iterations: 8 (– –); 12 (–); 16 (–·–). See §A.4.3 for a full parameter list.

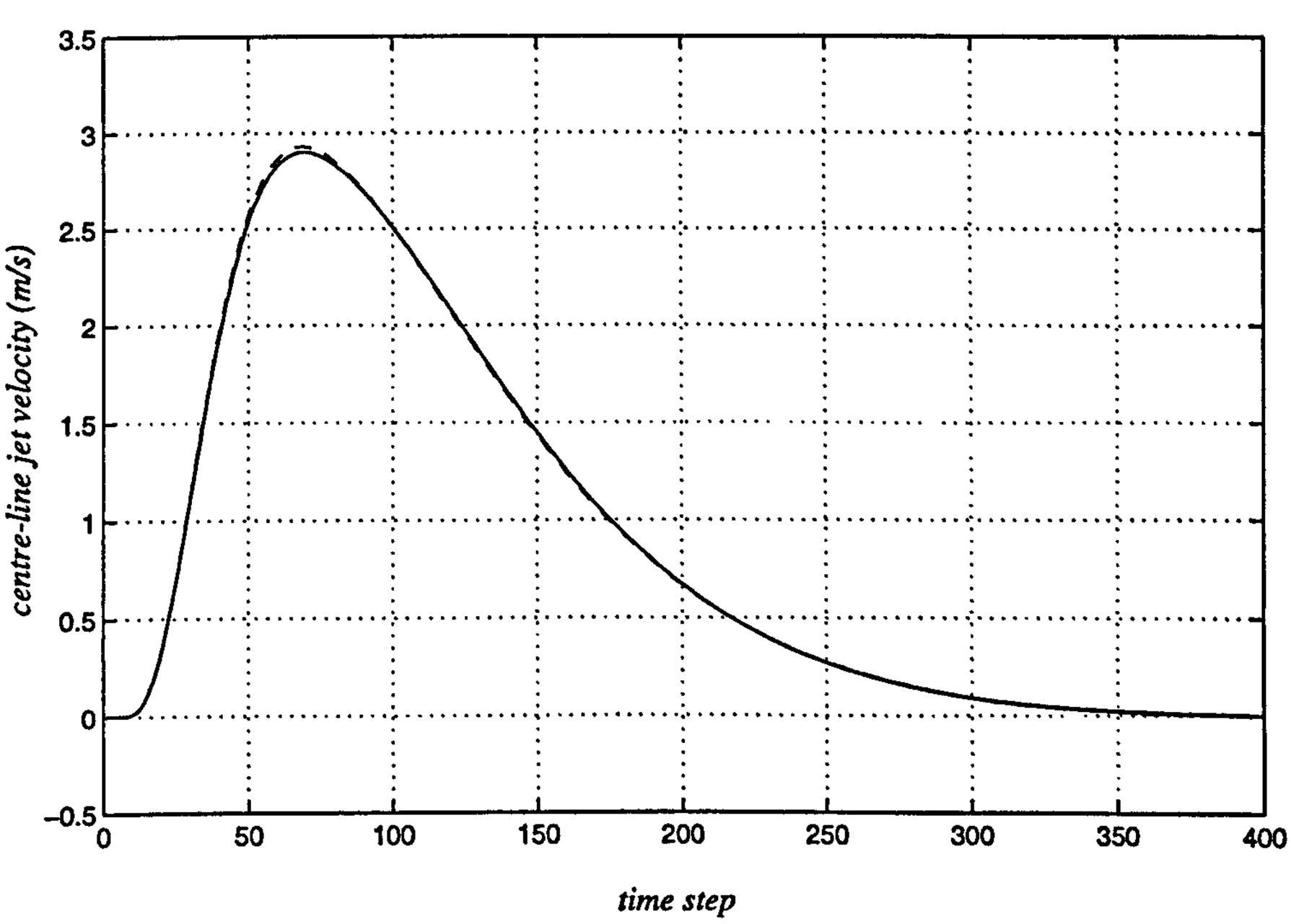

Figure 6.4: The effect of the number of Chebyshev polynomials on jet velocity. Number of Chebyshev polynomials: 16 (– –); 32 (–); 64 (–·–). See §A.4.4 for a full parameter list.

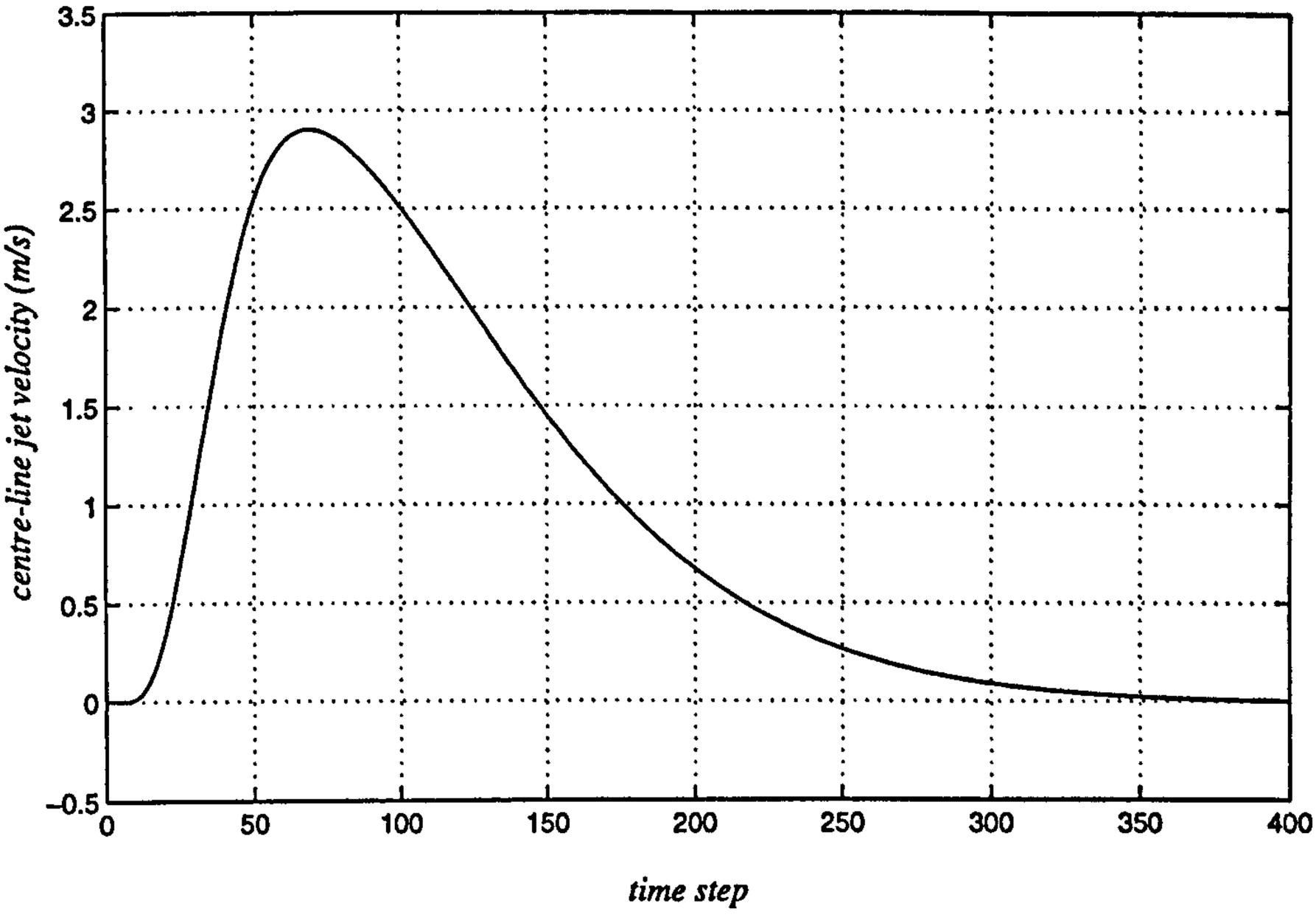

Figure 6.5: The effect of streamwise domain length (X_d) on jet velocity. Domain length: 0.1 (––); 0.2 (–); 0.3 (–·–). See §A.4.5 for a full parameter list.

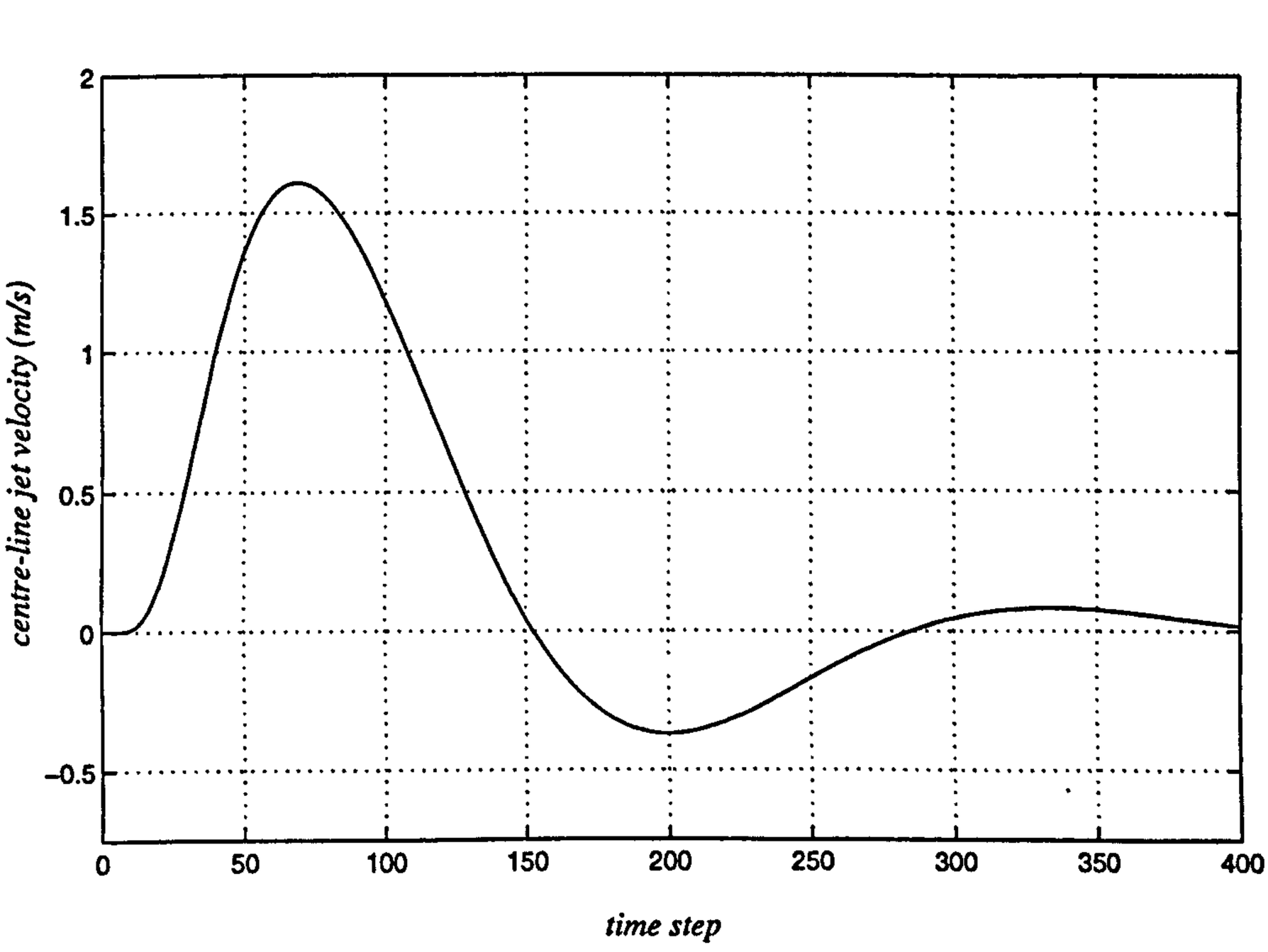

Figure 6.6: The effect of spanwise domain length (Y_d) on jet velocity. Domain length: 0.06 (––); 0.08 (–); 0.1 (–·–). See §A.4.6 for a full parameter list.

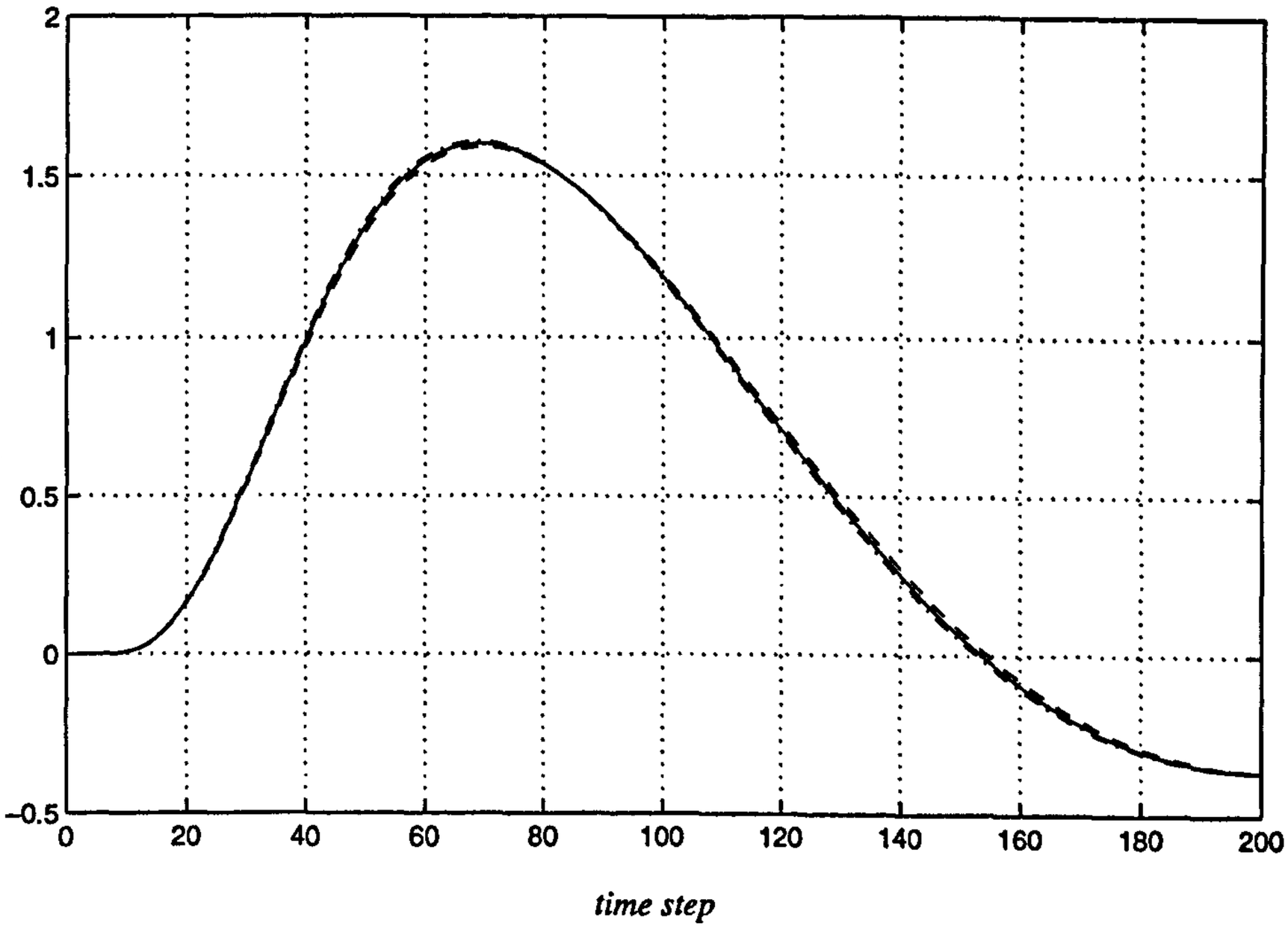

Figure 6.7: The effect of streamwise grid spacing (Δx) on jet velocity. Grid spacing: 0.002 (−−); 0.0015 (–); 0.001 (–·–). See §A.4.7 for a full parameter list.

6.2 Blasius Boundary-Layer Disturbances

This section concentrates on the disturbances created in the boundary layer during interactive calculations. The boundary conditions are not prescribed, as they were in Chapter 5, but are obtained directly from the actuator code with which the boundary-layer code is coupled.

Firstly, disturbances in a Blasius boundary layer are investigated. Figure 6.8 shows the results from an interactive simulation in a Blasius boundary layer (R=2000, U_∞=30 m s^{-1}, δ^*=1 mm) at different times during a MEMS' actuation period (g=1 μm). The results show the familiar double vortex pair (of spanwise vorticity) that was exhibited in some of the prescribed-jet results in Chapter 5. Plan-view plots of streamwise vorticity are also shown. The main point of interest from the results of Figure 6.8 is that the disturbance is seemingly unaffected by the boundary-layer flow. As a contrast, disturbances in a high-speed boundary layer are investigated in §6.3.

6.2.1 Grid Refinement

A grid-refinement study has been performed, to check the integrity of the results from Figure 6.8 and similar simulations. Figure 6.9 shows a comparison of results from a coarse grid and time stepping (the typical resolution used in this thesis) against results from a fine grid and time stepping (one and a half times as many grid and collocation points, and five times as many time steps). It is obvious from the results that the solutions are grid and time-step independent. Again, the reason for the apparent lack of numerical error is because, for stability reasons, quite a fine discretisation is a minimum requirement. This means that a bad choice of grid spacing or time step is easily detectable.

6.2.2 Altering the Actuator Design

In this section the effect of changing the actuator design on the boundary-layer disturbance is demonstrated. Figure 6.10 shows a comparison between the disturbances produced by a MEMS with a 6 μm orifice radius and a MEMS with an 8 μm orifice radius. The left-hand column of spanwise-vorticity contour plots are the same as those from Figure 6.8, whereas the right-hand column of contours have been generated using a MEMS with a larger orifice radius. The increase in orifice radius occasions the onset of Helmholtz oscillation in the device (see Chapter 3, §3.5). This causes significantly different disturbances during the actuation period. This example demonstrates how quite subtle changes in actuator design can drastically affect the flow field that it produces.

6.2.3 Varying the Reynolds Number

In an attempt to understand the effect of the boundary-layer flow on the disturbance, calculations have been performed in boundary layers with varying Reynolds numbers. Figure 6.11 shows how the Reynolds number influences the non-dimensional and dimensional solution (δ^* is fixed and U_∞ varied in the dimensional results). The figure indicates that the Reynolds number has no observable influence on the dimensionalised results. This result goes further to highlight the benign state of the boundary layer on such small spatial and temporal scales. The results in the following section demonstrate how this is not the case when using a high-speed turbulent profile in the calculations.

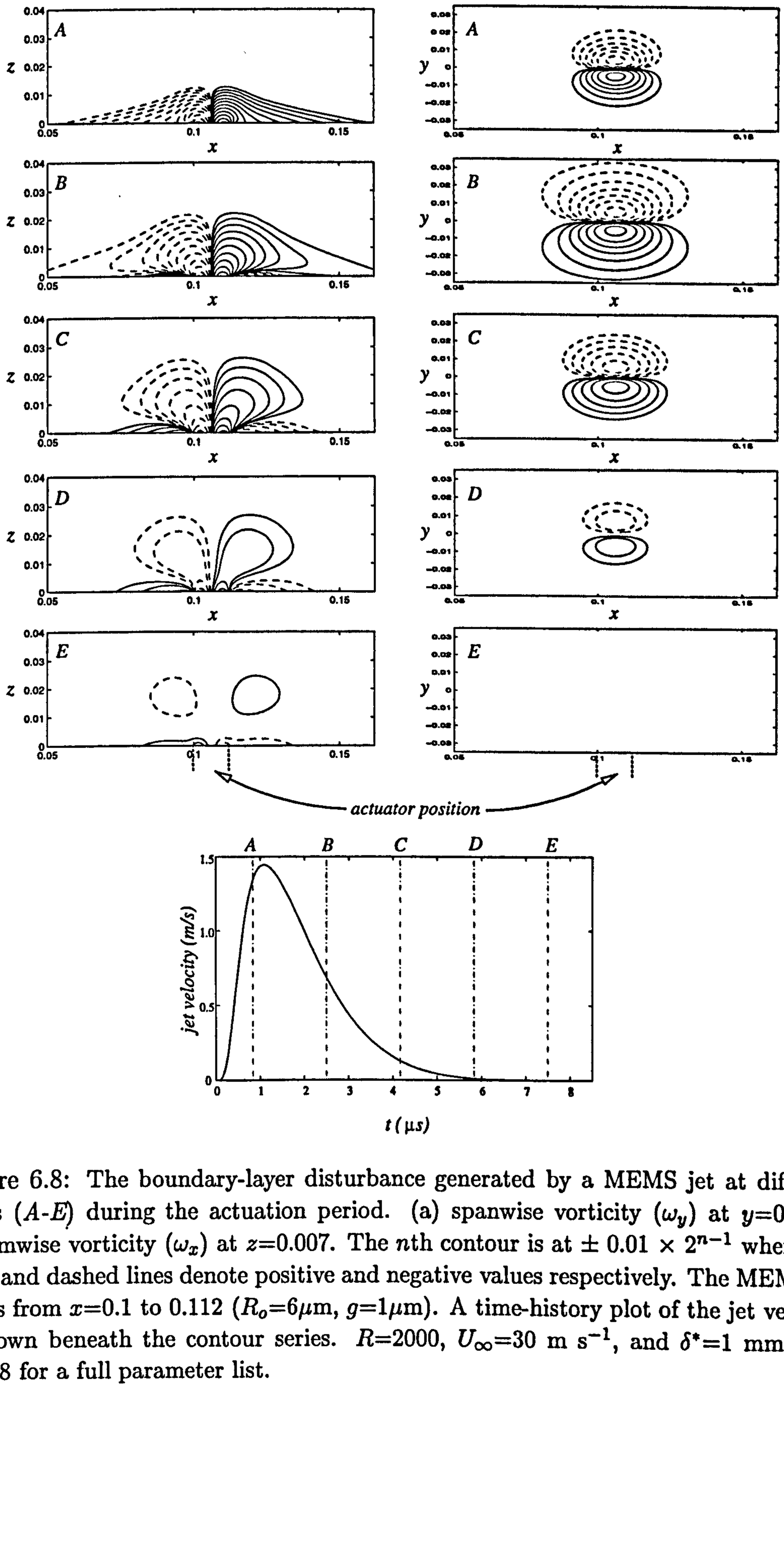

Figure 6.8: The boundary-layer disturbance generated by a MEMS jet at different times (*A*-*E*) during the actuation period. (a) spanwise vorticity (ω_y) at y=0. (b) streamwise vorticity (ω_x) at z=0.007. The nth contour is at $\pm$ 0.01 $\times$ 2^{n-1} where the solid and dashed lines denote positive and negative values respectively. The MEMS jet issues from x=0.1 to 0.112 (R_o=6μm, g=1μm). A time-history plot of the jet velocity is shown beneath the contour series. R=2000, U_∞=30 m s^{-1}, and δ^*=1 mm. See §A.4.8 for a full parameter list.

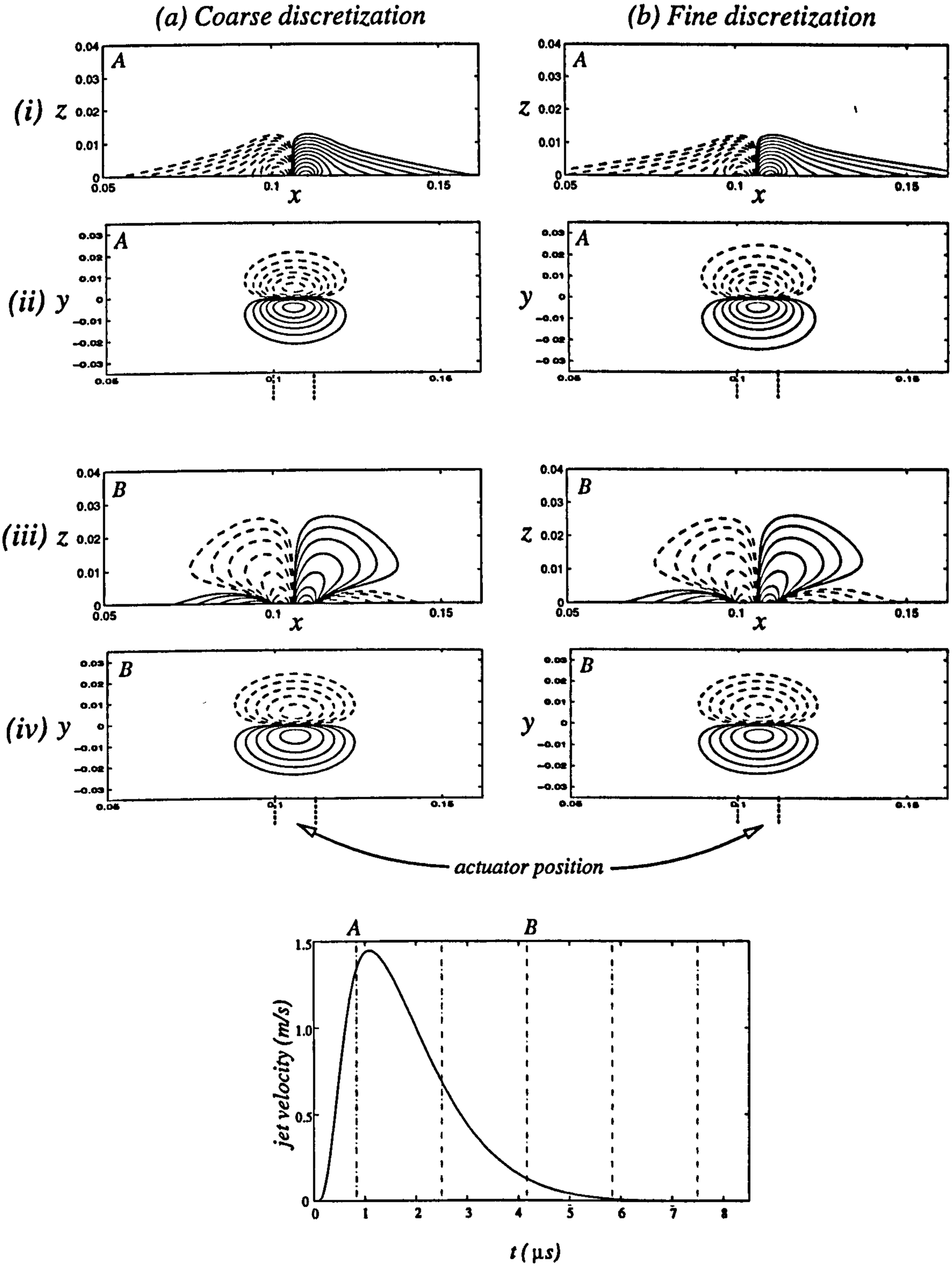

Figure 6.9: The boundary-layer disturbance generated by a MEMS jet at different times (*A*-*E*) during the actuation period. A comparison of coarse (a) and fine (b) discretisations. (*i*),(*iii*) spanwise vorticity (ω_y) at y=0. (*ii*),(*iv*) streamwise vorticity (ω_x) at z=0.007. The nth contour is at $\pm$ 0.01 $\times$ 2^{n-1} where the solid and dashed lines denote positive and negative values respectively. The MEMS jet issues from x=0.1 to 0.112 (R_o=6μm). A time-history plot of the jet velocity is shown beneath the contour series. R=2000, U_∞=30 m s^{-1}, and δ^*=1 mm. See §A.4.9 for a full parameter list.

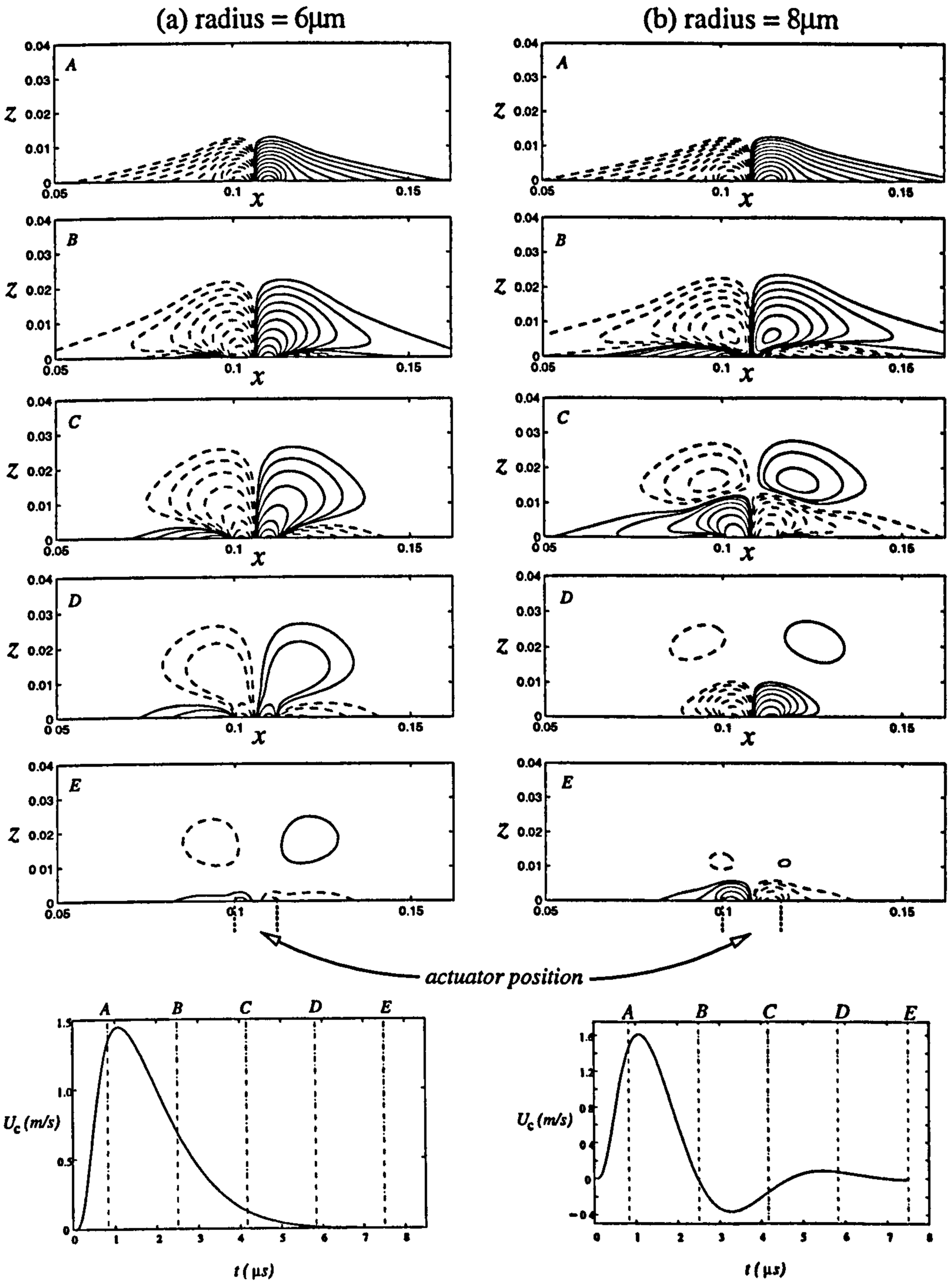

Figure 6.10: A comparison of the boundary-layer disturbances generated by MEMS jets with different orifice radii. Plots are of spanwise vorticity (ω_y) at $y = 0$, at times *A*-*E* during their actuation periods. (a) R_o=6 μm; the MEMS is positioned at x=0.1 to 0.112, (b) R_o=8 μm; the MEMS is positioned at x=0.1 to 0.116. The nth contour is at $\pm$ 0.01 $\times$ 2^{n-1} where the solid and dashed lines denote positive and negative values respectively. Time-history plots of the jet velocities are shown beneath the contour series. R=2000, U_∞=30 m s^{-1}, and δ^*=1 mm. See §A.4.10 for a full parameter list.

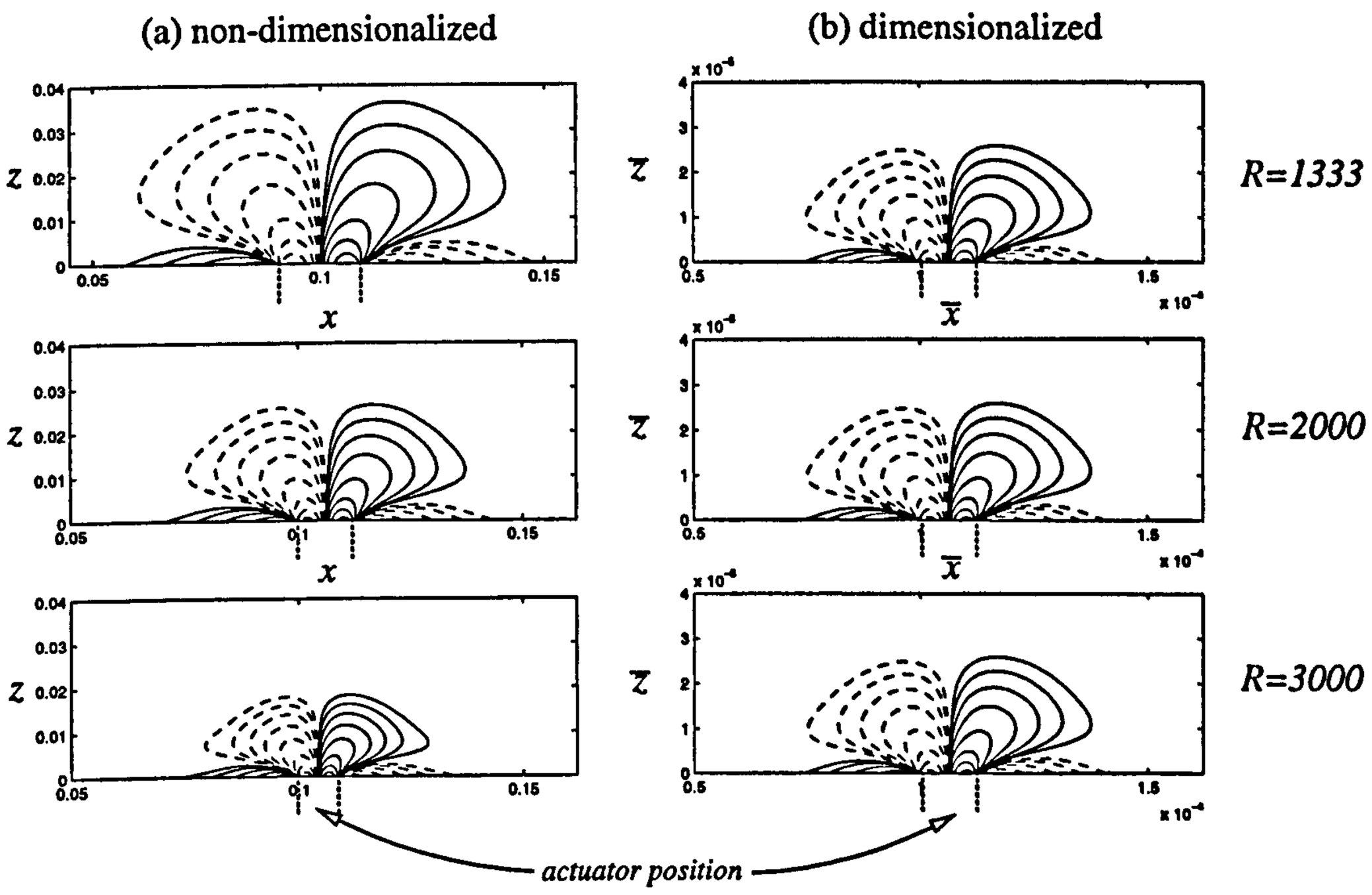

Figure 6.11: The effect of Reynolds number on the boundary-layer disturbance generated by a MEMS jet. (a) non-dimensionalised results, (b) dimensionalised results. Plots are of spanwise vorticity (ω_y) at y=0 and t=0.125. The nth contour is at $\pm$ 0.01 $\times$ 2^{n-1} where the solid and dashed lines denote positive and negative values respectively. The MEMS jet issues from x=0.1 to 0.112 (R_o=6μm). R=2000, U_∞=30 m s^{-1}, and δ^*=1 mm. See §A.4.11 for a full parameter list.

6.3 Turbulent Boundary-Layer Disturbances

The turbulent profile is characterised by the friction velocity, v^*, which in this section is equal to 10 m s^{-1}; this is comparable to flight-scale conditions. This turbulent boundary layer has a shear force at the wall 400 times greater than that of the Blasius boundary layer used in this chapter (R=2000, U_∞=30 m s^{-1}, δ^*=1 mm), and 70 times greater than the turbulent boundary layer of Chapter 5, §5.3.2 (v^*=1.186 m s^{-1}).

Figure 6.12 shows the evolution of the spanwise-vorticity perturbations (at y=0) in the high-speed boundary layer. The disturbance is rapidly sheared and generates structures very different to those in the slow-moving boundary layer (see Figure 6.8). The negative vorticity downstream of the actuator in Figure 6.12 is not seen until much later times in the low-speed simulations. Also, the positive vorticity, that in the low-speed simulations maintains a reflection of the negative vorticity, is sucked away from the wall and subsequently stretched downstream.

Figure 6.13 shows contour plots of streamwise velocity from the same simulation. These show that the puff-type actuation has in fact caused a streaky disturbance of negative streamwise velocity perturbation which extends much further downstream than the actuator itself (when superposed onto the undisturbed flow field this produces a low-speed streak). This is an encouraging result for MEMS-based turbulence control, based on the premise that a MEMS will have a much greater chance of cancelling or enhancing a 'coherent structure' if it produces a similar structure itself.

Figure 6.14 shows the magnitude of the damped jet velocity in the high-speed turbulent boundary layer (×) compared to those in a low-speed Blasius boundary layer (–∗–), and equivalent non-interactive simulations (–). The damping effect in the turbulent case is slightly stronger, and from this it can be inferred that the increased shear in the high-speed boundary layer somehow influences the damping phenomenon discussed in §6.1.

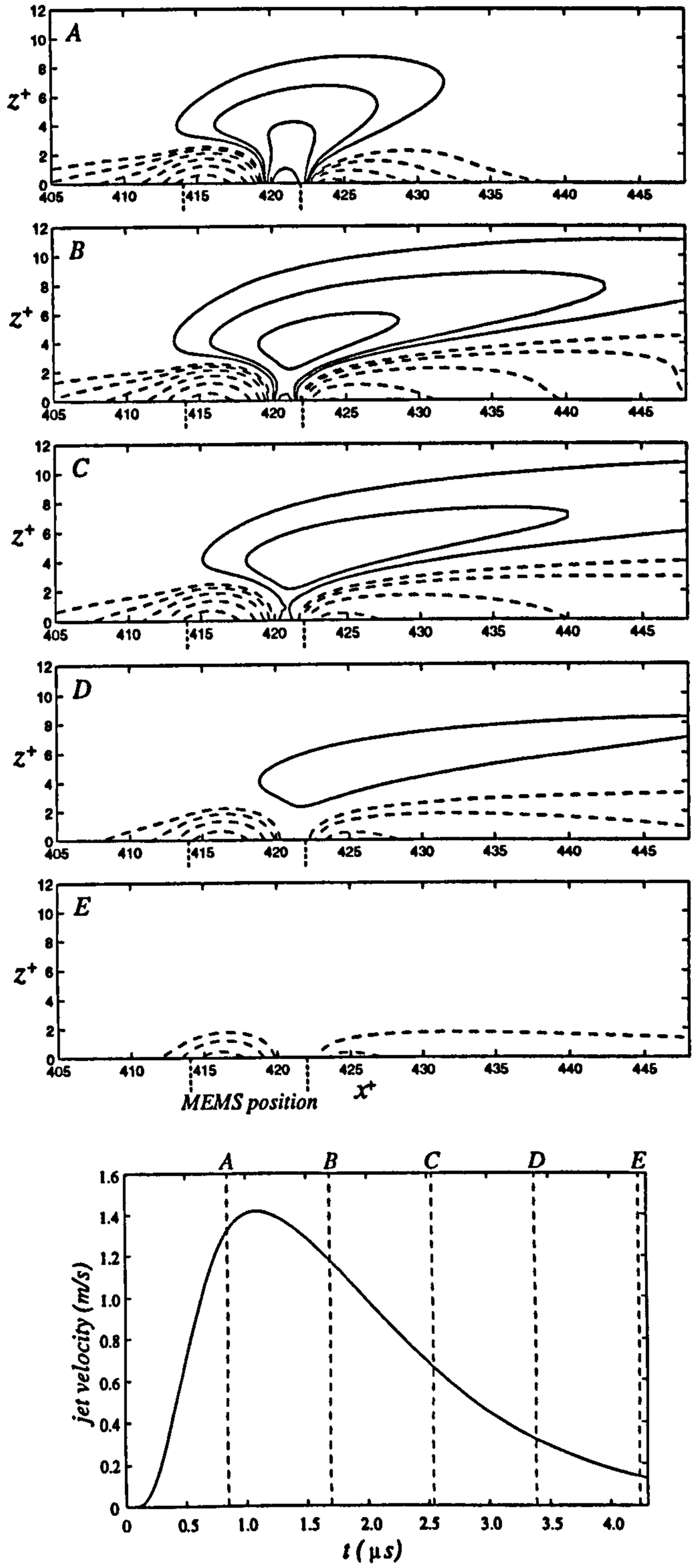

Figure 6.12: The disturbance generated in a turbulent boundary layer by a MEMS jet. Contours of spanwise vorticity (ω_y^+) at y^+=0, at times (*A*-*E*) during the actuation period. The nth contour is at $\pm$ 2.43 $\times$ 10^{-3} $\times$ 2^{n-1} where the solid and dashed lines denote positive and negative values respectively. The MEMS jet issues from x^+=414 to 422 (R_o=6μm). A time-history plot of the jet velocity is shown beneath the contour series. v^*=10 m s^{-1}, ν/v^*=1.5 μm, R=5161, U_∞=253 m s^{-1}, and $\delta^* \approx 3.06 \times 10^{-4}$. See §A.4.12 for a full parameter list.

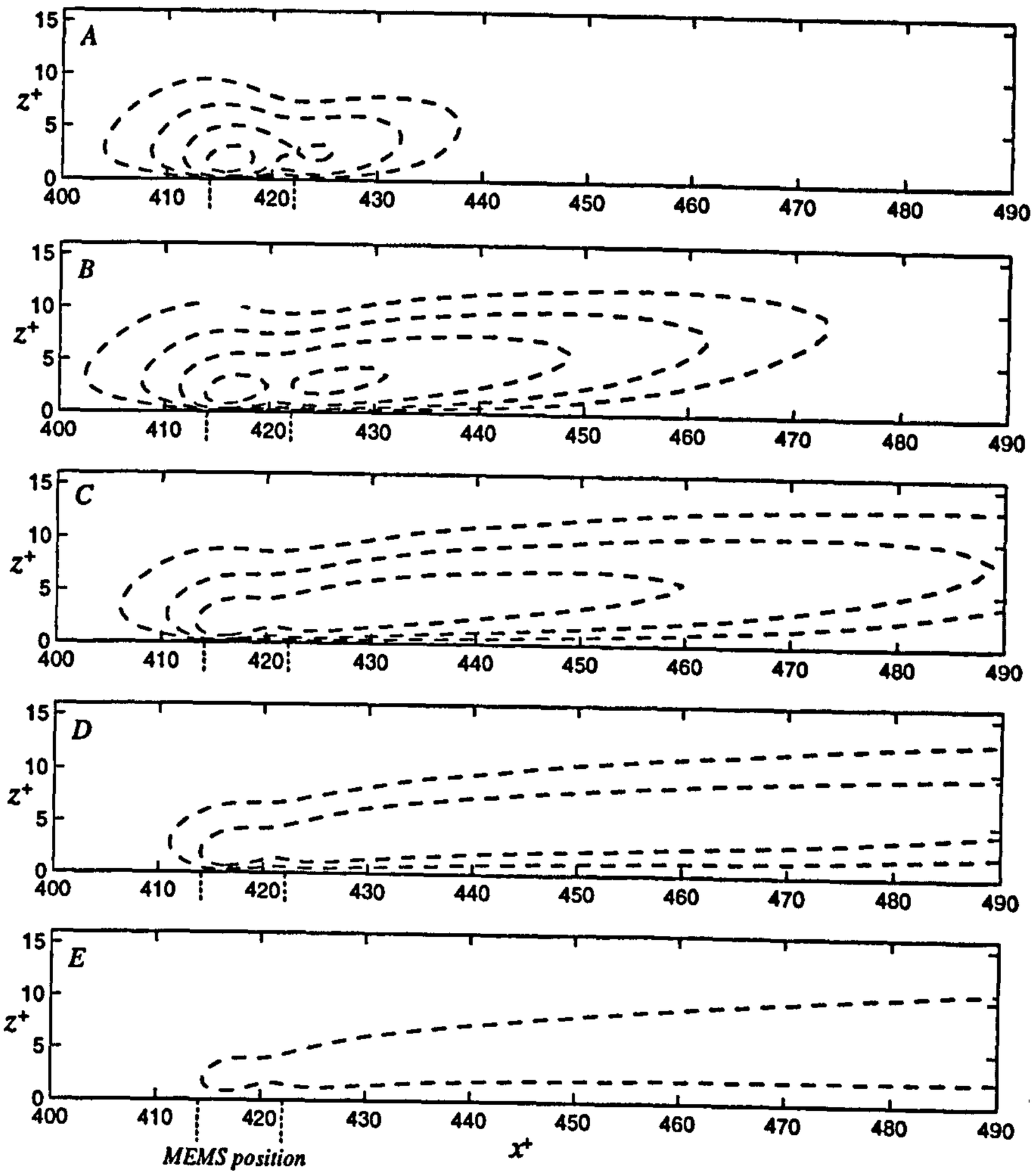

Figure 6.13: The disturbance generated in a turbulent boundary layer by a MEMS jet. Contours of streamwise velocity (u^+) at y^+=0, at times (*A*-*E*) during the actuation period. The nth contour is at $\pm\ 5.06 \times 10^{-3} \times 2^{n-1}$ where the solid and dashed lines denote positive and negative values respectively. The MEMS jet issues from x^+=414 to 422 (R_o=6μm). A time-history plot of the jet velocity is shown beneath the contour series. v^*=10 m s^{-1}, ν/v^*=1.5 μm, R=5161, U_∞=253 m s^{-1}, and $\delta^* \approx 3.06 \times 10^{-4}$. See §A.4.12 for a full parameter list.

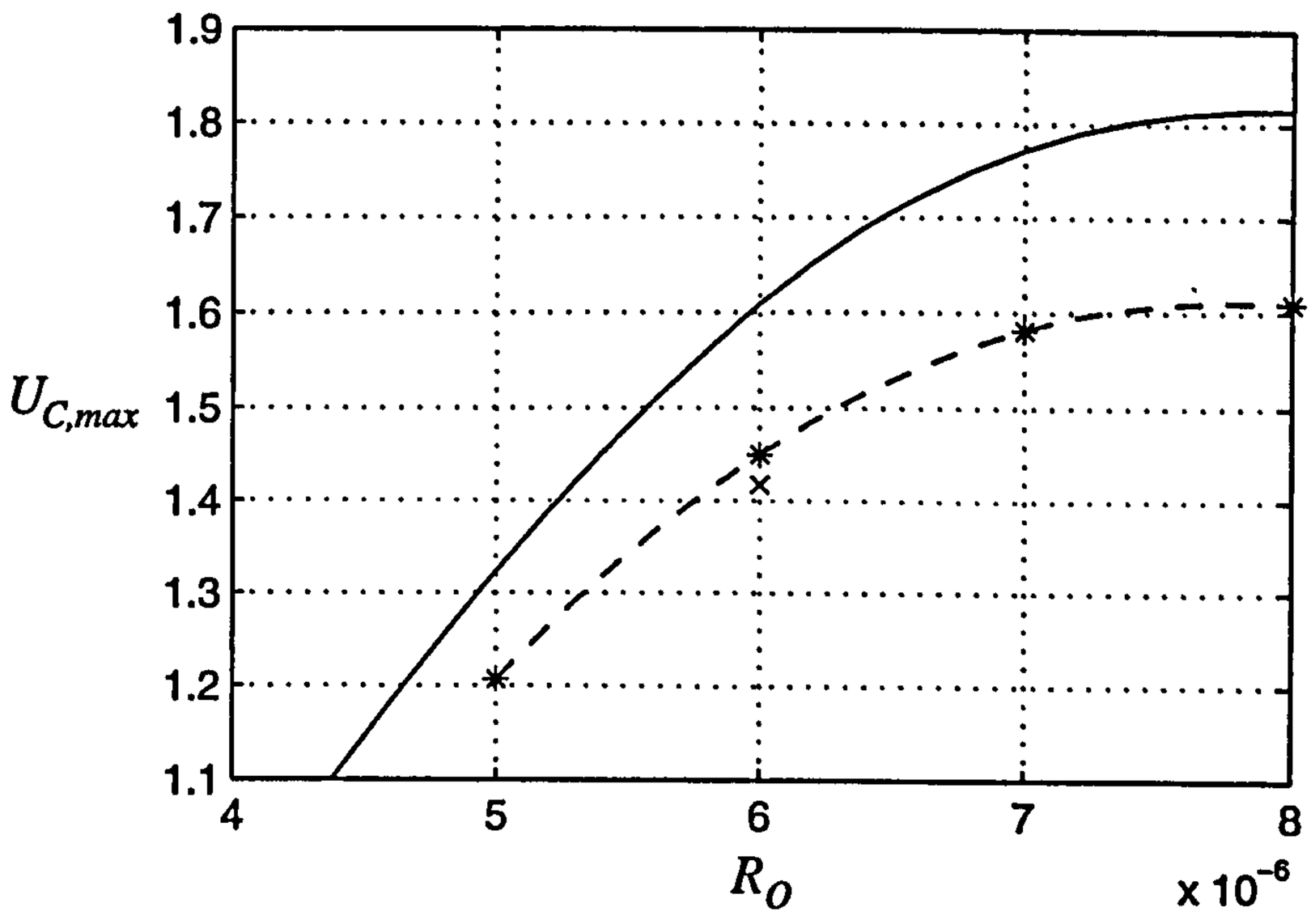

Figure 6.14: The maximum centre-line velocity ($U_{c,max}$) against orifice radius (R_o) for MEMS-scale actuators (g=1 μm). Non-interactive simulations, (-); interactive simulations in a Blasius boundary layer, R=2000, U_∞=30 m s^{-1}, δ^*= 1 mm, (-∗-); and an interactive simulation in a high-speed turbulent boundary layer, v^*=10 m s^{-1}, (×). See §A.4.12 for a full parameter list.

6.4 Helmholtz Resonance

In Chapter 3, §3.5, it was shown that some jet actuators of the diaphragm-cavity design have a Helmholtz frequency at which pressure fluctuations will tend to oscillate. It was also suggested that an external pressure could force the actuator at this frequency producing Helmholtz resonance. Only interactive simulations, of the kind shown in this chapter, are capable of demonstrating this phenomenon – such a simulation is performed in this section.

For this demonstration a quasi-two-dimensional Tollmien-Schlichting wave is generated upstream of an inactive micro-scale actuator. As the wave train passes over the site of the actuator, pressure fluctuations within the disturbance provoke Helmholtz resonance. Figures 6.15 (a) and (b) are side and plan views of the simulation after some time has elapsed. These clearly show a strong disturbance being created by the 'inactive' actuator, that produces further Tollmien-Schlichting waves of increased amplitude. Probably more importantly for practical purposes is Figure 6.15 (c), which shows the velocity history of the actuator experiencing rapidly-increasing amplitudes (nonlinear effects would prevent the continual growth of the velocity). In this example the frequency of the Tollmien-Schlichting wave is comparable to the Helmholtz frequency, but it was not necessary to finely tune the two frequencies to get this resonant effect.

This result has serious implications. Specifically, that any actuator made with a cavity may have the potential to act as a Helmholtz resonator. Spontaneous and uncontrolled Helmholtz resonance of this sort will have detrimental effects in operating, as well as non-operating, modes.

An acknowledgement should be made to Cullen, who inspired this section of work by originally suggesting that actuators of this type could act as Helmholtz resonators. His recent work includes a receptivity study for a laminar flat-plate boundary layer passing over Helmholtz resonators (Cullen 1999).

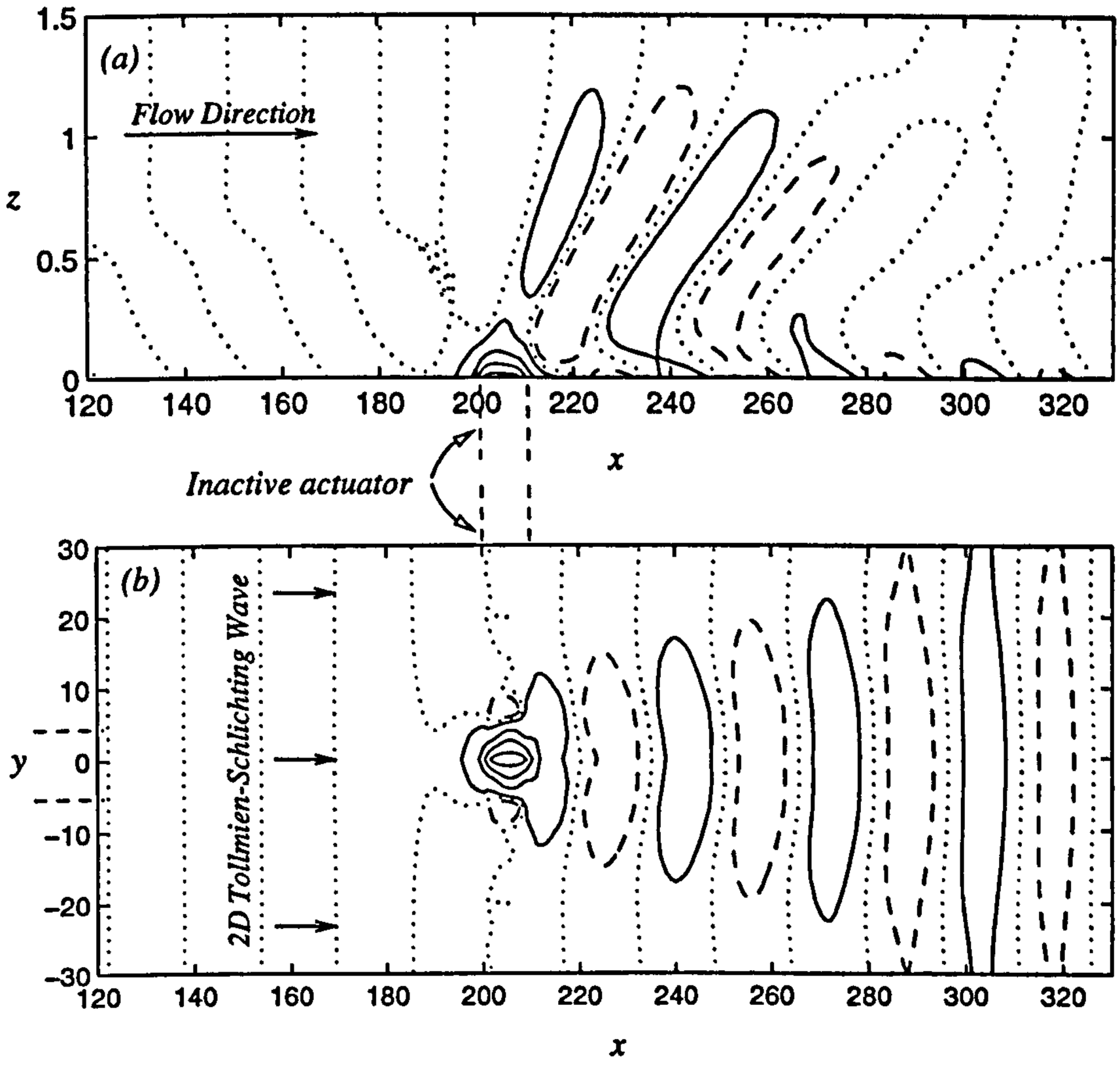

Figure 6.15: An inactive actuator exhibiting Helmholtz resonance caused by an incident quasi-two-dimensional Tollmien-Schlichting wave. (a) Side view – contours of spanwise vorticity perturbation (ω_y) at y=0. (b) Plan view – contours of spanwise vorticity (ω_y) perturbation at z=0. The nth contour is at $\pm$ 1 + 3(n-1) where solid and dashed lines denote positive and negative values respectively; dotted lines are zero-level contours. (c) The corresponding variation with time of the centre-line exit velocity from the inactive actuator. R=2000, U_∞=30 m s^{-1} and δ^*=1 mm. See §A.4.13 for a full parameter list

6.5 Chapter Summary

In this chapter, simulations have been performed using the coupled boundary-layer and actuator code. This code is capable of simulating the interaction between the boundary layer and the actuator.

In §6.1 MEMS- and micro-actuators were tested in a Blasius boundary layer. In the MEMS case, significant damping of the actuator's jet velocity was observed (around 10%). There was little effect on the micro-scale actuator's output. In §6.1.1 a numerical refinement study demonstrated the independence of the results in §6.1 to parameters such as grid spacing and domain length.

The disturbances created by a MEMS pressure-jump actuator in a Blasius boundary layer were shown in §6.2, and a grid-refinement study was performed in §6.2.1. The effect of altering the actuator design was investigated in §6.2.2, where it was illustrated that small changes in orifice radius can seriously affect the boundary-layer disturbance that is generated. In §6.2.3 the Reynolds number of the Blasius boundary layer was varied, although this had no appreciable effect on the dimensionalised results. This demonstrates that the MEMS-scale disturbances are effectively independent of the Blasius boundary layer being considered.

In contrast to this, in §6.3 a MEMS pressure-jump actuator was simulated within a high-speed turbulent boundary layer. Here the disturbance was strongly sheared and a low-speed streamwise-velocity streak was produced downstream of the actuator. The damping effect was shown to be slightly stronger in the turbulent boundary layer.

Finally, in §6.4 the potential for cavity-driven devices to exhibit Helmholtz resonance was demonstrated. This phenomenon occurs as a result of strong interaction between the boundary layer and the MEMS actuator. Such interactive behaviour could not have been simulated by using pre-determined boundary conditions to model the actuator.

Chapter 7

Modelling the Effect of MEMS Actuation on Streaks

In this chapter the principle of targeted control is demonstrated using MEMS-scale jet actuators. In §7.1 the streamwise streaks associated with turbulence reproduction are modelled – these are the targets for control. In §7.2, prescribed simulations (simulations that use prescribed boundary conditions to model the actuator) demonstrate and investigate the basic concept of streak control. Finally, in §7.3, simulations are performed that model the interactive behaviour of the MEMS and the streaks.

Nomenclature

A superscript '+' denotes non-dimensionalisation using the friction velocity, v^*, and the viscous length scale, ν/v^*.

$\bar{}$ = an over bar denotes a dimensional quantity

a^+, b^+ = forcing function constants

d = diaphragm damping (N s m^{-3})

d_{31}, d_{32} = radial/azimuthal piezoelectric constant (m V^{-1})

E_d = elastic modulus of diaphragm material (N m^{-2})

E_p = elastic modulus of PZT material (N m^{-2})

H_c = cavity height (m)

l = orifice length (m)

L = mapped domain stretching factor (dimensionless)

N_c = number of Chebyshev polynomials

N_d = number of grid points in diaphragm finite-difference scheme

N_o = number of grid points in orifice finite-difference scheme

N_y = number of spanwise Fourier modes

R_d = diaphragm radius (m)

R_p = PZT disc radius (m)

R_o = radius of jet/orifice (m)

$R = U_\infty \delta^* / \nu$ = Reynolds number (dimensionless)

t_j = duration of prescribed jet (s)

$t^+ = \bar{t}\, v^{*2} / \nu$ = time (dimensionless)

T_f^+ = duration of body forcing (dimensionless)

$\bar{T} = T^+ \nu / v^{*2}$ = total simulation time (s)

u^+ = streamwise velocity (dimensionless)

u_{max}^+ = maximum streamwise velocity of streak (dimensionless)

U_∞ = free-stream velocity (m s^{-1})

v^* = friction velocity (m s^{-1})

V = voltage (V)

V_m = maximum prescribed-jet velocity (m s^{-1})

x^+, y^+, z^+ = streamwise, spanwise and wall-normal directions (dimensionless)

X_d^+ = streamwise domain length (dimensionless)

X_b^+, X_e^+ = streamwise position of actuator (dimensionless)

Y_d^+ = extent of spanwise domain (dimensionless)

y_f^+ = the wall-normal position of the body force (dimensionless)

δ^* = boundary layer thickness (m)

λ_{opt}^+ = the optimum spanwise wavelength (dimensionless)

ν = kinematic viscosity ($m^2\ s^{-1}$)

ν/v^* = the wall unit (m)

ν_d = Poisson's ratio of the diaphragm material

ν_p = Poisson's ratio of the PZT material

ρ_d = density of diaphragm material ($kg\ m^{-3}$)

ρ_p = density of PZT material ($kg\ m^{-3}$)

7.1 Streak Generation

It is known that three-dimensional disturbances in any shear flow can grow via an *algebraic* instability, termed as such to distinguish it from exponential instabilities. This has been demonstrated by Ellingson and Palm (1975) and Landahl (1980) for three-dimensional perturbations in an inviscid shear flow. The inviscid algebraic growth, together with a viscous-induced damping, constitutes what is sometimes called transient growth. This phenomenon has been demonstrated in viscous shear flows by Hultgren and Gustavsson (1981), Butler and Farrell (1992), and Henningson *et al.* (1993). Transient or algebraic growth is believed to be the cause of 'bypass' transition in boundary layers. It is thought that small perturbations might grow sufficiently during the transient growth period for non-linear effects or secondary instabilities to induce transition, hence *bypassing* traditional mechanisms. The Klebanoff mode (Westin *et al.* 1994, Kendall 1985, Andersson *et al.* 1999, Leib *et al.* 1999), generated by free-stream turbulence, could be a manifestation of algebraic/transient growth (Herbert and Lin 1993, Bertolotti 1997, Goldstein and Wundrow 1998). This hypothesis is in support of the findings of Landahl (1980, 1990), Breuer and Haritonidis (1990), and Henningson *et al.* (1993), who have demonstrated how the *lift-up* effect (a phrase coined by Landahl to describe the mechanism of algebraic growth) leads to longitudinal streaky structures similar to that observed in the Klebanoff mode. Landahl (1980, 1990) and Butler and Farrell (1992) made a connection between the longitudinal streaks and vortices in a fully-turbulent boundary layer and algebraic growth. There is, therefore, an implied equivalence of the Klebanoff mode in the transitional boundary layer to the streamwise vortices in a fully-turbulent boundary layer. The algebraic growth mechanism induces streaks in both cases, and is forced by free-stream turbulence in the transitional case, and inner-boundary-layer turbulence in the developed case. This furthers the analogy between the transitional and the turbulent boundary layer (see Blackwelder 1983).

Here, this analogy has been used to guide the modelling of the turbulent

streaks. Meitz (1996) developed a method of modelling the Klebanoff mode using body forces to emulate the free-stream turbulence. A variation on this approach was used in Chapter 4 to validate the three-dimensional boundary-layer code. Given the apparent similarity between the Klebanoff mode and the streaks in a turbulent boundary layer, it seems reasonable to use similar methods to model them. So in a similar way to that described in §4.3.2, body forces have been used to generate streaks and find the optimum spanwise vortical mode for the turbulent mean-flow profile. There are, however, two main differences from the Klebanoff case. Firstly, an optimum normal position for the body force is also sought, whereas in the Klebanoff case the forcing is free-stream and fixed at a distance from the wall. Secondly, the body forcing acts for a discrete time rather than continuously. This time has been chosen to match the non-dimensional period (t^+=15) of suction used by Gad-el-Hak and Hussain (1986) to artificially generate streaks.

The method used here is similar to that employed by Butler and Farrell (1992) who sought an optimum perturbation to a turbulent profile. They achieved some success by defining the optimum as the disturbance that grows the most in energy during a particular period. The choice of this period was the turbulent eddy turnover time ($t^+\approx$100). Recently, Kim and Lim (2000) suggested that this approximation was incorrect, and that the time for optimum growth is, in fact, much shorter.

Here the optimum streak is not restricted to growth during a predetermined period, but is defined as the streak with the largest streamwise velocity at any time during its evolution (it turns out that the optimum streak reaches its maximum at around t^+=50, which is significantly shorter than the eddy turnover time, and therefore in agreement with Kim and Lim 2000).

7.1.1 Results

The turbulent velocity profile used here, is described in Chapter 5 (§5.3.1) and the following flight-scale boundary-layer characteristics hold for all simulations in this chapter: v^*=10 m s^{-1}; ν/v^*=1.5 μm; $R\approx$5161; U_∞=253 m s^{-1}; and $\delta^*\approx$300 μm. The body-forcing function used to generate the streaks is described in Chapter 4, equation (4.25).

Figure 7.1 shows an example of the algebraic growth initiated by the body force. The same result, in logarithmic form, is shown in Figure 7.2. This highlights the algebraic nature of the growth and the onset of viscous-induced decay at later times.

A series of these simulations were performed to find the optimum spanwise wavelength of the perturbation for a given wall-normal position (note that at different heights, the body force is normalised to generate the same strength of vorticity at the point of application). Figure 7.3 shows how the optimum spanwise wavelength varies linearly with wall-normal position. Butler and Farrell (1992) also observed an increase in optimum spanwise wavelength with wall-normal position. Figure 7.4 shows the maximum streamwise velocity against optimised spanwise wavenumber; an optimum of optimums is clearly shown at around 100 ν/v^*. This result is in agreement with the average streak spacing observed in many experiments, including those of Kline *et al.* (1967).

The spatial and temporal development of the optimum streak are shown in Figure (7.5), and side-, plan-, and front-view contours of the streak (at t^+=50) are shown in Figure 7.6. The streaks do continue to elongate after this time, although the magnitude of the streamwise velocity reduces. At the later times the streamwise convection velocity of the streak is approximately 11v^*. This is in very close agreement with the experimental observations of Johansson *et al.* (1987), 13v^* (as cited in Rathnasingham 1997) and the numerical results of Johansson *et al.* (1991), 10.6v^*.

The negative perturbations in Figure 7.6, indicated by the dashed lines, are

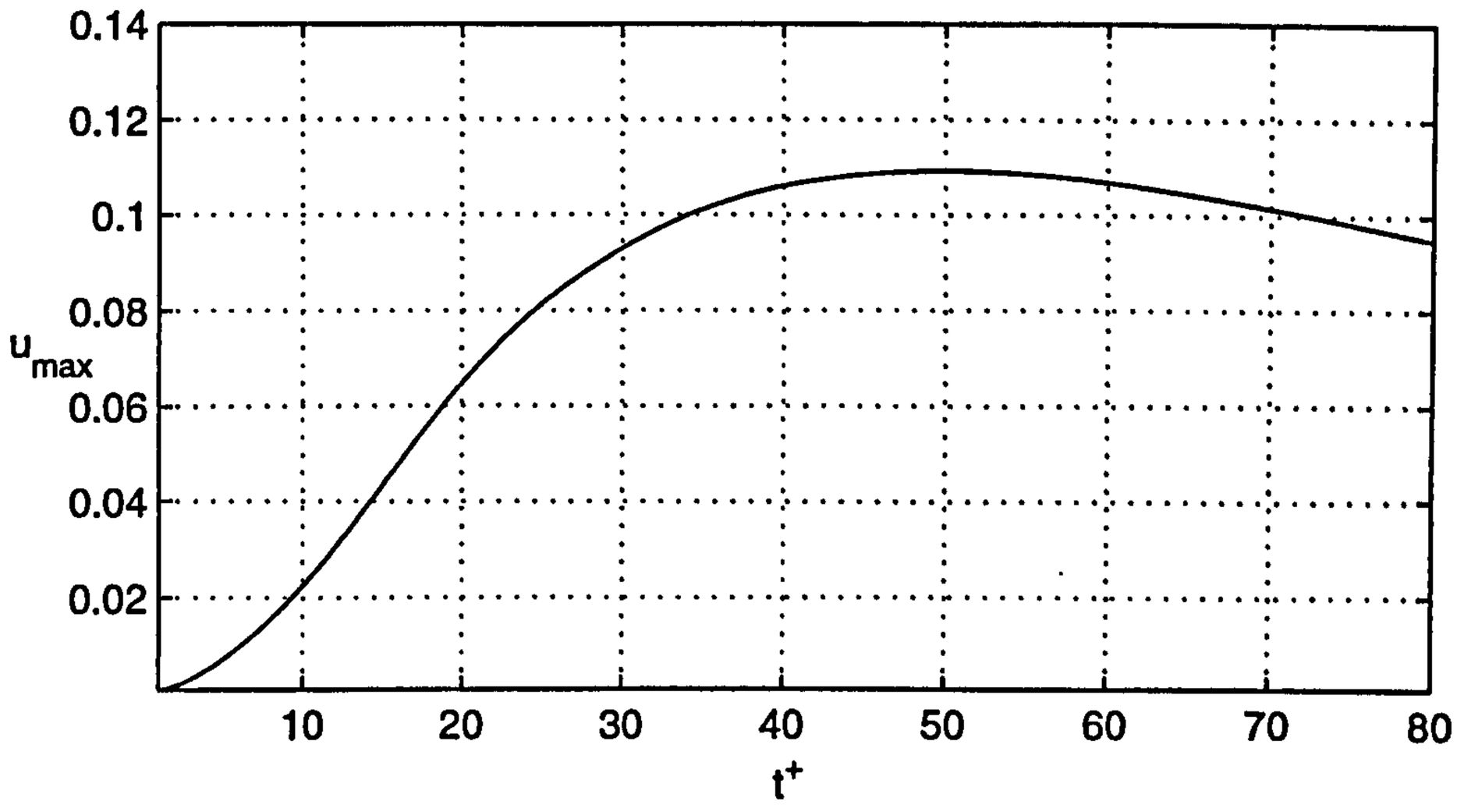

Figure 7.1: The variation of maximum streamwise velocity with time of a three-dimensional perturbation generated by a body force. See §A.5.2 for simulation parameters.

the low-speed streaks. In reality these have a more active role in turbulence reproduction, but in these linear simulations they behave identically to the high-speed streaks. This is not a serious limitation of the model as it is not necessarily the breakdown stages of the streak that are of interest to targeted control – if the streak is already breaking down, control might be too late or superfluous. Linearity in itself, is not a flaw of the current simulations, since many authors have supported and demonstrated the role of linear mechanisms in turbulence production (Landahl 1980, 1990, Johansson *et al.* 1987, Rathnasingham 1997, Rathnasingham and Breuer 1997b).

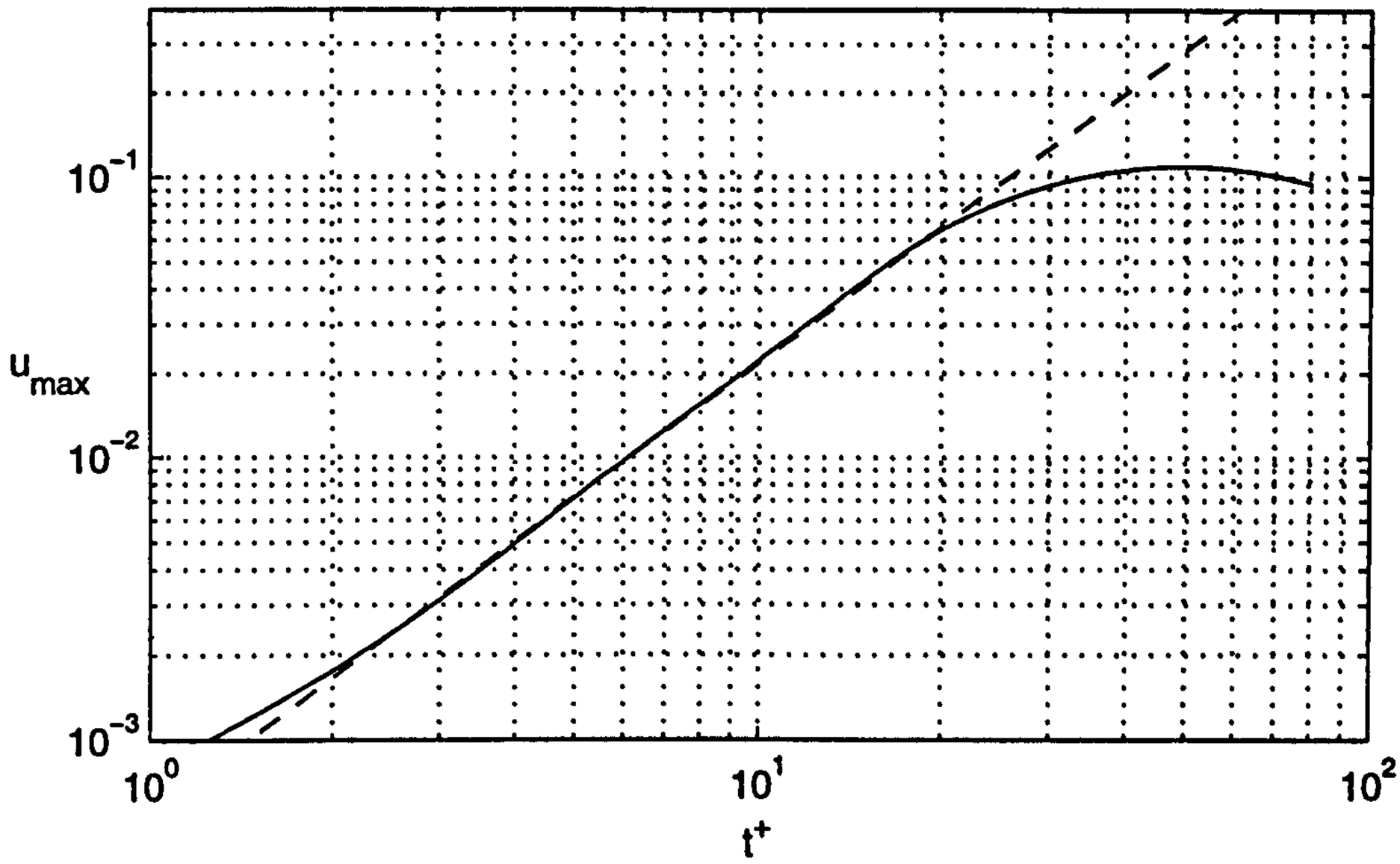

Figure 7.2: The variation of maximum streamwise velocity with time (–). The broken line is the function: $u_{max} \propto (t^+)^{1.6}$. See §A.5.2 for simulation parameters.

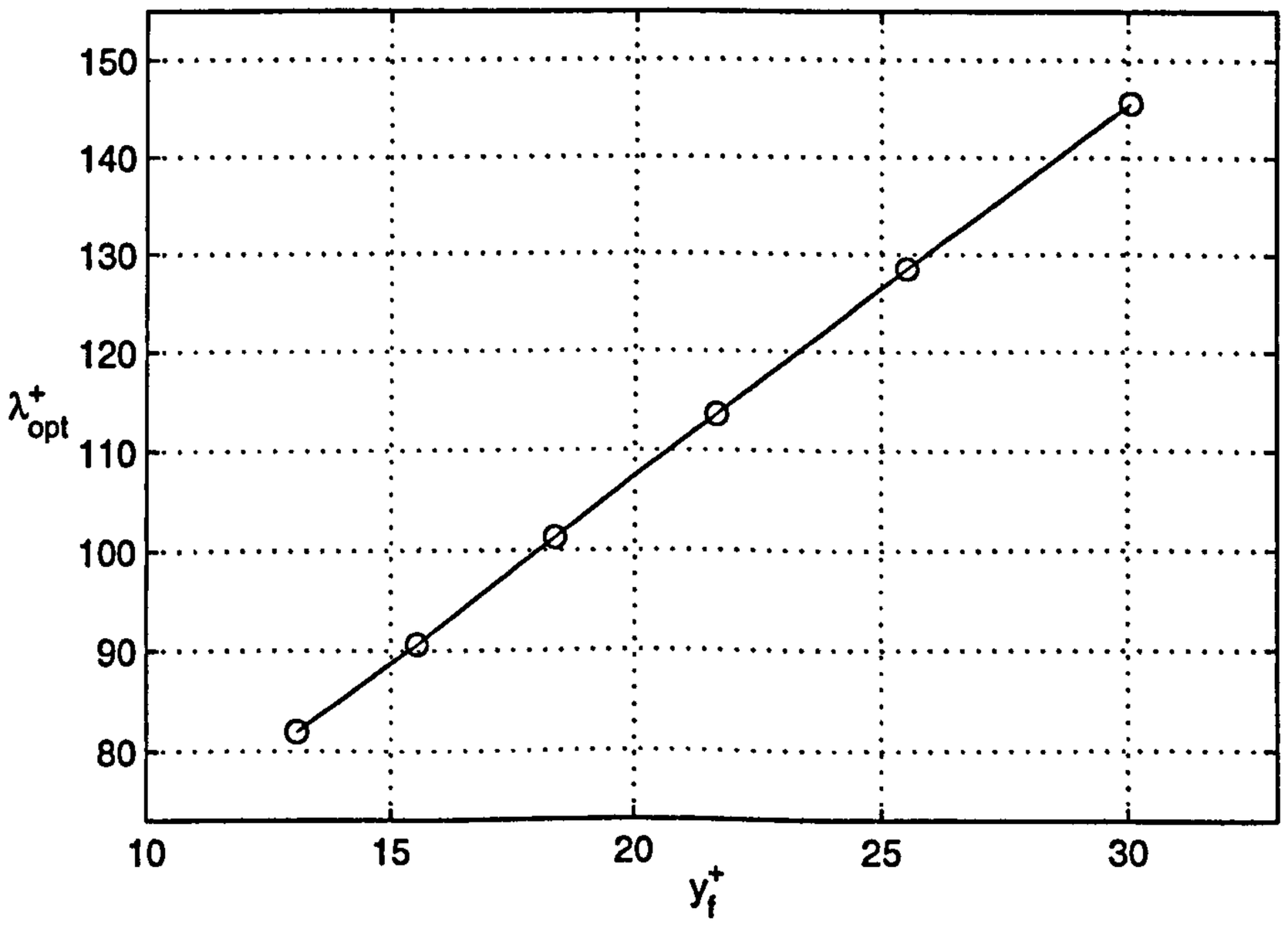

Figure 7.3: The optimum spanwise wave length of the body force (λ^+_{opt}) versus the normal distance from the wall (y^+_f). See §A.5.1 for simulation parameters.

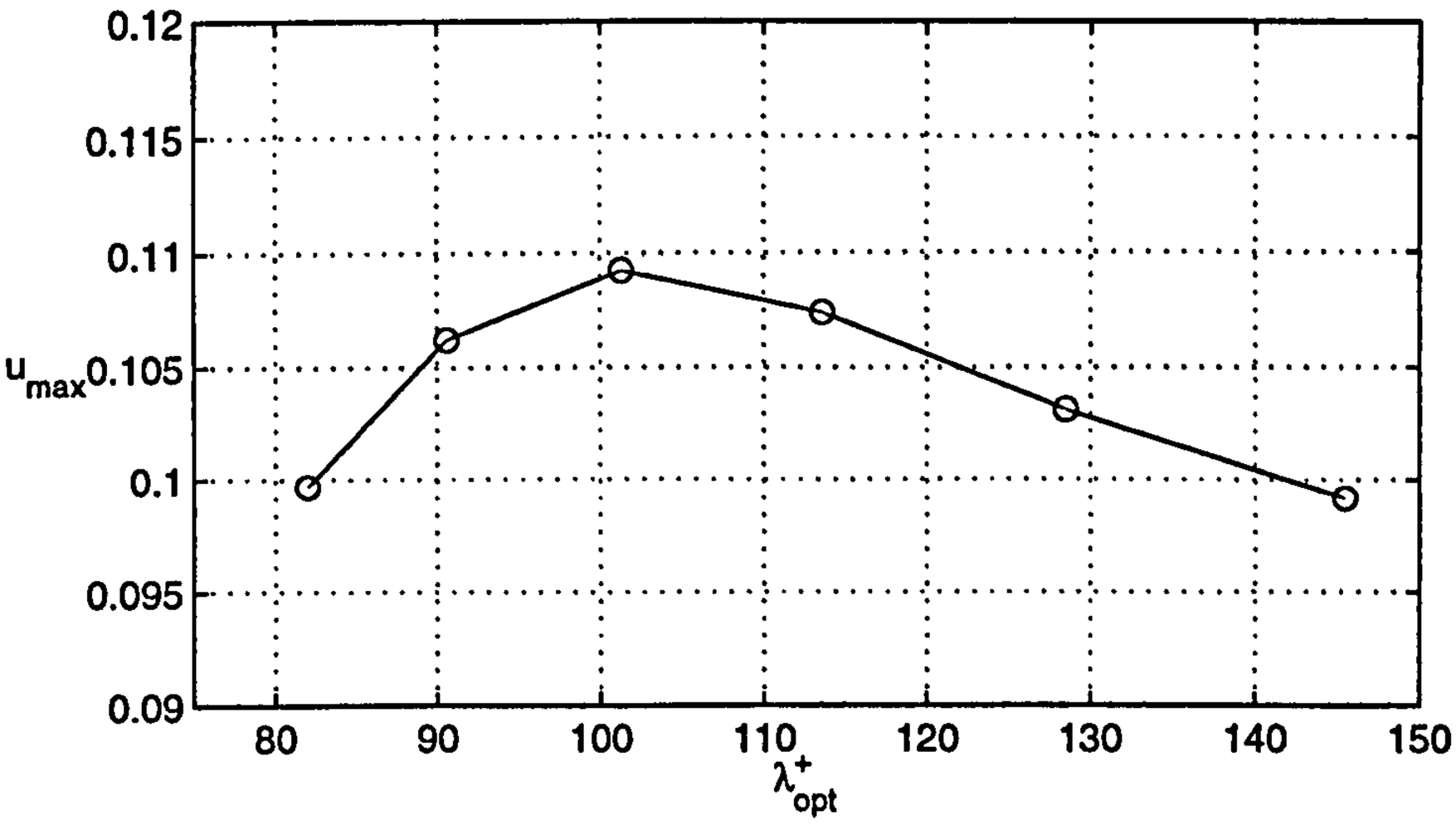

Figure 7.4: The maximum streak magnitude (u_{max}) versus the optimum spanwise wavelength of the body force (λ^+_{opt}) for the particular wall-normal position. See §A.5.1 for simulation parameters.

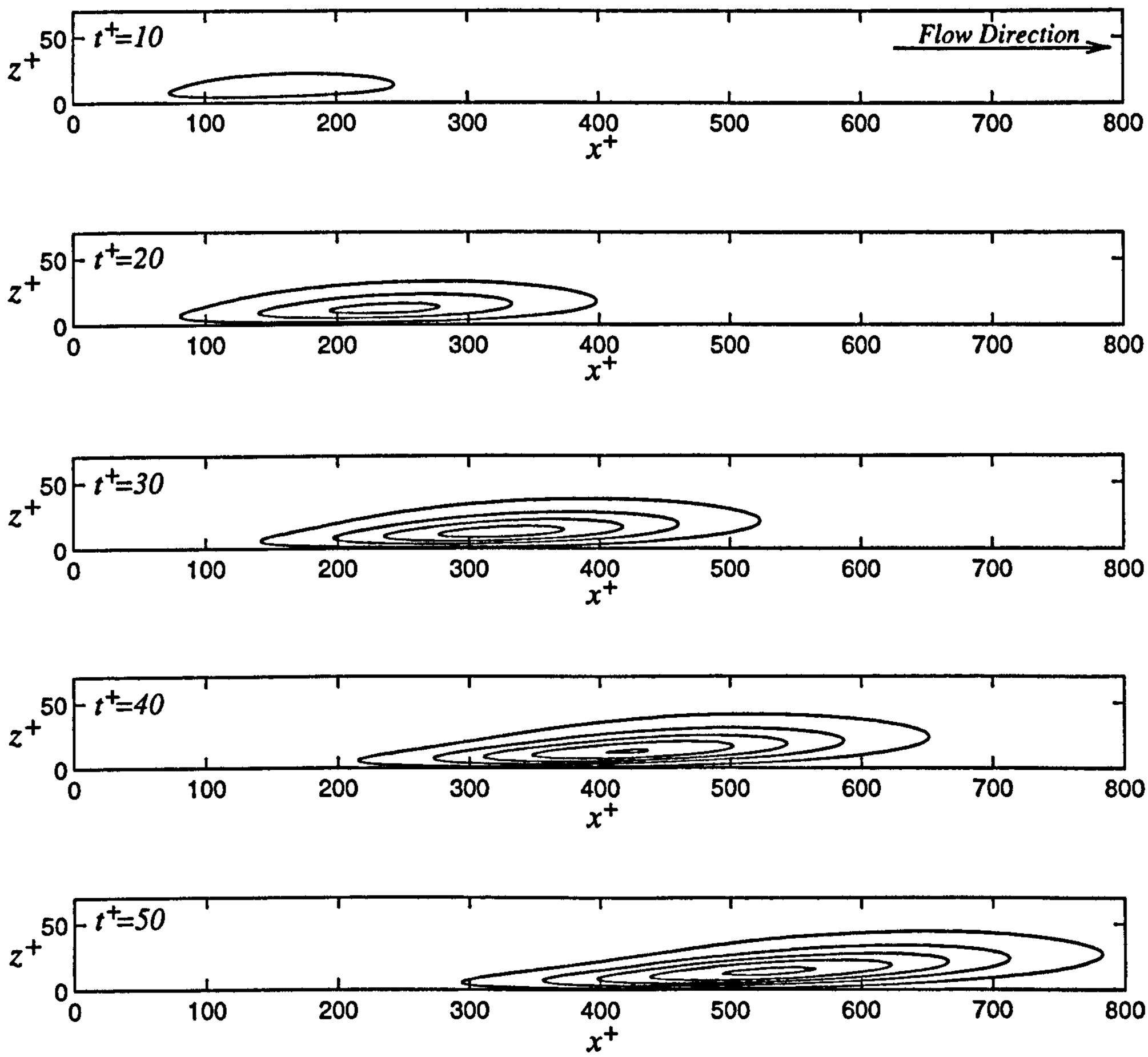

Figure 7.5: The temporal and spatial development of the optimum streak. Side-view contours of streamwise velocity at times leading to the point of the streak's maximum magnitude. The nth contour is at u^+=0.019 + 0.038(n–1). The body force is positioned at x^+=125, z^+=18.4, and is applied from t^+=0 to 15. See §A.5.2 for simulation parameters.

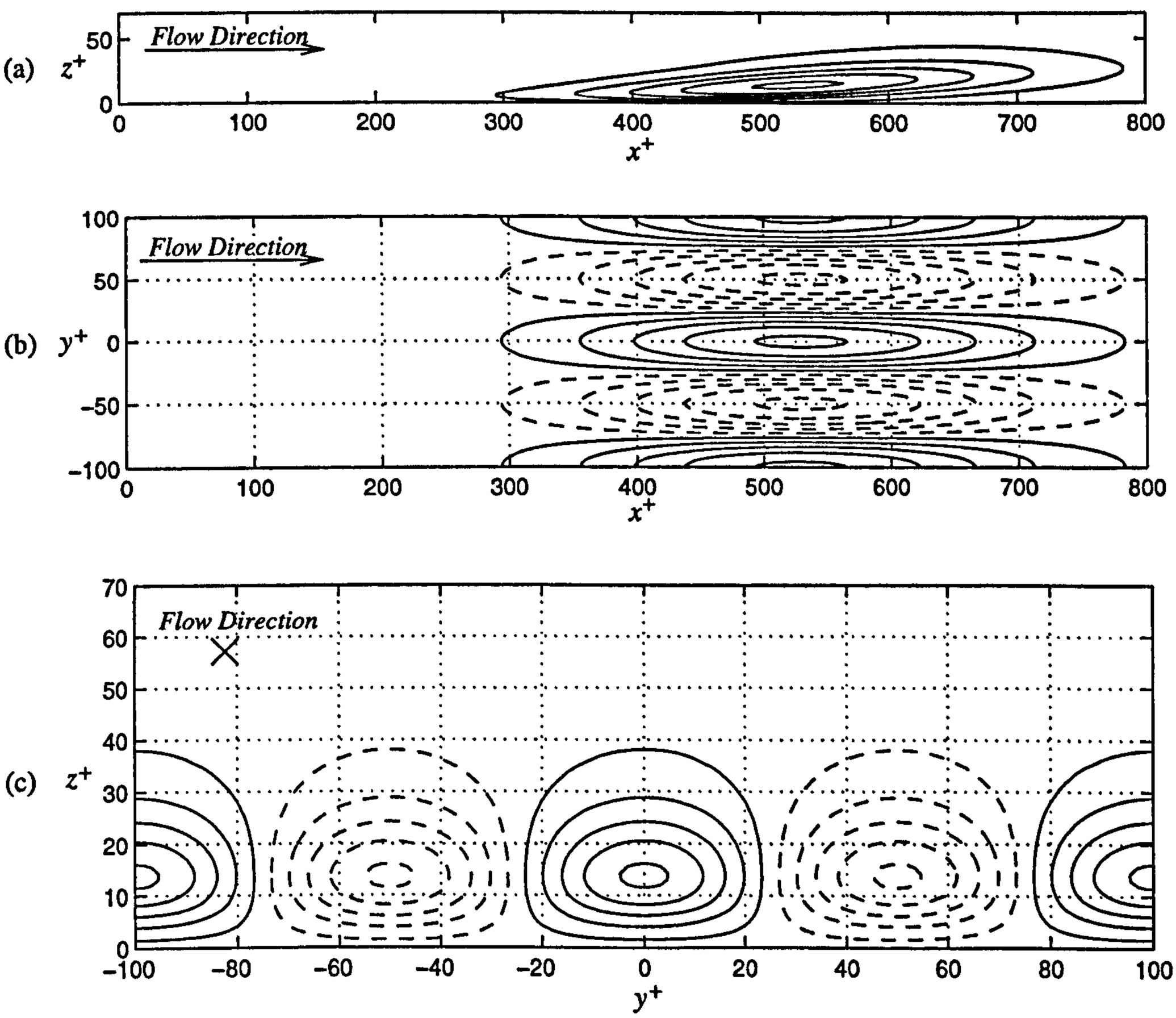

Figure 7.6: The optimum streak at its maximum amplitude. Side-, plan-, and front-view contours of streamwise velocity (u^+) at $t^+ = 50$. The nth contour is at $u^+ = \pm(0.019 + 0.038(n\text{-}1))$ where solid and broken lines denote positive and negative values, respectively. (a) Side view at $y^+ = 0$; (b) plan view taken at the wall-normal position (z^+) that has the greatest velocity for each streamwise position; (c) front view at $x^+ = 528$. See §A.5.2 for simulation parameters.

7.2 Streak Control: Prescribed Simulations

The streaks modelled in the previous section are used here to test the effectiveness of MEMS actuation in targeted control. There are two main concepts to be investigated: streak enhancement and streak cancellation. The motive of streak enhancement is to increase the bursting frequency, and thereby turbulence production. This is achieved by making the structure more prone to the spanwise inflectional instability (Swearingen and Blackwelder 1987) or to the onset of nonlinear effects. Either way, this means increasing the magnitude of the streaks. The motive of streak cancellation is to reduce the bursting frequency, thereby inhibiting the production of turbulence. This is achieved by reducing the magnitude of the streaks (direct skin-friction reduction schemes are only interested in reducing the magnitude of the high-speed streaks near the wall – Carlson and Lumley 1996).

The actuation is modelled as prescribed boundary conditions as in Chapter 5 (see equation (5.3) for the prescribed function). Because the boundary-layer code is linear, superposition makes it easy for different configurations of a jet disturbance to be applied to the streak with relatively few numerical simulations. In this section, only two computations have been performed: The disturbances created from a long-duration MEMS jet (simulation parameters §A.5.3) and the disturbance created from a short-duration MEMS jet (simulation parameters §A.5.4). The results from each case are superposed onto the streak (simulation parameters §A.5.2) in various ways to investigate the basic concepts of streak control.

7.2.1 The General Principle

Figure 7.7 is a demonstration of the control of a high-speed streak using positive actuation (blowing as opposed to suction). The streak has been reduced in magnitude owing to the negative streamwise-velocity perturbation caused by the blowing. Similar effects were observed by Carlson and Lumley (1996a) and Ja-

cobson and Reynolds (1998). Note that all the linear simulations shown here, are equivalent to simulations of opposite sign; for example, in this case, the results can be inverted to represent the effect of suction on a low-speed streak.

The disturbance created by the jet is very localised and Figure 7.8 demonstrates a better positioning of the MEMS device. A slightly greater reduction in streak magnitude is achieved along with a reduction of shear stress at the wall (at t^+=50).

Figure 7.9 shows front-view contours of the streaks and actuation. The central high-speed streak is pushed away from the wall, although the effect is limited to the spanwise extent of the device itself. This suggests that to efficiently reduce the drag associated with the high-speed streaks, devices should be made as wide (or diameter as large) as the streak width. However, as with streak spacing, there is likely to be significant variation in the streak width. The stronger actuation generates a negative perturbation underneath the high-speed streak, and is perhaps more likely to make the structure unstable than to reduce its chances of breakdown. There will certainly be some point at which increasing the velocity of the jet will fail to yield further rewards.

The high-speed streak in Figure 7.10 is controlled with negative actuation (suction). The aim of such control is to increase the magnitude of the streak and this is clearly demonstrated in the figure. Figure 7.11 shows the front view of the streak at its maximum magnitude. Here it can be seen that the point of maximum streak magnitude is brought closer to the wall and that there is a significant increase in wall shear. These suction results are also equivalent to a simulation of blowing underneath low-speed streaks. In fact, since there is not the risk of ingesting dust, blowing in this way is perhaps a better method of enhancing bursting.

It is envisaged that arrays of MEMS will be used to control large numbers of streaks randomly distributed in space and in time. An idealised demonstration of this is shown in Figure 7.12. The method for turbulence enhancement is to

apply blowing under high-speed streaks and suction under low-speed streaks; the opposite configuration is used for cancellation. A similar scheme was applied in Choi *et al.* (1994), referred to as out-of-phase control for cancellation, and in-phase control for enhancement.

7.2.2 Actuator Effectiveness

So far, considerable attention has been drawn to the optimisation of actuators and the jets they produce. In Chapter 5 it was conjectured that the net mass flow from a jet was the most appropriate performance criterion for the actuators being considered (pressure-jump actuators – see Chapter 3, §3.4). To test whether or not the conjecture holds for streak control, a definition of effective actuation in terms of streak control must be established. The most obvious measure of the success of control is the reduction in maximum streak velocity. However, a reduction in velocity magnitude over the entire streak is more desirable than a very localised velocity reduction. Hence, the chosen measure of actuator effectiveness is the integrated velocity reduction over the entire streak area (this is only performed at the wall-normal position where the streak velocity is maximum – where velocity reduction/enhancement is most crucial).

Two jets of different durations, but with the same jet velocity, are tested separately on the streaks. Their actuation is timed and positioned for maximum effect (at t^+=50); the results are shown in Figure 7.13. The long-duration jet, which is twice as long as the short-duration jet, has certainly been more effective at reducing the maximum streak velocity. To get a clearer picture, the disturbances from the two jets are shown in Figure 7.14 without the presence of the streaks. The long-duration jet produces a low-speed streak that is much longer (spatially) than the short-duration jet. Figure 7.15 compares the velocity reductions of the two jets on the centre-line of the streak regions. As the spanwise extent of the disturbances are almost the same in both cases, integration of the curves in Fig-

ure 7.15 provide suitable estimations for the performance – the longer jet is found to be twice as effective as the shorter jet. This is in agreement with the net-mass-flow performance criterion, as the long-duration jet has twice the net mass flow of the short-duration jet.

Although it does depend on how you define effective actuation, this result suggests that the net mass flow from an actuator is a key feature in the design of devices for targeted control. It is also relevant to other actuators, such as the rising bump of Carlson and Lumley (1996a,b). According to the net-mass-flow performance criterion the effectiveness of the bump is governed by its area and its maximum displacement, not necessarily by its velocity.

7.2.3 Distributed Control

The results in §7.2.1 have shown that the bulk of the disturbance tends to stay localised around the orifice of the actuator. If it is desirable to strengthen or weaken the streak at all times during the evolution, the single actuation method is very inefficient. In this section, eight weaker and shorter actuators are used to follow the streak and apply the actuation at appropriate times. Figure 7.16 shows the cancellation of a high-speed streak using an array of actuators distributed in the streamwise direction that are triggered at different times. Figure 7.17 shows the enhancement of a low-speed streak using the same method. The combined net mass flow of the shorter and weaker jets is the same as the net mass flow in a single long-duration jet of §7.2.1 (Figures 7.7 and 7.8). For the given mass flux this is a much more effective means of control, albeit more complicated to implement.

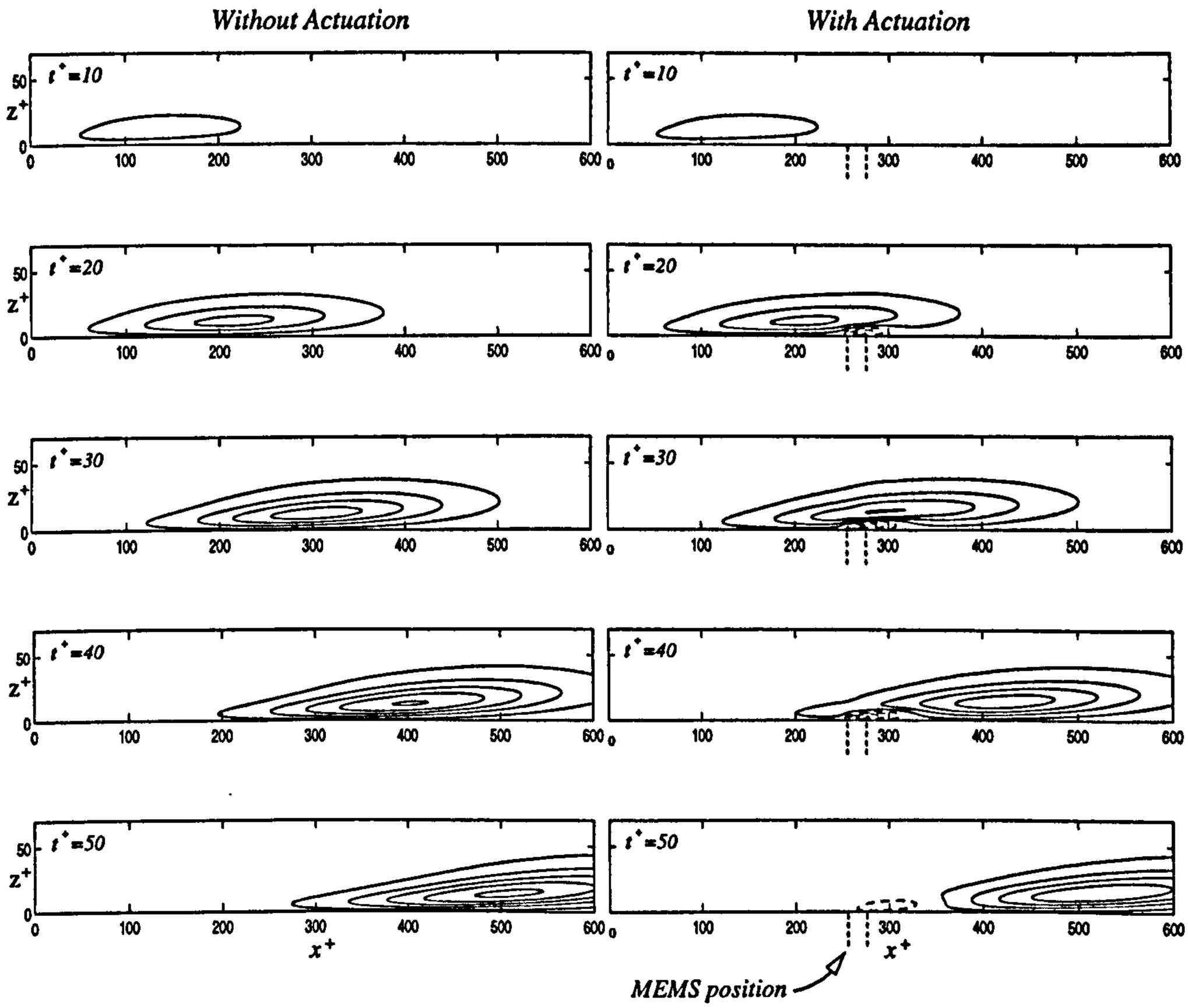

Figure 7.7: The effect of actuation on the development of a high-speed streak. Side-view contours (y^+=0) of streamwise velocity at times leading to the point of the streak's maximum magnitude. The MEMS jet issues during the period t^+=10–50, and its position is indicated by the vertical dashed lines at x^+=257–277 (R_o=15μm, t_j=6μs, V_m=2.56 m s^{-1}). The nth contour is at u^+=± (0.019 + 0.038(n–1)) where solid and broken lines denote positive and negative values, respectively. See §A.5.2 and §A.5.3 for simulation parameters. This simulation is also equivalent to negative actuation (suction) on a low-speed streak; in this case contour values would be inverted.

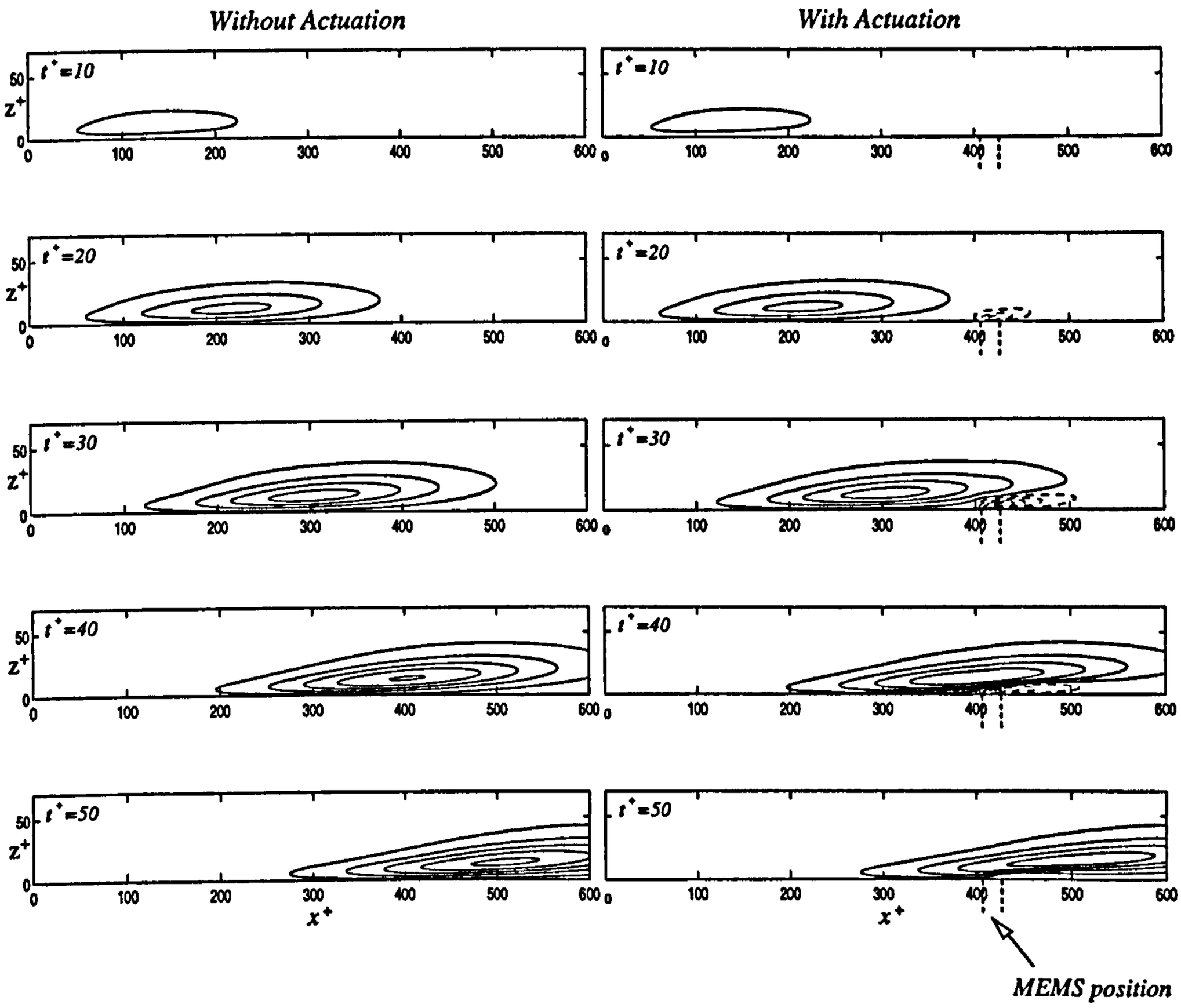

Figure 7.8: The effect of actuation on the development of a high-speed streak. Side-view contours (y^+=0) of streamwise velocity at times leading to the point of the streak's maximum magnitude. The MEMS jet issues during the period t^+=10–50, and its position is indicated by the vertical dashed lines at x^+=407–427 (R_o=15μm, t_j=6μs, V_m=2.56 m s^{-1}). The nth contour is at u^+=± (0.019 + 0.038(n–1)) where solid and broken lines denote positive and negative values, respectively. See §A.5.2 and §A.5.3 for simulation parameters. This simulation is also equivalent to negative actuation (suction) on a low-speed streak; in this case contour values would be inverted.

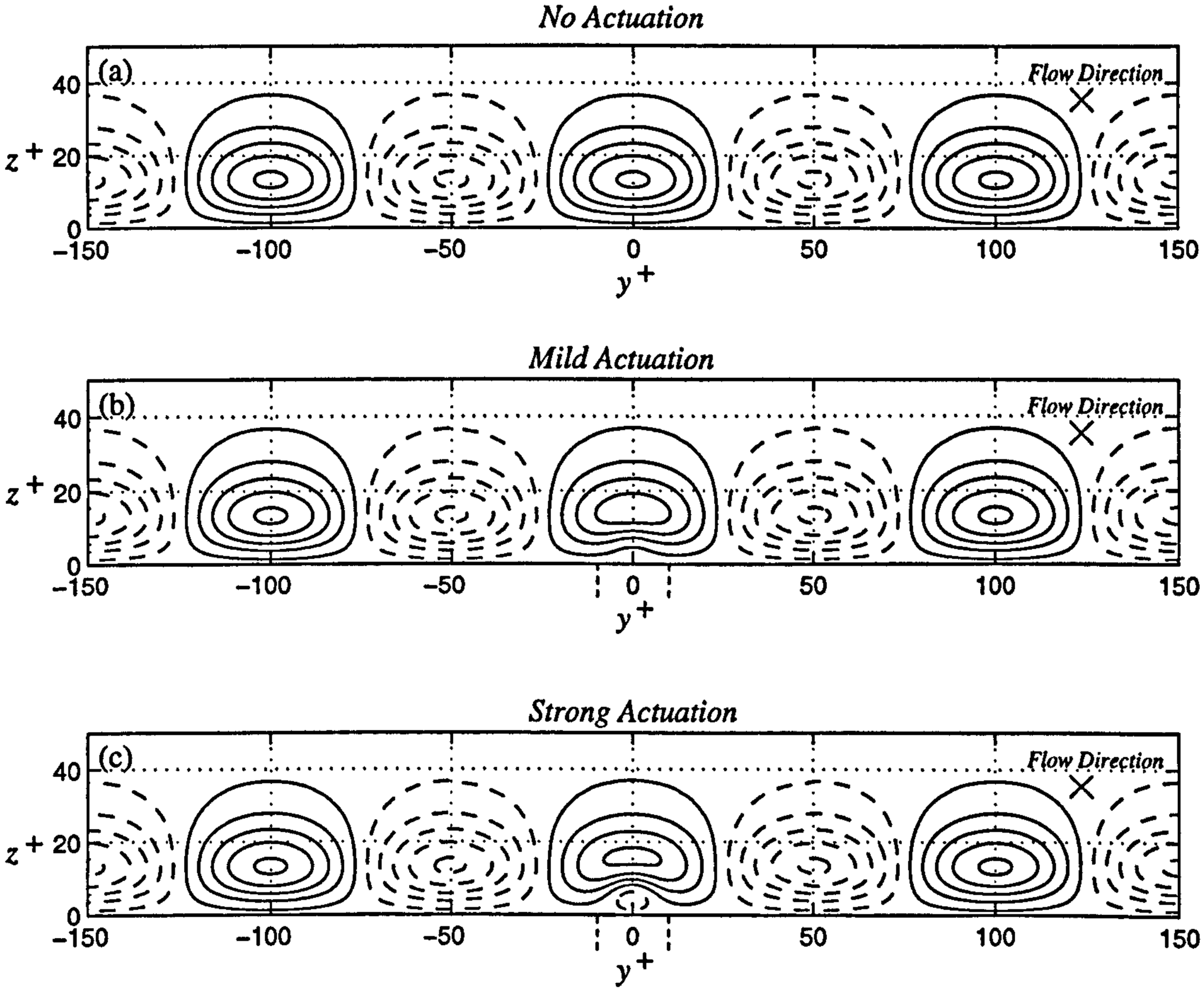

Figure 7.9: The effect of actuation on the magnitude of a high-speed streak. Front-view contours of streamwise velocity (u^+) at $t^+ = 50$ and $x^+ = 528$; the nth contour is at $u^+ = \pm$ (0.019 + 0.038(n–1)) where solid and broken lines denote positive and negative values, respectively. (a) No actuation V_m=0, (b) mild actuation V_m=2.53 m s^{-1}, (c) strong actuation V_m=5.06 m s^{-1}. The spanwise position of the MEMS is indicated by the vertical dashed lines at y^+=-10–10 (R_o=15μm, t_j=6μs). See §A.5.2 and §A.5.3 for simulation parameters. This simulation is also equivalent to negative actuation (suction) on a low-speed streak; in this case contour values would be inverted.

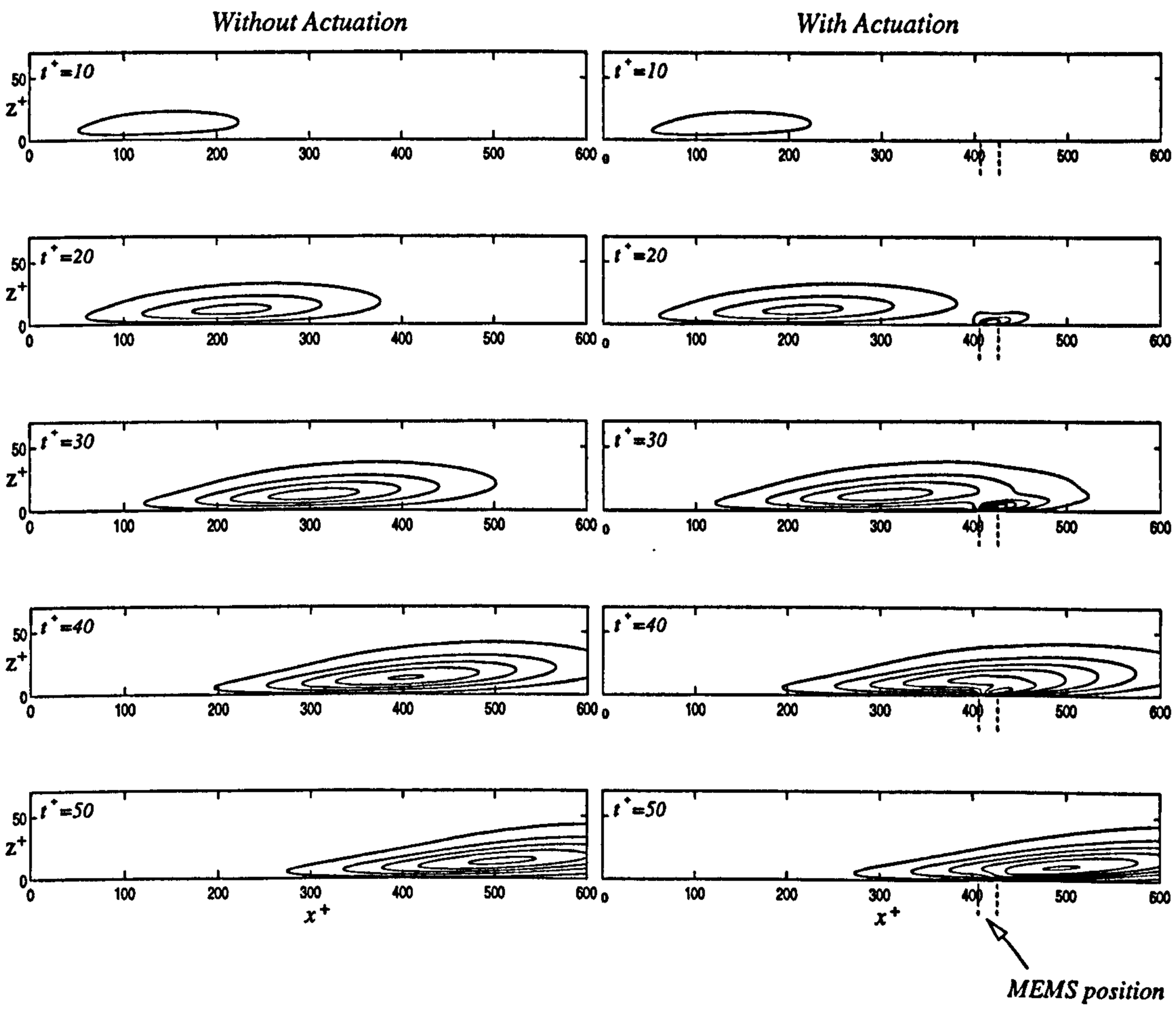

Figure 7.10: The effect of negative actuation (suction) on the development of a high-speed streak. The actuation occurs during the period t^+=10–50, and its location is indicated by the vertical dashed lines at x^+=407–427 (R_o=15μm, t_j=6μs, V_m=–2.56 m s^{-1}). The nth contour is at $u^+=\pm(0.019 + 0.038(n–1))$ where solid and broken lines denote positive and negative values, respectively. See §A.5.2 and §A.5.3 for simulation parameters. This simulation is also equivalent to positive actuation on a low-speed streak; in this case contour values would be inverted.

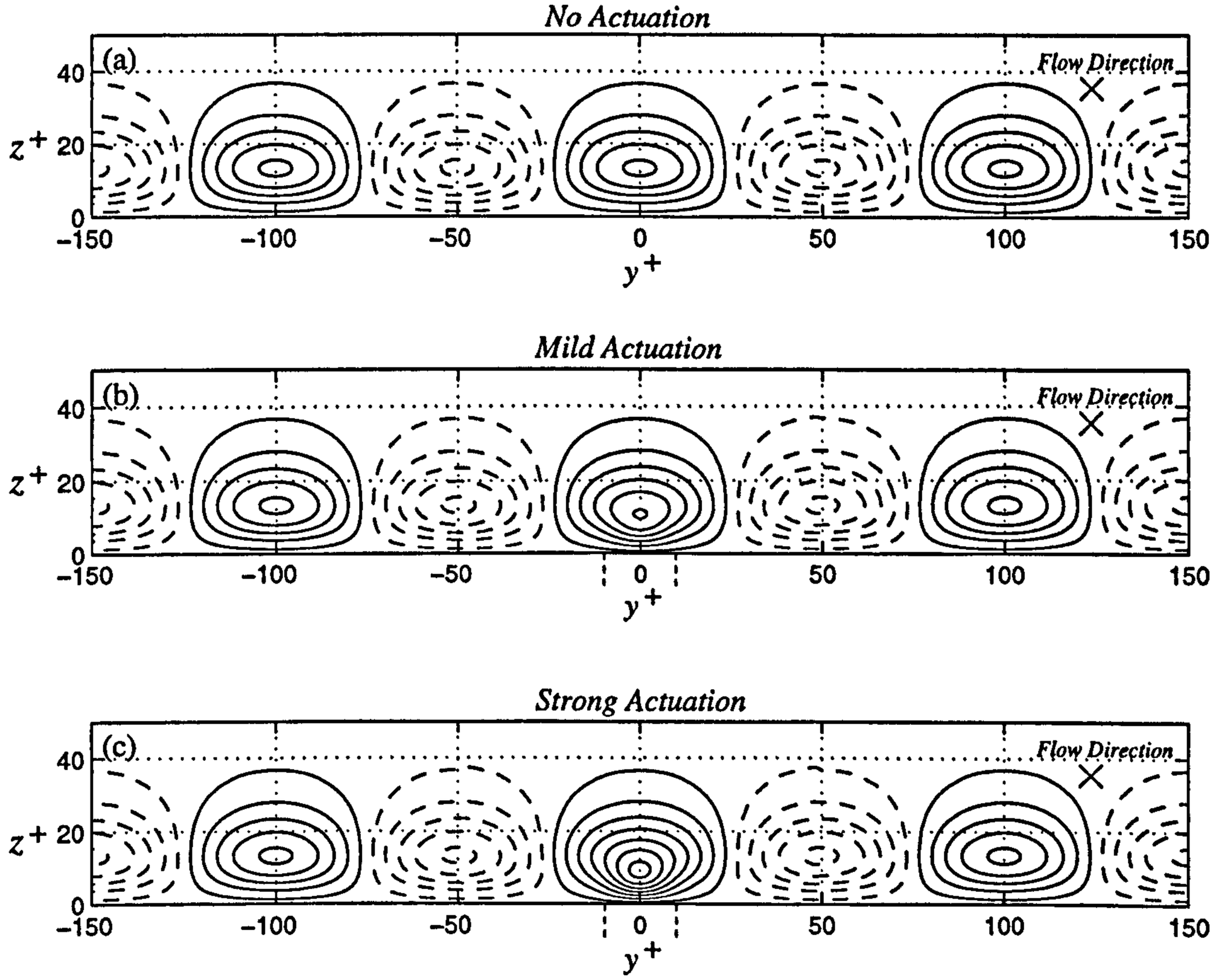

Figure 7.11: The effect of negative actuation (suction) on the magnitude of a high-speed streak. Front-view contours of streamwise velocity at t^+=50 and x^+=528; the nth contour is at $u^+=\pm(0.019 + 0.038(n-1))$ where solid and broken lines denote positive and negative values, respectively. (a) No actuation V_m=0, (b) mild actuation V_m=-2.53 m s^{-1}, (c) strong actuation V_m=-5.06 m s^{-1}. The spanwise extent of the MEMS is indicated by the vertical dashed lines at y^+=-10–10 (R_o=15μm, t_j=6μs). See §A.5.2 and §A.5.3 for simulation parameters. This simulation is also equivalent to positive actuation on a low-speed streak; in this case contour values would be inverted.

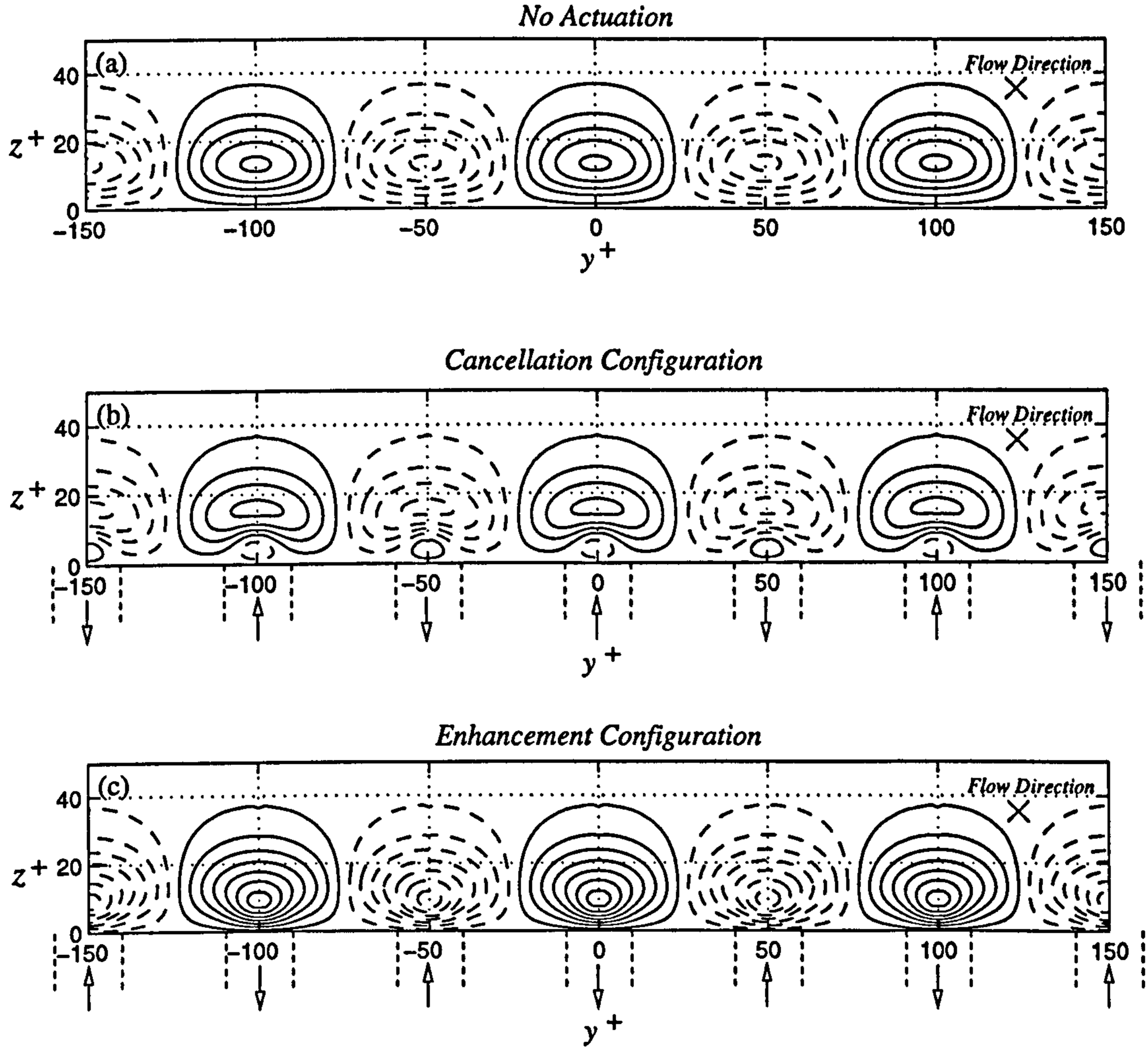

Figure 7.12: The effect of distributed actuation on the magnitude of an array of high- and low-speed streaks. Front-view contours of streamwise velocity at t^+=50 and x^+=528; the nth contour is at u^+=± (0.019 + 0.038(n–1)) where solid and broken lines denote positive and negative values, respectively. (a) No actuation V_m=0, (b) cancellation configuration – suction under low-speed streaks and blowing under high-speed streaks, V_m=±5.06 m s^{-1} (c) enhancement configuration – blowing under high-speed streaks and suction under low-speed streaks, V_m=±5.06 m s^{-1}. See §A.5.2 and §A.5.3 for simulation parameters. The spanwise positions of the MEMS are indicated by the vertical dashed lines at y^+=50i–10 and 50i+10, for i=-3,-2,..,3. (R_o=15μm, t_j=6μs)

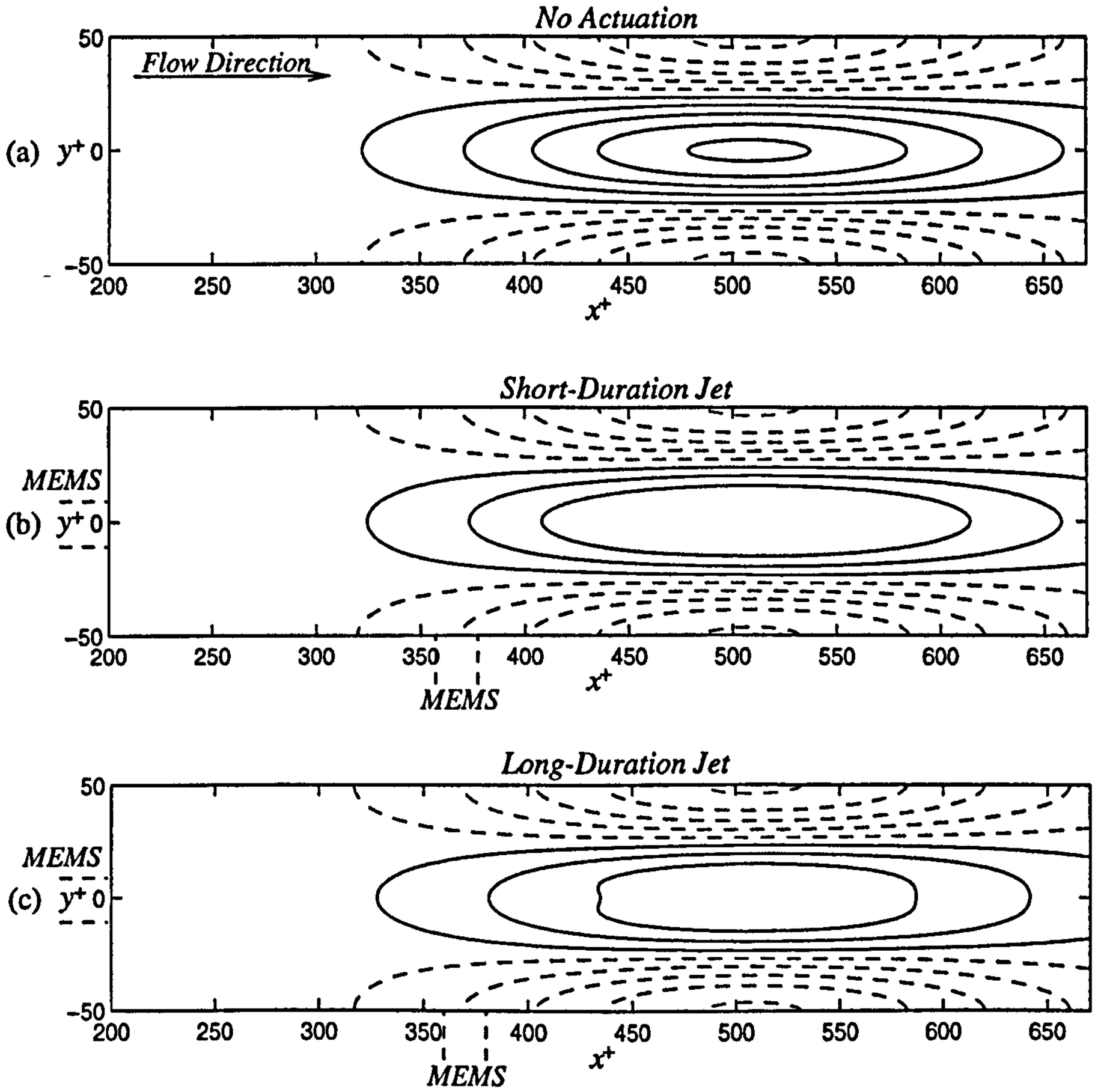

Figure 7.13: The effect of jet duration on the magnitude reduction of a high-speed streak. Plan-view contours of streamwise velocity at t^+=50 and z^+=13.8; the nth contour is at u^+=± (0.019 + 0.038(n–1)) where solid and broken lines denote positive and negative values, respectively. (a) No actuation: V_m=0; (b) short-duration jet: period of actuation t^+=30–50, MEMS location x^+=357–377 (R_o=15μm), V_m=5.06 m s^{-1}; (c) long-duration jet: period of actuation t^+=10–50, MEMS location x^+=360–380 (R_o=15μm), V_m=5.06 m s^{-1}. See §A.5.2, §A.5.3, and §A.5.4 for simulation parameters. This simulation is also equivalent to negative actuation (suction) on a low-speed streak; in this case contour values would be inverted.

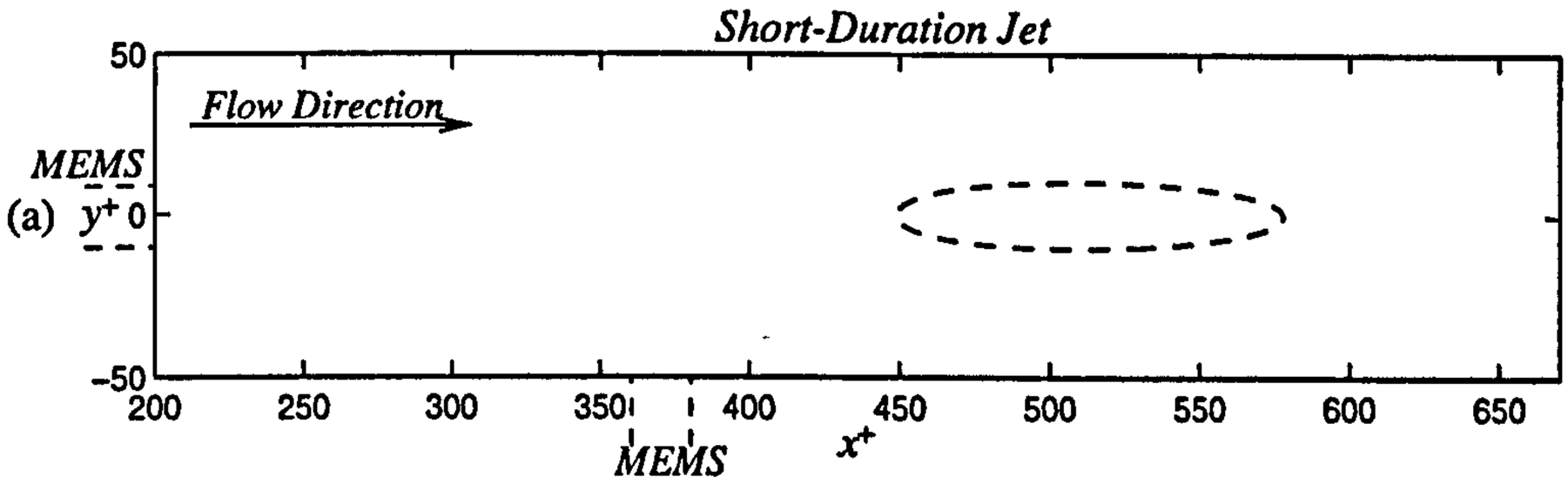

Figure 7.14: The streamwise velocity perturbation generated by a MEMS jet in the absence of streaks. Plan-view contours of streamwise velocity at t^+=50 and z^+=13.8; the broken contour is at u^+=-0.019. (a) short-duration jet: period of actuation t^+=30–50, MEMS location x^+=357–377 (R_o=15μm), V_m=5.06 m s^{-1}; (b) long-duration jet: period of actuation t^+=10–50, MEMS location x^+=360–380 (R_o=15μm), V_m=5.06 m s^{-1}. See §A.5.2, §A.5.3, and §A.5.4 for simulation parameters.

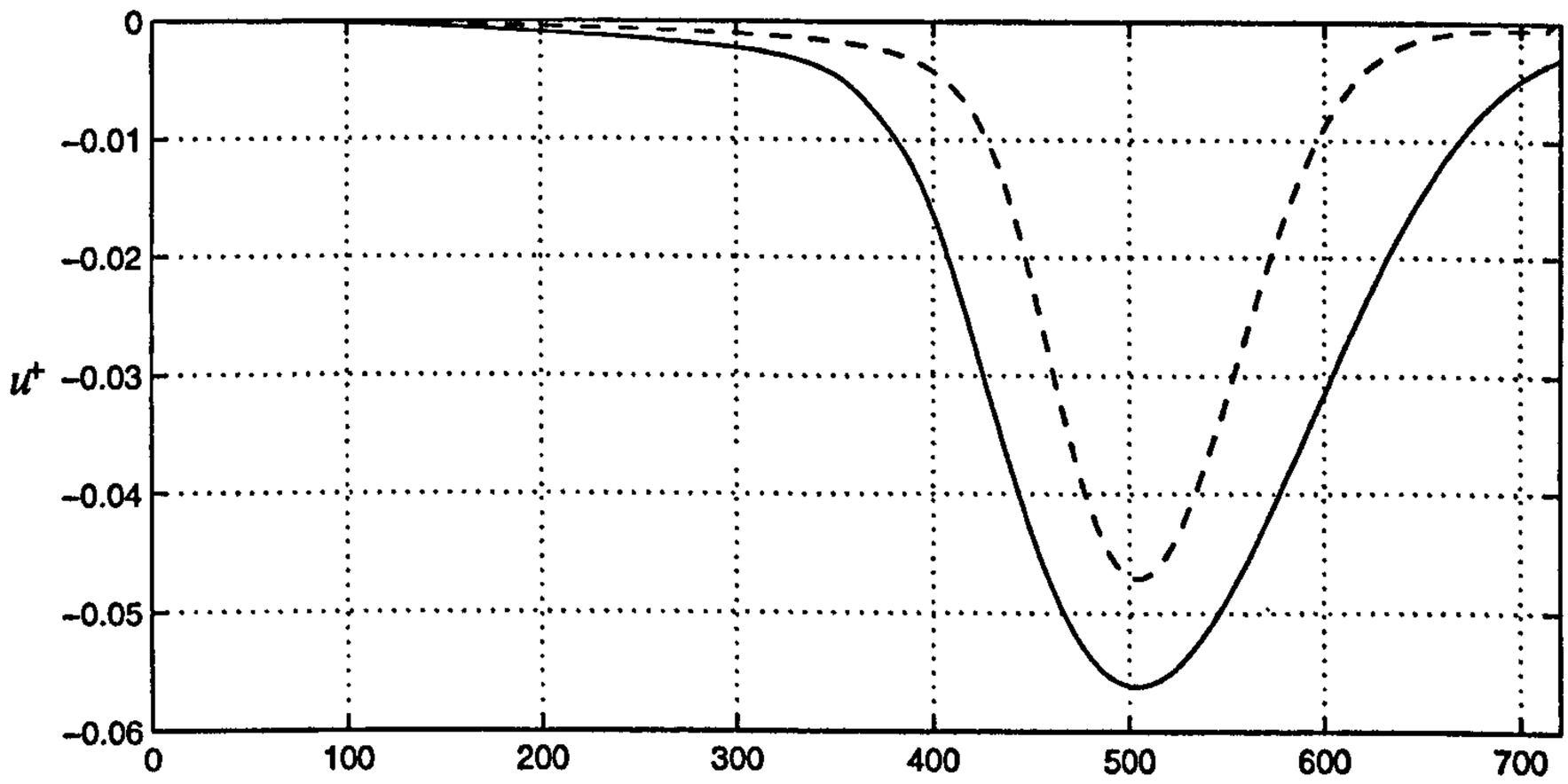

Figure 7.15: The streamwise velocity perturbation generated by a MEMS jet in the absence of streaks (t^+=50, y^+=0 and z^+=13.8). Short-duration jet (--): period of actuation t^+=30–50, MEMS location x^+=357–377 (R_o=15μm), V_m=5.06 m s^{-1}; long-duration jet (-): period of actuation t^+=10–50, MEMS location x^+=360–380 (R_o=15μm), V_m=5.06 m s^{-1}. See §A.5.2, §A.5.3, and §A.5.4 for simulation parameters.

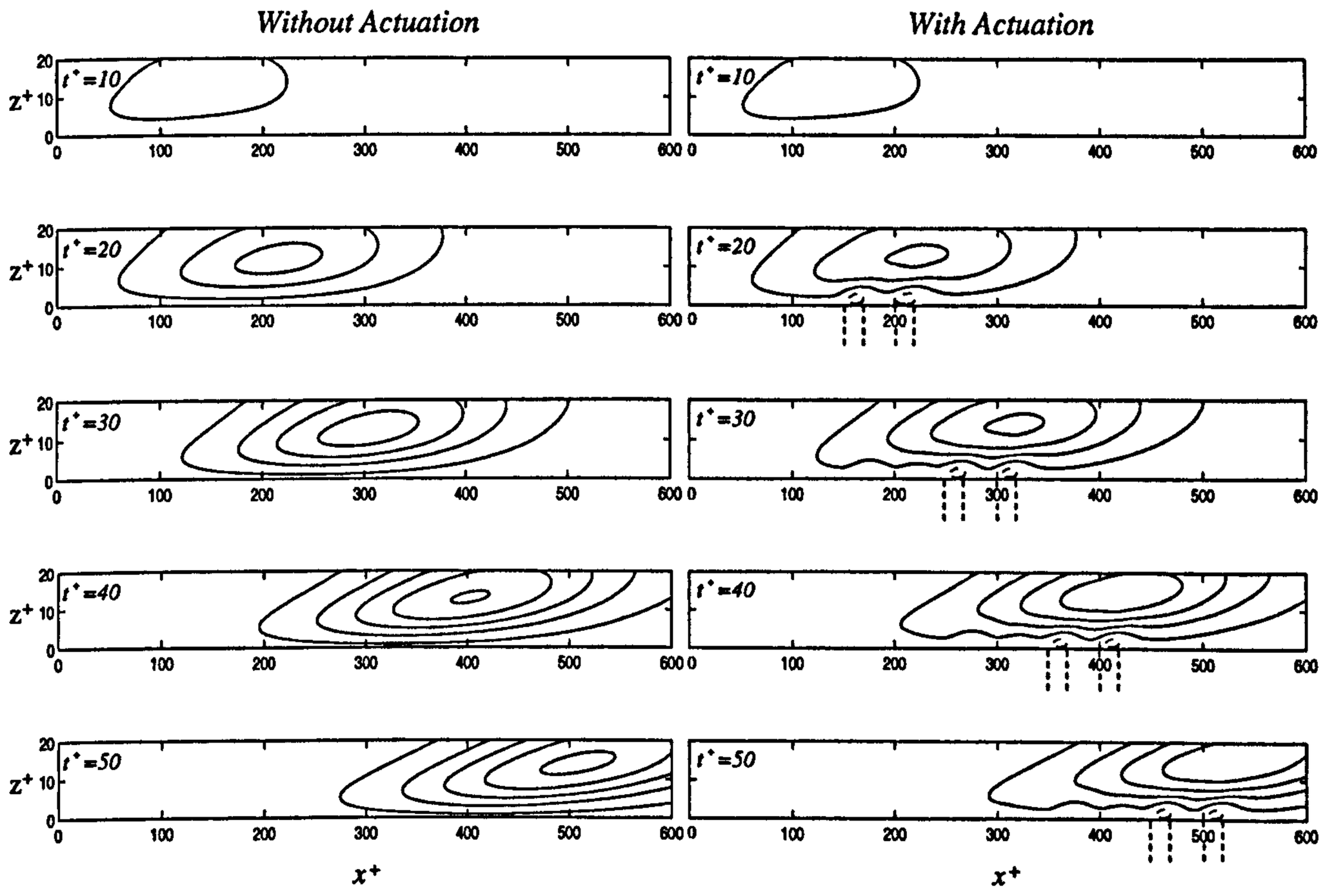

Figure 7.16: The effect of distributed actuation on the development of a high-speed streak. Side-view contours (y^+=0) of streamwise velocity at times leading to the point of the streak's maximum magnitude; the nth contour is at u^+=± (0.019 + 0.038(n–1)) where solid and broken lines denote positive and negative values, respectively. There are eight actuators in total each with V_m = 0.63 m s^{-1}. The mth actuator is positioned at x^+=100+50m, 120+50m (R_o=15μm) and its period of actuation is from t^+=10m to 10+10m (t_j=3μs). See §A.5.2 and §A.5.4 for simulation parameters. This simulation is also equivalent to negative actuation (suction) on a low-speed streak; in this case contour values would be inverted.

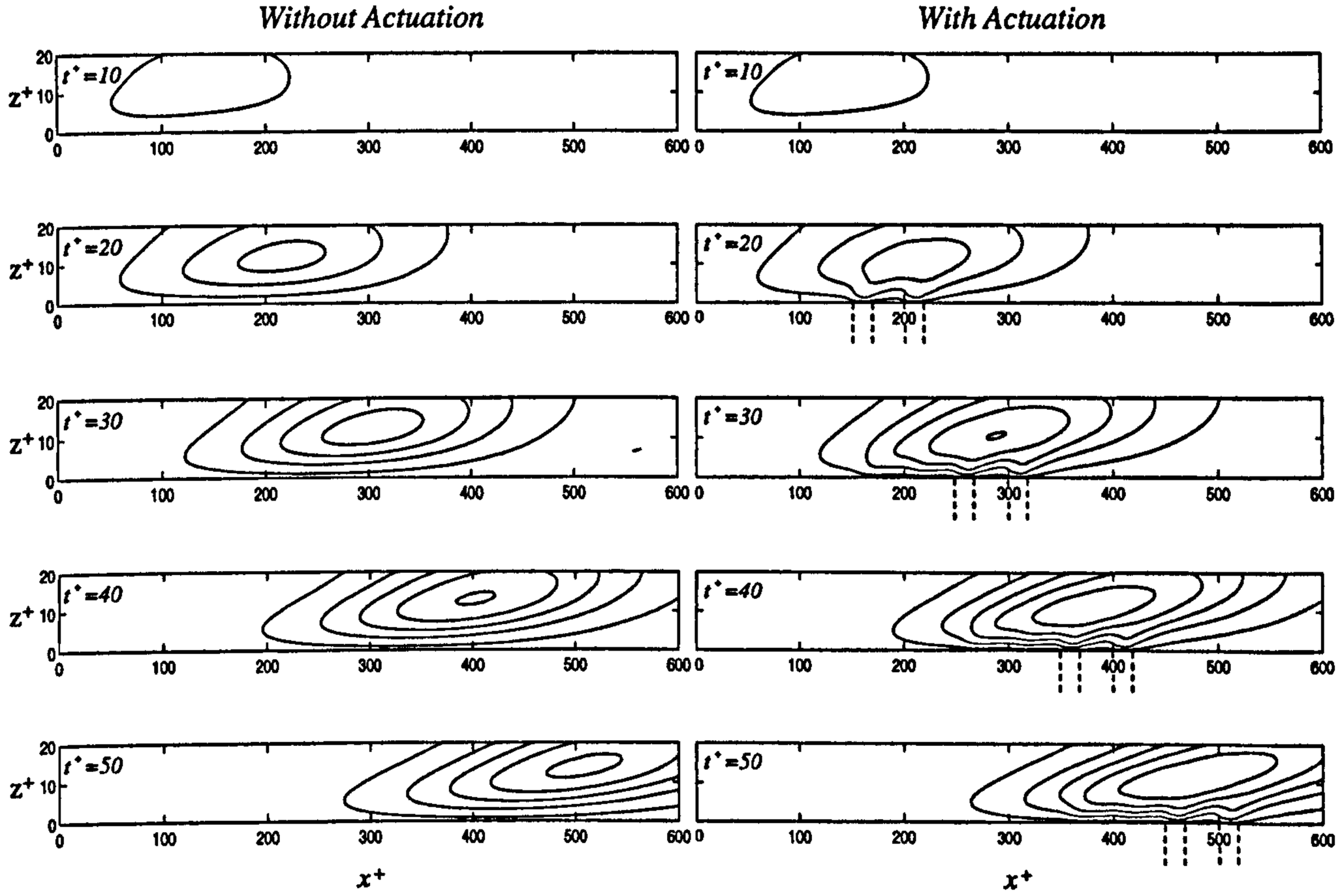

Figure 7.17: The effect of distributed actuation on the development of a low-speed streak. Side-view contours (y^+=0) of streamwise velocity at times leading to the point of the streak's maximum magnitude; the nth contour is at u^+=–(0.019 + 0.038(n–1)) where solid lines denote *negative* values. There are eight actuators in total, each with V_m = 0.63 m s^{-1}. The mth actuator is positioned at x^+=100+50m, 120+50m (R_o=15μm) and its period of actuation is from t^+=10m to 10+10m (t_j=3μs). See §A.5.2 and §A.5.4 for simulation parameters. This simulation is also equivalent to negative actuation (suction) on a high-speed streak; in this case contour values would be inverted.

7.3 Streak Control: Interactive Simulations

All previous studies based on numerical simulation have disregarded the interactive effects between the actuator and the external flow to be controlled (apart from Rizzetta *et al.* 1999, although only synthetic-jet flow into still air was investigated). In this section attempts are made to model the interactive behaviour of actuators and streaks.

7.3.1 Numerical Method

In the last section many scenarios were investigated with only a few prescribed simulations having been performed. However, the same superposition method cannot be exercised for interactive simulations. Another advantage of prescribed simulations is that the streaks and the jets can be simulated separately on different grids, with grid resolutions set to appropriate levels for resolving the separate flow structure's details. The problem with combining the two onto a mutual grid for a coupled simulation is that the combination of the maximum grid spacing, defined by the jet, and the minimum domain length, defined by the streak, creates a very demanding computation. However, with some assumptions, this problem can be circumvented.

As the streak is much larger than the actuator it can be safely assumed that the pressure variations over the orifice due to the streak disturbance do not need to be resolved to the same scale as the actuator. If this is accepted then an interactive simulation can be performed in an undisturbed turbulent boundary layer (with a grid of reasonable size) by superposing the pressure resulting from the streak (calculated earlier on a larger and coarser domain) onto the pressure due to the actuator disturbances. The final result is then obtained by interpolating and superposing both streak and streak/actuator results onto a common grid.

It is in fact slightly more economical to simulate the interaction of a streak and an inactive actuator, and separately simulate an active actuator in an undisturbed

boundary layer. This way three qualitatively different results can be obtained using superposition: the interaction of positive actuation with a high-speed streak (or negative actuation on a low-speed streak); the interaction of positive interaction with a low-speed streak (or negative actuation on a high-speed streak); and the interaction of an inactive actuator with a high- or low-speed streak.

The actuator model is in fact slightly nonlinear, but these effects are negligible for the magnitudes of velocity being considered.

7.3.2 Results

Figure 7.18 shows the effect of interaction on the jet velocity of the MEMS actuator. The difference between the interactive cases and the still-air case is quite significant. What this effectively means, is that streaks that are weak enough to be controlled by MEMS jets (see the previous sections) can still strongly influence the outputs of some MEMS actuators. However, what these simulations cannot model is the pressure fluctuations that would arise from the turbulent nature of the boundary layer – this would increase the interactive effect and could make the devices as unpredictable as the boundary layer itself.

The effect on the high-speed streak is shown in Figure 7.19. As with the prescribed simulations, the actuation successfully reduces the magnitude of the streak but is very localised in comparison. The effect of the MEMS on the low-speed streak (Figure 7.20) is more significant as the interaction makes the jet stronger. However, in general, the actuation in this section is less effective than that of §7.2, owing to the difference in net mass flow out of the devices. The strongest jet in this section has ten times less mass output than the average jet of section §7.2. The distributed scheme in §7.2.3 would perhaps be required to generate efficient actuation.

Finally, the interaction of the streaks with an 'inactive' actuator is shown in Figure 7.21. Although the effect of the inactive MEMS is quite weak in compar-

ison to the devices of §7.2, relative to the actuation in Figures 7.19 and 7.20 the disturbance is significant. The combined effect of a streamwise array of inactive MEMS could be enough to alter the bursting of the streaks in an uncontrolled manner. It is very difficult to know exactly how the streaks would be affected in this way, as the pressure perturbations over the MEMS will be strongly influenced by non-deterministic motions.

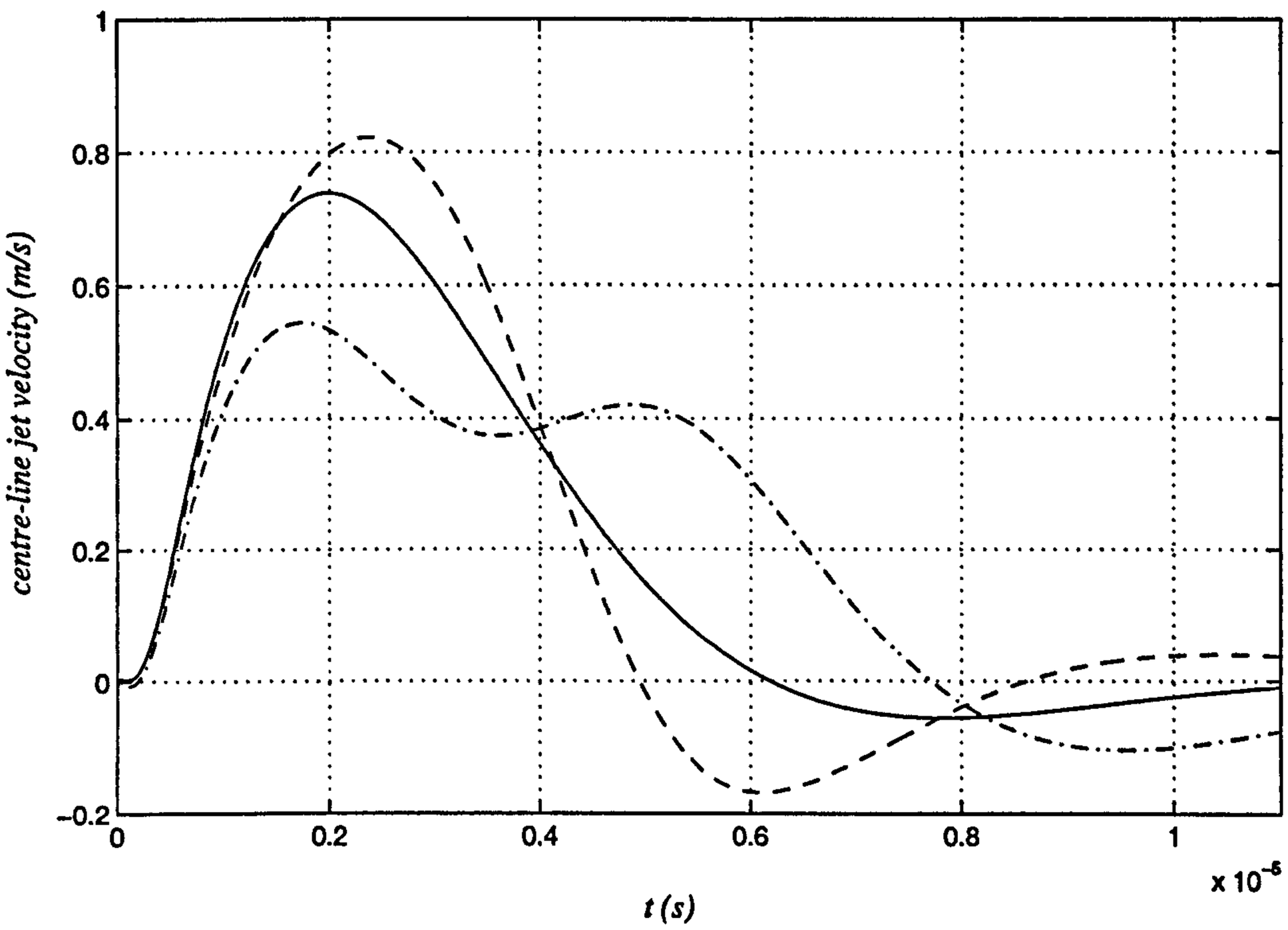

Figure 7.18: The variation of jet velocity with time. A MEMS actuator (R_o=10μm) issuing into still air (–); a MEMS actuator interacting with a high-speed streak (–·–); a MEMS actuator interacting with a low-speed streak (– –). See §A.5.5 for simulation parameters.

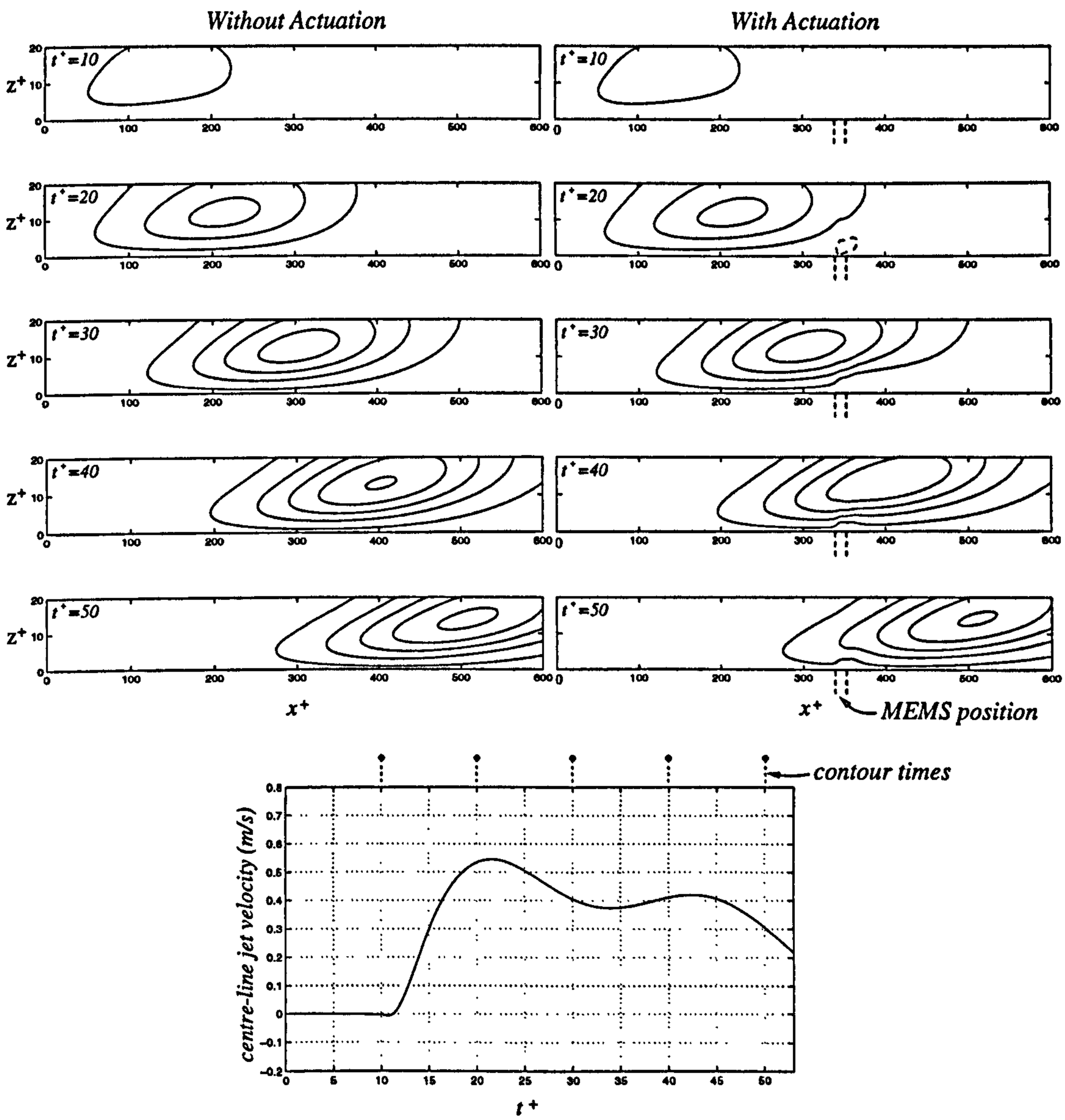

Figure 7.19: The effect of actuation on the development of a high-speed streak. Side-view contours (y^+=0) of streamwise velocity at times leading to the point of the streak's maximum magnitude; the nth contour is at u^+=± (0.019 + 0.038(n–1)) where solid and broken lines denote positive and negative values, respectively. The MEMS location is indicated by the vertical dashed lines at x^+=340.13–353.47 (R_o=10μm). For reference, the evolution of actuator jet velocity is shown beneath the contour plots. See §A.5.5 for simulation parameters. This simulation is also equivalent to negative actuation on a low-speed streak; in this case contour values and the velocity plot would be inverted.

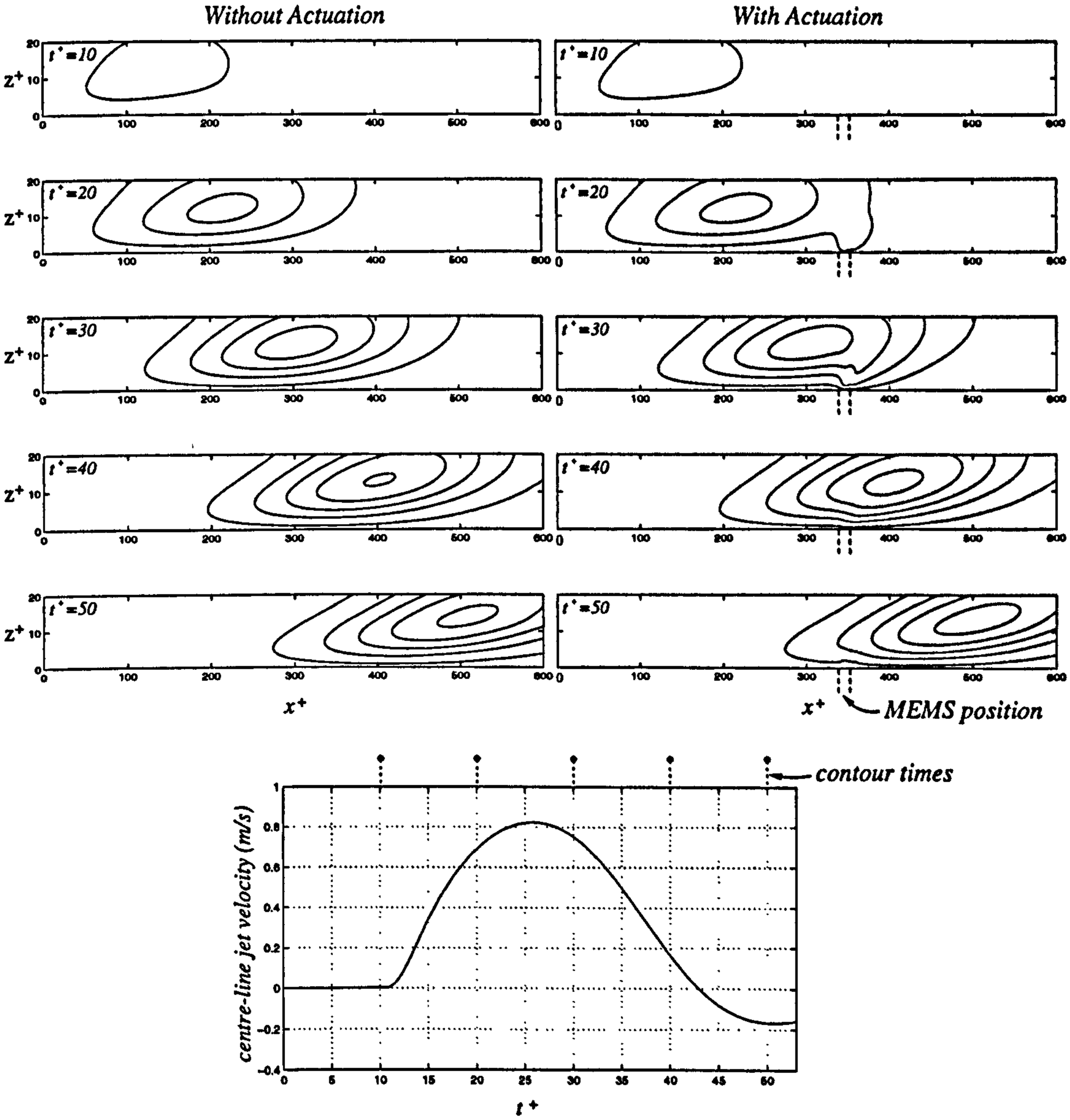

Figure 7.20: The effect of actuation on the development of a low-speed streak. Side-view contours (y^+=0) of streamwise velocity at times leading to the point of the streak's maximum magnitude; the nth contour is at u^+=–(0.019 + 0.038(n–1)) where solid lines denote *negative* values. The MEMS location is indicated by the vertical dashed lines at x^+=340.13–353.47 (R_o=10μm). For reference, the evolution of actuator jet velocity is shown beneath the contour plots. See §A.5.5 for simulation parameters. This simulation is also equivalent to negative actuation on a high-speed streak; in this case contour values and the velocity plot would be inverted.

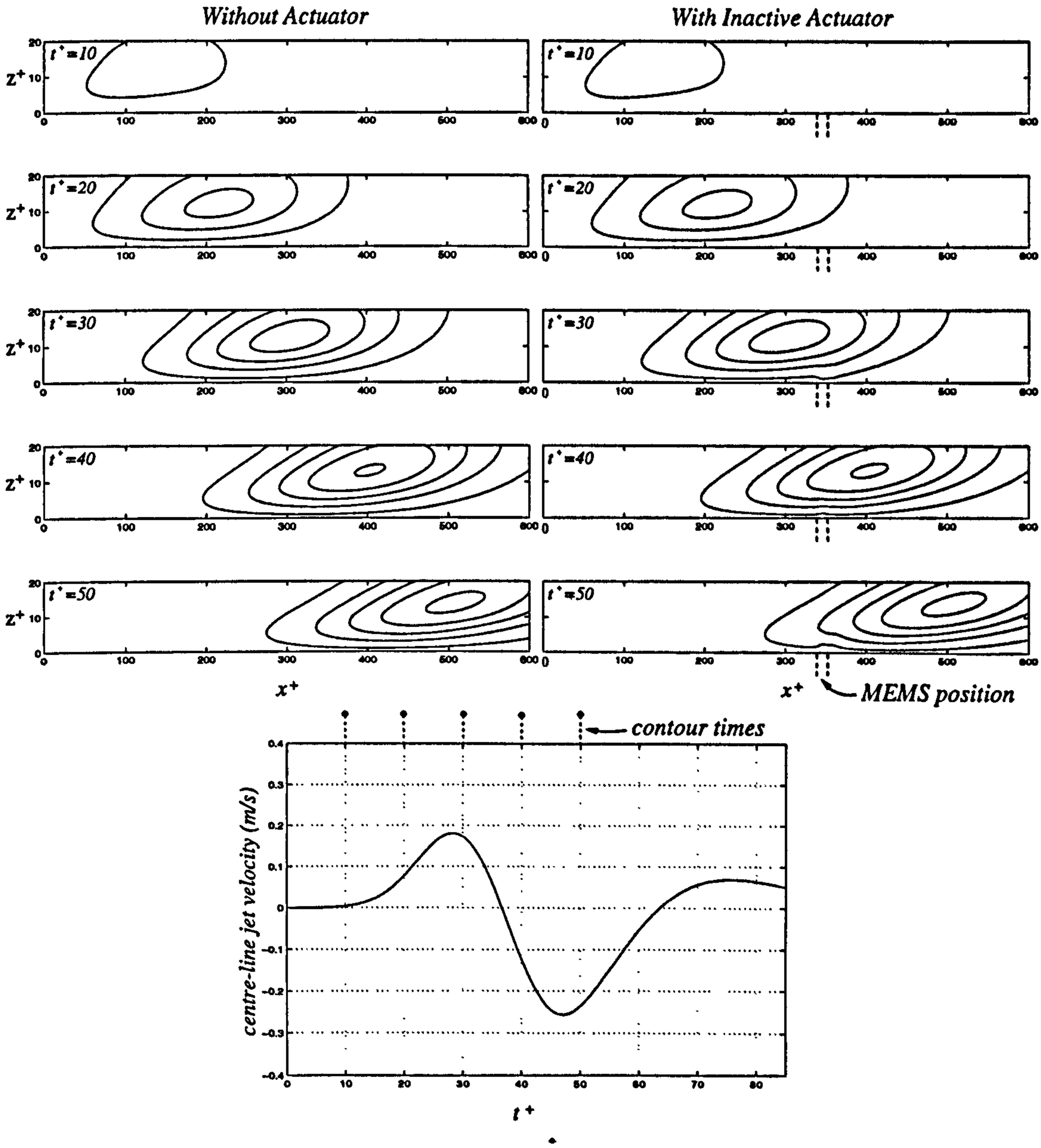

Figure 7.21: An 'inactive' MEMS actuator being driven by a high-speed streak. Side-view contours (y^+=0) of streamwise velocity at times leading to the point of the streak's maximum magnitude; the nth contour is at u^+=0.019 + 0.038(n–1) where solid lines denote positive values. The MEMS location is indicated by the vertical dashed lines at x^+=340.13–353.47 (R_o=10μm). The generated actuator jet velocity is shown beneath the contour plots. See §A.5.5 for simulation parameters. This simulation is also equivalent to a MEMS driven by a low-speed streak; in this case contour values and the velocity plot would be inverted.

7.4 Chapter Summary

In this chapter, streak control has been demonstrated using MEMS-jet actuators. The streaks were generated in §7.1 using an optimum body force. The spanwise wavelength of the optimum body force was found to be equal to the average streak spacing observed in experiments.

In §7.2 prescribed simulations were used to study streak control, and a number of different combinations and placements of MEMS jets were investigated (§7.2.1). The basic rules for actuation are as follows: to increase the level of turbulence, blowing should be applied to low-speed streaks and/or suction applied to high-speed streaks; to decrease the level of turbulence, blowing should be applied to high-speed streaks and/or suction applied to low-speed streaks.

The results in §7.2.2 reinforce the net-mass-flow performance criterion established in Chapter 5, and those in §7.2.3 demonstrate the efficiency of streamwise distributed control.

In §7.3 the interactive effects between the MEMS and the streaks were considered. Potentially, the interaction between the chaotic motions of the turbulent boundary layer and an inactive MEMS could produce severe actuator responses.

Chapter 8

Conclusions and Recommendations

In this final chapter the main conclusions of the thesis are summarised (§8.1). This is followed by some recommendations for future research (§8.2).

8.1 Conclusions

The main findings from the research can be listed as follows:

1. Synthetic jets are unsuitable for MEMS-based targeted control for two reasons: a) they would need to operate at incredibly-high driving frequencies in order to control the coherent structures, (b) at MEMS scale there is a risk of dust clogging the system during the inflow cycle. A modified design is proposed in Chapter 3 that does not have the aforementioned drawbacks.

2. The net mass flow has been shown to be the most appropriate choice of performance criterion for a pressure-jump diaphragm-cavity actuator. This was deduced by examining the ability of jets of different design to generate Tollmien-

Schlichting waves (§5.4) and to reduce/increase the magnitude of turbulent streaks (§7.2.2). This has implications for many types of flow actuator, not only the particular design considered here. For example, it implies that microflaps (Ho and Tai 1996) and microbumps (Carlson and Lumley 1996a,b) should be designed to generate maximum net deflection (maximum mass displacement), and not, as sometimes thought, maximum velocity.

3. Predicting the behaviour of scaled-down actuators is not a trivial matter. Chapter 3 has shown that many features of the system, such as optimum orifice radius and maximum velocity, are greatly affected by actuator size.

The disturbances generated from the actuators are also scale dependent, and can differ greatly from MEMS- to micro-scale (§5.2). This is of particular importance to researchers wishing to draw comparison between super-scale experiments and flight-scale conditions. For this reason a method is described by which, under certain circumstances, scale comparisons can be made safely (§5.2.3, §5.3.3).

4. In Chapter 5, §5.5, MEMS actuation was shown to eventually produce a Tollmien-Schlichting wave packet. This is a crucial result regarding the viability of MEMS-based control, as it demonstrates the ability of MEMS actuators to have macro impact.

5. It has been shown in Chapter 6, §6.4, that cavity-driven actuators (Coe *et al.* (1994), Rathnasingham 1997, Roos 1997, Smith and Glezer 1998, Jacobson and Reynolds (1998), Lachowicz *et al.* 2000) can experience Helmholtz resonance. Accordingly, if the pressure perturbations in a boundary layer are comparable to the Helmholtz frequency of a cavity-driven device, large mass flow rates in and out of the cavity will occur. If supposedly inactive devices have the potential to amplify flow instabilities, this could produce unpredictable effects to the boundary layer such as premature transition to turbulence. For an active control actuator this is a very negative effect, and a design condition is described in Chapter 3, §3.6.5, that will avoid uncontrolled Helmholtz resonance.

6. In Chapter 7 a method for modelling streaks (streamwise vortices) has been developed. Using this model it has been demonstrated that flight-scale turbulent streaks can be controlled by MEMS-scale actuation. However, the MEMS disturbance is quite localised in comparison to the developing streak and to accommodate this, a method of streamwise distributed control has been proposed and demonstrated that is more efficient (§7.2.3).

7. It has been shown that the interaction between cavity-driven devices and the boundary layer within which they perform is not negligible; Helmholtz resonance is an example of this. The interaction is also responsible for a significant damping effect which occurs in MEMS-scale devices (§6.1). Finally, some of the interactive simulations in Chapter 7 suggest that there is potential for the device to strongly interact with the pressure fluctuations in a turbulent boundary layer.

8.2 Recommendations for Further Work

As yet our knowledge of turbulence, and the technology of MEMS, is not sufficiently developed to enable a MEMS-based active control scheme to be developed. There is much work to be done in all areas before this becomes possible. In this section, recommendations for further research that can build on the current work are detailed.

8.2.1 Improved Actuator Modelling

In Chapter 2, the modelling of a MEMS actuator was described. It was established that several improvements could be made to the model. Firstly, that the diaphragm and PZT system should be modelled more comprehensively. In this thesis the PZT is incorporated into the linear plate model using an effective stiffness, a mid-plate boundary condition, and a vertical-force couple. To test or improve this method, governing equations for the active PZT should be established and solved; these would include all facets of the electrostrictive effect. The PZT model could then be coupled with a nonlinear plate model (see for example Lucey *et al.* 1997) to achieve an accurate description of the PZT and diaphragm system. Equally important, however, is the accurate estimation of structural damping for the system at MEMS scale – this may prove to be very difficult to obtain as estimating damping is problematic for many mechanical systems.

The essential two pieces of information to be obtained from an improved model are as follows: the maximum deflection that can be produced (this determines the maximum net mass flow of the device), and the speed at which the diaphragm can deflect (this affects the velocity and the duration of the jet). If this information can be calculated using an accurate model, then a simpler model, such as that described in Chapter 2, could be calibrated for use in the full application simulations.

The most limiting aspect of the current actuator model is the assumption

that the fluid is static in the cavity; it has been demonstrated that this is not an appropriate assumption in all cases. It seems that the only way to overcome this difficulty would be to solve the compressible Navier-Stokes equations in the cavity and the orifice in a similar fashion to Rizzetta *et al.* 1999. The compressible cavity/orifice code could be coupled to the existing incompressible boundary-layer code by enforcing continuity of pressure, velocity, and density at the orifice exit. Also, the compressible code could be used to help define more clearly the appropriate range for the more-economical model described in Chapter 2.

Finally, a compressible code could help evaluate an accurate Knusden number for the cavity-driven MEMS devices. It may be the case that at the small scales and high density variations, the continuum assumption is invalid. If so, research into the micro-fluidic effects and 'rarefied' modelling techniques would be of paramount importance.

8.2.2 A Simulated Control Scheme

One of the major successes of the current project has been the ability to model streaks without compromising the economy of the computations. This method could also be used in simulating a single-streak control scheme with various sensing/actuator configurations and control algorithms. Since the method of control is far from decided, an economical model, that can allow many ideas to be tested, is perhaps more relevant than a computationally-expensive DNS experiment.

8.2.3 The Suitability of Synthetic Jets

Many of the arguments and findings of this thesis have built a strong case against using synthetic-jet technology for targeted control. However, further simulations could be performed to establish this point more conclusively. Streak-control simulations, such as those in Chapter 7, could be used to demonstrate the difficulties of using a synthetic-jet mechanism to control single streaks.

8.2.4 Other Types of Flow Control and Actuator

The actuator and boundary-layer code could be used to investigate other types of flow control. In transition control, for example; large-scale jet devices could be used to cancel Tollmien-Schlichting waves or algebraically growing disturbances.

Different actuator types could also be simulated. Devices such as surface bumps or microvalves, could be modelled by a minimal adaption of the current techniques. There is much flexibility in both the boundary-layer and the actuator model.

8.2.5 The Nonlinear Behaviour of Streaks

The simulations of the streaks in this thesis have been completely linear. In reality of course, nonlinearities will occur at some point in the streak's development leading to breakdown and perhaps turbulent production. It is the promotion or delay of the breakdown that is the purpose of control. A serious limitation of the linear research is that it has to guess the property of the streak that determines the onset of the nonlinear instability (for example, maximum streamwise velocity).

It would be particularly insightful to incorporate the key nonlinear terms in the simulation of the evolution of the streaks, using the method of Chapter 7. Firstly, the breakdown process can be observed in isolation. Secondly, with nonlinear simulations, quantitative information can be extracted, in contrast to the qualitative results obtained in the linear simulations of Chapter 7. Finally, the effect of actuation can be judged in terms of its ability to delay or promote breakdown. In this way the optimum type, and configuration, of actuation could be established. This would be a very important piece of information for the progression of MEMS-based targeted control.

The nonlinear simulations, including the improvements to the actuator model suggested in §8.2.1, would be far more computationally demanding than those performed in this thesis. It can be expected, however, that future researchers will

have the advantage of greater computing power.

Appendix A

Simulation Parameters

A.1 Parameters for Chapter 3

The following parameters are constant for all simulations performed in Chapter 3 : gas constant for air k=287.1 J kg^{-1} K^{-1}; air temperature T=293 K, the kinematic viscosity of air ν=15 x10^{-6} m^2 s^{-1}; ambient air density ρ_o=1.196 kg m^{-3}; piezoelectric constant d_{31}=d_{32}=220 x 10^{-12} m V^{-1}. For nomenclature, refer to the beginning of Chapter 3.

A.1.1 Parameters for §3.1.1

H_c=2 mm; R_d 12.7 mm; w_{max}=5 μm; l=1.6 mm; ω_d=1366 Hz; R_o=0.1–1 mm; N_o=20; Δt=10 μs

A.1.2 Parameters for §3.1.2

H_c=1.2–5.25 mm; R_d=12.7 mm; w_{max}=5 μm; l=1.6 mm; ω_d=1366 Hz; R_o=0.6 mm; N_o=20; Δt=10 μs

A.1.3 Parameters for §3.1.3

R_d=12.7 mm; R_p=11 mm; t_d=0.1 mm; t_p=0.1 mm; N_d=80; E_d=110 GPa; E_p=63 GPa; ν_d=0.35; ν_p=0.3; ρ_d=8520 kg m^{-3}; ρ_p= 7600 kg m^{-3}; d=7 kN s m^{-3}

A.1.4 Parameters for §3.1.4

R_d=12.7 mm; t_d=0.1 mm; N_d=180; V/t_p=constant; E_d=110 GPa; E_p=63 GPa; ν_d=0.35; ν_p=0.3; ρ_d=8520 kg m^{-3}; ρ_p= 7600 kg m^{-3}.

A.1.5 Parameters for §3.1.5

H_c=2mm; R_o=0.3 mm; l=1.6 mm; N_o=20; Δt=10 μs; ω_d=1366 Hz; V=40 V; R_d=12.7 mm; R_p=11 mm; t_d=0.1 mm; t_p=0.1 mm; N_d=80; E_d=110 GPa; E_p=63 GPa; ν_d=0.35; ν_p=0.3; ρ_d=8520 kg m^{-3}; ρ_p= 7600 kg m^{-3}; d=7 kN s m^{-3}.

A.1.6 Parameters for §3.2.1

R_d=12.7g; R_p=11g; t_d=0.1g; t_p=0.1g; N_d=80; E_d=110 GPa; E_p=63 GPa; ν_d=0.35; ν_p=0.3; ρ_d=8520 kg m^{-3}; ρ_p= 7600 kg m^{-3}; d=7 kN s m^{-3}.

A.1.7 Parameters for §3.2.2

H_c=2g; R_o=0.3g; l=1.6g; N_o=20; V/t_p=400 kV m^{-1}; R_d=12.7g; R_p=11g; t_d=0.1g; t_p=0.1g; N_d=80; E_d=110 GPa; E_p=63 GPa; ν_d=0.35; ν_p=0.3; ρ_d=8520 kg m^{-3}; ρ_p= 7600 kg m^{-3}; d=7 kN s m^{-3}.

A.1.8 Parameters for §3.2.3

R_d=254 μm; t_d=1 μm; N_d=180; V/t_p=constant; E_d=80 GPa; E_p=63 GPa; ν_d=0.35; ν_p=0.3; ρ_d=8520 kg m^{-3}; ρ_p= 7600 kg m^{-3}.

A.1.9 Parameters for §3.2.4

H_c=2g; l=1.6g; N_o=20; w_{max}=.005g; R_d=12.7g; R_p=11g; t_d=0.1g; t_p=0.1g; N_d=80; E_d=110 GPa; E_p=63 GPa; ν_d=0.35; ν_p=0.3; ρ_d=8520 kg m^{-3}; ρ_p= 7600 kg m^{-3}.

A.1.10 Parameters for §3.3.1

H_c=1–50 mm; R_o=0; R_d=12.7 mm; R_p=11 mm; t_d=0.1 mm; t_p=0.1 mm; N_d=80; E_d=110 GPa; E_p=63 GPa; ν_d=0.35; ν_p=0.3; ρ_d=8520 kg m^{-3}; ρ_p= 7600 kg m^{-3}.

A.1.11 Parameters for §3.3.2

R_o=0–0.4 mm;H_c=2mm R_d=12.7 mm; R_p=11 mm; t_d=0.1 mm; t_p=0.1 mm; N_d=80; E_d=110 GPa; E_p=63 GPa; ν_d=0.35; ν_p=0.3; ρ_d=8520 kg m^{-3}; ρ_p= 7600 kg m^{-3}.

A.1.12 Parameters for §3.3.3

H_c=50μm; R_o=5 μm; l=10 μm; N_o=20; Δt=0.02 μs; V/t_p=400 kVm^{-1}; R_d=50 μm; R_p=40 μm; t_d=1 μm; t_p=1 μm; N_d=80; E_d=100 GPa; E_p=63 GPa; ν_d=0.27; ν_p=0.3; ρ_d=2300 kg m^{-3}; ρ_p= 7600 kg m^{-3}; d=100 kN s m^{-3}.

A.1.13 Parameters for §3.4.1

d=10–1000 kN s m^{-3}; H_c=50μm; R_o=5 μm; l=10 μm; N_o=20; Δt=0.02 μs; V/t_p=400 kVm^{-1}; R_d=50 μm; R_p=40 μm; t_d=1 μm; t_p=1 μm; N_d=80; E_d=100 GPa; E_p=63 GPa; ν_d=0.27; ν_p=0.3; ρ_d=2300 kg m^{-3}; ρ_p= 7600 kg m^{-3}.

A.1.14 Parameters for §3.4.2

R_o=3.8–9.8 μm; H_c=50μm; l=10 μm; N_o=20; Δt=0.02 μs; V/t_p=400 kVm^{-1}; R_d=50 μm; R_p=43 μm; t_d=1 μm; t_p=1.22 μm; N_d=80; E_d=100 GPa; E_p=63 GPa; ν_d=0.27; ν_p=0.3; ρ_d=2300 kg m^{-3}; ρ_p= 7600 kg m^{-3}; d=100 kN s m^{-3}.

A.1.15 Parameters for §3.4.3

R_o=7.8 μm; H_c=50μm; l=10 μm; N_o=20; R_d=50 μm.

A.1.16 Parameters for §3.5.2

R_o=250–450 μm; H_c=31.25 mm; l=6.25 mm; N_o=20; R_d=31.25 mm; N_d=80.

A.1.17 Parameters for §3.6.1

H_c=50g; l=10g; N_o=20; V/t_p=400 kVm^{-1}; R_d=50g; R_p=43g; t_d=1g; t_p=1.22g; N_d=80; E_d=100 GPa; E_p=63 GPa; ν_d=0.27; ν_p=0.3; ρ_d=2300 kg m^{-3}; ρ_p= 7600 kg m^{-3}; d=100 kN s m^{-3}.

A.2 Parameters for Chapter 4

Unless otherwise indicated all variables in Chapter 4 are non-dimensionalised using the length scale δ^* and the time scale δ^*/U_∞. In all simulations the kinematic viscosity is given by ν= 15 mm^2 s^{-1}. For nomenclature, refer to the beginning of Chapter 4.

A.2.1 Parameters for §4.3.1, Figures 4.2 and 4.4

R=769.56 (δ^*U_∞/ν); β=0.15391; ω_f=0.076956; X_d=600; Δx=1; N_c=64; L=4; T=653.17; Δt=0.50244; X_b–X_e=100–110; V_m=0.1U_∞.

A.2.2 Parameters for §4.3.1, Figure 4.3

R=666.4–719.86–769.56 (δ^*U_∞/ν); U_∞=30 m s^{-1}; $\bar{\beta}$=0–400; ω_f=6000δ^*/U_∞; X_d=600; Δx=1; N_c=32; L=4; T=16π/ω_f; X_b–X_e=100–110; V_m=0.1U_∞;

A.2.3 Parameters for §4.3.2, Figure 4.5

R=1720.8 (δ^*U_∞/ν); β=0.4; X_d=6400; Δx=32; N_c=64; L=2.4814; Δt=16; x_f=1600; z_f=2.485; a=64, b=0.08.

A.2.4 Parameters for §4.3.2, Figure 4.6

R=1720.8 (δ^*U_∞/ν); β=0.1–0.7; X_d=6400; Δx=32; N_c=64; L=2.4814; Δt=16; x_f=1600; z_f=2.485; a=64, b=0.08.

A.3 Parameters for Chapter 5

Unless otherwise indicated all variables in Chapter 5 are non-dimensionalised with the length scale δ^* and the time scale δ^*/U_∞. Variables with a superscript '+' are non-dimensionalised with friction velocity, v^*, and the viscous length scale (wall unit), ν/v^*. In all simulations the kinematic viscosity is given by ν= 15 $mm^2\ s^{-1}$. For nomenclature, refer to the beginning of Chapter 5.

A.3.1 Parameters for §5.2, Figure 5.3

For variables with MEMS- and Micro- scale alternatives the MEMS value is quoted first. R=2000 ($\delta^* U_\infty/\nu$); δ^*= 1 mm; U_∞=30 m s^{-1}; r_j=0.008δ^* and 8δ^*; t_j=12.5 r_j/U_∞; V_m=0.1U_∞; X_d=0.3 and 300; Δx=0.001 and 1; N_c=32; L=0.05 and 2; N_y=16; Y_d= 0.12 and 120; $\bar{T}$=t_j; Δt= 0.0005 and 0.5; X_b–X_e=0.15–0.166 and 150–166.

A.3.2 Parameters for §5.2, Figure 5.4

For variables with MEMS- and Micro- scale alternatives the MEMS value is quoted first. R=2000 ($\delta^* U_\infty/\nu$); δ^*= 1 mm; U_∞=30 m s^{-1}; r_j=0.008δ^* and 8δ^*; t_j=12.5 r_j/U_∞; V_m=0.1U_∞; X_d=1.5 and 400; Δx=0.005 and 1; N_c=32 and 48; L=0.05 and 2; N_y=16; Y_d= 0.2 and 120; $\bar{T}$=4.5t_j; Δt= 0.002 and 0.5; X_b–X_e=0.735–0.751 and 100–116.

A.3.3 Parameters for §5.3, Figure 5.7

For variables with MEMS- and Micro- scale alternatives the MEMS value is quoted first. v^*=1.186 m s^{-1}, U_∞=30 m s^{-1}; $\delta^* \approx$ 2.6 mm; r_j=8 μm and 8 mm; t_j=3.33 μs and 3.33 ms; V_m=3 m s^{-1}; X_d^+=21.82 and 2182; Δx^+=0.0727 and 72.7; N_c=32 and 64; L^+=10.2 and 816; N_y=16; Y_d^+= 4.743 and 4743; $\bar{T}$=t_j;

Δt^+= 0.00121 and 1.21; X_b^+–X_e^+=8.16–9.324 and 8160–9324.

A.3.4 Parameters for §5.4, Figure 5.8

R=2000, U_∞=30 m s^{-1}; δ^*= 1 mm; A_j=10δ^*; t_j= 10 δ^*/U_∞; V_m= 0.1U_∞; X_d=300; Δx=1; N_c=32 and 64; L=4; T=180; Δt= 0.5; X_b–X_e=60–70.

A.3.5 Parameters for §5.4, Figure 5.9

R=2000, U_∞=30 m s^{-1}; δ^*= 1 mm; A_j=10δ^*; t_j= 10–15 δ^*/U_∞; V_m= 0.1U_∞; X_d=300; Δx=1; N_c=32 and 64; L=4; T=180; Δt= 0.5; X_b–X_e=60–70.

A.3.6 Parameters for §5.4, Figure 5.10

R=2000, U_∞=30 m s^{-1}; δ^*= 1 mm; A_j=10δ^*; t_j= 10–12.5 δ^*/U_∞; V_m= 0.08–0.1 U_∞; X_d=300; Δx=1; N_c=32 and 64; L=4; T=180; Δt= 0.5; X_b–X_e=60–70.

A.3.7 Parameters for §5.5, Figure 5.12

R=2000, U_∞=30 m s^{-1}; δ^*= 1 mm; r_j=0.008δ^*; t_j= 0.1δ^*/U_∞; V_m=0.1 U_∞; X_d=0.3 and 0.6; Δx=0.001 and 0.002; N_c=32; L=0.1; $\bar{T}$=2t_j; Δt=0.0005 and 0.001; X_b–X_e=0.3–0.316.

A.3.8 Parameters for §5.5, Figures 5.13 and 5.14

R=2000, U_∞=30 m s^{-1}; δ^*= 1 mm; 2 r_j=0.01δ^*; t_j= 0.1δ^*/U_∞; V_m=0.1 U_∞; X_d=0.8 to 480; Δx=0.001 to 0.96; N_c=32; L=0.05 to 2; $\bar{T}$=2045t_j; Δt=0.0005 to 0.48; X_b–X_e=9.775–9.785.

A.4 Parameters for Chapter 6

Unless otherwise indicated all variables in Chapter 6 are non-dimensionalised with the length scale δ^* and the time scale δ^*/U_∞. Variables with a superscript '+' are non-dimensionalised with friction velocity, v^*, and the viscous length scale (wall unit), ν/v^*. In all simulations the kinematic viscosity is ν= 15 mm^2 s^{-1} and the piezoelectric constant d_{31}=d_{32}=220 x 10^{-12} m V^{-1}. For nomenclature, refer to the beginning of Chapter 6.

A.4.1 Parameters for §6.1, Figure 6.1

Boundary-layer code (interactive runs only): R=2000; δ^*= 1 mm; U_∞=30 m s^{-1}; X_d=0.2; Δx=1 $\times$ 10^{-3}; N_c=32; L=0.02, 1, 2.5; N_y=16; Y_d= 0.08; T=0.2; Δt=5 $\times$ 10^{-4}.

MEMS code: g=1 μm; H_c=50g; l=10 g; N_o=20; V/t_p=400 kVm^{-1}; R_o=5g-11g; R_d=50 g; R_p=43 g; t_d=1 g; t_p=1.22 g; N_d=80; E_d=100 GPa; E_p=63 GPa; ν_d=0.27; ν_p=0.3; ρ_d=2300 kg m^{-3}; ρ_p= 7600 kg m^{-3}; d=100 kN s m^{-3}.

A.4.2 Parameters for §6.1, Figure 6.2

For variables with more than one alternative the values are quoted in order of actuator scale (smallest first).

Boundary-layer code (interactive runs only): R=2000; δ^*= 1 mm; U_∞=30 m s^{-1}; X_d=0.2, 3, 40; Δx=1 $\times$ 10^{-3}, 2 $\times$ 10^{-2}, 0.2; N_c=32; L=0.02, 1, 2.5; N_y=16; Y_d= 0.08, 0.8, 12; T=0.2, 5, 150; Δt=5 $\times$ 10^{-4}, 0.01, 0.1 .

MEMS code: g=1 μm, 25 μm, 625 μm; H_c=50g; l=10 g; N_o=20; V/t_p=400 kVm^{-1}; R_o=5g to 11g, 2g to 4.4g, 0.64g to 1.6g; R_d=50 g; R_p=43 g; t_d=1 g; t_p=1.22 g; N_d=80; E_d=100 GPa; E_p=63 GPa; ν_d=0.27; ν_p=0.3; ρ_d=2300 kg m^{-3}; ρ_p= 7600 kg m^{-3}; d=100 kN s m^{-3}.

A.4.3 Parameters for §6.1.1, Figure 6.3

Boundary-layer code: R=2000; δ^*= 1 mm; U_∞=30 m s^{-1}; X_d=0.3; Δx=1 × 10^{-3}; N_c=32; L=0.5; N_y=16; Y_d=0.08; T=0.2; Δt= 5 × 10^{-4}; X_b–X_e=0.15–0.162.

MEMS code: H_c=50 μm; l=10 μm; N_o=20; V/t_p=800 kVm^{-1}; R_o=6 μm; R_d=50 μm; R_p=43 μm; t_d=1 μm; t_p=1.22 μm; N_d=80; E_d=100 GPa; E_p=63 GPa; ν_d=0.27; ν_p=0.3; ρ_d=2300 kg m^{-3}; ρ_p= 7600 kg m^{-3}; d=100 kN s m^{-3}.

A.4.4 Parameters for §6.1.1, Figure 6.4

Boundary-layer code: R=2000; δ^*= 1 mm; U_∞=30 m s^{-1}; X_d=0.3; Δx=1 × 10^{-3}; N_c=16, 32, 64; L=0.5; N_y=16; Y_d=0.08; T=0.2; Δt= 5 × 10^{-4}; X_b–X_e=0.15–0.162.

MEMS code: H_c=50 μm; l=10 μm; N_o=20; V/t_p=800 kVm^{-1}; R_o=6 μm; R_d=50 μm; R_p=43 μm; t_d=1 μm; t_p=1.22 μm; N_d=80; E_d=100 GPa; E_p=63 GPa; ν_d=0.27; ν_p=0.3; ρ_d=2300 kg m^{-3}; ρ_p= 7600 kg m^{-3}; d=100 kN s m^{-3}.

A.4.5 Parameters for §6.1.1, Figure 6.5

Boundary-layer code: R=2000; δ^*= 1 mm; U_∞=30 m s^{-1}; X_d=0.1, 0.2, 0.3; Δx=1 × 10^{-3}; N_c=32; L=0.5; N_y=16; Y_d=0.08; T=0.2; Δt= 5 × 10^{-4}; X_b–X_e=0.05–0.62, 0.1–0.112, 0.15–0.162.

MEMS code: H_c=50 μm; l=10 μm; N_o=20; V/t_p=800 kVm^{-1}; R_o=6 μm; R_d=50 μm; R_p=43 μm; t_d=1 μm; t_p=1.22 μm; N_d=80; E_d=100 GPa; E_p=63 GPa; ν_d=0.27; ν_p=0.3; ρ_d=2300 kg m^{-3}; ρ_p= 7600 kg m^{-3}; d=100 kN s m^{-3}.

A.4.6 Parameters for §6.1.1, Figure 6.6

Boundary-layer code: R=2000; δ^*= 1 mm; U_∞=30 m s^{-1}; X_d=0.2; Δx=1 × 10^{-3}; N_c=32; L=0.5; N_y=16; Y_d=0.06, 0.08, 0.1; T=0.2; Δt= 5 × 10^{-4}; X_b–X_e=0.1–0.116.

MEMS code: H_c=50 μm; l=10 μm; N_o=20; V/t_p=400 kVm^{-1}; R_o=8 μm; R_d=50 μm; R_p=43 μm; t_d=1 μm; t_p=1.22 μm; N_d=80; E_d=100 GPa; E_p=63 GPa; ν_d=0.27; ν_p=0.3; ρ_d=2300 kg m^{-3}; ρ_p= 7600 kg m^{-3}; d=100 kN s m^{-3}.

A.4.7 Parameters for §6.1.1, Figure 6.7

Boundary-layer code: R=2000; δ^*= 1 mm; U_∞=30 m s^{-1}; X_d=0.2; Δx=1 × 10^{-3},1.5 × 10^{-3},2 × 10^{-3}; N_c=32; L=0.5; N_y=16; Y_d=0.08; T=0.2; Δt= 5 × 10^{-4}; X_b–X_e=0.1–0.116.

MEMS code: H_c=50 μm; l=10 μm; N_o=20; V/t_p=400 kVm^{-1}; R_o=8 μm; R_d=50 μm; R_p=43 μm; t_d=1 μm; t_p=1.22 μm; N_d=80; E_d=100 GPa; E_p=63 GPa; ν_d=0.27; ν_p=0.3; ρ_d=2300 kg m^{-3}; ρ_p= 7600 kg m^{-3}; d=100 kN s m^{-3}.

A.4.8 · Parameters for §6.2, Figure 6.8

Boundary-layer code: R=2000; δ^*= 1 mm; U_∞=30 m s^{-1}; X_d=0.2; Δx=1 × 10^{-3}; N_c=32; L=0.02; N_y=16; Y_d=0.08; T=0.225; Δt= 5 × 10^{-4}; X_b–X_e=0.1–0.112.

MEMS code: H_c=50 μm; l=10 μm; N_o=20; V/t_p=400 kVm^{-1}; R_o=6 μm; R_d=50 μm; R_p=43 μm; t_d=1 μm; t_p=1.22 μm; N_d=80; E_d=100 GPa; E_p=63 GPa; ν_d=0.27; ν_p=0.3; ρ_d=2300 kg m^{-3}; ρ_p= 7600 kg m^{-3}; d=100 kN s m^{-3}.

A.4.9 Parameters for §6.2.1, Figure 6.9

For variables with alternatives, fine-discretisation values are quoted first.

Boundary-layer code: R=2000; δ^*= 1 mm; U_∞=30 m s^{-1}; X_d=0.2; Δx=6.66 × 10^{-4}, 1 × 10^{-3}; N_c=48, 32; L=0.019, 0.02; N_y=24, 16; Y_d= 0.12, 0.08; T=0.125; Δt= 1 × 10^{-4}, 5 × 10^{-4}; X_b–X_e=0.1–0.112.

MEMS code: H_c=50 μm; l=10 μm; N_o=20; V/t_p=400 kVm^{-1}; R_o=6 μm; R_d=50 μm; R_p=43 μm; t_d=1 μm; t_p=1.22 μm; N_d=80; E_d=100 GPa; E_p=63 GPa; ν_d=0.27; ν_p=0.3; ρ_d=2300 kg m^{-3}; ρ_p= 7600 kg m^{-3}; d=100 kN s m^{-3}.

A.4.10 Parameters for §6.2.2, Figure 6.10

Boundary-layer code: R=2000; δ^*= 1 mm; U_∞=30 m s^{-1}; X_d=0.2; Δx=1 × 10^{-3}; N_c=32; L=0.02; N_y=16; Y_d=0.08; T=0.225; Δt= 5 × 10^{-4}; X_b–X_e=0.1–0.112, 0.1–0.116.

MEMS code: H_c=50 μm; l=10 μm; N_o=20; V/t_p=400 kVm^{-1}; R_o=6 μm, 8 μm; R_d=50 μm; R_p=43 μm; t_d=1 μm; t_p=1.22 μm; N_d=80; E_d=100 GPa; E_p=63 GPa; ν_d=0.27; ν_p=0.3; ρ_d=2300 kg m^{-3}; ρ_p= 7600 kg m^{-3}; d=100 kN s m^{-3}.

A.4.11 Parameters for §6.2.3, Figure 6.11

Boundary-layer code: R=2000; δ^*= 1 mm; U_∞=30 m s^{-1}; X_d=0.2; Δx=1 × 10^{-3}; N_c=32; L=0.02; N_y=16; Y_d=0.08; T=0.125; Δt= 5 × 10^{-4}; X_b–X_e=0.1–0.112.

MEMS code: H_c=50 μm; l=10 μm; N_o=20; V/t_p=400 kVm^{-1}; R_o=6 μm; R_d=50 μm; R_p=43 μm; t_d=1 μm; t_p=1.22 μm; N_d=80; E_d=100 GPa; E_p=63 GPa; ν_d=0.27; ν_p=0.3; ρ_d=2300 kg m^{-3}; ρ_p= 7600 kg m^{-3}; d=100 kN s m^{-3}.

A.4.12 Parameters for §6.3

Boundary-layer code: v^*=10 m s^{-1}; ν/v^*=1.5 μm, R=5161; U_∞=253 m s^{-1}; $\delta^* \approx 3 \times 10^{-4}$; X_d^+=1067; Δx^+=1.333; N_c=32; L^+=10.2; N_y=16; Y_d^+=53.33; T^+=28.26; Δt^+= 0.0262; X_b^+–X_e^+=414–422.

MEMS code: H_c=50 μm; l=10 μm; N_o=20; V/t_p=400 kVm^{-1}; R_o=6 μm; R_d=50 μm; R_p=43 μm; t_d=1 μm; t_p=1.22 μm; N_d=80; E_d=100 GPa; E_p=63 GPa; ν_d=0.27; ν_p=0.3; ρ_d=2300 kg m^{-3}; ρ_p= 7600 kg m^{-3}; d=100 kN s m^{-3}.

A.4.13 Parameters for §6.4, Figure 6.15

Boundary-layer code: R=2000; δ^*= 1 mm; U_∞=30 m s^{-1}; X_d=400; Δx=1; N_c=64; L=8; N_y=16; Y_d=60; T=640; Δt=0.5; X_b–X_e=200–210; ω_{ts}=0.06.

MEMS code: H_c=50 mm; l=10 mm; N_o=20; R_o=5 mm; R_d=30 mm.

A.5 Parameters for Chapter 7

Variables with a superscript '+' are non-dimensionalised with friction velocity, v^*, and the viscous length scale (wall unit), ν/v^*. In all simulations the kinematic viscosity is taken as ν= 15 mm^2 s^{-1} and the piezoelectric constant d_{31}=d_{32}=220 x 10^{-12} m V^{-1}. For nomenclature, refer to the beginning of Chapter 7.

A.5.1 Parameters for Streak Generation Simulations

The body force magnitude is varied to ensure that equal strengths of vorticity are created at the application point.

v^*=10 m s^{-1}; ν/v^*=1.5 μm; $R\approx$5161; U_∞=253 m s^{-1}; $\delta^*\approx 3\times10^{-4}$ m; X_d^+=4080; Δx^+=20.4; N_c=64; L^+=40.8; T^+=120; Δt^+=0.4; λ_f^+= 80-160; x_f^+=1020 in domain, 125 in §7.1, and 100 in §7.2; z_f^+=13-30; a_f^+=81.6; b_f^+=2.04; T_f^+=15.

The body force is only applied at wall-normal positions equivalent to *even*-numbered collocation points; i.e. $z_f^+=L^+/\cos((i-1)\,0.5\,\pi/64)-L^+$ for i=30,32,..,40.

A.5.2 Parameters for Optimum Streak

v^*=10 m s^{-1}; ν/v^*=1.5 μm; $R\approx$5161; U_∞=253 m s^{-1}; $\delta^*\approx 3\times10^{-4}$ m; X_d^+=4080; Δx^+=20.4; N_c=64; L^+=40.8; T^+=80; Δt^+=0.4; λ_f^+= 100; x_f^+=1020 in domain, 125 in §7.1, and 100 in §7.2 ; z_f^+=18.4; a_f^+=81.6; b_f^+=2.04; T_f^+=15.

A.5.3 Parameters for Long Prescribed Jet Simulation

v^*=10 m s^{-1}; ν/v^*=1.5 μm; $R\approx$5161; U_∞=253 m s^{-1}; $\delta^*\approx 3\times10^{-4}$ m; r_j=15 μm; t_j=6 μs (t_j^+=40); X_d^+=1000; Δx^+=3.33; N_c=32; L^+=10.2; N_y=16; Y_d^+=100; T^+=40; Δt^+=0.0645.

A.5.4 Parameters for Short Prescribed Jet Simulation

v^*=10 m s^{-1}; ν/v^*=1.5 μm; $R\approx$5161; U_∞=253 m s^{-1}; $\delta^*\approx 3\times10^{-4}$ m; r_j=15 μm; t_j=3 μs (t_j^+=20); X_d^+=1000; Δx^+=3.33; N_c=32; L^+=10.2; N_y=16; Y_d^+=100; T^+=40; Δt^+=0.0645.

A.5.5 Parameters for interactive simulations

Interaction between MEMS and undisturbed boundary layer

Boundary-layer code: v^*=10 m s^{-1}; ν/v^*=1.5 μm; $R\approx$5161; U_∞=253 m s^{-1}; $\delta^* \approx 3.06\times10^{-4}$; X_d^+=444.44–666.66; Δx^+=2.222; N_c=32; L^+=10.2; N_y=16; Y_d^+=100; T^+=85.7; Δt^+= 0.0439; X_b^+–X_e^+=340.13–353.47.

MEMS code: H_c=250 μm; l=20 μm; N_o=20; V/t_p=800 kVm^{-1}; R_o=10 μm; R_d=50 μm; R_p=43 μm; t_d=1 μm; t_p=1.22 μm; N_d=80; E_d=100 GPa; E_p=63 GPa; ν_d=0.27; ν_p=0.3; ρ_d=2300 kg m^{-3}; ρ_p= 7600 kg m^{-3}; d=100 kN s m^{-3}.

Interaction between streak and 'inactive' MEMS

Boundary-layer code: v^*=10 m s^{-1}; ν/v^*=1.5 μm; $R\approx$5161; U_∞=253 m s^{-1}; $\delta^* \approx 3.06\times10^{-4}$; X_d^+=444.44–666.66; Δx^+=2.222; N_c=32; L^+=10.2; N_y=16; Y_d^+=100; T^+=85.7; Δt^+= 0.0439; X_b^+–X_e^+=340.13–353.47.

MEMS code: H_c=250 μm; l=20 μm; N_o=20; V/t_p=0 kVm^{-1}; R_o=10 μm; R_d=50 μm; R_p=43 μm; t_d=1 μm; t_p=1.22 μm; N_d=80; E_d=100 GPa; E_p=63 GPa; ν_d=0.27; ν_p=0.3; ρ_d=2300 kg m^{-3}; ρ_p= 7600 kg m^{-3}; d=100 kN s m^{-3}.

Appendix B

Chapter 2

B.1 The Eccentrically Loaded Beam

This section demonstrates the difference in magnitude of lateral and vertical, deflections and accelerations, produced by a configuration similar to that of the PZT and diaphragm. This is used to justify the assumption that the lateral deflection of the PZT is effectively instantaneous. The example configuration is an axially and eccentrically loaded beam, and is shown in Figure B.1.

Firstly we can compare, assuming linearity, the magnitudes of static deflections in the lateral and vertical directions. The lateral strain, (ε), experienced by

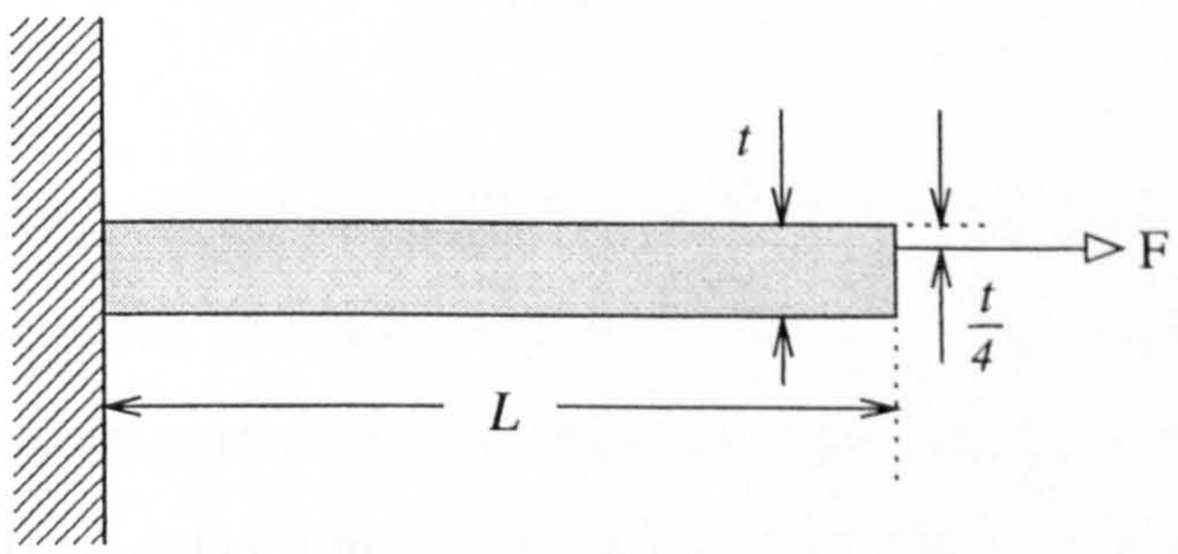

Figure B.1: An axially loaded cantilever with eccentricity.

the beam is expressed as

$$\varepsilon = \frac{F}{Ebt} \tag{B.1}$$

where E is the elastic modulus, F is the applied load, and b and t are the breadth and thickness of the beam respectively. The lateral extension (ξ) is then simply

$$\xi = \frac{FL}{Ebt} \tag{B.2}$$

where L is the beam's length. By calculating the moment generated, the vertical deflection can be estimated and compared with the lateral extension from equation (B.2). The applied moment per unit length is $M_a = Ft/4b$, and its relationship to the curvature of bending is given by

$$\frac{d^2\eta}{dx^2} = \frac{12M_a}{Et^3} = \frac{3F}{Ebt^2} \tag{B.3}$$

The vertical deflection at the end point (η) can be calculated by integrating equation (B.3) twice:

$$\eta = \frac{3FL^2}{2Ebt^2} \tag{B.4}$$

Now equations (B.2) and (B.4) can be combined to compare the magnitudes of lateral (ξ) and vertical (η) deflections:

$$\eta = \frac{3L}{2t}\xi \tag{B.5}$$

As $L \gg t$ it follows from equation (B.5) that $\xi \ll \eta$. And so to conclude the first section of this example; in configurations similar to this, such as the PZT and diaphragm, the lateral extension (ξ) caused by a lateral force, will be significantly less than the vertical deflection (η) caused by the induced moment.

The second part of this example compares the lateral and vertical accelerations

at time zero; at this point the beam will not have deflected. The lateral force per unit area at time zero is given by

$$q = \frac{2Fx}{bL^2} \tag{B.6}$$

where x is the distance along the beam. This gives an end of beam *lateral* acceleration of

$$\ddot{\xi} = \frac{2F}{bL\rho t} \tag{B.7}$$

where ρ is the density of the plate and the double-dot notation refers to a second derivative with respect to time.

To calculate the angular acceleration ($\ddot{\theta}$) due to the torque, the second moment of mass (I_m) must be calculated:

$$I_m = bL^3\rho t \tag{B.8}$$

The angular acceleration is then

$$\ddot{\theta} = \frac{T}{I_m} = \frac{F}{4bL^3\rho} \tag{B.9}$$

where the torque is given by $T = Ft/4$. The linear acceleration at x=L can be obtained from equation (B.9):

$$\ddot{\eta} = \frac{F}{4bL^2\rho} \tag{B.10}$$

Now the vertical ($\ddot{\eta}$) and lateral ($\ddot{\xi}$) accelerations can be compared by combining equations (B.7) and (B.10)

$$\ddot{\eta} = \frac{t}{8L}\ddot{\xi} \tag{B.11}$$

as $L \gg t$ it follows from equation (B.11) that $\ddot{\xi} \gg \ddot{\eta}$; i.e. the lateral acceleration is much greater than the vertical acceleration. Since it has already been shown

that the lateral deflection is likely to be much less than the vertical deflection, it can be safely assumed that lateral motion is instantaneous.

Appendix C

Chapter 3

C.1 Optimum R_o for Synthetic Jets

Rathnasingham and Breuer (1997a) derived an expression for the optimum Stokes parameter for any given design. This can be used to determine the optimum orifice width if the frequency of oscillation is already determined.

The method equates the maximum average jet velocity in two flow regimes; a viscous-dominated regime, where fluid is driven out through pressure fluctuations, and an incompressible regime, which allows velocities to be assumed in the cavity. Firstly, mass conservation is used to calculate the average jet velocity ($\overline{u}$) that occurs when incompressibilty is assumed:

$$\overline{u} = \frac{A_d \dot{\overline{w}}}{\pi R_o^2} \tag{C.1}$$

where A_d is the area of the diaphragm, R_o is the radius of the orifice, and $\dot{\overline{w}}$ is the average diaphragm velocity.

For the viscous-dominated regime the equation for quasi-steady Poiseuille flow

is used:

$$\overline{u} = \frac{\Pi R_o^2}{8\nu} \tag{C.2}$$

where ν is the kinematic viscosity, and Π is the pressure gradient approximatcly given by:

$$\Pi \approx \frac{P_o \overline{w}}{\rho l H_c} \tag{C.3}$$

where P_o is the ambient pressure, ρ is the density, H_c is the cavity height, and l is the length of the orifice.

It is assumed that the pressure in the cavity is unaffected by the mass extraction that $\overline{u}$ is responsible for, and governed only by the average diaphragm deflection ($\overline{w}$). In other words, the mass of the fluid in the cavity is assumed to be constant.

In order to estimate the optimum orifice width, the maximum average velocity in the two regimes are equated. If a sinusoidal diaphragm motion is assumed ($\overline{w} = G\sin(\omega t)$) the maximum velocity in each regime can be estimated. For the incompressible solution (equation C.1) the maximum average velocity is given by:

$$\overline{u}_{\max} = \frac{\omega A_d G}{\pi R_o^2} \tag{C.4}$$

For the quasi-steady Poiseuille flow (equation C.2) the maximum average velocity is given by:

$$\overline{u}_{\max} = \frac{G P_o R_o^2}{8\mu l H_c} \tag{C.5}$$

where μ is the dynamic visosity. Equations (C.4) and (C.5) are equated and the

optimum orifice radius is obtained:

$$R_o = \left(\frac{8\mu\omega l A_d H_c}{\pi P_o} \right)^{\frac{1}{4}} \tag{C.6}$$

C.2 The Correction Factor

In Section §3.6.2 the optimum orifice radius for a pressure-jump actuator was analytically estimated and compared with numerical simulations. The analytical solution under-estimated the optimum by 14% at all scales. A linear correction factor, c=1.14, was introduced to offset this constant error. In this section, an actuator of different proportions has been modelled, to test whether or not c is design independent. Figure C.1 shows the variation of maximum average velocity with orifice radius for the alternative design – the simulation parameters are as follows: H_c=100 μm; l=20 μm; N_o=20; ΔP=1000; R_d=50 μm; R_p=43 μm; t_d=1 μm; t_p=1.22 μm; N_d=120; E_d=100 GPa; E_p=63 GPa; ν_d=0.27; ν_p=0.3; ρ_d=2300 kg m^{-3}; ρ_p= 7600 kg m^{-3}; d=100 kN s m^{-3} (for nomenclature see the beginning of Chapter 3). The dashed line is the uncorrected analytical optimum, and the dashed/dotted line is the corrected optimum where c=1.14. The corrected analytical optimum is equal to the numerical optimum despite the dimensional changes, which implies that c is design independent.

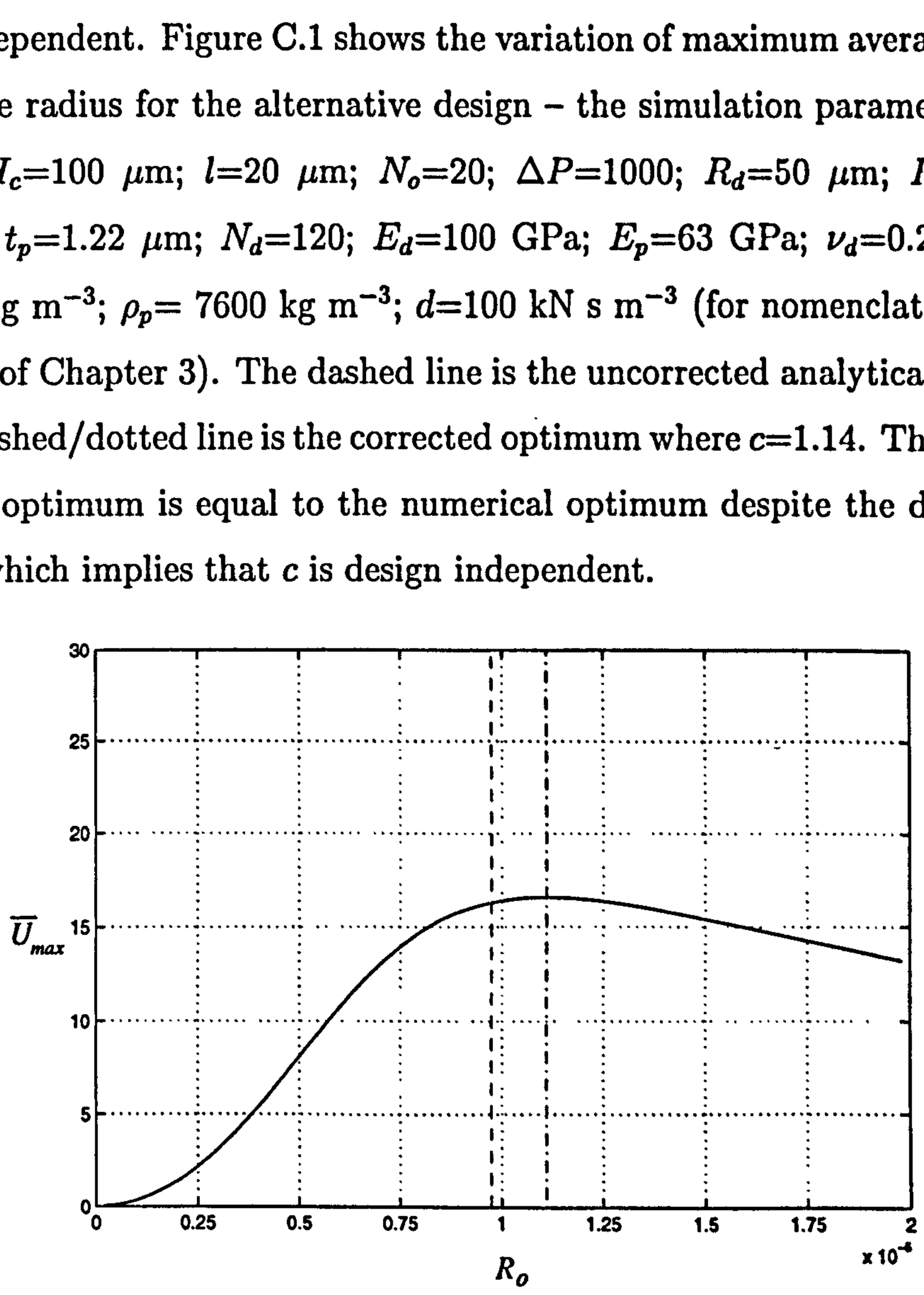

Figure C.1: The variation of maximum average velocity ($\overline{U}_{max}$) with orifice radius (R_o); analytical optimum (– –); corrected analytical optimum with c=1.14 (–·–)

Bibliography

ACARLAR, M. S. & SMITH, C. R. 1987 A study of hairpin vortices in a laminar boundary layer. Part 2. Hairpin vortices generated by fluid injection. *J. Fluid Mech.* **175**, 43–83.

AMITAY, M., HONOHAN, A., TRAUTMAN, M. & GLEZER, A. 1997 Modification of the aerodynamic characteristics of bluff bodies using fluidic actuators. *AIAA Paper* 97–2004.

AMITAY, M., SMITH, B. L. & GLEZER, A. 1998 Aerodynamic flow control using synthetic jet technology. *AIAA Paper* 98-0208.

ANDERSSON, A., BERGGREN, M. & HENNINGSON, D. S. 1999 Optimal disturbances and by-pass transition in boundary layers. *Phys. Fluids* **11**, 134–150.

ASKELAND, D. R. 1990 *The Science and Engineering of Materials.* Second SI Edition, London: Chapman and Hall.

BECH, K. H., HENNINGSON, D. S. & HENKES, R. A. W. M. 1998 Linear and nonlinear development of localized disturbances in zero and adverse pressure gradient boundary-layers. *Phys. Fluids* **10**, 1405–1418.

BÉRA, J. -C., MICHARD, M., SUNYACH, M. & COMTE-BELLOT, G. 2000 Changing lift and drag by jet oscillation: experiments on a circular cylinder with turbulent separation. *Eur. J. Mech. B - Fluids* **19**, 575–595.

BERLIN, S. & HENNINGSON, D. S. 1999 A nonlinear mechanism for receptivity of free-stream disturbances. *Phys. Fluids* **11**, 3749–3760.

BERTOLOTTI, F. P. 1997 Response of the Blasius boundary-layer to free-stream vorticity. *Phys. Fluids* **9**, 2286–2299.

BLACKWELDER, R. F. 1983 Analogies between transitional and turbulent boundary layers *Phys. Fluids* **26**, 2807–2815.

BLACKWELDER, R. F. & ECKELMANN, H. 1979 Streamwise vortices associated with the bursting phenomenon *J. Fluid Mech.* **94**, 577–594.

BLACKWELDER, R. F. & HARITONIDIS, J. H. 1983 Scaling of the bursting frequency in turbulent boundary layers. *J. Fluid Mech.* **132**, 87–103.

BREUER, K. S. & HARITONIDIS, J. H. 1990 The evolution of a localized disturbance in a laminar boundary layer. Part 1. weak disturbances. *J. Fluid Mech.* **220**, 569–594.

BREUER, K. S., HARITONIDIS, J. H. & LANDAHL, M. T. 1989 The control of transient disturbances in a flat plate boundary layer through active wall motion. *Phys. Fluids* **1**, 574–582.

BREUER, K. S. & LANDAHL, M. T. 1990 The evolution of a localized disturbance in a laminar boundary layer. Part 2. strong disturbances. *J. Fluid Mech.* **220**, 595–621.

BRYANT, R. G., FOX, R. L., LACHOWICZ, J. T. & CHEN, F. -J. 1999 Piezoelectric synthetic jets for aircraft control surfaces. *SPIE Conference on Industrial and Commercial Applications of Smart Structures Technologies, Newport Beach, California, March 1999.* SPIE Vol.3674, pp 220–227.

BUSHNELL, D. M. & MCGINLEY, C. B. 1989 Turbulence control in wall flows. *Ann. Rev. Fluid Mech.* **21**, 1–20.

BUTLER, K. M. & FARRELL, B. F. 1992 Three-dimensional optimal perturbations in viscous shear flow. *Phys. Fluids* 4, 1637–1650.

BUTLER, K. M. & FARRELL, B. F. 1993 Optimal perturbations and streak spacing in wall-bounded turbulent shear flow. *Phys. Fluids* 4, 774–777.

CARLSON, H. A. & LUMLEY J. L. 1996a Active control in the turbulent wall layer of a minimal flow unit. *J. Fluid Mech.* **329**, 341–371.

CARLSON, H. A. & LUMLEY J. L. 1996b Flow over an obstacle emerging from the wall of a channel *AIAA J.* **34**, 924–931.

CHAPRA, S. C. & CANALE, R. P. 1990 *Numerical methods for engineers.* Second Edition, London: McGraw-Hill.

CHOI, H., MOIN, P. & KIM, J. 1994 Active turbulence control for drag reduction in wall-bounded flows. *J. Fluid Mech.* **262**, 75–110.

COE, D. J., ALLEN, M. G., TRAUTMAN, M. A. & GLEZER, A. 1994 Micromachined jets for manipulation of macro flows. *Solid-State Sensor and Actuator Workshop, Hilton Head, South Carolina, June 13–16, 1994.* pp 243–247.

COLES, D. 1956 The law of the wake in the turbulent boundary layer. *J. Fluid Mech.* 1, 191–226.

CROOK, A., SADRI, A. M., & WOOD, N. J. 1999 The development and implementation of synthetic jets for the control of separated flow. *AIAA Paper* 93–3176.

CULLEN, L. M. 1999 Acoustic receptivity in boundary layers with surface roughness. *PhD thesis, Queen Mary and Westfield College London.*

DAVIDSON, B. J. & RILEY, N. 1972 Jets induced by oscillatory motion. *J. Fluid Mech.* **53**, 287–303.

DAVIES, C. & CARPENTER, P. W. 1997 Numerical simulation of the evolution of Tollmien-Schlichting waves over finite compliant walls. *J. Fluid Mech.* **335**, 361–392.

DAVIES, C. & CARPENTER, P. W. 1999 A novel velocity-vorticity formulation of the Navier-Stokes equations. pt. 1: mathematical and numerical methods with application to convective instabilities of the rotating-disk boundary layer. *University of Warwick, Fluid Dynamics Research Centre*, Tech. Rept 97/1, Dec. 1999.

DONOVAN, J. F., KRAL, L. D. & CARY, A. W. 1998 Active flow control applied to an airfoil. *AIAA Paper* 98–0210.

DOWLING, A. P. & FFOWCS WILLIAMS, J. E. 1983 *Sound and Sources of Sound.* Ellis Horwood Pubs., Chichester, UK, pp. 130–134.

ELLINGSON, T. & PALM, E. 1975 Stability of linear flow. *Phys. Fluids* **18**, 487–488.

FASEL, H. F., RIST, U. & KONZELMANN, U. Numerical investigation of the three-dimensional development in boundary-layer transition. *AIAA J.* **28**, 29–37

FERZIGER, J. H. 1998 *Numerical Methods for Engineering Applications.* Second Edition, Wiley-Interscience, New York.

FIEDLER, H. E. & FERNHOLZ, H. H. 1990 On management and control of turbulent shear flows. *Prog. Aerospace Sci.* **27**, 305–387.

GAD-EL-HAK, M. 1993 Innovative control of turbulent flows. *AIAA Paper* 93-3268.

GAD-EL-HAK, M. 1999 The fluid dynamics of microdevices – The Freeman scholar lecture. *J. Fluids Eng.* **121**, 5–33.

GAD-EL-HAK, M. & BLACKWELDER R. F. 1989 Selective suction for controlling bursting events in a boundary layer. *AIAA J.* **27**, 308–314.

GAD-EL-HAK, M. & HUSSAIN, F. 1986 Coherent structures in a turbulent boundary layer. Part 1: generation of "artificial" bursts. *Phys. Fluids* **29**, 2124–2139.

GASTER, M. 1975 A theoretical model of a wave packet in the boundary layer on a flat plate. *Proc. R. Soc. Lond.* **A347**, 271–289.

GASTER, M. & GRANT, I. 1975 An experimental investigation of the formation and development of a wave packet in a laminar boundary layer. *Proc. R. Soc. Lond.* **A347**, 253–269.

GOLDSTEIN, M. E. & WUNDROW, D. W. 1998 On the environmental realizability of algebraically growing disturbances and their relation to Klebanoff modes. *Theoretical and Computational Fluid Dynamics* **10**, 171–186.

HASSAN, A. A. & JANAKIRAM, R. D. 1997 Effects of zero-mass "synthetic" jets on the aerodynamics of the NACA-0012 airfoil. *AIAA Paper* 97–2326.

HASSAN, A. A. 1998 Numerical simulation and potential applications of zero-mass jets for enhanced rotorcraft aerodynamic performance. *AIAA Paper* 98–0211.

HENNINGSON, D. S., LUNDBLADH, A. & JOHANSSON, A. V. 1993 A mechanism for bypass transition from localized disturbances in wall-bounded shear flows. *J. Fluid Mech.* **250**, 169–207.

HERBERT, TH. & LIN, N. 1993 Studies on boundary-layer receptivity with parabolized stability equations. *AIAA Paper* 93–3053.

HO, C.-M. & TAI, Y. -C. 1996 Review: MEMS and its applications for flow control. *J. Fluids Eng.* **118**, 437–447.

HO, C.-M. & TAI, Y. -C. 1998 Micro-electro-mechanical-systems (MEMS) and fluid flows. *Annu. Rev. Fluid Mech.* **30**, 579–612.

HOFMANN, L. M. & HERBERT, TH. 1997 Disturbances produced by the motion of an actuator. *Phys. Fluids* **9**, 3727–3732.

HOFMANN, L. M. & HERBERT, TH. 1998 Reproducing the flow response to actuator motion. *J. Comp. Phys.* **142**, 264–268.

HULTGREN, L. S. & GUSTAVSSON, L. H. Algebraic growth of disturbances in a laminar boundary layer. *Phys. Fluids* **24**, 1000–1004.

JACOBS, J.W., JAMES, R. D., RATLIFF, C. T. & GLEZER, A. 1993 Turbulent jets induced by surface actuators. *AIAA Paper* 93–3243.

JACOBSON, S. A. & REYNOLDS, W. C. 1993 Active boundary layer control using flush-mounted surface actuators. *Bull. Am. Phys. Soc.* **38** 2197.

JACOBSON, S. A. & REYNOLDS, W. C. 1998 Active control of streamwise vortices and streaks in boundary layers. *J. Fluid Mech.* **360** 179–211.

JAEGER, L. G. 1964 *Elementary theory of elastic plates.* Oxford; New York: Pergamon; Macmillan (NY).

JAMES, R. D., JACOBS, J. W. & GLEZER, A. 1994 Experimental investigation of a turbulent jet produced by an oscillating surface actuator. *Appl. Mech. Rev.* **47**, S127–S131.

JIMÉNEZ, J. & MOIN, P. 1991 The minimal flow unit in near-wall turbulence. *J. Fluid Mech.* **225**, 213–240.

JOHANSSON, A. V., ALFREDSSON P. H. & ECKELMANN, H. 1987 *Advances in Turbulence.* Springer Verlag.

JOHANSSON, A. V., ALFREDSSON P. H. & KIM, J. 1991 Evolution and dynamics of shear layer structure in near-wall turbulence. *J. Fluid Mech.* **224**, 579–599.

JOSLIN, R. D., LACHOWICZ, J. T. & TAO, C. 1998 DNS of flow induced by a multi-flow actuator. *ASME Fluids Engineering Division Meeting* ASME paper number FEDSM98-5302.

KENDALL, J. M. 1985 Experimental study of disturbances produced in a pretransitional laminar boundary layer by weak free stream turbulence. *AIAA Paper* 85–1695.

KIM, J. & LIM, J. 2000 A linear process in wall-bounded turbulent shear flows. *Phys. Fluids* **12**, 1885–1889.

KLINE, S. J., REYNOLDS, W. C., SCHRAUB, F. A. & RUNSTADLER, P. W. 1967 The structure of turbulent boundary layers. *J. Fluid Mech.* **30**, 741–773.

KOUMOUTSAKOS, P. 1995 Simulations of vortex generators. *Annual Research Briefs, Centre for Turbulence Research, Stanford University,* pp 233–240.

KOUMOUTSAKOS, P. 1997 Active control of vortex-wall interactions. *Phys. Fluids* **9**, 3808–3816.

KOUMOUTSAKOS, P. 1999 Vorticity flux control for a turbulent channel flow. *Phys. Fluids* **11**, 248–250.

KRAL, L. D., DONOVAN, J. F., CAIN, A. B. & CARY, A. W. 1997 Numerical simulation of synthetic jet actuators. *AIAA Paper* 97–1823.

LACHOWICZ, J. T., YAO, C. & WLEZIEN, R. W. 1998 Scaling of an oscillatory flow-control actuator. *AIAA Paper* 98–0330.

LACHOWICZ, J. T., YAO, C. & WLEZIEN, R. W. 1999 Flow field characterization of a jet and vortex actuator. *Experiments in Fluids* **27**, 12–20.

LANDAHL, M. T. 1980 A note on algebraic instability of inviscid parallel shear flows. *J. Fluid Mech.* **98**, 243–251.

LANDAHL, M. T. 1990 On sublayer streaks. *J. Fluid Mech.* **212**, 593–614.

LEE, C., KIM, J., BABCOCK, D. & GOODMAN, R. 1997 Application of neural networks to turbulence control for drag reduction. *Phys. Fluids* **9**, 1740–1747.

LEIB, S. J., WUNDROW, D. W. & GOLDSTEIN, M. E. 1999 Effect of free-stream turbulence and other vortical disturbances on a laminar boundary-layer. *J. Fluid Mech.* **380**, 169–203.

LEISSA, A. W. 1969 *Vibration of Plates.* Washington, DC: NASA special publications no 160.

LIGHTHILL, M. J. 1978 Acoustic streaming *J. Sound Vib.* **61**, 391.

LÖFDAHL, L. & GAD-EL-HAK, M. 1999 MEMS applications in turbulence and flow control. *Prog. Aerospace Sci.* **35**, 101–203.

LUCEY, A. D., CAFOLLA, G. J., CARPENTER, P. W. & YANG, M. 1997 The nonlinear hydroelastic behaviour of flexible walls. *Journal of Fluids and Structures* **11**, 717–744.

LUCEY, A. D. & CARPENTER, P. W. 1993 The Hydroelastic stability of three-dimensional disturbances of a finite compliant wall *J. Sound and Vibration* **165**, 527–552.

MALLINSON, S. G., REIZES, J. A., HONG, G. & BUTTINI, M. 1999 Synthetic jet actuators for flow control. *SPIE Conference on Electronics and*

Structures for MEMS, Royal Pines Resort, Queensland, Australia, October 1999. SPIE Vol. 3891, pp 146–156.

MARGUERRE, K. & WOERNLE, H.-T. 1969 *Elastic Plates.* Blasidell Publishing Company, Waltham, Massachusetts.

MEHREGANY, M., DEANNA, R. G. & RESHOTKO, E. 1996 Microelectromechanical systems for aerodynamics applications. *AIAA Paper* 96–0421.

MEITZ, H. L. 1996 Numerical investigation of suction in a transitional flat-plate boundary layer. *PhD thesis, University of Arizona.*

NISHRI, B. & WYGNANSKI, I. 1998 Effects of periodic excitation on turbulent flow separation from a flap. *AIAA J.* **36**, 547–556.

ORLANDI, P. & JIMÉNEZ, J. 1994 On the generation of turbulent wall friction *Phys. Fluids* **6**, 634–641.

PIEKOS, E. S. & BREUER, K. S. 1996 Numerical modelling of micromechanical devices using the direct simulation Monte Carlo method *J. Fluids Eng.* **118**, 464–469.

RAO, K., NARASHIMA, R. & BADRI NARAYANAN, M. A. 1971 The 'bursting' phenomenon in a turbulent boundary layer. *J. Fluid Mech.* 48, 339.

RATHNASINGHAM, R 1997 System identification and active control of a turbulent boundary layer *PhD thesis, Department of Aeronautics and Astronautics, MIT.*

RATHNASINGHAM, R. & BREUER, K. S. 1997a Coupled fluid-structural characteristics of actuators for flow control. *AIAA J.* **35**, 832–837.

RATHNASINGHAM, R. & BREUER, K. S. 1997b System identification and control of a turbulent boundary layer *Phys. Fluids* **9**, 1867–1869.

RICHARDSON, E. G. & TYLER, E. 1929 The transverse velocity gradients near the mouth of a pipe in which an alternating or continuous flow of air is established. *Proc. Phys. Soc. London* **42**, 1–15.

RIZZETTA, D. P., VISBAL, M. R. & STANEK, M. J. 1999 Numerical investigation of sythetic-jet flow fields. *AIAA J.* **8**, 919–927.

ROBINSON, S. K. 1991 Coherent motions in the turbulent boundary layer *Annu. Rev. Fluid Mech.* **23**, 601–639.

ROOS, F. W. 1997 Synthetic-jet microblowing for vortex asymmetry management on a hemisphere-cylinder forebody. *AIAA Paper* 97–1973.

SADDOUGHI, S. G. 1994 Investigations of 'on-demand' vortex generators. *Annual Research Briefs, Centre for Turbulence Research, Stanford University* pp 197–203.

SCHAAF, S. A. & CHAMBRÉ, P. L. 1958 Flow of rarefied gases. *High Speed Aerodynamics and Jet Propulsion, Vol. 3, Princetown Univ. Press, Princeton, N.J.*

SCHOPPA, W. & HUSSAIN, F. 1998 A large-scale control strategy for drag reduction in turbulent boundary layers. *Phys. Fluids* **10**, 1049–1051.

SEIFERT, A., BACHAR, T., KOSS, D., SHEPSHELOVICH, M. & WYGNANSKI, I. 1993 Oscillatory blowing: a tool to delay boundary-layer separation *AIAA J.* **31**, 2052–2060.

SEIFERT, A. & PACK, L. G. 1999 Oscillatory control of separation at high Reynolds numbers. *AIAA J.* **37**, 1062–1071.

SEXL, T. 1930 Über den von E. G. Richardson entdeckten 'Annulareffekt'. *Z. Phys.* **61**, 349–362.

SHERMAN, F. S. 1990 *Viscous Flow.* McGraw Hill, New York.

SMITH, B. L. & GLEZER, A. 1997 Vectoring and small-scale motions effected in free shear flows using synthetic jet actuators. *AIAA Paper* 97–0213.

SMITH, B. L. & GLEZER, A. 1998 The formation and evolution of synthetic jets. *Phys. Fluids* **10** 2281–2297.

SMITH, C. R., WALKER, J. D. A., HAIDARI, A. H. & SOBRUN, U. 1991 On the dynamics of near-wall turbulence *Phil. Trans. R. Soc. Lond. A* **336**, 131–175.

SMITH, D. R., AMITAY, M., KIBENS, V., PAREKH, D. & GLEZER, A. 1998 Modification of lifting body aerodynamics using synthetic jet actuators. *AIAA Paper* 98–0209.

SPALDING, D. B. 1961 A single formula for the law of the wall. *J. Appl. Mech.* **28**, 455–457.

SWEARINGEN, J. D. & BLACKWELDER, R. F. 1987 The growth and breakdown of streamwise vortices in the presence of a wall. *J. Fluid Mech.* **182**, 255–290.

SZYMANSKI, F. 1932 Quelques solutions exactes des équations de l'hydrodynamique de fluide visqueux dans le cas d'un tube cylindrique. *J. Math. Pures Appl., (9).* **11**, 67–107.

WESTIN, K. J. A., BOIKO, A. V., KLINGMANN, B. G. B, KOZLOV, V. V. & ALFREDSSON, P. H. 1994 Experiments in a boundary layer subjected to free stream disturbances. *J. Fluid Mech.* **281**, 193–245.

WHITE, F. M. 1991 *Viscous Fluid Flow. Second Edition, McGraw Hill, New York.*

WILTSE, J. M. & GLEZER, A. 1993 Manipulation of free shear flows using piezoelectric actuators. *J. Fluid. Mech.* **249**, 261–285.

WOOD, N. J., SADRI, A. M. & CROOK, A. 2000 Control of turbulent separation by synthetic jets. *AIAA Paper* 2000–4331.

VANDELLI, N., WROBLEWSKI, D., VELONIS, M. & BIFANO, T. 1998 Development of a MEMS microvalve array for fluid control. *J. Micromechanical Systems* **7**, 395–402.

YANG, F. & KAO, I. 2000 Analysis of fluid flow and deflection for pressure-balanced MEMS diaphragm valves. *Sensors and Actuators* **79**, 13–21.